



MONASH University

**Investigations on Victorian brown coal as a fuel for power
generation in direct carbon fuel cells**

Adam Carl Rady

BEng (Hons)

Thesis submitted for the degree of Doctor of Philosophy at Monash University

February 2015

Faculty of Engineering, Department of Chemical Engineering

Copyright Notices

Notice 1

Under the Copyright Act 1968, this thesis must be used only under the normal conditions of scholarly fair dealing. In particular no results or conclusions should be extracted from it, nor should it be copied or closely paraphrased in whole or in part without the written consent of the author. Proper written acknowledgement should be made for any assistance obtained from this thesis.

Notice 2

I certify that I have made all reasonable efforts to secure copyright permissions for third-party content included in this thesis and have not knowingly added copyright content to my work without the owner's permission.

Acknowledgements

The support I have received throughout my candidature, as is the case with these acknowledgements, is first and foremost in realising this submission. I would like to acknowledge Brown Coal Innovation Australia (BCIA) for funding this research.

Firstly I would like to thank all of my supervisors for their tireless work and assistance during my studies. Sukhvinder Badwal, Sarb Giddey, Sankar Bhattacharya, and Bradley Ladewig, your efforts and knowledge are world class and it has been an honour to work in so many fantastic research groups. I have also been privileged in the quality of the facilities provided to me for the completion of this work at both CSIRO and Monash University. Also, thankyou to Justin Kimpton from the powder diffraction beamline at the Australian Synchrotron for his assistance with conducting synchrotron experiments and refinement of the data.

Secondly, to all my friends and colleagues at CSIRO, thank you for your support. To Ani Kulkarni for showing me the ropes of the DCFC and Chris with XRD, Gary for his curries, HyungKuk for his noises, and Daniel, without whom I would have no doubt submitted earlier. Thanks also to the friendship from all members of the Energy, Fuels and Reaction Engineering Research Group, as well as the Ladewig Membrane Research Group at Monash.

A special thanks to my family and friends, whom I am looking forward to catching up with, for their love and understanding.

Finally, to my fiancé Ashleigh, you have been a great supporter and believer in me. Here's to the next chapter in our life.

Table of content

Acknowledgements.....	i
Abstract.....	viii
Declaration by author.....	x
Publications.....	xii
List of figures.....	xiv
List of tables.....	xx
Abbreviations	xxii
Nomenclature.....	xxiv
Chapter 1: Introduction	2
1.1 Background.....	2
1.2 Motivation and aims of this research	5
1.2.1 Aims	6
1.3 Thesis structure	6
References.....	9
Chapter 2: A review of fuels for direct carbon fuel cells.....	13
Abstract.....	14
2.1 Introduction	14
2.1.1 DCFC reaction basics	16
2.2 Molten hydroxide DCFC.....	17
2.3 Molten carbonate DCFC	18
2.4 Solid oxide DCFC	21
2.4.1 Common design features of the solid oxide DCFC.....	22
2.4.2 Deposited-type solid oxide DCFC (RDCFC)	23
2.4.3 Physical contact-type solid oxide DCFC	25
2.4.4 Detached-type solid oxide DCFC.....	28
2.4.5 Gasification-driven SOFC	30
2.5 Solid oxide electrolyte DCFC with molten anode.....	33
2.5.1 Molten carbonate as a medium for carbon oxidation or “hybrid direct carbon fuel cell” (HDCFC)	33
2.5.2 Molten metal as a medium for carbon oxidation	36
2.6 Cell performance – effect of coal composition	37
2.6.1 Role of metals in coal.....	38

2.6.2 Composition of Victorian brown coals	42
2.7 Fuel preparation options and coal characteristics	43
2.7.1 Heat treatment	43
2.7.2 Acid washing	46
2.8 Analytical techniques	49
2.8.1 XPS – X-ray photoelectron spectroscopy	49
2.8.2 ICPOES – Inductively coupled plasma optical/atomic emission spectroscopy	49
2.8.3 XRD – X-ray diffraction	50
2.8.4 SEM – Scanning electron microscopy	50
2.8.5 Surface area measurement by gas adsorption	51
2.8.6 TDS/TPD – Thermal desorption spectroscopy	51
2.8.7 TGA – Thermogravimetric analysis	52
2.8.8 Frequency response analyser	52
2.8.9 Fuel analysis overview	52
2.9 Fuel types used in DCFCs	53
2.10 Concluding comments	54
References	63
Chapter 3: Common experimental	73
Chapter objective	73
3.1 Fuel preparation	74
3.2 Fuel characterisation and analysis	75
3.2.1 Thermogravimetric analysis	75
3.2.2 Inorganic content analysis	75
3.2.3 Carbon conductivity measurements	76
3.3 DCFC button cell fabrication and materials	76
3.3.1 Electrolyte disc fabrication	77
3.3.2 Electrode application	77
3.4 DCFC cell design and assembly	78
3.4.1 Test station	78
3.4.2 Test fixtures	78
3.5 Fuel cell operation and electrochemical techniques	81
3.6 Laboratory XRD measurements and analysis	82
3.7 Scanning electron microscopy and SEM-EDX	82
3.8 Experimental design overview	83
References	84

Chapter 4: Direct carbon fuel cell operation on brown coal	87
Chapter objective	87
Abstract	88
4.1 Introduction	88
4.2 Experimental	90
4.2.1 Fuel characterisation and analysis	90
4.2.2 Fuel cell testing	91
4.3 Results and discussion	91
4.3.1 Analysis of fuels	91
4.3.1.1 Proximate analysis and inorganic content of fuels	91
4.3.1.2 Assessment of volatile content of fuel	93
4.3.1.3 Boudouard gasification reactivity of fuels via TGA	94
4.3.2 Conductivity data for fuels	96
4.3.3 Fuel cell results	97
4.4 Conclusions	103
References	104
 Chapter 5: Degradation mechanism in a direct carbon fuel cell operated with demineralised brown coal	 109
Chapter objective	109
Abstract	110
5.1 Introduction	110
5.2 Experimental	111
5.3 Results and interpretation	112
5.3.1 Cell #1	113
5.3.1.1 Cell loading and diagnostics	113
5.3.1.2 Investigation of anode structure and microstructure	119
5.3.2 Cell #2	125
5.3.2.1 Cell loading and diagnostics	125
5.3.2.2 Effect of anode chamber atmosphere	128
5.4 Discussion	129
5.4.1 Anode structure and microstructure	130
5.4.2 Cell ohmic resistance	131
5.4.3 V-j measurements, current reversal and power overshoots	133
5.4.4 Analysis of electrode behaviour with electrochemical impedance spectroscopy	134
5.4.5 Effect of gas atmosphere in the anode chamber	135

5.5 Conclusions	138
References.....	139

Chapter 6: Direct carbon fuel cell operation on brown coal with a Ni-GDC/YSZ

anode	143
Chapter objective	143
Abstract.....	144
6.1 Introduction	144
6.2 Experimental	145
6.2.1 Anode preparation and fuel cell conditioning	146
6.2.2 Fuel cell operation and diagnostics.....	146
6.3 Results and interpretation	147
6.3.1 Demineralised Morwell char.....	147
6.3.2 Raw Morwell char	152
6.3.2.1 Cell #1	152
6.3.2.2 Cell #2.....	155
6.4 Discussion.....	156
6.4.1 Impedance behaviour of DM fuelled cell.....	157
6.4.1.1 Cell polarisation resistance	157
6.4.1.2 Cell ohmic resistance	159
6.4.2 Cell performance under different atmospheres.....	159
6.4.2.1 Effect on cell OCV.....	159
6.4.2.2 Effect on cell ohmic resistance	160
6.4.2.3 Effect on cell performance	160
6.4.3 Cell long-term chronopotentiometric tests	161
6.4.4 V-j curve trends and additional support for ash deposition	162
6.5 Conclusions	164
References.....	165

Chapter 7: Catalytic gasification of carbon in direct carbon fuel cells

Chapter objective	169
Abstract.....	170
7.1 Introduction	170
7.2 Experimental	172
7.3 Results and discussion	175
7.3.1 Fuel analysis	175
7.3.2 Carbon reactivity studies.....	176

7.3.3 Fuel cell testing	178
7.3.3.1 Cell ohmic resistance	179
7.3.3.2 DCFC operation under N_2/CO_2	179
7.3.3.3 DCFC operation under N_2	182
7.4 Conclusions	185
References.....	186
 Chapter 8: Conclusions and recommendations	 188
8.1 Conclusions	188
8.2 Contribution to knowledge in the field	189
8.3 Recommendations for future work	190

Abstract

Coal accounts for almost forty-percent of global power generation. Globally, coal is likely to retain a central role in power generation given its abundance and economic advantage over other fuels for the foreseeable future. However, current coal-fired power stations are inefficient (25-35% efficiency) and contribute to significant CO₂ emissions. Therefore, there is a concerted effort to improve the efficiency of coal use, potentially resulting in reduced CO₂ emissions.

Amongst alternative coal-based technologies, research into the direct carbon fuel cell (DCFC) has gathered momentum over the last decade. This is largely due to the high efficiency and carbon capture and storage compatibility of this promising and novel technology. Current research efforts in the DCFC field include the trialling of various types of carbons, predominantly from coal and biomass derived fuels, and assessing the influence of fuel properties on fuel cell performance and operability. In addition, understanding carbon reaction and conversion mechanisms, long-term fuel cell operation, as well as the compatibility of critical fuel cell components with cell operating environments are all pressing issues for advancing this technology. The present work addresses some of these key areas of interest in this field, in the context of Victorian brown coal char as a fuel in physical-contact solid oxide electrolyte DCFC. The studies were mostly focussed on lanthanum strontium cobalt ferrite (LSCF), a mixed ion-electronic conducting (MIEC) anode for the cell with yttria-stabilised zirconia (YSZ) as the electrolyte and LSCF as the cathode. However, due to long term instability of the LSCF in fuel environments, an alternative anode was also investigated.

Following a review of the desirable properties of solid fuels for use in a DCFC, the first investigation in this body of work directly addresses the influence of fuel-based properties on the performance of a DCFC. The results from DCFCs operated on Victorian brown coal are encouraging. A thorough characterisation and analysis of chars produced from the coal used has highlighted the contribution of inorganic species, inherent in the coal, to fuel reactivity and ultimately to fuel cell performance. These results were benchmarked against pure carbon in the form of carbon black.

Subsequent investigation into extended cell operation revealed insights into potential sources of cell performance degradation. Through careful monitoring of cell performance *via* electrochemical impedance spectroscopy, a mechanism of carbon

consumption contributing to loss of electrical conducting pathways was proposed. The state of the MIEC anode before and after cell operation was also investigated and showed that there were changes occurring to the anode phase relating to the coarsening of LSCF particles as well as minor phase instabilities. In addition, a phenomenon of power overshoots, not reported in any detail in the literature, during voltage-current density scans was observed and the influence of the fuel chamber atmosphere on this was evaluated.

Noting the structural changes to the LSCF electrode over extended periods of operation in strongly reducing atmospheres, a new anode was fabricated and trialled in the DCFC. The anode, composed of nickel, Gadolinia-Doped Ceria (GDC), and YSZ, delivered promising stability and operability when using a demineralised coal char as the fuel. Ash accumulation at the anode has been proposed as a likely contributor to degradation in the cell performance with time in the case of raw coal char.

In order to gain further insight into the role of coal impurities within the DCFC, carbon black was impregnated with various catalytic species (compounds of Ca, Mg and Fe) for a targeted investigation into the effect of these inorganic species on DCFC performance. Thermogravimetric analysis revealed effects of these catalytic elements on the reactivity ($\text{Ca} > \text{Fe} > \text{Mg}$) of the catalysed carbon fuels towards Boudouard gasification under a carbon dioxide atmosphere. The catalysed carbon reactivity translated into enhanced fuel cell performance in a similar order, supporting the relationship between carbon reactivity and cell performance identified in the earlier study.

The research outcomes from this project have generated substantial knowledge in the field of fuel (Victorian brown coal) preparation and characterisation, DCFC operation, carbon oxidation mechanism, cell performance, and lifetime of critical cell components with Victorian brown coal as a fuel for power generation. The findings presented in this study are expected to contribute to the development of this technology for the operation of direct-contact solid electrolyte based DCFCs using solid carbonaceous fuels.

Declaration by author

I hereby declare that this thesis contains no material which has been accepted for the award of any other degree or diploma at any university or equivalent institution and that, to the best of my knowledge and belief, this thesis contains no material previously published or written by another person, except where due reference is made in the text of the thesis. I have renumbered sections of submitted or published papers in order to generate a consistent presentation within the thesis.

This thesis includes three original papers published in peer reviewed journals and no unpublished publications. The ideas, development and writing up of all the papers in the thesis were the principal responsibility of myself, the candidate, working within the Department of Chemical Engineering under the supervision of Assoc. Prof. Bradley Ladewig, Prof. Sankar Bhattacharya, as well as within CSIRO Energy under the supervision of Dr. Sukhvinder Badwal and Dr. Sarbjit Giddey.

[The inclusion of co-authors reflects the fact that the work came from active collaboration between researchers and acknowledges input into team-based research.]

In the case of Chapters 1, 2, 3, 4, 5, 6, and 7, my contribution to the work involved the following:

Thesis chapter	Publication title	Publication status	Nature and extent of candidate's contribution
1	Includes excerpts from: Review of fuels for direct carbon fuel cells, Direct carbon fuel cell operation on brown coal, Degradation Mechanism in a Direct Carbon Fuel Cell Operated with Demineralised Brown Coal	Published	100 % of writing work used as excerpt

Thesis chapter	Publication title	Publication status	Nature and extent of candidate's contribution
2	Review of fuels for direct carbon fuel cells	Published	100 % of review work, writing
3	Includes excerpts from: Direct carbon fuel cell operation on brown coal, Degradation Mechanism in a Direct Carbon Fuel Cell Operated with Demineralised Brown Coal	Published	100 % of writing work used as excerpt
4	Direct carbon fuel cell operation on brown coal	Published	100 % of experiment and analysis work, writing
5	Degradation Mechanism in a Direct Carbon Fuel Cell Operated with Demineralised Brown Coal	Published	100 % of experiment and analysis work, writing
6	Direct carbon fuel cell operation on brown coal with a Ni-GDC/YSZ anode	Unpublished	100 % of experiment and analysis work, writing
7	Catalytic gasification of carbon in direct carbon fuel cells	Unpublished	100 % of experiment and analysis work, writing

I have / have not (circle that which applies) renumbered sections of submitted of published papers in order to generate a consistent presentation within the thesis.

Signed: 

Date:27 / 02 / 2015.....

Publications

Journal articles:

The following publications were prepared based on results presented within this thesis, and are included in chapters where stated:

Rady AC, Giddey S, Badwal SPS, Ladewig BP, Bhattacharya S. Review of fuels for direct carbon fuel cells. *Energy Fuels*. 2012;26:1471-88.

Rady AC, Giddey S, Kulkarni A, Badwal SPS, Bhattacharya S, Ladewig BP. Direct carbon fuel cell operation on brown coal. *Appl Energy*. 2014;120:56-64.

Rady AC, Giddey S, Kulkarni A, Badwal SPS, Bhattacharya S. Degradation Mechanism in a Direct Carbon Fuel Cell Operated with Demineralised Brown Coal. *Electrochim Acta*. 2014;143:278-90.

Published conference papers:

Rady AC, Giddey S, Badwal SPS, Ladewig BP, Bhattacharya S. Victorian brown coal as a fuel for direct carbon fuel cells – benefits and technical challenges. The 37th international technical conference on clean coal & fuel systems, Clearwater, USA. 2012:797-806.

List of figures

Chapter 1: Introduction	2
Figure 1.1: <i>Flow diagram of chapters in this thesis with key investigations highlighted</i>	8
 Chapter 2: A review of fuels for direct carbon fuel cells.....	13
Figure 2.1: <i>Reaction mechanism for electrochemical oxidation of carbon in molten carbonate</i>	20
Figure 2.2: <i>Cell voltage and Current density for a deposited-type solid oxide DCFC with different time of open circuit operation and significant activation polarization at high voltages (circled) - adapted from Li and co-authors</i>	24
Figure 2.3: <i>Depiction of the fuel oxidation in a physical contact-type solid oxide DCFC as proposed by Nakagawa and Ishida</i>	27
Figure 2.4: <i>Depiction of the fuel oxidation in a detached-type solid oxide DCFC as proposed by Nakagawa and Ishida</i>	29
Figure 2.5 <i>Single-step (in-situ) gasification</i>	32
Figure 2.6: <i>Indirect gasification (IDG)</i>	32
Figure 2.7: <i>Autothermal gasification (ATG)</i>	32
Figure 2.8: <i>Comparison between direct carbon SOFC cell performance with and without molten carbonate, adapted from Nabae and co-workers</i>	35
Figure 2.9: <i>CO molar percentage as a function of temperature and presence of Fe, adapted from Tang and Liu</i>	39
Figure 2.10: <i>Cell performance for different anodic materials, Cell-I (pure Ag anode), Cell-II (Ag-GDC anode), Cell-III (Ag-GDC anode with Fe)</i>	41
Figure 2.11: <i>Temperature map of AAEM species volatilisation during pyrolysis of Victorian brown coal</i>	46
Figure 2.12: <i>Typical TGA curve for activated carbon and response to acid washing</i>	48
 Chapter 3: Common Experimental	73
Figure 3.1: <i>Flow diagram of fuel preparation and utilization</i>	75
Figure 3.2: <i>DCFC test station in CSIRO Laboratories, picture courtesy of CSIRO Energy, with: 1. DCFC and furnace; 2. Gas pressure regulators and flow valves; 3. Exhaust</i>	78
Figure 3.3: <i>Schematic of cell arrangements</i>	79

Figure 3.4: <i>Fuel cell setup and components</i>	80
Chapter 4: Direct carbon fuel cell operation on brown coal	87
Figure 4.1: <i>Temperature profile and thermogravimetric mass loss curves for carbon fuel samples during thermal treatment under N_2. m: sample mass at a given time ; m_0: initial sample mass</i>	93
Figure 4.2: <i>Temperature profile and thermogravimetric mass loss curves for DM and RM during CO_2 gasification at 700 °C. m: sample mass at a given time ; m_0: initial sample mass</i>	94
Figure 4.3: <i>Temperature profile and thermogravimetric mass loss curves for carbon fuels during CO_2 gasification at 800 °C. m: sample mass at a given time ; m_0: initial sample mass</i>	96
Figure 4.4: <i>Voltage - Current density – Power density curves for DM and RM using two similar LSCF/GDC/LSCF button cells at 700 °C</i>	97
Figure 4.5: <i>Voltage – Current density – Power density curves for DM, RM, and carbon black (XC72) using three similar LSCF/GDC/LSCF button cells at 800 °C</i>	98
Figure 4.6: <i>Scanning electron micrographs of (a) carbon black, (b) demineralised Morwell char, (c) raw Morwell char</i>	99
Figure 4.7: <i>Impedance spectra for DM and RM at 700 °C under open circuit voltage</i>	100
Figure 4.8: <i>Impedance spectra for DM and RM at 800 °C under open circuit voltage</i>	101
Chapter 5: Degradation mechanism in a direct carbon fuel cell operated with demineralised brown coal	109
Figure 5.1: <i>(a) Cell timeline of all electrochemical cell measurements and voltages with V-j runs in grey for Cell #1 including Chronopotentiometric cell loading (20 $mA\ cm^{-2}$) at loading times of 1 hr 47 min (CP1): following 4th EIS, and 2 hrs (CP2) following 6th EIS. (b) Cell timeline of all electrochemical cell measurements and voltages with V-j runs in grey for Cell #2 including change of anode purge gas from N_2 to N_2/CO_2 between V-j Runs 3 and 4</i>	114
Figure 5.2: <i>First four electrochemical impedance spectra for cell #1 at 850 °C</i>	115
Figure 5.3: <i>Electrochemical impedance spectra for cell #1 at 850 °C before and after first CP loading (CP1)</i>	117

Figure 5.4: Voltage-current density and power density-current density curves of cell #1 under high purity N_2 at 850 °C for Runs 1, 2 and 3. Run 2 taken 68 min after Run 1 & Run 3 taken 3 hrs, 17 min after Run 1	118
Figure 5.5: SEM images of anode surfaces. (a) & (c): Cell #3 – unused cell. (b) & (d): Cell #1 - post-DCFC testing	120
Figure 5.6: SEM images of anode surfaces. (a) Cell #1 anode - post-DCFC testing showing surface particles and EDX scan windows for Spectrums 1-4. (b) showing surface particle scanned in Spectrum 1. (c) Cell #3 anode surface showing EDX scan window for Spectrum 5	120
Figure 5.7: EDX Spectra of cell #1 anode, post-DCFC testing, for windows as displayed in Fig. 5.6(a) as (a) Spectrum 1, (b) Spectrum 2, (c) Spectrum 3, (d) Spectrum 4; and for cell #3 as displayed in Fig. 5.6(c) as (e) Spectrum 5	121
Figure 5.8: SE Image of scan area for cell #1 anode post-DCFC testing, (a) with EDX-mapping micrographs for: (b) Oxygen, (c) Carbon, (d) Cobalt, (e) Iron, (f) Lanthanum, (g) Strontium, (h) Sulphur	123
Figure 5.9: XRD spectrum of an unused LSCF electrode (blue line) overlaid with used cell #1 anode diffractogram (red line), with phases as identified by Diffrac.EVA software	124
Figure 5.10: Voltage-current density and power density-current density curves of cell #2 under N_2 at 850 °C for Runs 1, 2 and 3. Run 2 taken 57 min after Run 1, and Run 3 taken 2 hrs, 20 min after Run 1	126
Figure 5.11: First three (taken under open circuit voltage) electrochemical impedance spectra for cell #2 at 850 °C, illustrating the effect of cell loading inbetween and holding time on cell resistances	127
Figure 5.12: Electrochemical impedance spectra (EIS) taken for cell #2 at 850 °C at OCV and under different loads	127
Figure 5.13: Voltage-current density and power density-current density curves of cell #2 at 850 °C for Runs 3 (N_2 anode purge gas), and Run 4 (N_2/CO_2 anode purge gas) at 850 °C	128
Figure 5.14: Effect of anode purge gas on electrochemical impedance spectra for cell #2 at 850 °C at OCV: 5 th EIS (N_2), and 6 th EIS (N_2/CO_2). Inset: equivalent circuit diagram used for modelling to calculate impedance data in Table 5.2	129

Chapter 6: Direct carbon fuel cell operation on brown coal with a Ni-GDC/YSZ anode

Figure 6.1: (a) Impedance spectra for DM under open circuit and under loadings of 10, 20, 30, and 40 mA cm ⁻² at 850 °C. Impedance spectra translated in the real	
--	--

axis so that all spectra intercept the graph origin, (b) EIS model fit impedance values as a function of loading for the high frequency arc (R_{hf}), intermediate frequency arc (R_1), low frequency arc (R_{Lf} and Ws_1), and sum of these values (R_p (tot)), with the ZView™ model's equivalent circuit diagram included above plot	148
Figure 6.2: Chronopotentiometric loadings of 20 mA cm^{-2} (CP1) and 40 mA cm^{-2} (CP2) for DM. Inset: EIS spectra taken after 7 min and 30 min of sustained loading at 40 mA cm^{-2} for first and second EIS, respectively, with voltage ranges of scans indicated on main axis	149
Figure 6.3: Voltage-current density-power density curves for DM under N_2 at 850°C	150
Figure 6.4: System ohmic resistance, taken as real axis intercept of impedance curves, as a function of time for all EIS taken in DM cell operation under N_2 . Results from loaded EIS marked as outlined data points with EIS loading indicated (mA cm^{-2}), open circuit EIS scans included as solid data points. Results from EIS spectra included in Figures 6.1(a) and 6.2 as indicated	151
Figure 6.5: Voltage-current density-power density curves for RM cell #1 under N_2 at 850°C	153
Figure 6.6: Voltage-current density-power density curves for RM cell #1, final run under N_2 (run 3) and subsequent run under N_2/CO_2 mixture (run 4) at 850°C	154
Figure 6.7: Impedance spectra for RM cell #1 under open circuit for anode atmospheres of N_2 and N_2/CO_2 gas mixtures at 850°C . Impedance spectra translated in the real axis so that all spectra intercept the graph origin	154
Figure 6.8: Chronopotentiometric loadings of 20 mA cm^{-2} for RM cell #2 taken under anode atmospheres of N_2 (CP1) and N_2/CO_2 gas mixture (CP2)	155
Figure 6.9: System ohmic resistance, taken as real axis intercept of impedance curves, as a function of time for all EIS taken in RM cell #2 operation under anode atmosphere of N_2 and N_2/CO_2 gas mixture as indicated. Results from loaded EIS marked as outlined data points with EIS loading indicated (mA cm^{-2}), open circuit EIS scans included as solid data points	156
Chapter 7: Catalytic gasification of carbon in direct carbon fuel cells	169
Figure 7.1: Fuel preparation, treatment, and utilisation flow diagram	174
Figure 7.2: XRD spectra and identified phases of Vulcan XC-72 as-received (CB-Plain), Mg-added (CB-Mg), Fe-added (CB-Fe), and Ca-added (CB-Ca), following heat treatment under N_2 and CO_2	176

Figure 7.3: <i>Thermogravimetric weight loss curves for carbon fuels under N_2 (during heating and cooling) and N_2/CO_2 (at 850 °C), as indicated, with temperature profile included. m: instantaneous sample mass, m_0: initial sample mass</i>	177
Figure 7.4: <i>Voltage – current density – power density curves for CB fuels at 850 °C under N_2/CO_2 anode purge</i>	180
Figure 7.5: <i>Impedance spectra for CB fuels at 850 °C under open circuit conditions and N_2/CO_2 anode purge</i>	180
Figure 7.6: <i>Voltage – current density – power density curves for CB fuels at 850 °C under N_2 anode purge</i>	182
Figure 7.7: <i>Impedance spectra for CB fuels at 850 °C under open circuit conditions and N_2 anode purge</i>	184

List of tables

Chapter 2: A review of fuels for direct carbon fuel cells	13
Table 2.1: <i>Summary of cell performance trends for physical contact-type solid oxide DCFC</i>	27
Table 2.2: <i>Summary of cell performance trends for detached-solid oxide DCFC</i>	27
Table 2.3: <i>Molten carbonate DCFC performance at 700 °C using Activated Carbon (AC) impregnated with various metal oxides</i>	38
Table 2.4: <i>Effect of different anodic materials on cell performance - summary of Figure 2.10 results</i>	40
Table 2.5 <i>Catalytic effects of selective coal inorganics on performance of CO₂-fed detached-type solid oxide DCFC</i>	40
Table 2.6: <i>Summary of catalysts and inhibitors for molten carbonate and solid oxide DCFCs</i>	41
Table 2.7: <i>Ash analysis of Victorian coal (atomic wt%) conducted by Brown and co-workers</i>	42
Table 2.8: <i>Typical ultimate analysis ranges of Victorian brown coals on a % mass-dry basis</i>	42
Table 2.9: <i>Summary of heat treatment results on raw coal properties and effect on molten carbonate DCFC performance</i>	45
Table 2.10: <i>Effect of acid washing on various coal properties and performance in molten carbonate DCFCs</i>	47
Table 2.11: <i>Analytical techniques used for DCFC fuel analysis</i>	53
Table 2.12: <i>DCFC Performances using various solid fuels under inert anode purge, PPD (peak power density), OCV (open circuit voltage)</i>	56
 Chapter 3: Common Experimental	 73
Table 3.1: <i>Experimental matrix for chapters involving DCFC experiments</i>	83
 Chapter 4: Direct carbon fuel cell operation on brown coal	 87
Table 4.1: <i>Proximate analysis of carbon fuels (wt%)</i>	91
Table 4.2: <i>Inorganic content of char samples as determined by ICP-OES (ppm as metals on dry basis)</i>	92
Table 4.3: <i>The weight loss as wt% of samples over a 15 min period just before (in N₂), and after CO₂ purge at a given temperature in TGA analysis</i>	96

Chapter 5: Degradation mechanism in a direct carbon fuel cell operated with demineralised brown coal	109
Table 5.1: <i>Summary of cell #1 and #2 operation with time (hrs:min) after first loading</i>	113
Table 5.2: <i>EIS model parameters calculated from the impedance data in Figure 5.14. The values are in $\Omega\text{-cm}^2$. The total cell impedance from model has been compared with that from the V-j data in Figure 5.13. The cell resistance was calculated from the linear portion of V-j curves. In the case of C/N₂, the first linear segment closer to OCV has been considered. The values in bracket are the per cent errors given by the model circuit fitted to the experimental impedance data</i>	136
Chapter 7: Catalytic gasification of carbon in direct carbon fuel cells	169
Table 7.1: <i>Catalysed CB makeup as C (carbon as XC-72) plus either Mg (for CB-Mg), Fe (for CB-Fe), or Ca (for CB-Ca) catalysed carbon fuels</i>	173

Abbreviations

AAEM	Alkali & alkaline earth metallic (species)
AC	Activated carbon
ATG	Autothermal gasification
BET	Brunauer-Emmett-Teller (method)
BSE	Backscattered electrons
BTX	Benzene, toluene, xylene
CB	Carbon black
CB-Ca	Calcium-impregnated carbon black
CB-Fe	Iron-impregnated carbon black
CB-Mg	Magnesium-impregnated carbon black
CPE	Constant phase element
CSIRO	the Commonwealth Scientific and Industrial Research Organisation
db	Dry basis
DCFC	Direct carbon fuel cell
DM	Demineralised Morwell char
DR	Dubinin-Raduskerich (method)
EDX	Energy-dispersive X-ray spectroscopy
EIS	Electrochemical impedance spectroscopy
FB-DCFC	Fluidised bed direct carbon fuel cell
GDC	Gadolinia-doped ceria
HDCFC	Hybrid direct carbon fuel cell
HHV	Higher heating value
ICP-OES	Inductively coupled plasma optical/atomic emission spectroscopy
ID	Inner diameter
IDG	Indirect gasification
LSCF	Lanthanum strontium cobalt ferrite
MCFC	Molten carbonate fuel cell
MHFC	Molten hydroxide fuel cell
MIEC	Mixed ion-electronic conductor
MSW	Municipal solid waste
OCV	Open circuit voltage
OD	Outer diameter
pMDF	Pyrolysed medium density fibreboard
PPD	Peak power density

ppm	Parts per million
RDCFC	Rechargeable direct carbon fuel cell
RM	Raw Morwell char
ScSZ	Scandia-stabilised zirconia
SDC	Samarium-doped ceria
SEM	Scanning electron microscopy
SOFC	solid oxide fuel cell
TDS	Thermal desorption spectroscopy
TGA	Thermogravimetric analysis
TPB	Three-phase boundary
TPD	Temperature programmed desorption
XC-72	A commercially produced carbon black (Cabot)
XPS	X-ray photoelectron spectroscopy
XRD	X-ray diffraction
YDC	Yttria-doped ceria
YSZ	Yttria-stabilised zirconia

Nomenclature

D_{micro}	Average pore diameter (Dubinin-Radushkevich method)
D_{pore}	Average pore diameter (Barrett-Joyner-Hallenda method)
ΔG°	Standard Gibbs free energy change of a reaction
$\Delta H^\circ_{\text{std}}$	Standard enthalpy change of a reaction
j	current density
K	Kelvins
L_a	Crystallinity parameter
m	mass
m_0	Initial mass
P	Power density
P_{max}	Maximum power density
pO_2	Partial pressure of O_2
R_1	Resistive magnitude ('size') of intermediate arc (EIS spectra)
R_{hf}	Resistive magnitude ('size') of high frequency arc (EIS spectra)
R_{Lf}	Resistive magnitude ('size') of low frequency arc (EIS spectra)
R_{ct}	Charge transfer resistance
R_Ω	Ohmic impedance
S	Siemens
S_{BET}	N_2 specific surface area (by Brunauer-Emmett-Teller method)
S_{micro}	CO_2 specific surface area
T	Temperature
V	Voltage
V_{micro}	Pore volume (CO_2)
V_{total}	Pore volume (N_2)
W_{s1}	Warburg component
Z'	Real component of impedance
Z''	Imaginary component of impedance

Declaration for thesis chapter 1

Declaration by candidate

In the case of Chapter 1, the nature and extent of my contribution to the work was the following:


Nature of contribution	Extent of contribution (%)
Writing	100

The following co-authors contributed to the work. If co-authors are students at Monash University, the extent of their contribution in percentage terms must be stated:

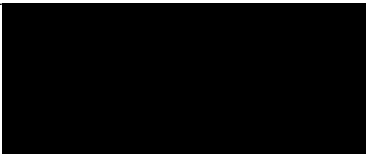
Name	Nature of contribution	Extent of contribution (%)
Dr Sukhvinder Badwal	Advisory role	-
Dr Sarbjit Giddey	Advisory role	-
Assoc Prof Bradley Ladewig	Advisory role	-
Prof Sankar Bhattacharya	Advisory role	-
Dr Aniruddha Kulkarni	Advisory role	-

The undersigned hereby certify that the above declaration correctly reflects the nature and extent of the candidate's and co-authors' contributions to this work.

Candidate's
Signature

	Date 27/02/2015
---	------------------------

Main
Supervisor's
Signature

	Date 27/02/2015
---	------------------------

1

Introduction

**Reproduced in part from: Rady AC, Giddey S, Kulkarni A, Badwal SPS, Bhattacharya S. Degradation Mechanism in a Direct Carbon Fuel Cell Operated with Demineralised Brown Coal. Electrochim Acta. 2014;143:278-90.*

&

Rady AC, Giddey S, Badwal SPS, Ladewig BP, Bhattacharya S. Review of fuels for direct carbon fuel cells. Energy Fuels. 2012;26:1471-88.

&

Rady AC, Giddey S, Kulkarni A, Badwal SPS, Bhattacharya S, Ladewig BP. Direct carbon fuel cell operation on brown coal. Appl Energy. 2014;120:56-64.

1.1 Background

With increasing global consumption of fossil fuels for electricity generation resulting in growing levels of CO₂ in the atmosphere, the search for low CO₂ emission technologies is paramount.

Fuel cells are widely considered as a clean, alternative means of electricity generation, due to their high efficiencies and predictable, low emissions and typically operate on a gaseous fuel [1-8]. Direct carbon fuel cells (DCFCs) operate on the same electrochemical principles as conventional fuel cells but are the only such fuel cell that can operate on a solid carbonaceous fuel, potentially negating the need for a costly transition to an alternative fuel-based economy [1].

DCFCs are also unique in that they are the only means by which electrical energy can be attained directly from solid carbon fuel, or the oxidation of solid carbonaceous material, without a reforming process. Potential sources of carbon fuel include coal, coke, graphite, municipal solid waste (MSW), natural gas and other carbonaceous material including biomass such as rice, nut, and corn casings, grasses and woods. These fuels are cheap, abundant and readily available, and unlike other fuel cells,

widespread implementation of DCFCs would not require a radical change to infrastructure to accommodate a hydrogen-based or gas-based economy.

DCFCs operate at high temperatures, typically in the range of 600 – 900 °C with the overall cell reaction given as Eq. (1.1). This reaction is a familiar reaction in the oxidation or combustion of carbon, however, the oxidation of carbon in a DCFC is electrochemical in nature and involves various intermediate reactions. These reactions may be electrochemical and/or thermochemical and depend on the DCFC type as well as reaction environment that the fuel is exposed to.



The entropy change associated with this reaction is small and this allows for a theoretical efficiency close to 100% for DCFCs across a broad range of operating temperatures [1,9,10]. The theoretical energy efficiency for Eq. (1.1) can be calculated as:

$$\text{Theoretical Efficiency} = [\Delta G^{\circ}(T)/\Delta H_{std}^{\circ}] \times 100 \quad (1.2)$$

The actual efficiency of DCFCs is a product of the theoretical efficiency, utilisation efficiency and the voltage efficiency and is equivalent to the electrical energy output of a cell divided by the combustion HHV of the fuel used. This value lies between 80-95% [9] for complete fuel utilisation, with operating efficiencies projected to be around 60% [1,11], roughly twice that of coal-fired power stations. Not limited by the Carnot cycle, the superior efficiency of DCFCs over conventional stationary coal-fired power generation could realise reductions in CO₂ emissions in the order of 50%, even without capture and storage. In addition, the product stream of carbon consumption is near-pure CO₂, making carbon capture an attractive option for further reduction of the DCFCs carbon footprint. There is also scope for integration of DCFCs within other coal-based power generation technologies [12,13].

The high temperatures of DCFC operation are necessary for maintaining high ionic conductivity of the electrolyte, as well as assisting with the reaction kinetics at the electrodes. The operating temperature depends on the type of DCFC, which is broadly defined by its electrolyte. There are two main families of DCFCs, these are molten electrolyte DCFCs and solid electrolyte DCFCs. A number of variations in materials and design exist within these two classes, which will be discussed in greater detail in the following chapter (Chapter 2).

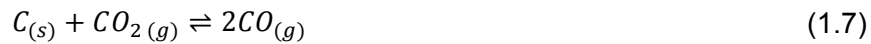
The operation of the DCFC has been described in previous publications [1,12]. In summary, for solid oxide electrolyte DCFCs the oxygen in air supplied to the cathode (Eq. 1.3) is reduced to oxygen ions at the cathode or air electrode.



Electrons are supplied *via* the electrical circuit and the produced oxygen ions migrate across the electrolyte to the anode. For the physical contact solid electrolyte DCFC arrangement, the oxygen ions are consumed by either solid carbon or gaseous carbon monoxide *via* Eq. (1.4), (1.5), or (1.6).



Eq. (1.4) and (1.5) require the solid carbon to be in direct contact with the anode. Under this arrangement, given the proximity of the product CO_2 and the carbon fuel, and with typical operating temperatures in excess of 700 °C, the CO_2 may react with the carbon in the form of Boudouard gasification (Eq. 1.7).



Eq. (1.7) is also sometimes referred to as “Boudouard corrosion” of the carbon in the context of DCFC systems. This is because the conversion of solid carbon to CO *via* Boudouard gasification is non-electrochemical, contributing no electrons to the circuit, and in general reduces the fuel utilisation efficiency of the system as a portion of the CO gas will escape the system in the anode purge gas stream.

The kinetics of this reaction depends strongly on temperature and the reactivity of the carbonaceous fuel toward Boudouard gasification. This can be an important factor in fuel cell performance as the CO generated *via* Boudouard gasification can contribute to current generation *via* Eq. (1.6). The relative concentration of these gaseous species can also influence cell performance in other more subtle ways. The equilibrium between CO, CO_2 and O_2 (Eq. 1.8) can have a considerable impact on cell open circuit voltage (OCV), which is highly sensitive to the partial pressure of oxygen at the anode/electrolyte interface.



It is clear that Boudouard gasification of the carbon fuel *in-situ* during DCFC operation has a considerable influence on the nature of fuel cell performance. As such, understanding the contribution of this reaction pathway to fuel cell output, in addition to the direct electrochemical conversion of solid carbon, is a focus of the research delivered in this thesis.

Amongst many challenges facing the development of DCFC technology, the delivery of a solid fuel to the effective reaction zones or triple phase boundaries for continuous operation of the fuel cell is a key issue for solid electrolyte based DCFC systems. An approach to overcome this problem is to mix solid fuel with a molten media such as molten carbonates and use traditional SOFC anodes such as Ni-YSZ (yttria-stabilised zirconia) to improve charge and ionic transfer between the anode and the solid fuel particles [14]. Anodes with low melting point metals such as Sn, Sb or Bi have also been trailed instead of molten carbonates in DCFCs with varying degree of success [15]. In short life-time experiments, these DCFCs demonstrate impressive performances, however, these systems present challenging technical issues such as rapid degradation of fuel cell components due to the corrosive nature of the molten media. In comparison, direct contact type solid oxide electrolyte DCFCs potentially have fewer corrosion related issues during long-term operation. In these systems, particulate carbon is directly pressed onto the anode with external loading. Traditional SOFC anodes such as porous Ni/YSZ and Ni/SDC (samarium-doped ceria) cermets have been trialled in such DCFCs [16,17] with limited success, however such anodes are unsuitable for continuous operation of a DCFC [18]. Recently promising power densities have been reported in DCFCs with single phase mixed ionic electronic conductor (MIEC) anodes such as (LaSr)(CoFe)O_{3.5} (LSCF) and doped ceria [18,19]. MIEC anodes can carry O²⁻ ions to the anode surface thereby extending effective reaction zone beyond anode/electrolyte interface to anode/fuel interface thus facilitating the solid carbon oxidation on the anode surface itself. For this reason LSCF has been employed as the anode in the majority of works included in this thesis.

1.2 Motivation and aims of this research

One of the largest and most pertinent global challenges the world currently faces is the human influence on climate change. A key contributor to this issue is the large amount of CO₂ produced by the burning of fossil fuels in various applications, such as the generation of power in stationary power plants. Significant improvements in the efficient utilisation of coal, the world's primary energy source for electrical power, is necessary in order to satisfy both the globally increasing demand for electricity, as well as the need to reduce emissions. DCFCs offer a step change in the efficient conversion of solid fuels directly into high-grade electrical energy without the need for a large-scale switch to an alternative fuel economy. However, the technology is still

in its infancy and further detailed investigations into mechanisms of carbon conversion as well as the influence of fuel properties on DCFC performance and lifetime is warranted. Furthermore, the trialling of readily available ‘real world’ fuels such as low-ranked coals within DCFC systems only a relatively recent venture by researchers in the international DCFC community.

1.2.1 Aims

- To investigate the performance of Victorian brown coal in a DCFC and compare this with other benchmark fuels used in DCFCs
- To identify the influence of inorganic content, coal characteristics, and fuel preparation on DCFC performance
- To assess the long-term operability of a solid oxide DCFC on Victorian brown coal
- To assess the compatibility of critical cell components of a DCFC with Victorian brown coal in DCFC operating conditions

1.3 Thesis structure

The thesis is written in a traditional style with relevant journal articles written by the author/co-authors incorporated into the body of the thesis. At the beginning of each chapter containing results, a short introduction is provided to contextualise the scope of the work.

The introduction has provided background knowledge including established reaction mechanism for the DCFC type used in this thesis, the physical contact type solid oxide electrolyte DCFC.

- Chapter 2 provides a critical review of literature on (1) reaction mechanisms within various DCFC types, (2) fuels used in DCFC systems with an emphasis on the two most commonly studied versions – the molten carbonate DCFC and the solid oxide electrolyte DCFC, (3) the current understanding of the role that fuel impurities play in DCFC performance, (4) fuel preparation, analytical techniques, and characterisation methods used by researchers in the DCFC community

- Chapter 3 describes the experimental methodology behind the research undertaken in this thesis. This chapter covers experimental background common to several following chapters, with unique experimental methodology provided in the relevant chapter.
- Chapter 4 investigates the performance of Victorian brown coal at two different temperatures within a DCFC and relates the performance to fuel reactivity studies in a thermogravimetric analyser (TGA). Coal char, both with and without acid washing, is assessed to investigate the influence of inherent inorganic impurities on DCFC performance, and compares the performance to that of a high-purity synthetic carbon.
- Chapter 5 details the effects of extended operating times and cell loadings of a DCFC fuelled by Victorian brown coal on both cell performance and the stability of the anode in use. A mechanism for the degradation in cell performance with extended cell operation is proposed. The influence of anodic atmosphere on cell performance is also assessed.
- Chapter 6 investigates the stability and performance of an alternative anode material for use in a DCFC with Victorian brown coal and proposes an inhibitive role of coal ash on solid carbon conversion during long-term cell operation.
- Chapter 7 details the individual contributions of specific catalytic species on DCFC performance *via* impregnation into high purity synthetic carbon. The DCFC results are related to carbon reactivity under different atmospheres *via* TGA analysis.

Finally, Chapter 8 summarises the conclusions and major outcomes of the work contained in this thesis as well as providing recommendations for future work. A summary of the thesis structure is provided in Figure 1.1.

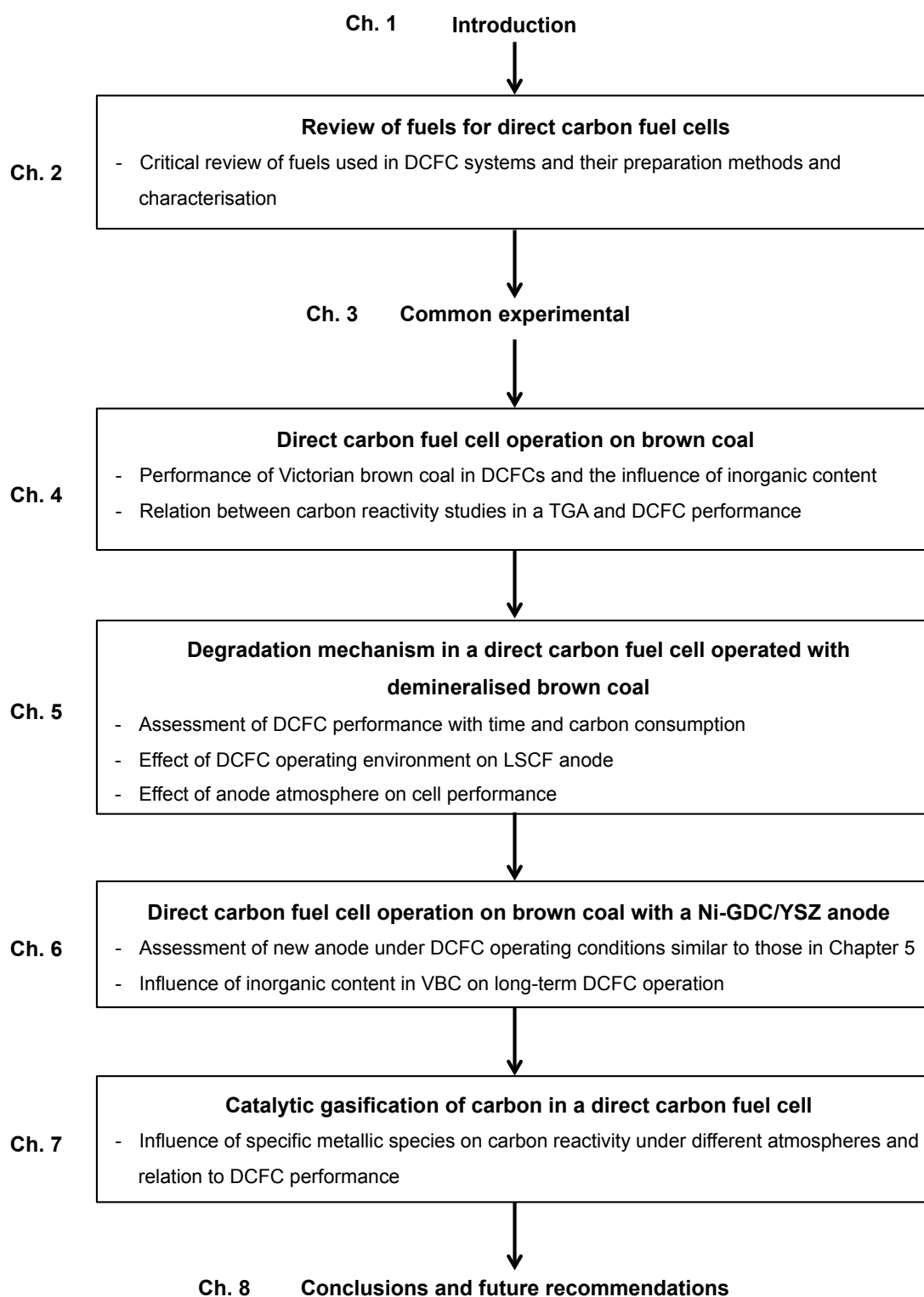


Figure 1.1: Flow diagram of chapters in this thesis with key investigations highlighted

References

1. Giddey S, Badwal SPS, Kulkarni A, Munnings C. A comprehensive review of direct carbon fuel cell technology. *Progr Energy Combust Sci.* **2012**;38:360-99.
2. Kurzweil P. HISTORY | Fuel Cells. In: Jürgen G, editor. Encyclopedia of Electrochemical Power Sources. Amsterdam: *Elsevier*, **2009**. p. 579-95.
3. Badwal SPS, Giddey S, Munnings C, Kulkarni A. Review of Progress in High Temperature Solid Oxide Fuel Cells. *Journal of the Australian Ceramics Society.* **2014**;50:23-37.
4. Hellman HL, van den Hoed R. Characterising fuel cell technology: Challenges of the commercialisation process. *Int J Hydrogen Energy.* **2007**;32:305-15.
5. Carrette L, Friedrich KA, Stimming U. Fuel Cells – Fundamentals and Applications. *Fuel Cells.* **2001**;1:5-39.
6. Kordesch KV, Simader GR. General Aspects of Fuel Cell Systems. Fuel Cells: *Wiley-VCH Verlag GmbH & Co. KGaA*; **2006**. p. 9-21.
7. Stolten D, Emonts B, editors in Fuel Cell Science and Engineering: Materials, Processes, Systems and Technology, 2 Volume Set, *Wiley*, **2012**
8. Angrisani G, Roselli C, Sasso M. Distributed microtrigeneration systems. *Progr Energy Combust Sci.* **2012**;38:502-21.
9. Muthuvel M, Jin X, Botte GG. FUEL CELLS - EXPLORATORY FUEL CELLS | Direct Carbon Fuel Cells. In: Jürgen G, editor. Encyclopedia of Electrochemical Power Sources. Amsterdam: *Elsevier*, **2009**. p. 158-71.
10. Cao D, Sun Y, Wang G. Direct carbon fuel cell: Fundamentals and recent developments. *J Power Sources.* **2007**;167:250-7.
11. Alexander BR, Mitchell RE, Gür TM. Model of Carbon Utilization in a Solid Carbon Fuel Cell. *ECS Trans.* **2012**;41:45-55.
12. Gür TM. Critical review of carbon conversion in "carbon fuel cells". *Chem Rev.* **2013**;113:6179-206.
13. Ordowich C, Chase J, Steele D, Malhotra R, Harada M, Makino K. Applying Learning Curves to Modeling Future Coal and Gas Power Generation Technologies. *Energy Fuels.* **2011**;26:753-66.
14. Nabae Y, Pointon KD, Irvine JTS. Electrochemical oxidation of solid carbon in hybrid DCFC with solid oxide and molten carbonate binary electrolyte. *Energy & Environmental Science.* **2008**;1:148-55.
15. Jayakumar A, Javadekar A, Gissinger J, Vohs JM, Huber GW, Gorte RJ. The stability of direct carbon fuel cells with molten Sb and Sb–Bi alloy anodes. *AIChE J.* **2013**;59:3342-8.

16. Li S, Lee AC, Mitchell RE, Gür TM. Direct carbon conversion in a helium fluidized bed fuel cell. *Solid State Ionics*. **2008**;179:1549-52.
17. Dudek M, Tomczyk P, Juda KL, Tomov R, Glowacki BA, Batty S, et al. Comparison of the Performances of DCFC Fuelled with the Product of Methane RF Plasma Reforming and Carbon Black. *Int J Electrochem Sci*. **2012**;7:6704-21.
18. Kulkarni A, Giddey S, Badwal SPS. Electrochemical performance of ceria-gadolinia electrolyte based direct carbon fuel cells. *Solid State Ionics*. **2011**;194:46-52.
19. Werhahn MG, Schneider O, Stimming U. Thin Film Gadolinia Doped Ceria (GDC) Anode for Direct Conversion of Carbon Black Particles in a Single Planar SOFC. *ECS Trans*. **2013**;50:73-87.

Declaration for thesis chapter 2

Declaration by candidate

In the case of Chapter 2, the nature and extent of my contribution to the work was the following:


Nature of contribution	Extent of contribution (%)
Review of literature, writing	100

The following co-authors contributed to the work. If co-authors are students at Monash University, the extent of their contribution in percentage terms must be stated:

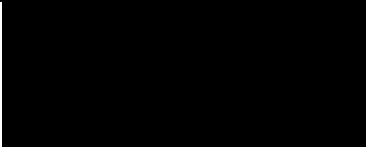
Name	Nature of contribution	Extent of contribution (%)
Dr Sukhvinder Badwal	Advisory role	-
Dr Sarbjit Giddey	Advisory role	-
Assoc Prof Bradley Ladewig	Advisory role	-
Prof Sankar Bhattacharya	Advisory role	-

The undersigned hereby certify that the above declaration correctly reflects the nature and extent of the candidate's and co-authors' contributions to this work.

Candidate's
Signature

	Date 27/02/2015
---	------------------------

Main
Supervisor's
Signature

	Date 27/02/2015
---	------------------------

2

A review of fuels for direct carbon fuel cells

**Reproduced in part from: Rady AC, Giddey S, Badwal SPS, Ladewig BP, Bhattacharya S. Review of fuels for direct carbon fuel cells. Energy Fuels. 2012;26:1471-88.*

A review of fuels for direct carbon fuel cells

Abstract

In this chapter, the current status of direct carbon fuel cell (DCFC) technology has been reviewed. Recent promising advances in the design of fuel cells has resulted in a reprisal of research into the DCFC. As a result, more is understood about the roles of species and mechanisms which govern the performance of DCFC systems. Of particular interest to industry and researchers are the molten carbonate DCFC and solid oxide DCFC arrangements, with the bulk of research articles and large-scale investment focused on these DCFC types. However, the variety of fuels used and trialled within these fuel cells is limited. This is especially true for the solid oxide electrolyte DCFCs with the fuel of choice for researchers being carbon black, and light gases for industry. The application of more readily available and cheaper fuels in this type of DCFC is only a recent enterprise, and there is significant scope for the expansion of these studies to include trials of low rank coals such as lignites. This review addresses this gap in the literature by reviewing all fuels tested in molten carbonate and solid oxide DCFC systems, and in particular, critically evaluating low-rank coals and biomass, amongst other alternative fuels.

2.1 Introduction

The first attempted use of carbon directly in a fuel cell was in 1855 by Antoine César Becquerel who used platinum and carbon electrodes immersed in a fused potassium nitrate electrolyte [1]. The cell generated a current in response to air passed over the platinum electrode, however, undesirable chemical oxidation of the carbon by the electrolyte was observed. In 1896 by William W. Jacques patented a molten hydroxide system which employed coal as both the fuel and anode in the form of carbon fuel rods, with air injected into the electrolyte in the cathode compartment [2]. The setup involved a stack consisting of around tubular 100 cells heated to 400 – 500 °C, with an output of 1.5 kW.

A number of less successful electrolyte mixtures were proposed before E. Baur [3], in 1910, investigated a molten sodium hydroxide fuel cell that ran on various fuels, including coal and sugar. However, issues surrounding the utilisation of coal and

other solid carbons in fuel cells, such as accumulation of ash in the electrolyte and design constraints surrounding carbon feed and conductivity persisted [4]. This ultimately resulted in a period of slow progress in the utilization of solid carbon within fuel cell systems and attention turned to gas-fed cells. In 1921 Baur and co-workers arrived on a design incorporating molten carbonate electrolyte [5] which paved the way for the modern molten carbonate fuel cell (MCFC).

During and after the 1980's industry involvement in MCFC development expanded rapidly and companies such as Mitsubishi, Hitachi, Toshiba, Fuji, IHI Corporation, MTU Friedrichshafen, FuelCell Energy, and Siemens, all made notable contributions to large-scale and long-life operation of MCFCs. FuelCell Energy produce a range of MCFC units ranging from 300 kW to 3.8 MW, and operate many power plants globally including a 59 MW power plant in South Korea [6], the largest fuel cell park in the world. However, in order for MCFCs to be a competitive source of electricity, the cost must reach a limit of around €1.500 kW⁻¹ [7].

The solid oxide fuel cell (SOFC) was developed shortly after the MCFC. The yttrium-stabilised zirconium (YSZ) material used as the electrolyte in many SOFCs today was first developed by Nernst in 1897 for light generation. A student of Nernst, W. Schottky realised the ceramic's potential as an electrolyte for a fuel cell (the SOFC) in 1935.

Industry interest in the SOFC has a rich history, beginning with Westinghouse Electric Corp. who developed the tubular SOFC in 1958. In 1987, Osaka Gas and Tokyo Gas operated a 3kW stack of cells for 15000 hours on natural gas. Since realising the industrial applications of SOFCs on gaseous fuels, many other companies have invested in SOFC development including Fuji Electric Corp., Siemens, Doriner, Mitsubishi Heavy Industries, Rolls-Royce, Bloom Energy and Ceramic Fuel Cells Limited. Thanks largely to industry investment in MCFCs and SOFCs, the modern DCFC can be either mobile or a stationary conglomerate of units close to the fuel source.

DCFC technology has enjoyed a reprisal in interest and has seen many new researchers enter the field in recent years. Much of this renewed interest is due to recent advances in DCFC design such as the work of Cherepy and co-workers at the Lawrence Livermore National Laboratory [8]. The authors dispersed carbon particulates in molten carbonate, improving reaction rates and shifted research away

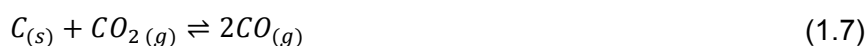
from utilisation of carbon rods in direct carbon MCFC systems. Also, for solid oxide DCFC systems, Gur and Huggins' [9] two-compartment high temperature fuel cell paved the way for future detached-type solid oxide DCFC cells. As of 2005 a new DCFC, the hybrid direct carbon fuel cell (HDCFC), has entered the scene *via* a patent filed by Lipilin et al. of SRI International [10]. The HDCFC combines the benefits of high reactivity offered by dispersion of carbon in molten carbonate with a solid oxide electrolyte to negate issues surrounding cathode corrosion as well as CO₂ recirculation in MCFC systems. Parallel research into this DCFC type commenced at St Andrews University in 2008 [11].

The focus of this review will be on solid fuels for direct carbon fuel cells, and in particular those for molten carbonate and solid oxide DCFCs.

2.1.1 DCFC reaction basics

DCFC reactions occur at temperatures below that of traditional coal combustion or gasification. However, the operating temperatures are still high, typically in the range of 600 – 900 °C and vary depending on electrolyte and cell type/design.

In all DCFCs a side reaction known as the reverse Boudouard reaction occurs due to favourable fuel cell operating conditions. This reaction is particularly prevalent in high-temperature fuel cells (such as molten carbonate and solid oxide DCFCs) since the reverse Boudouard reaction is thermodynamically favoured at temperatures above 700 °C [9,12]. The Boudouard reaction has great and unique implications for the performance of both the molten carbonate and solid oxide DCFC and hence is an extremely important consideration to the fuel cells of interest in this review. The reverse Boudouard reaction is also known as Boudouard gasification and is given below as Eq. (1.7):



The overall cell reaction for all DCFC arrangements simplifies to the familiar oxidation of carbon in Eq. (1.1):



However the oxidation is electrochemical in nature and involves several reaction steps involving the electrolyte for non-solid oxide arrangements.

Understanding the reaction mechanisms involved in all conversion steps from solid carbonaceous matter to carbon dioxide is crucial to pairing the most appropriate fuel

with a given DCFC system. It also allows researchers to determine which fuel preparation techniques will benefit fuel utilisation, cell performance and cell life. This review addresses recent advances in the design of, and knowledge surrounding DCFCs. This review also focuses on appropriate fuel sources, their composition, and preparation of these fuels for use in DCFCs, as well as what has been reported in literature.

In the following three sections (section 2.2 to 2.4), three prominent DCFC types and current arrangements will be introduced along with the current understanding of their reaction mechanisms. Section 2.5 will discuss the hybrid direct carbon fuel cell (HDCFC) technology, along with other molten metal anode arrangements. There are a large variety of direct carbon fuel cell types and designs. The focus of this review is on the effect of fuel type and fuel characteristics on cell performance, with a focus on molten carbonate and solid oxide DCFC systems.

Sections 2.6 and 2.7 explore properties of coals used in DCFC systems and the effect of impurities, physical nature of the coals and treatment options on the performance of DCFC systems. Section 2.8 investigates analytical techniques used by researchers on fuels used in molten carbonate and solid oxide DCFCs and section 2.9 summarises the performance of these and other fuels in DCFCs.

2.2 Molten hydroxide DCFC

The molten hydroxide fuel cell (MHFC) has a low operating temperature of around 650 °C. The anode in the form of rods or solid blocks is dipped in the molten hydroxide electrolyte, similar to the early Jacques design. The molten hydroxide DCFC has a similar arrangement to some MCFC designs, with the main advantage of the molten sodium hydroxide electrolyte having a greater ionic conductivity than that of molten carbonate mixtures [13]. Molten NaOH also has lower overpotentials and a greater oxidation rate than molten carbonates. These factors allow the MHFC to operate at lower temperatures, allowing for cheaper materials to be used for cell casing and cathodes such as 300 series Stainless steel and ultra-low carbon steel [13].

However, carbonate formation has been an issue preventing the industrial application of molten NaOH as a DCFC electrolyte since this design was first conceived in 1896 by William W. Jacques. The reaction mechanism for carbonate

formation as proposed by Goret and Tremillon [14] involved two reaction steps given below as Eq. (2.1) and (2.2):

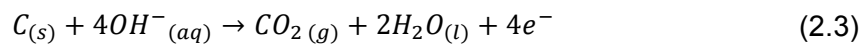


Eq. (2.1) is a fast chemical reaction whereas Eq. (2.2) is a rate limiting electrochemical reaction.

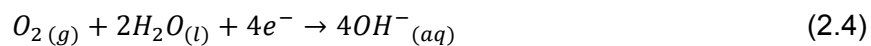
A mitigating technique for prevention of carbonate formation has since been proposed by Zecevic et al [15]. This technique involves increasing the concentration of water in the electrolyte solution to drive the equilibrium of Eq. (2.1) to the left, reducing the amount of O^{2-} in solution, which is an intermediate product in the formation of carbonate. Increasing the concentration of water in the electrolyte solution had several additional benefits viz. an increase in the ionic conductivity of the electrolyte/fuel solution and reduced corrosion rates of iron, nickel and chromium (key metals used in the cathode and cell casings). High corrosivity, as for MCFCs, is still an issue for MHFCs at operating temperatures of 400 – 800 °C [16]. While Ni and Ni foams are prominent cathodic materials, an alternative in Fe_2Ti shows good resistance to corrosion as a cathodic and cell casing applications [17].

The half-cell reactions are given as Eq. (2.3) and (2.4):

Anode Reaction:



Cathode Reaction:



2.3 Molten carbonate DCFC

The molten carbonate fuel cell (MCFC) and molten carbonate DCFC operate using molten carbonate salt electrolytes, which are composed of K_2CO_3 , Li_2CO_3 and Na_2CO_3 . These carbonates are present in the electrolyte as either binary eutectics of $(Li/K)_2CO_3$ or $(Li/Na)_2CO_3$, or ternary eutectics of $(Li/K/Na)_2CO_3$. The cell operating temperature required to achieve high conductivity of molten salt is 600 – 800 °C. Due to this high operating temperature, cell components may be exposed to a highly corrosive environment [16], limiting material options [16,18,19], and high pre-treatment costs are associated with fuels that contains sulfur impurities. Because of

the corrosive operating environment, rather exotic materials must be employed such as Inconel, Hastelloy and Kanthal-A [13].

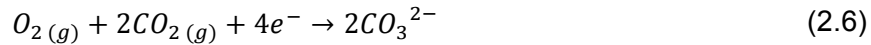
The high corrosivity of the electrolyte plagued the early development of commercial MCFC stacks. In the decade spanning 1996 to 2006 however, cell life was improved from just a few months to up to two years [20]. This advancement was largely thanks to incremental improvements to corrosivity resistance of critical cell components.

In the most common design for molten carbonate DCFCs carbon is first mixed with the molten carbonate and fed to the electrolyte. Non-reacting current collectors are used in both the anode and cathode compartments. Air and CO₂ are supplied as the oxidant in a separate cathode chamber. In some arrangements, a permeable partition is used to separate the gas and electrolyte phases [21], though the most common design involves the bubbling of cathode gas through the molten carbonate. The simple half-cell reactions are given as Eq. (2.5) & (2.6):

Anode Reaction:



Cathode Reaction:

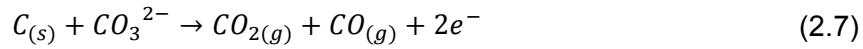


The process requires a recycling of two molecules of CO₂ from the anode chamber to the cathode chamber for each carbon atom converted to CO₂. This can be achieved by recirculation of anodic product gases into the cathode chamber, though is often controlled in laboratory settings by introduction of fresh CO₂ stream to the cathode compartment along with air.

A more detailed mechanism of the anodic electrochemical oxidation of coal as proposed by J. F. Cooper and colleagues [22], adapted from K. J. Vetter's original mechanism as cited in [1], is illustrated in Figure 2.1 The mechanism is similar to the Hall process and takes the form of a five-step reaction. Minor variations of this mechanism exist in literature such as that of Li and co-workers [23], which includes the necessary decomposition of a carbonate ion to form an oxygen ion as a preliminary step.

Boudouard Gasification also occurs when either the carbon in the anode compartment is not polarized (for example during cell standby, open circuit operation or remote regions of the anode which experience low current flow), or when the

carbon is not in physical contact with the anode [22]. An alternative electrochemical mechanism has been suggested for CO production at high temperatures (800 °C) in molten carbonate [24]:



Several authors [22,25] also realised a relatively pure product of CO₂ at operating temperatures of 700 – 900 °C, despite some earlier researchers predicting a high concentration of CO *via* Eq. (1.7) due to the high temperatures.

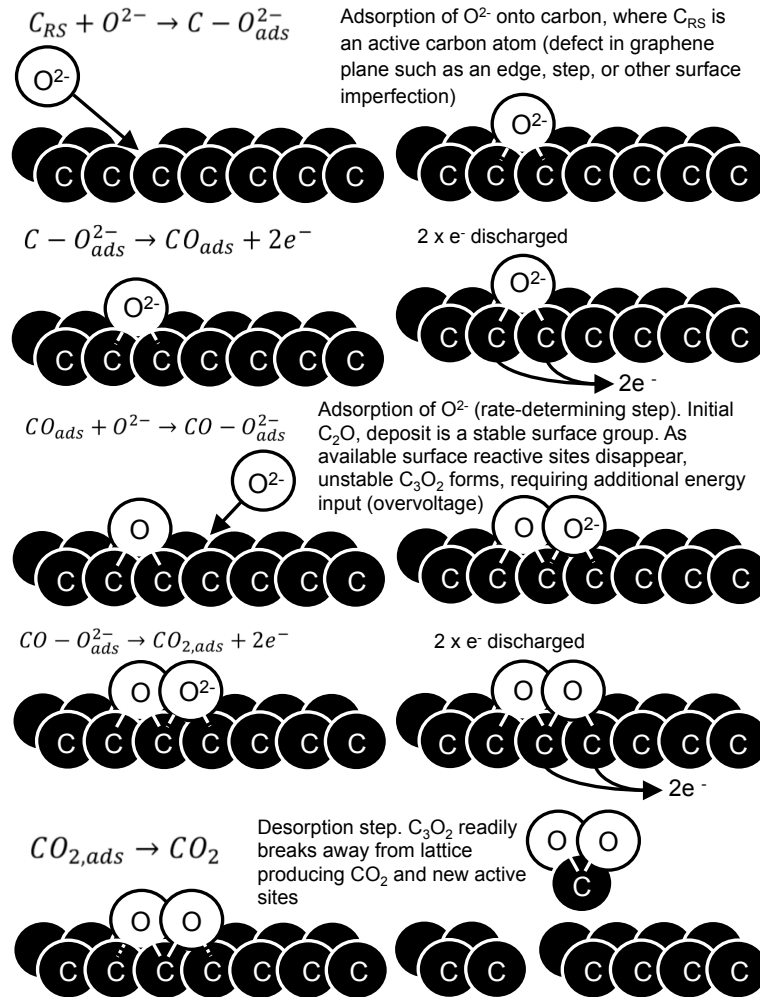


Figure 2.1: Reaction mechanism for electrochemical oxidation of carbon in molten carbonate

There exist a number of designs of the molten carbonate DCFC, notably differentiated by the method of utilisation of carbon within the cell, ranging from solid carbon anodes to the more modern and widely adopted coal/electrolyte slurry.

The early design of a solid carbon-based anode was hampered by various shortcomings such as the leakage of impurities (e.g. ash) into the electrolyte and mechanical instability of coal-based electrodes. Other key drawbacks of the early cell

designs as identified by Cherepy and co-workers [22] include low reaction rates as well as the economical and logistical impracticalities of carbon electrodes. While recent work has continued in the use of solid carbon anodes [21,26], the majority of the discussed issues were overcome to a large degree in a novel design by Vutetakis and co-workers [27], which involved suspending coal particulates within the molten carbonate electrolyte, and realised increased reaction rates. This work itself was developed by combining the work on coal slurry electrolysis by Coughlin and Farooque [28-31] and coal powered molten salt fuel cells.

Cherepy and co-workers further researched the effect of various solid fuel sources and their respective physical nature (particle size, surface area and crystallinity) on the performance of this arrangement. The authors believe that a specifically designed cell, which operated under constant polarization, should achieve a fuel utilisation at or about 100%. Li et al [23] believe that this fuel cell arrangement of Cherepy and co-workers showed potential for a continuous process and hence commercialisation. Indeed, the cell design from Lawrence Livermore National Laboratory (LLNL) involving bipolar stacks of tilted cells with a self-feeding mechanism [32] has attracted considerable interest and investment from Contained Energy.

2.4 Solid oxide DCFC

There are three main classes of solid oxide DCFC and their classification depends on the method of contacting between the fuel and the anode. The three classes are detached type-, physical contact type- and carbon-deposited (also referred to as the rechargeable direct carbon fuel cell – RDCFC) type DCFC. Other modern arrangements of solid oxide DCFC also exist such as gasification-driven DCFCs, fluidised bed DCFCs (FB-DCFC) [33,34] and the hybrid (solid oxide/molten carbonate) DCFC [35] (HDCFC – see section 2.5). This section will cover only the three main classes, along with an emerging variation of the detached-type in a gasification-driven DCFC.

The SOFC is a high-temperature fuel cell and so normal operating conditions involve temperatures around 800 – 1000 °C [36], required to achieve desirable ionic conductivity of the electrolyte. The ceramic-based electrolyte and electrodes means that there is little risk of corrosion of crucial cell components at the high temperatures. However, Sulfur and other impurities must first be removed from the

fuel prior to entering the SOFC to maximise the lifetime of the cell. Current research efforts into SOFC materials are focused on reducing the temperature requirements for high ionic conductivity to allow for lower temperature cell operation [37-40], as well as improved resistances to catalyst poisoning [41].

The cell performance is also heavily dependent on the kinetics of the gas-phase reactions, in particular the gasification of coal or the Boudouard reaction when gasified with CO₂. Therefore, an ideal coal preparation would be that of a carbon fuel which is easily gasified. This is opposed to the molten carbonate DCFC where surface oxygen functional groups play an important role (see section 2.7.2). However, the SOFC is flexible in terms of fuel sources and can operate on CO, H₂ or light hydrocarbon gases.

2.4.1 Common design features of the solid oxide DCFC

While there are three sub-classes of solid oxide DCFCs as already outlined, the cell arrangement may take several forms such as a tubular cell (electrolyte takes the form of a solid tube closed at one end, with electrodes applied to the inside and outside). Other designs include flat electrolytes such as planar arrangements and coin-type or “button” cells. Whilst the thickness of the electrolyte can vary, there must always be at least one component of the fuel cell that provides mechanical stability, leading to anode-support, cathode-support, and electrolyte-supported fuel cells.

Despite the numerous possible arrangements of the solid oxide DCFC, many design features such as materials used for cell components are rather universal. This section will outline a few well-established design characteristics of the modern solid oxide DCFC.

The SOFC typically consists of a dense ceramic electrolyte, with two porous electrodes. Common choices for the electrolyte include: 8YSZ (8% mol Yttrium oxide in YSZ), 9ScSZ (9% mol Sc₂O₃ Scandia Stabilised Zirconia), and GDC (Gadolinium Doped Ceria). A comprehensive overview of materials used in SOFCs can be found in Basu et al. [42]. The two foremost desirable properties of the ceramic electrolyte are low electronic conductivity, to minimise current leakage away from the anode, and high ionic conductivity. High temperatures allow for acceptable O²⁻ ion transport kinetics. Currently, the lower limit for operating temperature is around 600 °C, below which the resistance for ion transport is too high. Achieving current research targets

of 500 °C operating temperature would result in a marked increase in available materials for use in the SOFC.

The YSZ electrolyte is known to react with commonly used cathode materials at temperatures above about 1100 °C for Lanthanum Strontium Manganite (LSM) and 900 °C for LSCF. This is more of a problem where the cathode and electrolyte need to be heated above these temperatures during fabrication and can be negated by separating the electrolyte and cathode by a thin GDC film [43].

The cathodic material in a SOFC is typically a thin porous ceramic layer 50 – 100 µm thick. It should have high electronic conductivity or preferably be a Mixed Ionic Electronic Conductor (MIEC). A common material choice for the cathode is LSM, which is a popular candidate due to its thermomechanical compatibility with YSZ (similar thermal expansion properties, minimising stresses at the junction of the high-temperature fuel cell). The two materials are also chemically stable with respect to each other at fuel cell operating temperatures. These factors extend the lifetime of the cell.

The anodic material in a SOFC is a highly porous ceramic, which, like the cathode, must be conductive of electrons. However, it is also necessary for the anode to be conductive of ions as well to extend the reaction boundary. The common arrangement is a 'cermet' (a composite of a ceramic – 'cer' and a metal – 'met') composed of the electrolyte ceramic material and Ni. YSZ is a popular candidate for the ceramic component since grain growth of the metal component (Ni) is retarded by YSZ.

Oxidation occurs at the anode resulting in the generation of electrons with the loss of electrons from the oxygen ion, as well as generation of heat from the production of CO₂. As such, the anode may require cooling in some cases. This cooling may be satisfied *in-situ via* the gasification process where coal or other carbonaceous material is used as the fuel source. Gasification of the carbon with either H₂O or CO₂ is an endothermic process and so acts to cool the anode by supplying it with cooler gas.

2.4.2 Deposited-type solid oxide DCFC (RDCFC)

The carbon deposited-type solid oxide DCFC (also known as rechargeable direct carbon fuel cell – RDCFC) is a unique DCFC in that it requires the supply of a

gaseous hydrocarbon (usually light hydrocarbons) to the anode as the fuel. Therefore the application of coal-based fuels to this cell type is minimal. It is possible that light gases from coal and biomass pyrolysis may be used in this cell.

The deposited carbon is supplied via thermal decomposition of the gaseous fuel onto the porous anode surface. Initially the deposited carbon is electrochemically oxidised by oxygen ions at the anode/electrolyte interface as per Eq. (1.4) and (1.5). Once CO and CO₂ are formed, the kinetics of Eq. (1.6) and (1.7) (reproduced here for clarity) dominate and become the focus of the fuel cell operation [44]:

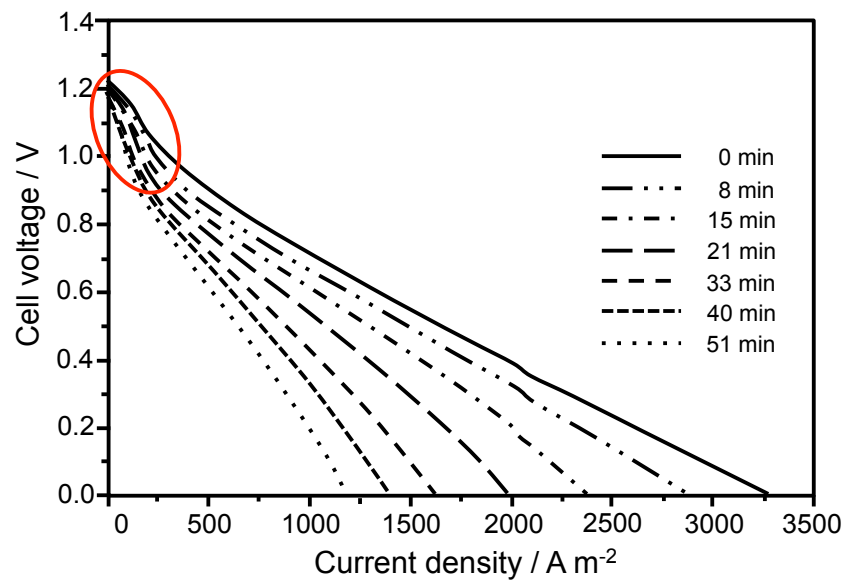


Figure 2.2: Cell voltage and Current density for a deposited-type solid oxide DCFC with different time of open circuit operation and significant activation polarization at high voltages (circled) - adapted from Li and co-authors [45]

Li and co-workers [45] analysed the performance of a button cell using CH₄ deposition. The author's results show significant activation polarization at high voltages (above 1 V – see Figure 2.2). These results support the mechanism above since activation polarisation is linked to the direct electrochemical oxidation of carbon, which requires an overpotential [45]. This type of DCFC is useful for study of carbon oxidation mechanism as well as in small-scale energy storage applications [46,47].

It is worth mentioning here that while carbon deposition is necessary in RDCFCs, with Ni employed to promote carbon deposition, coking remains an issue in conventional SOFC systems operating on gaseous hydrocarbons. Natural gas and/or syngas have been proposed as a cheap fuel that could aid in the commercialisation of SOFC technology and as a stepping-stone towards a hydrogen economy [47].

A number of researchers have investigated slightly humidified (3% H₂O) CH₄-fed SOFCs using YSZ electrolytes with encouraging results. High power densities have been achieved using Ni-YSZ anode at 800 °C (96 mW cm⁻² [48], and 127 mW cm⁻² [49]). However, these systems have issues surrounding Ni coking and sulfur poisoning as well as redox volume changes. Tao and Irvine extracted around 290 mW cm⁻² at 950 °C operating on 3% H₂O in CH₄ using a (La,Sr)(Cr,Mn)O₃ anode, which largely abated issues arising from the use of Ni in the anode [50].

2.4.3 Physical contact-type solid oxide DCFC

As the name suggests, the fuel is in physical contact with the anode. In research-based systems this is commonly achieved by sandwiching the carbon fuel to the cell, often with a thin, porous plate or felt [12,45] or between the anode and the electrolyte [16]. In other cases, the fuel is housed in a tubular SOFC where it is allowed to rest against the inner anode surface of the tube [51].

The reaction mechanisms proposed by authors are presented as case-specific and are dependent on not only the physical cell arrangement, but also the atmosphere in which the carbon fuel is consumed. Most notably the comparison between mechanisms for reactive atmospheres of CO/CO₂ and inert atmospheres are proposed.

What reactions occur in the presence of sufficient residual active gases (CO/CO₂) or recycled anode gas is a hot topic. It is widely understood that the direct electrochemical oxidation of carbon in solid carbonaceous fuels, as per Eq. (1.4) and (1.5) is possible [12,52,53] where carbon is in intimate contact with the anode [52]. It is largely accepted however, as with RDCFCs, that Eq. (1.6) and (1.7) also occur [52].





Some authors believe that Eq. (1.4) and (1.5) can only take place at the fuel/anode/electrolyte three-phase boundary (TPB), and for solid carbonaceous fuels this is an unfeasible mechanism, irrespective of intimate contact of the fuel with the anode [44]. Li et al (2010) also claim that electrochemical oxidation of carbon at the anode does not occur and so the anodic reaction mechanisms are the same as those for detached-type direct carbon SOFCs. If this statement were correct then there would be associated implications for the cell design, in that improving contact between fuel and anode will not enhance cell performance. However, much of the ongoing research in the DCFC community is focussed on enhancing the direct electrochemical oxidation of solid carbon. A key motivator behind the development of the HDCFC and molten metal anode direct carbon SOFCs (Section 2.5) was a desire to increase the surface area of solid carbon available to electrochemical conversion *via* Eq. (1.4) and (1.5) [51].

However, the trends of Li and co-workers [45] later results (summarised in Table 2.1 and Table 2.2) do not demonstrate that the exact same reaction mechanisms are taking place as those in the detached-type direct carbon SOFC, contrary to the early interpretation of the authors. The trends in Table 2.1 appear to be case-independent (for a given atmosphere) as opposed to those observed for the detached type (Table 2.2). The polarisation curves were produced after:

Case I: Cell attached to an open circuit for 30 minutes

Case II: Cell discharged at 0.5V for 5min

Figure 2.3 shows how CO acts as the fuel in the physical contact-type direct carbon SOFC where Eq. (1.6) and (1.7) are dominant. The dashed-arrows indicate two options for the CO₂ and CO products, to participate in further reactions or escape the anode as product gas.

As depicted in Figure 2.3, CO, and indeed all gaseous fuel species in a SOFC, react at the anode/electrolyte interface. Although CO likely plays a role in most solid oxide DCFC applications, including physical contact-type solid oxide DCFCs, the direct electrochemical conversion of solid carbon can still take place where the reaction zone is extended to include the anode/carbon interface, since solid carbon cannot penetrate through the porous anode structure. Such systems, proposed by Kulkarni

and co-workers at CSIRO Energy Technology [54], require a MIEC anode with sufficiently high ionic and electronic conductivity, such as Lanthanum Strontium Cobalt Ferrite (LSCF). LSCF, a popular cathode material in solid oxide DCFC systems, has demonstrated promising cell performances as well as structural stability under DCFC anodic operating conditions utilising carbon black [12,54], gaseous CO [54,55], and biomass chars [55]. Other promising MIEC candidates include yttria-doped ceria (YDC), which shows mixed ionic electronic conducting properties in reducing environments [56].

Table 2.1: Summary of cell performance trends for physical contact-type solid oxide DCFC [45]

Ar (Case I)		Ar (Case II)	
Ar Flow rate	↑	Ar Flow rate	↑
Cell Performance	↓	Cell Performance	↓
CO ₂ (Case I)		CO ₂ (Case II)	
CO ₂ Flow rate	↑	CO ₂ Flow rate	↑
Cell Performance	↑	Cell Performance	↑

Table 2.2: Summary of cell performance trends for detached-solid oxide DCFC [45]

Ar (Case I)		Ar (Case II)	
Ar Flow rate	↑	Ar Flow rate	↑
Cell Performance	↓	Cell Performance	↑
CO ₂ (Case I)		CO ₂ (Case II)	
CO ₂ Flow rate	↑	CO ₂ Flow rate	↑
Cell Performance	↓	Cell Performance	↓

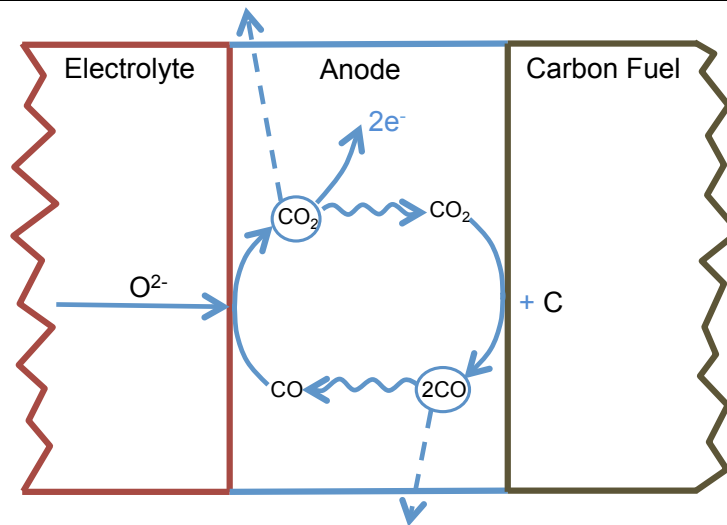


Figure 2.3: Depiction of the fuel oxidation in a physical contact-type solid oxide DCFC as proposed by Nakagawa and Ishida [57]

Detailed investigations using electrochemical impedance spectroscopy (EIS) have shed further light on reaction mechanisms occurring during direct contact solid electrolyte DCFC operation with other MIEC anodes [56,58]. These works offer strong support for the direct electrochemical conversion of solid carbon at the anode of such fuel cells, as well as the importance of good ionic conductivity of the MIEC anode [58]. Power generation from direct contact solid electrolyte DCFC with LSCF anode at 600 °C, well below 700 °C where Boudouard gasification commences, is also strongly suggestive of direct electrochemical conversion of solid carbon [12] in these systems.

2.4.4 Detached-type solid oxide DCFC

The detached-type solid oxide DCFC involves the fuel being physically removed from the anode. This system offers the greatest flexibility in cell design and there are many variations, most notably the gasification-driven SOFC.

As with physical contact-type solid oxide DCFCs, research into the effect of anodic cell atmosphere on reaction mechanisms has been conducted to help clarify the process.

Tang and Liu [51] reported that catalysing Boudouard gasification in the presence of sufficient residual active gases (CO/CO₂) markedly improved the performance of the cell. They concluded that the formation of CO from CO₂ *via* Boudouard gasification was a pivotal step in the function of the cell. The authors used their findings to support the mechanism proposed by Nakagawa and Ishida [57], which incorporated the following dual-reaction mechanism for the oxidation of carbon in the solid oxide fuel cell:



Reaction in Eq. (1.6) occurs at the gas/anode/electrolyte TPB [45]. The interfacial, polarisation and activation resistances govern the kinetics of this reaction. Eq. (1.7) occurs at the carbonaceous fuel source, with diffusion of gaseous reactive species governing the kinetics of cell operation. Since both reactions depend on each other for reactants, the kinetics of both reactions is critical to the overall reaction rate. The cell performance will be greatly compromised if one of the reactions is retarded. Therefore it is necessary to catalyse both reactions.

Figure 2.4 shows fuel oxidation in a detached-type direct carbon SOFC and how CO acts as the fuel in the cell where Eq. (1.6) and (1.7) are dominant. There is an option to recycle a

fraction of the anodic gas back to the detached carbon fuel source. Note however, that this is not necessarily a pure stream of CO_2 and will likely contain varying concentrations of unconverted CO . This relative concentration depends on factors such as anodic gas residence time in the anode chamber, temperature and reactivity of the carbonaceous fuel.

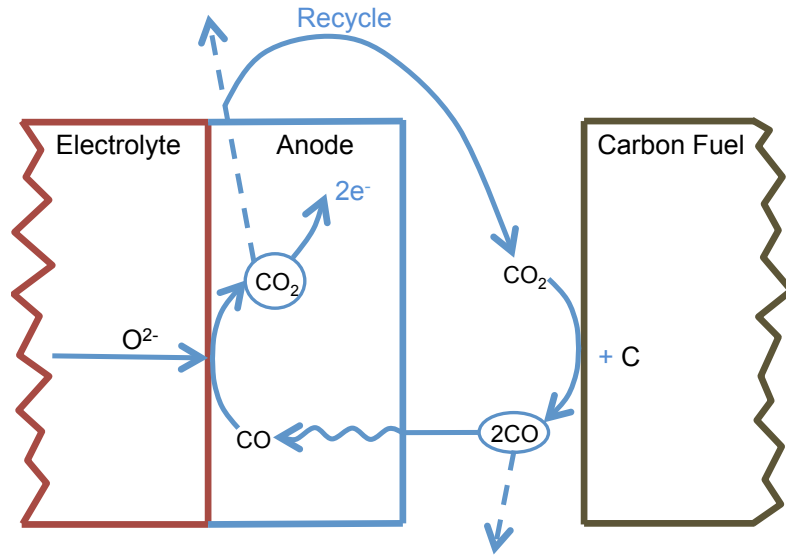


Figure 2.4: Depiction of the fuel oxidation in a detached-type solid oxide DCFC as proposed by Nakagawa and Ishida [57]

When the anode chamber is flushed with an inert gas, and the anodic gas (CO/CO_2) is diluted and purged from the system. Such arrangements are for the benefit of understanding reaction mechanisms, and are not a feasible industrial-scale practice. Under these conditions, Li and co-workers [44] proposed the following mechanism:



The above reaction mechanism, supported by Gur and Huggins [9], is most likely associated with very poor kinetics since the reactant gases are not present in high concentrations.

However, this mechanism does not require the intimate contact between the carbon and the anode and so occurs in the ‘detached’ reactor types such as was employed by Gur and Huggins [9]. The mechanism is similar to that proposed by Li and co-authors [33] in that O^{2-} ions combine to form O_2 at the anode when the concentration of other active gases is low.

Li and co-workers [45] investigated the effect of changing the flow rates of both an inert gas (Ar) and a reactive gas (CO_2) through the fuel sample and anode. The results are summarised in Table 2.2. Of interest is the relationship between the cell performance and the supply of and removal rate of CO_2 from the fuel sample and the use of this to justify the

proposed reaction mechanisms. Adjusting the flow rates influenced the concentration of CO₂ in and around the fuel, which has implications for Boudouard gasification of the fuel. The fact that there is a switch in cell performance between high Ar flow rates and low Ar flow rates makes it hard to pinpoint the exact reaction mechanism.

The authors argue that due to the varying results between cases for the Ar-rich anode gas and the CO₂-rich anode gas, the dominant reaction mechanisms differ depending on the atmosphere that the fuel and anode are subjected to. Low CO₂ flow rates for the detached-type solid oxide DCFC resulted in the greatest cell performance suggesting that the CO₂ flow is diluting the CO around the anode, necessary for electrochemical reaction, more than the CO₂ flow enhances the generation of CO. There would therefore be an ideal flow rate and recycle of CO₂ to the gasification chamber to maximise cell performance and fuel utilisation.

2.4.5 Gasification-driven SOFC

While it is largely accepted that the gasification of carbonaceous fuel is a necessary mechanism for operation of the detached-type solid oxide DCFC, the gasification-driven SOFC is so named since it often incorporates an external gasifier.

There are two classes of these gasification-driven fuel cells:

1. Single-step direct approach (unconstrained, *in-situ* gasification)
2. Multiple-step indirect approach (constrained, separate gasification)
 - a. Indirect gasification (IDG)
 - b. Autothermal gasification (ATG)

Lee and co-workers [59] investigated the effect of different fuel sources and different gasification feeds (H₂O and CO₂) on the thermal efficiencies of ATG and IDG systems. They reported (for their simulations) that the work output differed by less than 1%, despite changes to gas composition. Their model, as the authors acknowledge, did however, neglect certain inherent fuel cell irreversibilities contributing to cell resistances, as well as concentration and thermochemical driving forces. The authors noted that gas flow to the gasifier also affords some operational benefits. The solid fuel may be delivered to the gasifier *via* entrained flow within CO₂/H₂O/O₂ feed. Agitation *via* fluidisation of carbonaceous matter from the gaseous feed also improves mixing as well as enhancing segregation or removal of ash.

In the case of single-step gasification, the gasification occurs in the same chamber as the anode. This is a common arrangement for experimental research and is likened to the detached-type solid oxide DCFC. An example of a single-step gasification system is given as Figure 2.5, which is only constrained by the additional heat exchanger (a non-essential process, used only to pre-heat the incoming air, minimising heat loss from the system).

This single-step gasification arrangement is limited by several design constraints. Firstly, ash produced in the same chamber as the fuel cell may not be simple to remove, and some will undoubtedly interact with the anode. Secondly, independent control of the exothermic (electrochemical oxidation of CO) and endothermic (gasification) reactions is impossible with *in-situ* gasification. This makes temperature control of the fuel cell difficult. This arrangement may be appropriate for batch processes and laboratory-based exploratory work but would not be ideal for industrial application.

For indirect gasification, the gasification step occurs in a unit separate from the fuel cell. The gasification unit is located upstream of the fuel cell and supplies the syngas to the anode compartment. The fuel cell runs on the dominant species supplied by the gasification process (CO if CO₂-fed gasification and H₂/CO if H₂O-fed gasification). An example of an indirect gasification setup is depicted in Figure 2.6.

The gasifier requires heat input to sustain the endothermic gasification reaction. There are several potential sources of heat:

1. Addition of oxygen into the gasifier ('autothermal gasification system')
2. Recycling of flue gas back to gasifier (in a CO₂-fed gasification system)
3. Heat exchange of flue gas with steam (in a H₂O-fed gasification system)
4. Combustion of syngas (a side-stream) and transfer of heat through heat coils or pipes within gasifier, or upstream pyrolysis syngas

Considerations for gasifier operating temperature include the enhancement of gasification reaction rate with increased temperature or by catalytic means, as well as the impact on the downstream SOFC operating temperature. Considerations for SOFC operating temperature include enhancement of electrolyte ionic conductivity and faster anodic and cathodic reactions with increasing temperature and temperature dependence of Boudouard gasification. High operating temperatures are ideal for reaction kinetics, however, low temperatures are desired for material selection.

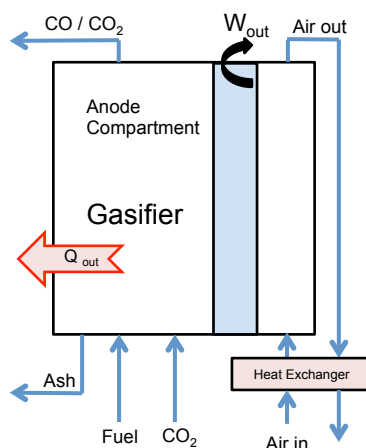


Figure 2.5: Single-step (in-situ) gasification

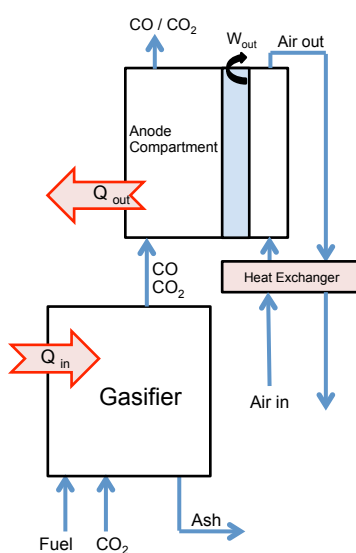


Figure 2.6: Indirect gasification (IDG)

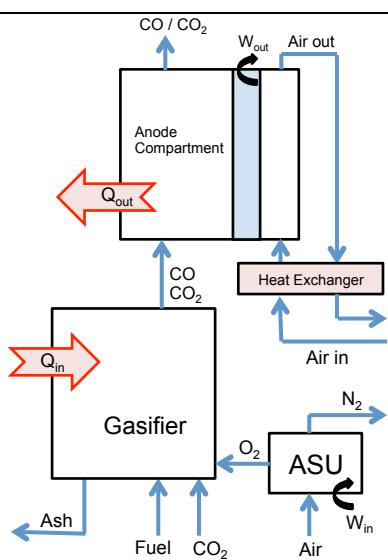


Figure 2.7: Autothermal gasification (ATG)

Unlike single-step gasification systems, the indirect approach allows for the possibility of hot gas clean-up after gasification, before reaching the anodic compartment. Single-step gasification systems must employ anodic barriers or sulfur resistant anodes if sulfur levels are too high. Also, ash is removed in a stage prior to and physically removed from the fuel cell.

Autothermal gasification systems are similar arrangement to IDG systems, but with the addition of an Air Separation Unit (ASU) and introduction of another reactive species, oxygen, into the gasification step. The oxygen is supplied to the fuel in order to generate heat necessary for the endothermic gasification reaction, through an exothermic reaction in the partial combustion of coal. The coal exposed to O₂ is mostly only partially oxidised to CO due to the low concentration of O₂ in the gasification atmosphere.

An example of an autothermal gasification setup is depicted in Figure 2.7. An ASU is often employed to avoid nitrogen diluting the gasification and anodic gas, as well as reducing additional heat required to heat up feed air.

2.5 Solid oxide electrolyte DCFC with molten anode

2.5.1 Molten carbonate as a medium for carbon oxidation or “hybrid direct carbon fuel cell” (HDCFC)

The hybrid direct carbon fuel cell (HDCFC) is a ‘hybrid’ of key elements of both the direct carbon MCFC and SOFC designs. Essentially both electrolytes from the MCFC and SOFC are used within the one cell with the fuel dispersed within the molten carbonate electrolyte. The physical cell resembles that of a typical SOFC cell with the molten electrolyte residing in the anode chamber so that it may wet the anode and supply fuel at the anode/electrolyte interface. The electrolyte consists of a binary eutectic mixture of Li₂CO₃ and K₂CO₃ [60]. There is scope, however, to trial alternative electrolyte mixtures such as the range used in molten carbonate DCFCs.

The HDCFC is a new technology (2005) and was conceived by Balachov and co-workers at SRI International, USA [10]. The cell concept was created with the vision to combine advantages of the molten carbonate and solid oxide DCFCs, and more so, to alleviate some issues with each cell type. Nabae and co-workers [11] address

some of the 'shortcomings' of traditional stand-alone molten carbonate and solid oxide DCFC systems and how the combination of the two technologies solves some of these key issues. These include separation of the cathode and the molten carbonate *via* a solid oxide electrolyte reducing the possibility of cathode corrosion as observed in MCFC systems [11,61]. Also, direct carbon MCFCs require management of CO₂ in the electrolyte mix [11] and delivering O²⁻ ions *via* a solid oxide electrolyte negates the need for CO₂ recycling from anode to cathode [11,20,61].

The primary motivation for incorporating molten carbonate in the SOFC anode chamber, however, is to improve the kinetics of electrochemical carbon oxidation in direct carbon SOFCs at low temperatures [11]. This is because, in a DCFC, contact between the anode and carbon fuel is necessary for the direct electrochemical oxidation of carbon (as per Eq. 1.4). The suspension of carbon in a molten carbonate solution effectively extends the anodic electrochemical reaction zone away from the TPB of SOFC systems. The electrochemical oxidation of carbon occurs in the slurry mixture with the carbonate ion and the carbon provides electron pathways to the anode current collector [62].

The benefit of the HDCFC cell over that of direct carbon SOFC cells, with respect to temperature, was evaluated by Nabae and co-workers [11] and their findings are reproduced in Figure 2.8. The 'cell' used to produce the results given in Figure 2.8 is essentially a tubular solid oxide DCFC, which upon addition of molten carbonate into the anode compartment becomes a makeshift HDCFC unit. The fuel used by the authors was carbon black and the 'cell (dry)' run was carried out as a physical contact-type solid oxide DCFC experiment, with no CO₂ feed.

It can be seen from Figure 2.8 that at temperatures above 820 °C, the solid oxide DCFC system becomes favourable as CO₂ produced in the anode compartment promotes Boudouard gasification of the fuel, improving the kinetics of reactions contributing to the overall conversion of C to CO₂ (see Section 2.4.3 & 2.4.4). It is also worth noting that the ionic conductivity of the YSZ electrolyte is highly dependent on temperature. There is an emphasis on minimising the solid oxide electrolyte thickness in HDCFC cells, since resistance to O²⁻ transfer through the electrolyte is high under the low operating temperature of these systems.

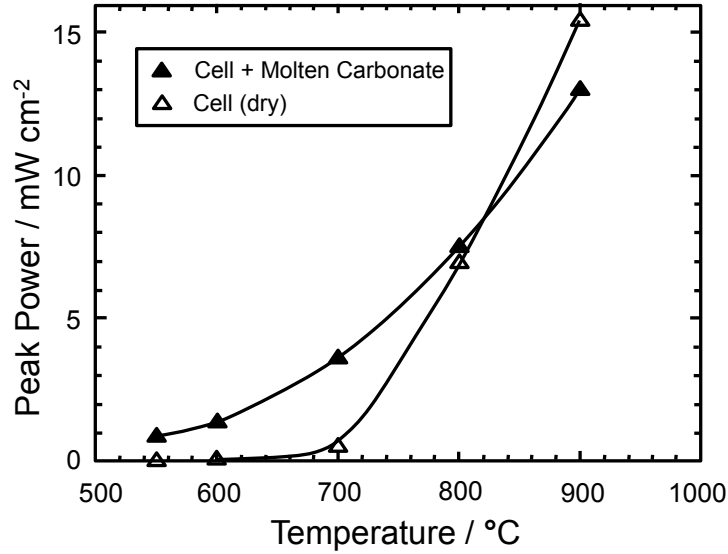


Figure 2.8: Comparison between direct carbon SOFC cell performance with and without molten carbonate, adapted from Nabae and co-workers [11]

At higher temperatures the HDCFC cell experiences significant decomposition of the molten carbonate producing CO_2 as well as O^{2-} ions in the melt *via* Eq. (2.10):



The presence of O^{2-} ions contributes to the high OCV values seen in HDCFC systems. This is due to the recombination of O^{2-} with CO_2 . The authors suggest that O^{2-} ions acts as a mediator in the carbonate mixture and the recombination of O^{2-} with CO_2 maintains a low activity of CO_2 , increasing the Nernst potential of Eq. (1.1) [11,62]. The same authors in the earlier study [11] investigated the effect of the thermal history of the cell on OCV. They noted that the OCV could be increased to 1.5 V at 550 and 700 °C after high-temperature operation (900 °C stepped down to 550 and 700 °C). In their subsequent study, the authors reported that the OCV could be improved, without compromising the carbonate electrolyte through high temperature treatment, by inclusion of a Ni catalyst into the carbon fuel [62]. The authors investigated the effect of loading carbon black with 10, 30, 50 wt% Ni on cell performance and OCV at various temperatures between 550 and 900 °C. They found the most significant improvement to peak power occurred at lower temperatures, and by a factor of 7.6 at 550 °C for a Ni loading of 50 wt%.

Jiang and Irvine [61] ran their HDCFC with a carbon black/carbonate mixture at varying carbonate loadings (0, 20, 50 and 80 mol% carbonate) and temperatures to determine the effect of operating conditions on OCV. The authors chose an 80:20 mol% carbon/carbonate for their subsequent cell runs. The low carbonate concentration was chosen as a compromise between anodic polarisation at high

carbon loadings, and sufficient carbonate to wet the carbon whilst minimising corrosion issues. After optimising for minimum activation polarisation, the authors then produced impedance spectra to assess cell performance and achieved a peak power density of around 18 and 53 mW cm⁻² at 700 and 800 °C respectively.

Jain and co-workers [60] investigated the performance of pyrolysed medium density fibreboard (pMDF). In an attempt to improve the poor performance of the pMDF in the fuel cell, the authors employed various fuel preparation techniques: immersion of pMDF sticks in eutectic molten carbonate mixture; immersion of pMDF sticks in a saturated aqueous solution of the carbonates before drying (a similar method to that employed by Cao and co-workers [63]); and milling of pMDF with carbonate powder.

The best performance was achieved by immersion of pMDF in the molten carbonate solution at an operating temperature of 800 °C. However, at temperatures below 700 °C, the pMDF samples prepared by immersion in aqueous solution and by milling show greater reactivity (with milled pMDF the standout performer). As the authors note, there are also handling issues associated with the use of molten carbonate mixtures outside of the cell.

There is much scope for further research into the benefits of low temperature operation of the HDCFC. However, advances in the ionic conductivity of the YSZ electrolyte at lower temperatures would significantly improve the output capability of these cells.

2.5.2 Molten metal as a medium for carbon oxidation

Similar to the molten carbonate system, carbon fuel can also be dispersed in a molten metal anode, with the metal acting as a medium in which O²⁻ ions are transferred between the solid electrolyte and the fuel. These systems necessarily operate at temperatures where the metal is in the liquid state. For tin, the most popular anode choice for this type of DCFC to date [36], this temperature range (~230 – 2770 °C) easily encompasses DCFC operating temperatures.

The benefits promised by the molten tin arrangement include a resistance to sulfur poisoning [64] and coking. CellTech Power have operated a molten tin anode tubular SOFC on hydrogen, jet fuel (JP-8, pyrolysed in the fuel cell) as well as solid fuels including coal and biomass [64,65]. Direct mixing of coal impurities with the molten

tin resulted in damage to the YSZ electrolyte [65]. However, the authors acknowledged that the experimental setup was a “worst case scenario” with the mixing of high concentrations of miscible heavy metal powders with the tin. The authors also propose that the molten tin could also act as a media for separation (via skimming off slag layer) or elimination of the impurities.

Alternative molten anode media has been trialled for this fuel cell, including Bi [66], In [67], Pb [67], Sb [67-69], Cu [70], and Ag [69].

Several of these researchers utilised solid carbon fuels in the molten anode, including charcoal [69], desulfurised coke particles [70], as well as de-ash coal [68]. In the operation of a liquid antimony anode on a reduced-ash coal, Wang and Co-authors [68] noted that Si and Fe in residual ash may have accumulated at the anode/electrolyte interface. In another study, desulfurised coke particles were mixed with molten Cu in a tubular cell arrangement where the molten anode existed on the outside of the tubes [70]. High power densities were reported (1700 mW cm^{-2}), largely due to the high operating temperatures of $1100 \text{ }^{\circ}\text{C}$, required to maintain Cu in the liquid state (above $1085 \text{ }^{\circ}\text{C}$ [71]). In this system, significant external heat input is required for the high temperature operation, which contributes to the power output of the cell.

2.6 Cell performance – effect of coal composition

Each coal sample has its own unique composition represented by ultimate analysis (carbon, hydrogen, nitrogen, sulfur, oxygen) and proximate analysis (moisture, ash, volatiles, fixed carbon, and sometimes includes the energy content). Ash analysis provides a breakdown of inorganic species in the coal expressed in terms of their oxides (oxides of silicon, aluminium, calcium, magnesium, sodium, iron, titanium and sulfur among others). The outcomes of these analyses hold important information regarding the make-up of the coal. This section will summarise the current understanding of how fuel composition, in particular sulphur and metallic oxides in ash, influence the performance of both molten carbonate and solid oxide DCFCs. Greater insight into fuel composition and its influence on fuel cell performance would enable screening of coal candidates for use within DCFCs.

2.6.1 Role of metals in coal

Every species present in coal may potentially have an impact on DCFC performance and operation. Some elements play an inhibitive role whereas others exhibit catalytic effects. Which category these species fall into for both molten carbonate and solid oxide DCFCs is very similar, however, the mechanisms by which they perform their catalytic or inhibitive effects may differ, and are largely unknown.

Less is known about the effects of species on molten carbonate systems than for solid oxide systems, however, species may be tentatively placed into categories of inhibitive and catalytic on the basis of work by Li and co-workers [72]. The authors studied the effect of metallic oxides common to coal ash on the electrochemical performance of molten carbonate DCFCs. These included fixed amount (8%) of oxides of calcium, magnesium, iron, aluminium and silicon impregnated in activated carbon (AC). Their results are summarised in Table 2.3:

Table 2.3: Molten carbonate DCFC performance at 700 °C using Activated Carbon (AC) impregnated with various metal oxides [72]

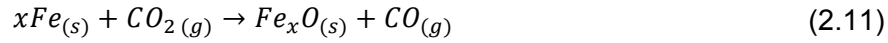
Fuel	OCV (V)	Current Density (mA cm ⁻² at -0.9V)	P _{max} (mW cm ⁻²)
AC (Pure)	-1.21	16	46.3
AC (8% MgO)	-1.22	22	51.8
AC (8% CaO)	-1.22	18	50.9
AC (8% Fe ₂ O ₃)	-1.20	17	47.3
AC (8% Al ₂ O ₃)	-1.19	15	43.3
AC (8% SiO ₂)	-1.18	14	40.8

From Table 2.3 it appears that for molten carbonate DCFCs, MgO, CaO and Fe₂O₃ act as catalysts for the electrochemical process whereas Al₂O₃ and SiO₂ act as inhibitors. However, the authors did not offer a detailed mechanism for the catalysis of electrochemical oxidation of carbon *via* inorganic species in the molten carbonate DCFC system. Systematic studies into the effect of these species at various concentrations and temperatures are required before they can be accurately categorised as either inhibitive or catalytic, and the extent of their inhibitive or catalytic effects understood.

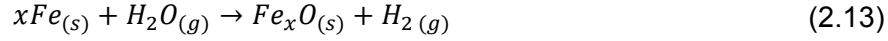
More is known about the effect of species on direct carbon SOFCs since in this case, the performance is directly dependant on the performance of the gasification

process, which in its own right is a well-studied field. The mechanism proposed by Furimsky and co-workers [73] for the catalysed gasification of coal is given as:

In the presence of CO_2 :



In the presence of steam:



The effect of catalysing Boudouard gasification on direct carbon SOFC performance has been investigated by Tang and Liu [51], who used pure activated carbon and Fe-loaded activated carbon as their fuel source. The presence of Fe is known to enhance the generation of CO as can also be seen in Figure 2.9.

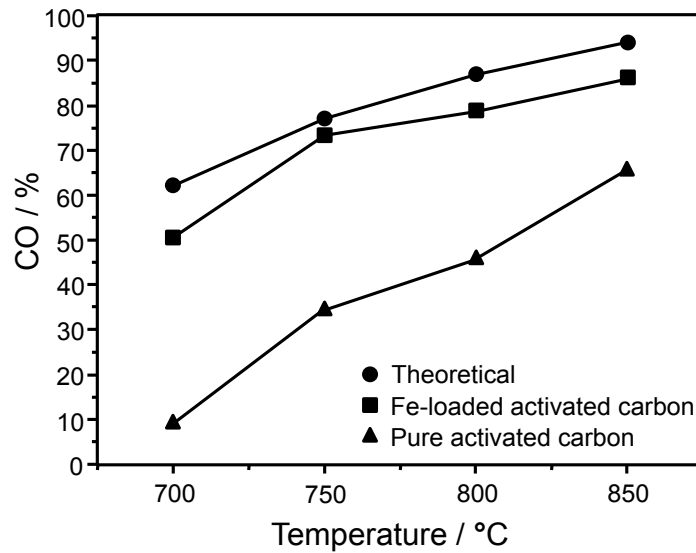


Figure 2.9: CO molar percentage as a function of temperature and presence of Fe, adapted from Tang and Liu [51]

The enhancement of cell performance due to the presence of Fe is also illustrated in Figure 2.10 and Table 2.4 (by comparison of 'Cell-II and Cell-III'). The maximum power output of the already GDC-catalysed cell was almost doubled upon the addition of Fe.

Other species were also tested for their impact on the solid oxide DCFC system. Li and co-workers [44] investigated the catalysis of CO_2 -fed gasification in a tubular reactor where the button cell and fuel were non-contacting and maintained at different temperatures (750 & 700 – 1000 °C respectively). They concluded that K, Ni and Ca all showed catalytic effects in order of decreasing effect of $\text{K} > \text{Ni} > \text{Ca}$. Their results are summarised in Table 2.5.

Table 2.4: Effect of different anodic materials on cell performance - summary of Figure 2.10 results [45]

	P_{\max} (mW cm ⁻²)	Polarisation Resistance (Ω cm ²)
Cell-I (pure Ag anode)	4	38
Cell-II (Ag-GDC anode)	24	2.3
Cell-III (Ag-GDC anode with Fe)	45	1

Table 2.5: Catalytic effects of selective coal inorganics on performance of CO₂-fed detached-type solid oxide DCFC [44]

Fuel	Power Density (mW cm ⁻²)		
	700°C	750°C	800°C
CB-K	95.6	147.7	185.3
CB-Ni	-	112.3	153.3
CB-Ca	57.7	103.4	149.1

As described earlier, it is necessary to catalyse both Eq. (1.6) and (1.7), which are coupled and widely accepted as the dominant reactions for most direct carbon SOFC arrangements. Therefore, catalysis of both the chemical and electrochemical oxidation of CO is required. The electrochemical oxidation of CO occurs at the anode three-phase boundary of the anode, electrolyte and fuel [45].

In terms of enhancing the electrochemical performance of the solid oxide DCFC however, due to the cell operating on a gaseous fuel and the desire to keep cell components isolated from impurities, catalysis *via* elements within the coal is limited. More work has been done to embed catalytic species into the anodes and cathodes themselves and so is a material selection issue. This is opposed to the potential for catalytic species to exist in the electrolyte solution in MCFCs.

One such material was investigated by Tang and Liu [51]. The authors used a silver anode and a silver-Gadolinia doped ceria Ag-GDC (GDC:Ag = 55:45 wt%), in a tubular cell design, to analyse the effect of GDC on the cell performance. The results of their experiments are shown in Figure 2.10 where the presence of GDC has a large positive impact on the cell performance ('Cell-I and Cell-II'). The results are summarised in Table 2.4.

Equally important as catalysing elements and reactions is monitoring and understanding the roles of species which have an inhibitive effect on cell

performance. Cherepy and co-workers [22] experienced degradation of molten carbonate DCFC performance via sulfidation corrosion when using cokes with 2.5 – 6 wt% sulfur. The authors found that Ni-based electrodes experienced densification of the porous electrodes through the formation of nickel sulphides, reducing contact with the carbon particulates. Indeed it has been found that many species react detrimentally with Ni, a common additive to DCFC cell components. A list of known catalysts and inhibitors to molten carbonate and solid oxide DCFCs is provided as Table 2.6.

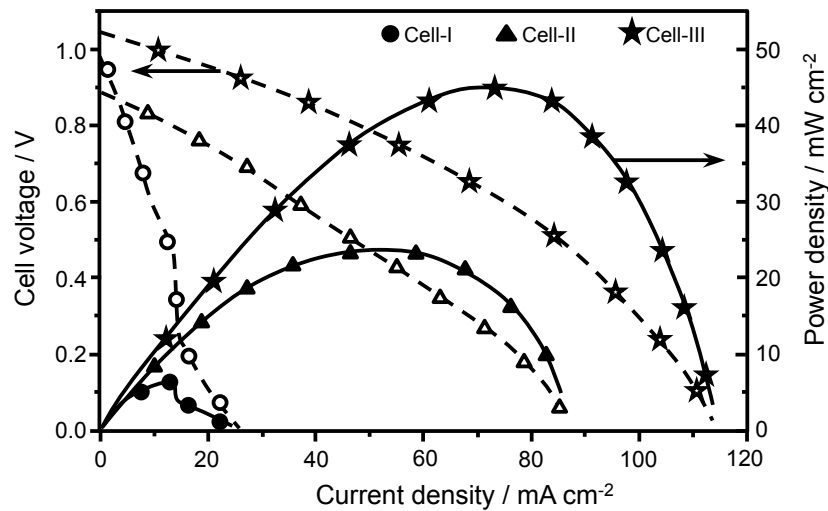


Figure 2.10: Cell performance for different anodic materials (Tang and Liu [51]), Cell-I (pure Ag anode), Cell-II (Ag-GDC anode), Cell-III (Ag-GDC anode with Fe)

Table 2.6: Summary of catalysts and inhibitors for molten carbonate and solid oxide DCFCs

MCFC Catalysts	MCFC Inhibitors	SOFC Catalysts	SOFC Inhibitors
MgO [72]	SiO ₂ [72]	Group I & II Metals [51]	S (as H ₂ S) – Reacts with Ni [75,76]
CaO [72]	Al ₂ O ₃ [72]	(K > Ni > Ca – decreasing catalytic effect on CO ₂ gasification reaction) [44]	Se (as H ₂ Se) – Reacts with Ni [75]
Fe ₂ O ₃ [72]	Cl > 0.01ppm (Vol) [74]		As – reacts with Ni [75]
	F > 0.01ppm (Vol) [74]		Cr ₂ O ₃ vapour [77]
	S (as COS, H ₂ S, mercaptanes and thiophenes) [22,74]		P (as PH ₃ or HPO _x) – reacts with Ni [75]
	Dust >5 μm (from gas streams) [74]	Group VIII Metals (Fe) [51,73]	
	Si (as silanes and siloxanes) [74]		

It is important to note that not all of the impurities are derived from the fuel source, but also from metallic components of the cell itself (as is the case with Cr_2O_3 evaporation).

2.6.2 Composition of Victorian brown coals

Victorian brown coals are high-moisture (around 60% as-received) and low-ash (around 2% when dried) coals. Ultimate analysis and ash analysis [15] of three major Victorian brown coals are presented in Tables 2.7 and 2.8 respectively.

Table 2.7: Ash analysis of Victorian coal (atomic wt%) conducted by Brown and co-workers [78]

	SiO_2	$\text{AlO}_{1.5}$	$\text{FeO}_{1.5}$	CaO	MgO	$\text{NaO}_{0.5}$	$\text{KO}_{0.5}$	TiO_2	SO_3
Morwell	0.19	1.21	11.57	29.95	24.12	14.29	0.60	0.22	16.76
Hazelwood PS	4.38	1.49	6.50	36.74	29.95	7.35	0.51	0.12	11.47
Hazelwood	5.20	3.57	10.14	15.97	33.42	17.78	0.84	0.21	10.08
Yallourn	0.85	1.89	24.73	11.78	36.52	13.57	0.30	0.11	10.23
Maryvale	3.18	1.09	41.68	11.56	22.81	10.74	0.58	0.12	5.47
Loy Yang	7.52	26.02	9.67	4.67	20.11	19.83	0.25	0.41	8.20
Vale Point	59.44	27.48	3.66	2.46	1.58	1.11	2.80	1.03	0.43

Table 2.8: Typical ultimate analysis ranges of Victorian brown coals on a % mass-dry basis [79]

	Yallourn	Morwell	Loy Yang
C, % db.	64.9 – 66.6	64.9 – 69.3	66.1 – 68.7
H, % db.	4.00 – 4.60	4.40 – 5.10	4.50 – 4.90
N, % db.	0.43 – 0.51	0.44 – 0.64	0.53 – 0.68
S, % db.	0.21 – 0.25	0.23 – 0.39	0.27 – 0.37
O, % db.	24	22.2	22.7
Ash, % db.	1.90 – 2.40	1.70 – 3.00	1.09 – 2.79
Na, % db.	0.08 – 0.09	0.05 – 0.09	0.05 – 0.15
Cl, % db.	0.06 – 0.10	0.04 – 0.07	0.04 – 0.10

As is evident, these coals have very low sulphur and ash content; however, in the ash, there are significant levels of metals that potentially may have both catalytic and inhibitive effects during their use in a DCFC. Given that no research has been conducted into the application of Victorian brown coals within DCFCs, predicting their performance in a DCFC is difficult. This is especially so due to the limited knowledge

of mechanisms surrounding the catalytic and inhibitive effects of individual species. However, Victorian brown coals show promise based on their low sulfur and ash contents, and relative abundance of catalytic elements.

Coals apparently suited to gasification-driven SOFCs (for a given ash content, high proportions of Fe, Ca, Mg, Na, K) are those from the Morwell, Hazelwood, Yallourn, and Maryvale mines.

Coals apparently suited to direct carbon MCFC application (low in ash but for a given ash content, high in Fe, Mg and Ca and low concentrations of Si and Al) are those from the Yallourn, Morwell and Maryvale mines. Volatile matter is also undesirable in direct carbon MCFCs. All Victorian brown coals are high in volatile content, therefore these would benefit from pyrolysis (devolatilisation) prior to their use in the direct carbon MCFCs.

For continuous operation of fuel cells, and in particular the direct carbon MCFC, a low-ash content is desirable. Also, for good fuel utilisation in a gasification-driven SOFC a high fixed carbon content is desired for high char yields. Table 2.8 gives the ultimate analysis ranges of some Victorian brown coals, and highlights their low-ash and low-sulfur content.

It is important to note however, that the analyses given in Table 2.7 and Table 2.8 are those of raw coals. Any form of fuel pre-treatment, such as heat treatment or acid washing, will have a marked effect on the fuel composition as well as, in some cases, its physical nature. The effects of pre-treatment for fuel preparation are discussed in the following section.

2.7 Fuel preparation options and coal characteristics

Two major classes of pre-treatment are heat treatment and acid washing. This section will address the effects of these two methods of pre-treatment as well as the potential for application of treated coals as fuels for DCFCs.

2.7.1 Heat treatment

There is an abundance of literature available on heat treatment of coals and other carbonaceous matter in the form of pyrolysis and gasification. The focus of this

literature review, in terms of heat treatment as a means of preparation of fuels for DCFC, was pyrolysis. The relevance of gasification to DCFC technology has been discussed in the previous section on direct carbon SOFCs, where it acts as not a pre-treatment method, but a necessary mechanism for fuel consumption.

Various papers on pyrolysis of low-rank coals, and in particular Victorian brown coals, were reviewed. The major types of reactors mostly used for coal pyrolysis are – fluidised bed reactor, wire-mesh reactor, drop-tube reactor (also called entrained flow reactor), and curie-point pyrolyser. While a variety of pyrolyser reactors have been employed by researchers, no discernable preference is noted for any given coal type.

The preparation of chars *via* pyrolysis for use in DCFCs and in particular, solid oxide DCFCs is a promising and apparently necessary concept, however, little is known about the performance of these chars in DCFC systems. It is possible to subject the raw coal to a single heat treatment of pyrolysis followed by gasification within the solid oxide DCFC but this may have undesirable consequences. Namely, the solid oxide DCFC would be subject to several impurities released during the pyrolysis of the coal in tars and other gaseous and condensable species, such as compounds of S and Cl. In addition, the heavy organic tar volatiles would condense in the cooler regions of the DCFC testing station. However, some authors have claimed enhanced fuel cell power output as a result of utilisation of organic volatiles liberated *in-situ* [80-82].

Pyrolysis would likely be of greatest benefit to a gasification-driven SOFC system as a means of generating char as the fuel. The volatiles produced may be used for an alternative means, such as generation of heat for the gasifier, or to satisfy another market such as BTX (Benzene, Toluene, Xylene) and other non-fuels chemical production. See Hayashi and Miura [83] for a concise overview of chemicals production from pyrolysis of coals. The authors also outline effects on soot formation, with the introduction of steam to the pyrolysing atmosphere greatly reducing soot formation as well as substantially increasing CO_x evolution.

Chars prepared *via* pyrolysis experience increase in surface area, however, have been found to be a poor fuel for molten carbonate DCFCs [84,85] (see Table 2.9). This is due to the reduction in surface oxygen-containing compounds on the char

surface, which are largely responsible for the reactivity of the coal in a molten carbonate environment.

Table 2.9: Summary of heat treatment results on raw coal properties and effect on molten carbonate DCFC performance [85]

Heat Treatment	Surface Functional Groups	S_{BET}	V_{total}	D_{pore}	Crystallinity	OCV	P_{max}
Oxidation in Air (500 °C)	6.6% increase in surface O, 66.7% decrease in surface S	10.1% increase	23.1% decrease	Negligible change	48% increase in L_a	0.06 V penalty (at 800°C cell operation)	53 mW cm ⁻² (52.3%) penalty (at 800°C cell operation)
Pyrolysis (750 °C)	16.5% decrease in surface O, 83.3% decrease in surface S	58.2% decrease	53.8% decrease	12.9% increase	76% increase in L_a	0.12 V penalty (at 800°C cell operation)	71 mW cm ⁻² (64.0%) penalty (at 800°C cell operation)
Pyrolysis (950 °C)	48.4% decrease in surface O, 83.3% decrease in surface S	10.1% decrease	69.2% decrease	15.2% increase	108% increase in L_a	0.16 V (73.9%) penalty (at 800°C cell operation)	82 mW cm ⁻² penalty (at 800°C cell operation)

- S_{BET} , V_{total} and D_{pore} were achieved via N_2 adsorption

There are also implications for the application of chars in solid oxide DCFCs based on the pyrolysis conditions. Many species are volatilised during pyrolysis and some of these leave with the volatiles components, whereas some reattach themselves to the char. Which species remain in the char is an important consideration for the downstream gasification of the char in a solid oxide DCFC and is largely dependent on the gasification reactor configuration. An overview of AAEM (alkali and alkaline Earth metallic) species volatilisation based on peak temperature is shown in Figure 2.11.

Figure 2.11 is not universal for all pyrolysis conditions. There are many variables for pyrolysis such as reactor type, heating rate, peak temperature and holding time [86]. Figure 2.11 is supplied as a guide for typical results of pyrolysis. Peak temperature has a greater effect on volatilisation of AAEM species than does heating rate [83,87]. However, peak temperature may still be misleading as Manzoori and Agarwal [88] demonstrated that at least 80% of Mg, Ca and Na can be volatilised at 700 °C with a holding time of 40 seconds, and a complete volatilisation of Cl. Therefore it is necessary to ensure that holding times are sufficient to allow for complete volatilisation, especially for fast pyrolysis.

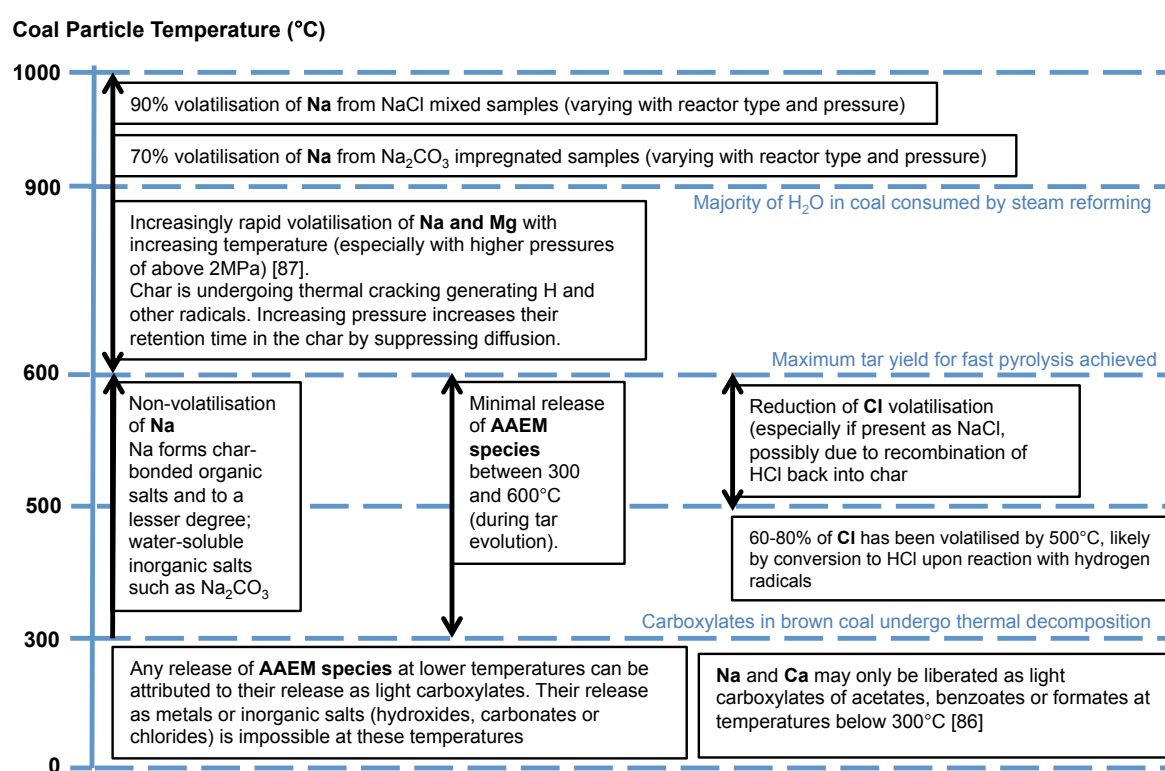


Figure 2.11: Temperature map of AAEM species volatilisation during pyrolysis of Victorian brown coal

2.7.2 Acid washing

As opposed to heat treatment, the use of acid washed coals in DCFCs is well documented. Researchers have implemented acid washing for various purposes, but primarily to remove metallic impurities to allow for selective impregnation of AAEM species, to determine their individual catalytic/inhibitive properties. The effect of acid washing on porosity, surface area as well as surface functional groups, and the associated impact of these factors on cell performance have also been examined. An

overview of the effects of acid washing on coal and other commonly studied carbon sources is given in Table 2.10.

Table 2.10: Effect of acid washing on various coal properties and performance in molten carbonate DCFCs

	Fuel Type	HNO ₃	HCl	HF
Species Removal	Raw Coal [85]	Modestly effective for Al and S removal, increase in surface N	Modestly effective for Al removal	Extremely effective for Si and Al removal
Surface Functional Groups	Raw Coal [85]	125.2% increase in surface O, 176.9% increase in surface N	30.8% increase in surface O	27.5% increase in surface O
	Activated Carbon [24]	32.5% increase in surface O	13.8% increase in surface O	-
	Carbon Black [24]	390% increase in surface O	190% increase in surface O	-
S_{BET}	Raw Coal [85]	92.4% increase	72.2% increase	112.7% increase
	Activated Carbon [63]	1.9% increase	-	6.1% increase
V_{total}	Raw Coal [85]	100.0% increase	84.6% increase	107.7% increase
	Activated Carbon [63]	2.4% increase	-	4.9% increase
D_{pore}	Raw Coal [85]	2.0% increase	4.6% increase	2.6% increase
Crystallinity (by L_a value)	Raw Coal [85]	Negligible change	Negligible change	Negligible change
	Activated Carbon [24]	Minor increase (6.7%)	Negligible increase	-
	Carbon Black [24]	Notable increase (31.0%)	Notable increase (27.6%)	-
P_{max} (Molten Carbonate)	Raw Coal [85]	18 mW cm ⁻² improvement (at 800°C)	4 mW cm ⁻² improvement (at 800°C)	6 mW cm ⁻² improvement (at 800°C)

- Signifies not reported

With respect to the values stated in Table 2.10, the percentages are case-specific and are not universal. They are provided as a means for quick comparison. It is accepted that HF is very effective at removing Al and Si from coal. However, due to the extreme hazards surrounding this acid, the use of HF in acid digestion is being

phased out. Unfortunately, the use of more benign acids such as HNO_3 and HCl do not achieve the desired Al/Si removal.

Microwave acid digestion is one method of increasing the capacity of an acid to adsorb metals from the coal. This method is particularly beneficial for weaker acids and is often a precursor to ICP spectrometry analysis [89-91]. Wang and co-workers [89] used microwave digestion of coal with HNO_3 at 250°C and 7.5 MPa, and reported good recovery of trace elements in the coal samples. The absence of HF from the digestion allowed for the use of a quartz vessel. Popular reagents for use in microwave acid digestion include HCl , HNO_3 and H_2O_2 .

The weight loss resulting from the decomposition of surface functional groups becomes more prominent with acid treatment, as shown in Figure 2.12 [30]. This is particularly evident with HNO_3 treatment as this acid is known to generate high amounts of surface oxygen functional groups [24]. Such acid treatment increases the reactivity to oxygen of the material, reducing its thermal stability. In some cases of acid washing the acid decreases the thermal stability of the surface functional groups, which lowers the onset temperature of decomposition. This is the case for CO-containing functional groups when washed with HCl [24].

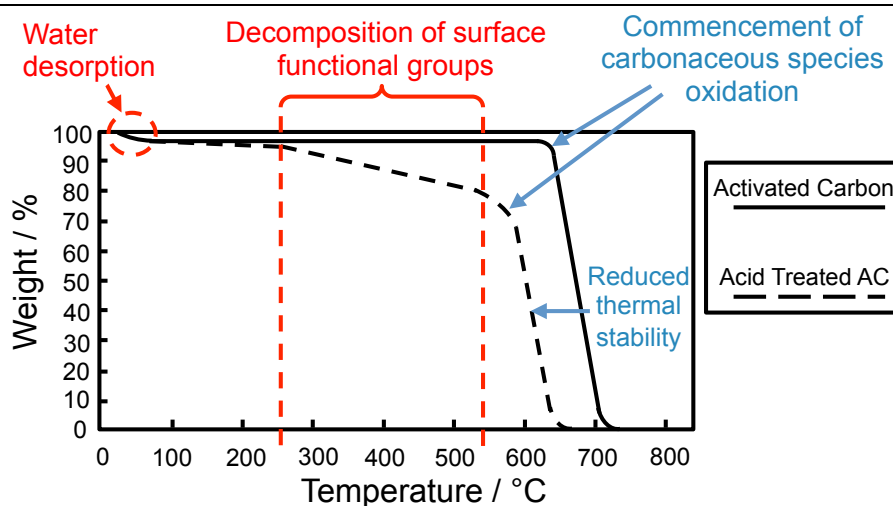


Figure 2.12: Typical TGA curve for activated carbon and response to acid washing

Acid washing holds benefits for research by allowing examination into the extent of pore blockage by metal ions as well as being a necessary precursor to ion-exchange analysis. Acid washing with HNO_3 has even been shown to significantly enhance the performance of molten carbonate DCFCs by increasing the number of surface oxygen groups. However, acid washing on an industrial scale is not feasible, and the primary benefit of laboratory-based acid washing of coals for use in DCFCs is insight

gained into the catalytic/inhibitive effect of individual AAEM species. Therefore, the most suitable coal for use in a commercial DCFC would be one low in ash, Al and Si content, to negate the need for a large-scale acid washing process.

Minimal examination into the effect of acid-washing on fuels used in solid oxide DCFCs has been performed since the fuel of choice for researchers has been carbon black (see Table 2.12). Investigations into the effects of metal ions on the reaction mechanisms for solid oxide DCFCs has been investigated through impregnation of carbon black (Fe-based catalysis [51]), and activated carbon (K, Ni, Ca based catalysis [44]). An overview of the analysis of these fuels is supplied in the following section (Section 2.8).

2.8 Analytical techniques

Typical analytical techniques used by authors to discern properties of fuels used in molten carbonate and solid oxide DCFCs are provided here.

2.8.1 XPS - X-ray photoelectron spectroscopy

The surface characteristics of fuel is accepted as one of the most important factors in the fuels reactivity, and hence the achievable current density from the DCFC. As one method of determining surface and sub-surface (to 12 nm depth) composition, XPS was a popular method for Li and co-workers [72,85]. Of particular interest to Li and co-workers was the surface oxygen to carbon ratio since surface oxygen functional groups have a significantly positive effect on the performance of DCFCs, and in particular molten carbonate DCFCs. It should be noted that Li examined several carbon fuels' surface compositions using various techniques including ICPOES, TPD and TGA.

2.8.2 ICPOES - Inductively coupled plasma optical/atomic emission spectroscopy

ICPOES method was used by Li and co-workers [72] to determine the ash composition in coal samples after the oxidation of the coal in an air-fed tube furnace at 700 °C for two hours. This technique was used in very few papers investigating DCFCs, due to the predominant use of carbon black in these fuel cells and carbon black's ash-free nature.

2.8.3 XRD - X-ray diffraction

Aside from surface characteristics, crystallinity, often measured by XRD, has been identified as the other main factor in influencing fuel reactivity in DCFCs. This method has been employed by authors to compare the crystallinity of fuel samples and its effect on DCFC performance, as well as the effect of preparation techniques on crystallinity and in particular heat-treatment [85].

Kulkarni and co-workers [12] employed XRD to investigate the stability of the Lanthanum Strontium Cobalt Ferrite (LSCF) anode in contact with carbon black. This was achieved via XRD analysis of a 50:50 (wt%) mixture of LSCF powder and carbon black.

All of the XRD measurements encountered were conducted at room temperature. Many of the fuel samples that have been analysed are those of chars produced by heat treatment. As the fuel sample cools down to room temperature the morphology of the char undergoes certain changes, including a change in crystallite properties. Therefore, crystallite size estimates from XRD measurements are limited to the conditions of the XRD analysis, and the properties of the char at those temperatures. They do not necessarily reflect the coals properties under the conditions experienced by the fuel during preparation (or more importantly those which the fuel undergoes during reforming in the fuel cell). Therefore, X-ray diffraction conducted with samples *in-situ* and at high temperature (high temperature XRD, HTXRD) will be a useful analytical technique for characterizing fuel samples for DCFC application.

2.8.4 SEM – Scanning electron microscopy

Most authors, including Cherepy and co-workers [22], employed SEM imaging to gauge coal particle size and observe particle size distribution, with further image processing.

SEM imaging was also employed to discern fuel properties for use in carbon deposit solid oxide DCFC fuel cell types [92,93]. The SEM was not used to analyse the raw fuel as such, but rather the deposited carbon on the anode, since the fuel sources analysed were methane.

2.8.5 Surface area measurement by gas adsorption

There are two main gas adsorption techniques used for the analysis of surface characteristics of coal and other carbon-based fuels. These are N₂ adsorption and CO₂ adsorption. N₂ adsorption is a popular method for analysis of the porosity of a fuel sample, and in particular a coal-based fuel sample. Most authors calculated the overall surface area using the Brunauer-Emmett-Teller (BET) method. Some authors estimated the mesoporous surface area as the total surface area minus the microporous surface area [63,84]. Accurate mesoporous volume calculations are crucial as mesoporous volume has been identified as an important factor for molten carbonate DCFC performance [84], since they are much more accessible to the molten carbonate electrolyte than are micropores. For this reason, total surface area is not a reliable base for predicting a fuel's reactivity in a molten carbonate DCFC. Li and co-workers [24] report that a mesoporous structure in the fuel can be detected by hysteresis loops in the N₂ adsorption isotherms.

Li and co-workers [72,85] utilised CO₂ adsorption to determine V_{micro} , S_{micro} and D_{micro} via the Dubinin-Raduskevich (DR) method. It is thought by many that differences between N₂ and CO₂ specific surface area results (in favour of larger CO₂ area readings) are due to an activated diffusion effect rendering the microporous structure inaccessible to N₂ at 77 K [85,94,95]. However, it may have just as much to do with CO₂ chemisorption in some cases. CO₂ chemisorbs onto alkaline earth metal oxides. This is consistent with CO₂ chemisorption onto Ca-loaded lignite chars [96]. Linares-Solano and co-workers [97] identified that this could result in misleading surface-area approximations based on CO₂ adsorption when comparing their analytical results for pore volume and surface area for various Ca loadings.

2.8.6 TDS/TPD - Thermal desorption spectroscopy

TPD is another useful method [24,72,84,85] for analysing the surface chemistry of fuels used in molten carbonate DCFCs. As was the case with XPS, the authors used TPD to investigate surface oxygen complexes. This was used to compare the reactivity of the fuels used in the molten carbonate DCFC based on their surface oxygen groups concentrations, as well as the effect of preparation techniques on the formation/destruction of these surface oxygen groups.

2.8.7 TGA - Thermogravimetric analysis

Li and co-workers [24,72,84,85] used TGA to measure the moisture, volatile matter, fixed carbon and ash content of various raw coals, as well as acid- and heat-treated coals, for use in a molten carbonate DCFC. They also compared the thermogravimetric results to assess changes to thermal stability of the coal post acid-washing (see Figure 2.12).

Zhao and co-workers [93] employed TGA in a deposited-type solid oxide DCFC study. The TGA was used to analyse the deposited carbon on the anode. This test was performed in support of SEM imaging, to gain insight into the reaction mechanism for CH₄-deposited direct carbon SOFCs.

2.8.8 Frequency response analyser

Electrical conductivity is an important factor for coal materials in DCFCs as they are the anodic material and sometimes used as the electrode. They play a major role in contributing to the global ohmic resistance of the cell. The electrical conductivity of a coal is directly related to its structure, and in particular its graphitic nature. Therefore frequency response analysers may be employed by researchers who are concerned with carbon fuels which are also used as the anode electrode, or what impact preparation techniques may have on the potential for certain fuels to be used as the anode in a DCFC. However, this arrangement has been somewhat superseded by the coal dispersed in liquid electrolyte-design for molten carbonate DCFC systems. Also, it is widely accepted that a coal's reactivity is more important than a high electrical conductivity, since an improvement in one factor often leads to a decline in the other, due to graphitisation of the carbon.

2.8.9 Fuel analysis overview

Table 2.11 shows the authors who have used various analytical techniques to discern certain properties of carbonaceous fuels used in both molten carbonate and direct carbon DCFCs. There were numerous other analytical techniques employed by many authors to evaluate the performance and output of cells such as online gas chromatography and soap-film burettes, however the focus of this table is purely on fuel analysis.

Table 2.11: Analytical techniques used for DCFC fuel analysis

Analytical Technique	Molten carbonate DCFC	Solid oxide DCFC	Used for
SEM	[22,98,99]	[92,93,100-103]	Particle size distribution
XPS	[72,85,98]	[80,89,101]	Surface functional complex, surface elemental composition
ICPOES	[72]	[55]	Ash composition
TDS/TPD	[24,72,84,85]	-	Surface oxygenated complex
TGA	[24,72,81,84,85,98, 104]	[55,80,93,100-102, 104]	Proximate analysis, reactivity studies
XRD	[22,24,72,84,85,98, 99]	[12,54,80,101-104]	Degree of crystallinity, crystallite size
Gas adsorption – N₂	[24,63,72,84,85,98]	[103]	Surface area
Gas adsorption – CO₂	[72,85]	-	Surface area
Frequency response analyser	[24,84]	-	Electrical conductivity

A high proportion of the fuels trialled in DCFCs were carbon black (see Table 2.12). This is especially true for solid oxide DCFC studies prior to ~2012. Since the carbon blacks used were commercial carbon blacks, most of the fuel properties are supplied by the supplier and so additional analysis of the carbon black was only required when the fuel was altered, such as when the carbon black underwent ion-impregnation. Also, most of the early solid oxide DCFC papers that included fuel analysis were deposited-types with the analysis focused on the anode post-deposition. Therefore, the majority of references listed in Table 2.11 for solid oxide DCFCs are from recent studies, where analysis of less homogenous carbon samples was necessary.

2.9 Fuel types used in DCFCs

Table 2.12 is a summary of the performance of modern DCFC arrangements based on the fuels used and is included at the end of the chapter.

As Table 2.12 highlights, the majority of research into solid oxide DCFCs has been conducted using carbon black samples. This is because carbon black is a highly pure source of carbon with low ash content and results in minimal degradation of the fuel cell. Because of the absence of impurities, carbon black also allows for accurate investigation into the effect of metal ions on the performance of the cell, post ion-exchange or ion-impregnation.

Despite the obvious advantages for research that carbon black has, there is a need to expand fuel sources to coal-derived carbon for industrial application of the DCFC. Minimal research has been conducted into the use of coal-derived fuels in solid oxide DCFCs and in particular, the use of lignite-based fuels. Investigation into application of raw coals and their products in DCFCs is paramount in assessing the feasibility of DCFCs as a large-scale provider of energy. A greater understanding of achievable outputs from raw coals as well as treated coals is therefore required. The use of these fuels would also help validate whether recent knowledge gained into the effect of individual metal ions on cell performance is translatable to the potential real-world application of coals with limited pre-treatment. This is particularly important as much remains unknown about the mechanisms of individual species as well as uncertainty about some fundamental reaction mechanisms. These factors all contribute to a lack in predictability of DCFC performance for a given fuel, much less one that has not been trialled before in Victorian brown coal.

2.10 Concluding comments

Direct carbon fuel cells (DCFCs) can operate at high temperatures and therefore has significant thermodynamic advantage of almost zero entropy change resulting in high theoretical electrochemical conversion efficiency. The current status of DCFC technology and its different configurations, and associated analysis requirements have been reviewed in this chapter. In particular, emphasis has been given on review of all fuels tested in molten carbonate and solid oxide DCFC systems, and critical evaluation of low-rank coals and biomass, amongst other alternative fuels.

Most of the research to date has focussed on molten carbonate- and solid oxide-type DCFC systems. Until recently only limited types of fuels have been used, with the majority of fuels being carbon black, with some studies involving activated carbons. However, carbon black is not an economically viable candidate for use in large-scale power generation systems.

Only a limited number of studies have used coal, assessing the catalytic and inhibitive effects of some of the metallic elements present in ash on cell performance. Compounds of Ni, Ca, Mg, and Fe have been demonstrated to exert catalytic effects, while presence of Si and Al are shown to exhibit inhibitive effects. However, a systematic study assessing the effects of their concentration on cell performance is warranted. There is also a limited understanding of the mechanisms by which these compounds interact with the fuels or fuel cell components (in particular the anode and electrolyte), and how they perform their catalytic and inhibitive roles.

Low-rank coals have not been assessed in general for DCFC applications. Some of the low-rank fuels, such as dried Victorian brown coal and dried biomass, and their heat-treated products can potentially be good fuel sources for DCFCs because of low ash content, and presence of significant amount of the catalytic elements. However, the effect of the levels of the inhibitive elements and the solid trace metals in these fuels on their electrochemical performance in a DCFC is unknown.

The review also identifies the typical fuel preparation methods for use of these fuels in DCFC systems. The associated analytical methods for characterising the prepared fuels and assess their performance in DCFC systems have also been identified and discussed.

Table 2.12: DCFC Performances using various solid fuels under inert anode purge, PPD (peak power density), OCV (open circuit voltage)

Fuel Class	Fuel Name / Origin	Electrolyte / Cell Arrangement	OCV (V)	PPD (mW cm ⁻²)	Temp. (°C)	Ref.
Miscellaneous fuels	Acetylene Black (from acetylene pyrolysis)	Molten Carbonate (eutectic Li-K)	-	61	800	[22]
	Carbon Aerogel Microspheres (Pyrolysed – glassy carbon)	Molten Carbonate (eutectic Li-K)	-	61	800	[22]
	Needle Petroleum Coke (calcined, milled)	Molten Carbonate (eutectic Li-K)	-	36	800	[22]
	Green Needle Coke, crushed (Jinzhou Petrochemical Co.)	Molten Carbonate (Li ₂ CO ₃ -K ₂ CO ₃ -Al ₂ O ₃ as 1.05:1.2:1 by mass)	0.82	141	650	[105]
	Vapour-Grown Carbon Fibre (Showa Denko K.K. Co., Japan)	Molten Carbonate (Li ₂ CO ₃ -K ₂ CO ₃ -Al ₂ O ₃ as 1.05:1.2:1 by mass)	0.7	85	650	[105]
Activated carbon / biomass chars	Granular AC (Calgon BPL)	Molten Carbonate	1.34	83	800	[84]
	Granular AC (Calgon BPL)	Molten Carbonate (eutectic Li-Na-K)	1.34	-	800	[24]
	Granular AC –HNO ₃ Washed (Calgon BPL)	Molten Carbonate (eutectic Li-Na-K)	1.35	-	800	[24]
	Granular AC –HCl Washed (Calgon BPL)	Molten Carbonate (eutectic Li-Na-K)	1.33	-	800	[24]
	Peach pit AC acid-washed	Molten Carbonate (eutectic Li-K)	-	84	800	[22]
	Coconut AC acid-washed	Molten Carbonate (eutectic Li-K)	-	56	800	[22]
	Coal-derived AC acid-washed	Molten Carbonate (eutectic Li-K)	-	51	800	[22]

Activated carbon / biomass chars

Fuel Class	Fuel Name / Origin	Electrolyte / Cell Arrangement	OCV (V)	PPD (mW cm ⁻²)	Temp. (°C)	Ref.
	Wood-derived AC (HF-washed)	Molten Carbonate (eutectic Li-K)	-	-	-	[63]
	Wood-derived AC	Molten Carbonate (eutectic Li-K)	1.0	25.2	700	[98]
	Coconut-derived AC	Solid oxide (Ni-YSZ anode-supported button cell, YSZ electrolyte)	~0.8	90	750	[106]
	Coconut-derived AC	Solid oxide (Button cells, YSZ electrolyte, YDC anode)	0.85	33	800	[56]
	Coconut-derived AC (Metal Clay Pty. Ltd., Australia)	Solid oxide (GDC electrolyte, YSZ-GDC anode, button cell)	0.87	12	800	[55]
	Bio-char (Black Earth Products, Australia)	Solid oxide (GDC electrolyte, YSZ-GDC anode, button cell)	1.07	~10	800	[55]
	Raw waste wood	Solid oxide (tubular, YSZ electrolyte, Ni-GDC anode)	0.95-1.0	~65	800	[101]
	Low-ash activated carbon (Sigma-Aldrich, USA)	Solid oxide (Ni-YSZ anode supported Button cell, YSZ electrolyte) – CO ₂ /N ₂ anode purge	0.78	15	800	[103]
	Pure AC, Taishan Yueqiao Reagent Plastic Co. Ltd.	Solid Oxide (Tubular, YSZ electrolyte, Ag-GDC anode)	0.90	24	800	[51]
	AC with Fe, Taishan Yueqiao Reagent Plastic Co. Ltd.	Solid Oxide (Tubular, YSZ electrolyte, Ag-GDC anode)	1.05	45	800	[51]
	Pine Charcoal (INCAR – CSIC, Spain)	Solid Oxide (Anode support, Molten Carbonate hybrid – Li ₂ CO ₃ /K ₂ CO ₃)	1.00	~96	700	[107]

Fuel Class	Fuel Name / Origin	Electrolyte / Cell Arrangement	OCV (V)	PPD (mW cm ⁻²)	Temp. (°C)	Ref.
Carbon black	Koppers Continox N220	Molten Carbonate	1.26	32	800	[84]
	Koppers Continox N220	Molten Carbonate (eutectic Li-Na-K)	1.26	-	-	[24]
	Koppers Continox N220 – HNO ₃ Washed	Molten Carbonate (eutectic Li-Na-K)	1.31	-	-	[24]
	Koppers Continox N220 – HCl Washed	Molten Carbonate (eutectic Li-Na-K)	1.28	-	-	[24]
	Koppers Continox N220 – Air Plasma Treated	Molten Carbonate (eutectic Li-Na-K)	1.29	-	-	[24]
	Koppers Continox N660	Molten Carbonate	1.25	46	800	[84]
	Conductive CB (Vulcan XC72, Cabot Co, USA)	Molten Carbonate (Li-K-Al as 1.05:1.2:1 by mass)	0.77	116	650	[105]
	Arosperse 3 (from furnace oil)	Molten Carbonate (eutectic Li-K)	-	39	800	[22]
	Arosperse 15 (from methane pyrolysis)	Molten Carbonate (eutectic Li-K)	-	46	800	[22]
	Black Pearls 2000 (K - catalysed), GP-3848, Cabot Corporation, USA	Solid oxide (detached-type, CO ₂ -fed, button cell)	-	185.3 (at 0.7 V, not PPD)	800	[44]
	Black Pearls 2000 (Ni - catalysed), GP-3848, Cabot Corporation, USA	Solid oxide (detached-type, CO ₂ -fed, button cell)	-	153.3 (at 0.7 V, not PPD)	800	[44]
	Black Pearls 2000 (Ca - catalysed), GP-3848, Cabot Corporation, USA	Solid oxide (detached-type, CO ₂ -fed, button cell)	-	149.1 (at 0.7 V, not PPD)	800	[44]
	Pressed Conductive CB (Vulcan XC72, Cabot Co, USA)	Solid Oxide (direct contact type – carbon pellet pressed between anode and electrolyte, N ₂ anodic gas)	-	49 (at 0.4 V)	900	[16]

Fuel Class	Fuel Name / Origin	Electrolyte / Cell Arrangement	OCV (V)	PPD (mW cm ⁻²)	Temp. (°C)	Ref.
Carbon black	Ball milled CB (Vulcan XC-72 R, Cabot Co., USA)	Solid Oxide (YSZ-GDC anode, button cell, He environment)	0.65	42	800	[12]
	Ball milled CB (Vulcan XC-72 R, Cabot Co, USA)	Solid Oxide (YSZ-GDC anode, button cell, CO ₂ environment)	0.65	52	800	[12]
	ShaoXing RenFei Carbon blacks Co.	Solid oxide (tube, ScSZ electrolyte film, no introduction of anodic gas – self contained)	-	75	800	[52]
	CB (N-220, Komimpex, Poland)	Solid oxide (YSZ electrolyte with various anode configurations, Ni-YSZ anode results given here)	-	50	800	[104]
	CB (Vulcan XC-72, Cabot Co, USA)	Solid oxide (tubular, YSZ electrolyte, LSCF anode)	1.1	25 (at 0.6 V, not PPD)	820	[54]
	CB (Printex® 90, Evonik GmbH)	Solid oxide (Button cell, ScCeSZ electrolyte, GDC thin film anode)	~0.8	-	800	[108]
	CB (Vulcan XC-72, Cabot Co, USA)	Solid oxide (tubular, YSZ electrolyte)	~0.99	30.2	800	[109]
	CB (Vulcan XC-72, Cabot Co, USA)	Solid oxide (button cells, YSZ electrolyte, Titanate-based anodes)	~1.0	25	800	[58]
	CB (Vulcan XC-72-R, Cabot Co, USA)	Solid Oxide (GDC electrolyte, YSZ-GDC anode, button cell)	1.0	50	800	[55]
	CB (ENSACO 350G, Timcal, Switzerland)	Solid oxide (Ni-YSZ anode supported button cell, YSZ electrolyte)	~0.86	~30	800	[80]
	CB (Vulcan XC72, Cabot Co, USA)	Solid oxide (LSCF anode tubular cell, YSZ electrolyte)	~1.0	~30	800	[110]
	CB (Vulcan XC-72-R, Cabot Co, USA)	Solid Oxide (Anode support, Molten Carbonate hybrid – Li ₂ CO ₃ /K ₂ CO ₃)	0.93	~145	700	[107]

Fuel Class	Fuel Name / Origin	Electrolyte / Cell Arrangement	OCV (V)	PPD (mW cm ⁻²)	Temp. (°C)	Ref.
Graphite	TIM-CAL M-292	Molten Carbonate	1.05	17	800	[84]
	Desulco Graphite Particles	Molten Carbonate (eutectic Li-K)	-	46	800	[22]
	Flake Graphite	Molten Carbonate (Li-K-Al as 1.05:1.2:1 by mass)	0.65	63	650	[105]
	Graphite powder	Molten Carbonate (eutectic Li-K)	-	-	750	[96]
	Micronized Graphite (IEA International Trading Qingdao Co. Ltd, China)	Solid Oxide (YSZ-GDC anode, button cell, He environment)	0.70	6.5	700	[12]
	Graphite Powder	Solid Oxide (YSZ) – Ar gas feed to fuel side	1.05	5.9	800	[111]
	Graphite (Fisher)	Solid Oxide (Anode support, Molten Carbonate hybrid – Li ₂ CO ₃ /K ₂ CO ₃)	0.87	~67	700	[107]
Bituminous coal	Newlands (QLD) coking-grade raw coal	Molten Carbonate (Li-Na-K ternary electrolyte mixed with coal)	1.25	63	800	[72]
	Blackwater (QLD) coking-grade raw coal	Molten Carbonate (Li-Na-K ternary electrolyte mixed with coal)	1.32	85	800	[72]
	Germancreek (QLD) coking-grade raw coal	Molten Carbonate (Li-Na-K ternary electrolyte mixed with coal)	1.31	111	800	[72,85]
	Germancreek coking-grade coal (QLD) pyrolysed (750°C)	Molten Carbonate (Li-Na-K ternary electrolyte mixed with coal)	1.19	40	800	[85]
	Germancreek coking-grade coal (QLD) pyrolysed (950°C)	Molten Carbonate (Li-Na-K ternary electrolyte mixed with coal)	1.15	29	800	[85]

Fuel Class	Fuel Name / Origin	Electrolyte / Cell Arrangement	OCV (V)	PPD (mW cm ⁻²)	Temp. (°C)	Ref.
Bituminous coal	Germancreek coking-grade coal (QLD) Heat Treated in Air (500°C)	Molten Carbonate (Li-Na-K ternary electrolyte mixed with coal)	1.24	58	800	[85]
	Germancreek coking-grade coal (QLD) acid washed (HF)	Molten Carbonate (Li-Na-K ternary electrolyte mixed with coal)	1.30	117	800	[85]
	Germancreek coking-grade coal (QLD) acid washed (HCl)	Molten Carbonate (Li-Na-K ternary electrolyte mixed with coal)	1.29	115	800	[85]
	Germancreek coking-grade coal (QLD) acid washed (HNO ₃)	Molten Carbonate (Li-Na-K ternary electrolyte mixed with coal)	1.33	129	800	[85]
	Berau (Korea Electric Power Research Institute), ash-free, solvent extraction	Molten carbonate (Li-K eutectic mixture), coin-type, Ni-Al Anode	~0.9-1.2	-	850	[112]
	Shenhua coal, China	Molten carbonate (Li-K eutectic electrolyte mixed with coal)	~1	49	700	[113]
	Drayton coal (NSW) ash-free, solvent extraction	Solid oxide (tubular, YSZ electrolyte, Ni-YSZ anode)	1.1	2.8	800	[100]
	Wieczorek raw coal (Silesia, Poland)	Solid oxide (button cell, YSZ electrolyte, Ni-YSZ anode)	-	90	850	[102]
	Wieczorek ash-free coal (Silesia, Poland) acid washed (HNO ₃)	Solid oxide (button cell, YSZ electrolyte, Ni-YSZ anode)	~1.0	120	850	[102]
	Shanxi coal char (Shanxi Lasen Energy Corporation, China)	Solid oxide (Ni-YSZ anode supported Button cell, YSZ electrolyte) – CO ₂ /N ₂ anode purge	0.64	25	800	[103]
	Spanish basin coal	Solid Oxide (Anode support, Molten Carbonate hybrid – Li ₂ CO ₃ /K ₂ CO ₃)	1.00	~115	700	[107]

Fuel Class	Fuel Name / Origin	Electrolyte / Cell Arrangement	OCV (V)	PPD (mW cm ⁻²)	Temp. (°C)	Ref.
Lower-ranked coals	Sub-bituminous raw coal (Indonesian coal)	Molten Carbonate (Li-K eutectic mixture)	0.95	52	700	[81]
	Sub-bituminous coal char (Indonesian coal)	Molten Carbonate (Li-K eutectic mixture)	0.72	37	700	[81]
	Adaro coal (Indonesia)	Molten carbonate (Li-K eutectic electrolyte mixed with coal)	~0.98	~66	700	[113]
	Openblue coal	Molten carbonate (Li-K eutectic electrolyte mixed with coal)	~1.02	~51	700	[113]
	Chinese lignite, raw coal	Solid oxide (Button cell, YSZ electrolyte, Ni-YSZ anode)	~0.91	175	800	[82]
	Sub-bituminous raw coal	Solid oxide (Ni-YSZ anode supported button cell, YSZ electrolyte)	~1.0	~80	800	[80]
	Sub-bituminous ash-free coal	Solid oxide (Ni-YSZ anode supported button cell, YSZ electrolyte)	~0.8	~30	800	[80]
	Lignite (Unspecified)	Solid oxide (tubular cell, YSZ electrolyte)	~0.92	6	800	[114]
	- Indicates data not reported					

References

1. Williams KR. An Introduction to Fuel Cells, Edited by Keith R. Williams. Contributors: M.R. Andrew (And Others): *Elsevier Publishing Company*; **1966**.
2. Jacques WW. Method of converting potential energy of carbon into electrical energy. *U. S. patent office*. patent no. 555,511, **1896**.
3. Baur E. *Z Elektrochem Angew Phys Chem*. **1910**;16:300.
4. Appleby AJ. From sir William Grove to today: fuel cells and the future. *J Power Sources*. **1990**;29:3-11.
5. Baur E, D. TW, Trumpler G. Über die Natrium-Sauerstoffkette. *Zeitschrift für Elektrochemie und angewandte physikalische Chemie*. **1921**;27:194-9.
6. Munnings C, Giddey S, Badwal S. Direct carbon fuel cells: an ultra-low emission technology for power generation. *CORNERSTONE MAG*. **2014**;2.
7. Kurzweil P. HISTORY | Fuel Cells. In: Jürgen G, editor. Encyclopedia of Electrochemical Power Sources. Amsterdam: *Elsevier*; **2009**. p. 579-95.
8. Cherepy N, Krueger R, Cooper JF. Power Sources for the New Millenium. In: Jain M, Ryan MA, Surampudi S, Marsh RA, Nagarajan G, editors. *The Electrochemical Society Proceedings Series*. Pennington, NJ, **2000**. p. 64.
9. Gür TM, Huggins RA. Direct Electrochemical Conversion of Carbon to Electrical Energy in a High Temperature Fuel Cell. *J Electrochem Soc*. **1992**;139:L95-L7.
10. Lipilin AS, Balachov II, Dubois LH, Sanjurjo A, McKubre MC, Crouch-Baker S, et al. Liquid anode electrochemical cell. *Google Patents*; **2012**.
11. Nabae Y, Pointon KD, Irvine JTS. Electrochemical oxidation of solid carbon in hybrid DCFC with solid oxide and molten carbonate binary electrolyte. *Energy & Environmental Science*. **2008**;1:148-55.
12. Kulkarni A, Giddey S, Badwal SPS. Electrochemical performance of ceria-gadolinia electrolyte based direct carbon fuel cells. *Solid State Ionics*. **2011**;194:46-52.
13. Muthuvel M, Jin X, Botte GG. FUEL CELLS - EXPLORATORY FUEL CELLS | Direct Carbon Fuel Cells. In: Jürgen G, editor. Encyclopedia of Electrochemical Power Sources. Amsterdam: *Elsevier*; **2009**. p. 158-71.
14. Goret J, Tremillon B. Propriétés chimiques et électrochimiques en solution dans les hydroxydes alcalins fondus--IV. Comportement électrochimique de quelques métaux utilisés comme électrodes indicatrices. *Electrochim Acta*. **1967**;12:1065-83.

15. Strahinja Z, Patton EM, Parhami P. Direct Electrochemical Power Generation from Carbon in Fuel Cells with Molten Hydroxide Electrolyte. *Chem Eng Commun.* **2005**;192:1655-70.
16. Desclaux P, Nürnberger S, Rzepka M, Stimming U. Investigation of direct carbon conversion at the surface of a YSZ electrolyte in a SOFC. *Int J Hydrogen Energy.* **2011**;36:10278-81.
17. Zecevic S, Patton EM, Parhami P. Carbon-air fuel cell without a reforming process. *Carbon.* **2004**;42:1983-93.
18. Cao D, Sun Y, Wang G. Direct carbon fuel cell: Fundamentals and recent developments. *J Power Sources.* **2007**;167:250-7.
19. Dicks AL. The role of carbon in fuel cells. *J Power Sources.* **2006**;156:128-41.
20. Selman JR. Molten-salt fuel cells-Technical and economic challenges. *J Power Sources.* **2006**;160:852-7.
21. Predtechensky MR, Varlamov YD, Ul'yankin SN, Dubov YD. Direct conversion of solid hydrocarbons in a molten carbonate fuel cell. *Thermophys Aeromech.* **2009**;16:601-10.
22. Cherepy NJ, Krueger R, Fiet KJ, Jankowski AF, Cooper JF. Direct Conversion of Carbon Fuels in a Molten Carbonate Fuel Cell. *J Electrochem Soc.* **2005**;152:A80-A7.
23. Li H, Liu Q, Li Y. A carbon in molten carbonate anode model for a direct carbon fuel cell. *Electrochim Acta.* **2010**;55:1958-65.
24. Li X, Zhu Z, Chen J, De Marco R, Dicks A, Bradley J, et al. Surface modification of carbon fuels for direct carbon fuel cells. *J Power Sources.* **2009**;186:1-9.
25. Liebhafsky HA, Cairns EJ. Fuel cells and fuel batteries. Guide to their research and development. New York: *John Wiley & Sons*; **1968**.
26. Predtechenskii MR, Varlamov YD, Bobrenok OF, Ul'yankin SN. Fuel elements with direct electrochemical oxidation of coal. *Doklady Physics.* **2009**;54:281-4.
27. Vutetakis DG, Skidmore DR, Byker HJ. Electrochemical Oxidation of Molten Carbonate-Coal Slurries. *J Electrochem Soc.* **1987**;134:3027-35.
28. Coughlin RW, Farooque M. Hydrogen production from coal, water and electrons. *Nature.* **1979**;279:301-3.
29. Coughlin RW, Farooque M. Consideration of electrodes and electrolytes for electrochemical gasification of coal by anodic oxidation. *J Appl Electrochem.* **1980**;10:729-40.
30. Coughlin RW, Farooque M. Electrochemical Gasification of Coal-Simultaneous Production of Hydrogen and Carbon Dioxide by a Single Reaction Involving

- Coal, Water, and Electrons. *Industrial & Engineering Chemistry Process Design and Development*. **1980**;19:211-9.
31. Farooque M, Coughlin RW. Electrochemical gasification of coal (investigation of operating conditions and variables). *Fuel*. **1979**;58:705-12.
 32. Cooper JF, Cherepy NJ, Krueger RL. Tilted fuel cell apparatus. *U. S. patent office*. patent no. 6,878,479, **2002**.
 33. Li S, Lee AC, Mitchell RE, Gür TM. Direct carbon conversion in a helium fluidized bed fuel cell. *Solid State Ionics*. **2008**;179:1549-52.
 34. Lee AC, Li S, Mitchell RE, Gür TM. Conversion of Solid Carbonaceous Fuels in a Fluidized Bed Fuel Cell. *Electrochem Solid-State Lett*. **2008**;11:B20-B3.
 35. Pointon K, Lakeman B, Irvine J, Bradley J, Jain S. The development of a carbon-air semi fuel cell. *J Power Sources*. **2006**;162:750-6.
 36. Giddey S, Badwal SPS, Kulkarni A, Munnings C. A comprehensive review of direct carbon fuel cell technology. *Progr Energy Combust Sci*. **2012**;38:360-99.
 37. Suzuki T, Hasan Z, Funahashi Y, Yamaguchi T, Fujishiro Y, Awano M. Impact of Anode Microstructure on Solid Oxide Fuel Cells. *Science*. **2009**;325:852-5.
 38. Hong Huang MN, Peichen Su, Rainer Fasching, Yuji Saito, and Fritz B. Prinz. High-Performance Ultrathin Solid Oxide Fuel Cells for Low-Temperature Operation. *J Electrochem Soc*. **2007**;154:B20-B4.
 39. Zongping Shao, Sossina M. Haile. A high-performance cathode for the next generation of solid-oxide fuel cells. *Nature*. **2004**;431:170-3.
 40. Steele BCH, Heinzl A. Materials for fuel-cell technologies. *Nature*. **2001**;414:345-52.
 41. Yang L, Wang S, Blinn K, Liu M, Liu Z, Cheng Z, et al. Enhanced Sulfur and Coking Tolerance of a Mixed Ion Conductor for SOFCs: BaZr_{0.1}Ce_{0.7}Y_{0.2-x}Yb_xO_{3-δ}. *Science*. **2009**;326:126-9.
 42. Basu RN. Materials for Solid Oxide Fuel Cells. In: Basu S, editor. Recent Trends in Fuel Cell Science and Technology: Jointly published by *Anamaya Publishers, New Delhi (India)* and *Springer, New York*, Chapter-12, **2007**. p. 286-331.
 43. Lars Rose MM, Kent Kammer, Olivera Kesler, Peter Halvor Larsen. Processing of Ce_{1-x}Gd_xO_{2-δ} (GDC) Thin Films from Precursors for Application in Solid Oxide Fuel Cells. *Advanced Materials Research*. **2006**;15-17:293-8.
 44. Li C, Shi Y, Cai N. Performance improvement of direct carbon fuel cell by introducing catalytic gasification process. *J Power Sources*. **2010**;195:4660-6.
 45. Li C, Shi Y, Cai N. Effect of contact type between anode and carbonaceous fuels on direct carbon fuel cell reaction characteristics. *J Power Sources*. **2011**;196:4588-93.

46. Ihara M, Matsuda K, Sato H, Yokoyama C. Solid state fuel storage and utilization through reversible carbon deposition on an SOFC anode. *Solid State Ionics*. **2004**;175:51-4.
47. Hanna J, Lee WY, Shi Y, Ghoniem AF. Fundamentals of electro- and thermochemistry in the anode of solid-oxide fuel cells with hydrocarbon and syngas fuels. *Progr Energy Combust Sci*. **2014**;40:74-111.
48. Liu J, Barnett SA. Operation of anode-supported solid oxide fuel cells on methane and natural gas. *Solid State Ionics*. **2003**;158:11-6.
49. Lin Y, Zhan Z, Liu J, Barnett SA. Direct operation of solid oxide fuel cells with methane fuel. *Solid State Ionics*. **2005**;176:1827-35.
50. Tao S, Irvine JTS. A redox-stable efficient anode for solid-oxide fuel cells. *Nat Mater*. **2003**;2:320-3.
51. Tang Y, Liu J. Effect of anode and Boudouard reaction catalysts on the performance of direct carbon solid oxide fuel cells. *Int J Hydrogen Energy*. **2010**;35:11188-93.
52. Liu R, Zhao C, Li J, Zeng F, Wang S, Wen T, et al. A novel direct carbon fuel cell by approach of tubular solid oxide fuel cells. *J Power Sources*. **2010**;195:480-2.
53. Badwal SPS, Giddey S. The Holy Grail of Carbon Combustion - The Direct Carbon Fuel Cell Technology. *Mater Forum*. **2010**;34:181-5.
54. Kulkarni A, Ciacchi FT, Giddey S, Munnings C, Badwal SPS, Kimpton JA, et al. Mixed ionic electronic conducting perovskite anode for direct carbon fuel cells. *Int J Hydrogen Energy*. **2012**;37:19092-102.
55. Munnings C, Kulkarni A, Giddey S, Badwal SPS. Biomass to power conversion in a direct carbon fuel cell. *Int J Hydrogen Energy*. **2014**;39:12377-85.
56. Kulkarni A, Giddey S, Badwal SPS. Yttria-doped ceria anode for carbon-fueled solid oxide fuel cell. *J Solid State Electrochem*. **2015**;19:325-35.
57. Nakagawa N, Ishida M. Performance of an internal direct-oxidation carbon fuel cell and its evaluation by graphic exergy analysis. *Ind Eng Chem Res*. **1988**;27:1181-5.
58. Kulkarni A, Giddey S, Badwal SPS, Paul G. Electrochemical performance of direct carbon fuel cells with titanate anodes. *Electrochim Acta*. **2014**;121:34-43.
59. Lee AC, Mitchell RE, Gür TM. Thermodynamic analysis of gasification-driven direct carbon fuel cells. *J Power Sources*. **2009**;194:774-85.
60. Jain SL, Barry Lakeman J, Pointon KD, Marshall R, Irvine JTS. Electrochemical performance of a hybrid direct carbon fuel cell powered by pyrolysed MDF. *Energy & Environmental Science*. **2009**;2:687-93.

61. Jiang C, Irvine JTS. Catalysis and oxidation of carbon in a hybrid direct carbon fuel cell. *J Power Sources*. **2011**;196:7318-22.
62. Nabae Y, Pointon KD, Irvine JTS. Ni/C Slurries Based on Molten Carbonates as a Fuel for Hybrid Direct Carbon Fuel Cells. *J Electrochem Soc*. **2009**;156:B716 - B20.
63. Cao D, Wang G, Wang C, Wang J, Lu T. Enhancement of electrooxidation activity of activated carbon for direct carbon fuel cell. *Int J Hydrogen Energy*. **2010**;35:1778-82.
64. Tao T, Bateman L, Bentley J, Slaney M. Liquid Tin Anode Solid Oxide Fuel Cell for Direct Carbonaceous Fuel Conversion. *ECS Trans*. **2007**;5:463-72.
65. Tao T, McPhee W, Koslowske M, Bentley J, Slaney M, Bateman L. Liquid Tin Anode SOFC For Direct Fuel Conversion - Impact of Coal and JP-8 Impurities. *ECS Trans*. **2009**;25:1115-24.
66. Jayakumar A, Lee S, Hornes A, Vohs J, Gorte R. A comparison of molten Sn and Bi for solid oxide fuel cell anodes. *J Electrochem Soc*. **2010**;157:B365-B9.
67. Jayakumar A, Vohs J, Gorte R. Molten-metal electrodes for solid oxide fuel cells. *Ind Eng Chem Res*. **2010**;49:10237-41.
68. Wang H, Cao T, Shi Y, Cai N, Yuan W. Liquid antimony anode direct carbon fuel cell fueled with mass-produced de-ash coal. *Energy*. **2014**;75:555-9.
69. Javadekar A, Jayakumar A, Pujara R, Vohs JM, Gorte RJ. Molten silver as a direct carbon fuel cell anode. *J Power Sources*. **2012**;214:239-43.
70. Jacob KT. A New Type of SOFC for Conversion of High Temperature Heat to Electricity without Carnot Limitation. *ECS Trans*. **2011**;35:573-82.
71. Toleuova A, Yufit V, Simons S, Maskell WC, Brett DJL. A review of liquid metal anode solid oxide fuel cells. *J Electrochem Sci Eng*. **2013**;3:91-135.
72. Li X, Zhu Z, De Marco R, Bradley J, Dicks A. Evaluation of raw coals as fuels for direct carbon fuel cells. *J Power Sources*. **2010**;195:4051-8.
73. Furimsky E, Sears P, Suzuki T. Iron-catalyzed gasification of char in carbon dioxide. *Energy Fuels*. **1988**;2:634-9.
74. Huppmann G. FUEL CELLS - MOLTEN CARBONATE FUEL CELLS | Systems. In: Jürgen G, editor. Encyclopedia of Electrochemical Power Sources. Amsterdam: Elsevier; **2009**. p. 479-96.
75. Yokokawa H, Yamaji K, Brito ME, Kishimoto H, Horita T. General considerations on degradation of Solid Oxide Fuel Cell anodes and cathodes due to impurities in gases. *J Power Sources*. **2011**;196:7070-5.

76. Cheng Z, Liu M. Characterization of sulfur poisoning of Ni-YSZ anodes for solid oxide fuel cells using in situ Raman microspectroscopy. *Solid State Ionics*. **2007**;178:925-35.
77. Liu Y, Chen DY. Protective coatings for Cr₂O₃-forming interconnects of solid oxide fuel cells. *Int J Hydrogen Energy*. **2009**;34:9220-6.
78. Brown L, Cashion J, Ledger R. Coal ash composition of Australian low rank coals. *Hyperfine Interact*. **1992**;71:1411-4.
79. Bhattacharya S, Beaupeurt I, Topping B. Gasification tests in a pressurised fluidised bed gasifier-process development unit using air/oxygen and steam as reactants. *Cooperative research centre for clean power from lignite*; **2006**.
80. Ju H, Eom J, Lee JK, Choi H, Lim T-H, Song R-H, et al. Durable power performance of a direct ash-free coal fuel cell. *Electrochim Acta*.
81. Rhie Y, Eom S, Ahn S, Choi G, Kim D. Effect of thermal decomposition products of coal on anodic reactions in direct carbon fuel cells. *J Mech Sci Technol*. **2014**;28:3807-12.
82. Xu K, Chen C, Liu H, Tian Y, Li X, Yao H. Effect of coal based pyrolysis gases on the performance of solid oxide direct carbon fuel cells. *Int J Hydrogen Energy*. **2014**;39:17845-51.
83. Hayashi J-i, Miura K. Chapter 4 - Pyrolysis of Victorian Brown Coal. In: Chun-Zhu L, editor. *Advances in the Science of Victorian Brown Coal*. Amsterdam: *Elsevier Science*; **2004**. p. 134-222.
84. Li X, Zhu ZH, Marco RD, Dicks A, Bradley J, Liu S, et al. Factors That Determine the Performance of Carbon Fuels in the Direct Carbon Fuel Cell. *Ind Eng Chem Res*. **2008**;47:9670-7.
85. Li X, Zhu Z, De Marco R, Bradley J, Dicks A. Modification of Coal as a Fuel for the Direct Carbon Fuel Cell†. *The Journal of Physical Chemistry A*. **2010**;114:3855-62.
86. Quyn DM, Wu H, Li C-Z. Volatilisation and catalytic effects of alkali and alkaline earth metallic species during the pyrolysis and gasification of Victorian brown coal. Part I. Volatilisation of Na and Cl from a set of NaCl-loaded samples. *Fuel*. **2002**;81:143-9.
87. Li CZ, Sathe C, Kershaw JR, Pang Y. Fates and roles of alkali and alkaline earth metals during the pyrolysis of a Victorian brown coal. *Fuel*. **2000**;79:427-38.
88. Manzoori AR, Agarwal PK. The fate of organically bound inorganic elements and sodium chloride during fluidized bed combustion of high sodium, high sulphur low rank coals. *Fuel*. **1992**;71:513-22.

89. Wang J, Nakazato T, Sakanishi K, Yamada O, Tao H, Saito I. Single-step microwave digestion with HNO₃ alone for determination of trace elements in coal by ICP spectrometry. *Talanta*. **2006**;68:1584-90.
90. Wang J, Nakazato T, Sakanishi K, Yamada O, Tao H, Saito I. Microwave digestion with HNO₃/H₂O₂ mixture at high temperatures for determination of trace elements in coal by ICP-OES and ICP-MS. *Anal Chim Acta*. **2004**;514:115-24.
91. Chang C-Y, Wang C-F, Mui DT, Chiang H-L. Application of methods (sequential extraction procedures and high-pressure digestion method) to fly ash particles to determine the element constituents: A case study for BCR 176. *J Hazard Mater*. **2009**;163:578-87.
92. Li C, Shi Y, Cai N. Mechanism for carbon direct electrochemical reactions in a solid oxide electrolyte direct carbon fuel cell. *J Power Sources*. **2011**;196:754-63.
93. Zhao XY, Yao Q, Li SQ, Cai NS. Studies on the carbon reactions in the anode of deposited carbon fuel cells. *J Power Sources*. **2008**;185:104-11.
94. Şenel IG, Gürüz AG, Yücel H, Kandas AW, Sarofim AF. Characterization of Pore Structure of Turkish Coals. *Energy Fuels*. **2001**;15:331-8.
95. Cazorla-Amoros D, Alcaniz-Monge J, de la Casa-Lillo MA, Linares-Solano A. CO₂ As an Adsorptive To Characterize Carbon Molecular Sieves and Activated Carbons. *Langmuir*. **1998**;14:4589-96.
96. Radović LaR, Walker PL, Jenkins RG. Importance of catalyst dispersion in the gasification of lignite chars. *J Catal*. **1983**;82:382-94.
97. Linares-Solano A, Hippo EJ, Walker Jr PL. Catalytic activity of calcium for lignite char gasification in various atmospheres. *Fuel*. **1986**;65:776-9.
98. Ahn SY, Eom SY, Rhie YH, Sung YM, Moon CE, Choi GM, et al. Utilization of wood biomass char in a direct carbon fuel cell (DCFC) system. *Appl Energy*. **2013**;105:207-16.
99. Liu J, Ye K, Cheng K, Wang G, Yin J, Cao D. The catalytic effect of CeO₂ for electrochemical oxidation of graphite in molten carbonate. *Electrochim Acta*. **2014**;135:270-5.
100. Kim J-P, Choi H-K, Chang Y-J, Jeon C-H. Feasibility of using ash-free coal in a solid-oxide-electrolyte direct carbon fuel cell. *Int J Hydrogen Energy*. **2012**;37:11401-8.
101. Magdalena Dudek, Robert Socha. Direct Electrochemical Conversion of the Chemical Energy of Raw Waste Wood to Electrical Energy in Tubular Direct Carbon Solid Oxide Fuel Cells. *Int J Electrochem Sci*. **2014**;9:7414-30.

102. Dudek M. On the utilization of coal samples in direct carbon solid oxide fuel cell technology. *Solid State Ionics*. **2015**;271:121-7.
103. Jiao Y, Tian W, Chen H, Shi H, Yang B, Li C, et al. In situ catalyzed Boudouard reaction of coal char for solid oxide-based carbon fuel cells with improved performance. *Appl Energy*. **2015**;141:200-8.
104. Dudek M, Tomczyk P, Juda KL, Tomov R, Glowacki BA, Batty S, et al. Comparison of the Performances of DCFC Fuelled with the Product of Methane RF Plasma Reforming and Carbon Black. *Int J Electrochem Sci*. **2012**;7:6704-21.
105. Chen M, Wang C, Niu X, Zhao S, Tang J, Zhu B. Carbon anode in direct carbon fuel cell. *Int J Hydrogen Energy*. **2010**;35:2732-6.
106. Siengchum T, Guzman F, Chuang SSC. Analysis of gas products from direct utilization of carbon in a solid oxide fuel cell. *J Power Sources*. **2012**;213:375-81.
107. Chien AC, Arenillas A, Jiang C, Irvine JTS. Performance of Direct Carbon Fuel Cells Operated on Coal and Effect of Operation Mode. *J Electrochem Soc*. **2014**;161:F588-F93.
108. Werhahn MG, Schneider O, Stimming U. Thin Film Gadolinia Doped Ceria (GDC) Anode for Direct Conversion of Carbon Black Particles in a Single Planar SOFC. *ECS Trans*. **2013**;50:73-87.
109. Giddey S, Kulkarni A, Munnings C, Badwal SPS. Performance evaluation of a tubular direct carbon fuel cell operating in a packed bed of carbon. *Energy*. **2014**;68:538-47.
110. Giddey S, Kulkarni A, Munnings C, Badwal SPS. Composite anodes for improved performance of a direct carbon fuel cell. *J Power Sources*. **2015**;284:122-9.
111. Kim J-P, Lim H, Jeon C-H, Chang Y-J, Koh K-N, Choi S-M, et al. Performance evaluation of tubular fuel cells fuelled by pulverized graphite. *J Power Sources*. **2010**;195:7568-73.
112. Lee C-G, Kim W-K. Oxidation of ash-free coal in a direct carbon fuel cell - In Press, Corrected Proof. *Int J Hydrogen Energy*. **2015**.
113. Eom S, Ahn S, Rhie Y, Kang K, Sung Y, Moon C, et al. Influence of devolatilized gases composition from raw coal fuel in the lab scale DCFC (direct carbon fuel cell) system. *Energy*. **2014**;74:734-40.
114. Kaklidis N, Garagounis I, Kyriakou V, Besikiotis V, Arenillas A, Menéndez JA, et al. Direct utilization of lignite coal in a Co–CeO₂/YSZ/Ag solid oxide fuel cell. *Int J Hydrogen Energy*. **2015**.

Declaration for thesis chapter 3

Declaration by candidate

In the case of Chapter 3, the nature and extent of my contribution to the work was the following:

Nature of contribution	Extent of contribution (%)
Writing	100

The following co-authors contributed to the work. If co-authors are students at Monash University, the extent of their contribution in percentage terms must be stated:

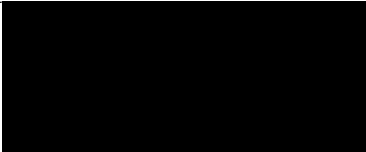
Name	Nature of contribution	Extent of contribution (%)
Dr Sukhvinder Badwal	Advisory role	-
Dr Sarbjit Giddey	Advisory role	-
Assoc Prof Bradley Ladewig	Advisory role	-
Prof Sankar Bhattacharya	Advisory role	-
Dr Aniruddha Kulkarni	Advisory role	-

The undersigned hereby certify that the above declaration correctly reflects the nature and extent of the candidate's and co-authors' contributions to this work.

Candidate's
Signature

	Date 27/02/2015
---	------------------------

Main
Supervisor's
Signature

	Date 27/02/2015
---	------------------------

3

Common experimental

**Reproduced in part from: Rady AC, Giddey S, Kulkarni A, Badwal SPS, Bhattacharya S, Ladewig BP. Direct carbon fuel cell operation on brown coal. Appl Energy. 2014;120:56-64.*

&

Rady AC, Giddey S, Kulkarni A, Badwal SPS, Bhattacharya S. Degradation Mechanism in a Direct Carbon Fuel Cell Operated with Demineralised Brown Coal. Electrochim Acta. 2014;143:278-90.

Chapter objective

The purpose of this chapter is to collate methodology and experimental procedures common to multiple works within this thesis. Experimental work unique to a particular study will be given in the respective chapter. In addition, an overview of the experimental design and DCFC assembly is presented.

Common experimental

3.1 Fuel preparation

Two coal chars were used throughout this study, derived from coal from the Morwell mine in the Latrobe Valley, Victoria, Australia. The chars were produced from demineralised Morwell coal and the parent (air-dried raw) Morwell coal, herein referred to as 'DM', and 'RM', respectively. Cabot XC72 carbon black, a synthetically produced carbon powder, was also used as a fuel in certain studies and is herein referred to as 'CB'.

To produce demineralised coal samples, 100 g of 150-212 μm air-dried raw Morwell coal was mixed with 2 L of 4 mol L⁻¹ HNO₃ at a stirring rate of 80 rpm for 24 hours at room temperature. The sample was then rinsed with no less than 20 L distilled water *via* Buchner funnel filtration until a constant pH of > 4.0 was achieved. A neutral filtrate was not attainable due to inherent carboxyl and phenol groups lending the coal acidic properties.

Approximately 20 g of the demineralised Morwell coal was then heated in a quartz fluidised bed reactor under an atmosphere of 99.999% N₂ flowing at 500 mL min⁻¹, at a heating rate of 10 °C min⁻¹ to 600 °C, where it was held for 1 hr before cooling to room temperature to generate DM. The same process was employed for the parent coal, air-dried raw Morwell coal, to produce RM. The temperature of 600 °C was chosen as a temperature for removal of the majority of organic volatiles, but it was not sufficiently above the volatilisation temperature range of many inorganic salts for fluidised bed pyrolysis [1,2]. Thus most of the inorganic salts would still remain in the char sample. CB was not exposed to any heat treatment prior to use in the fuel cell or fuel analysis.

A summary of the fuel preparation and treatment is given in the flow sheet provided in Figure 3.1.

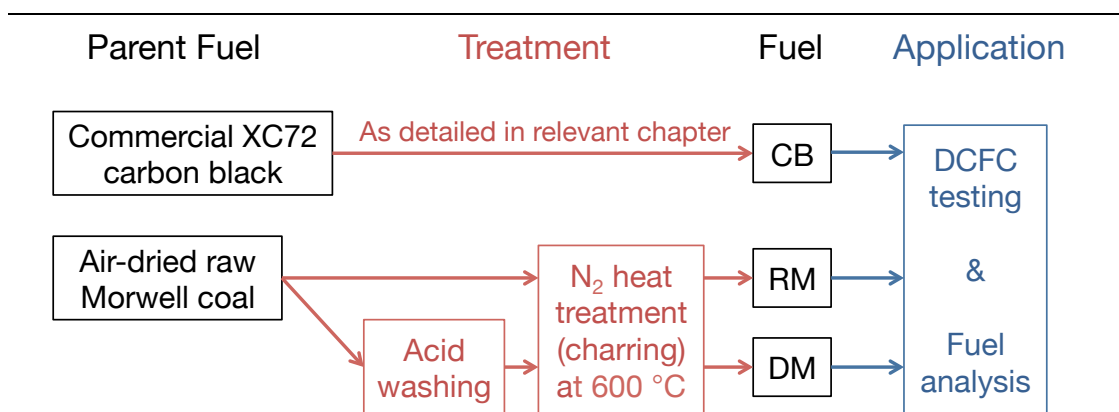


Figure 3.1: Flow diagram of fuel preparation and utilization

3.2 Fuel characterisation and analysis

3.2.1 Thermogravimetric analysis

Thermogravimetric analysis (TGA), with a Netzsch STA449 F3 *Jupiter*, was used to assess weight loss due to release of volatiles in the charred samples, as well as to investigate the reactivity of samples in the presence of CO_2 at fuel cell operating temperatures. The TGA reactivity studies of carbon fuels will be outlined in their respective chapters.

Determination of volatile and moisture contents for carbon fuels was achieved by heating the samples in the TGA furnace to 950 °C at heating rate of 10 °C min⁻¹ in N_2 and held for 7 minutes at this temperature. Heating rate and dwell time was as per Australian Standards [3], with 950 °C chosen to ensure the release of all volatiles.

For all TGA work, carbon samples were sieved to 90-106 μm size, and sample sizes of ~5 mg were used. Gases used were N_2 (99.999%) and ultra high purity CO_2 . A flow rate of 20 mL min⁻¹ was used for the protective N_2 atmosphere with an additional 80 mL min⁻¹ flow rate for the purge gas of either N_2 , CO_2 , or a mixture of the two gases. Prior to each TGA run, the furnace chamber pressure was reduced to near-vacuum before being flushed with N_2 .

3.2.2 Inorganic content analysis

Inorganic content and make-up of coal samples were determined *via* inductively coupled plasma optical emission spectrometry (ICP-OES) analysis following microwave digestion of the char samples using a 6:1 HNO_3 and HF mix. These results were adjusted for metal oxide weights to give the ash content.

3.2.3 Carbon conductivity measurements

Electrical conductivity measurements of carbon powders were made in an in-house designed and constructed 4-probe test fixture at temperatures in the 600 to 850 °C temperature range. The fixture was comprised of a high density alumina tube (ID: 6.0 mm; OD: 9.7 mm; and length: 25 mm) with two voltage probe wires (0.5 mm dia. Pt-Rh) passing through the middle of the tube cross section and separated from each other by 10mm. The carbon powder was ground and held packed in the ceramic tube (as per loading in the fuel cell) to about 20 mm depth in the alumina tube under spring loading. The current was passed through the cylindrical carbon bed in the tube by employing Pt foils (diameter same as the tube ID) placed on both sides of the carbon bed. The sample was taken up to 850 °C and held under N₂ where current was passed and voltage recorded, followed by measurements at 800, 700 and 600 °C.

3.3 DCFC button cell fabrication and materials

The materials listed here are used in the fabrication of electrolyte-supported DCFC button cells in this thesis:

- Gadolinia-doped Ceria (GDC, Fuel Cell Materials Inc., OH, USA), with composition $\text{Gd}_{0.20}\text{Ce}_{0.80}\text{O}_{2-x}$
- Yttria-stabilised Zirconia (YSZ, Tosoh Corporation, Japan) as 8 mol% Y₂O₃
- Lanthanum Strontium Cobalt Ferrite (LSCF, Fuel Cell Materials Inc., OH, USA) with composition $\text{La}_{0.6}\text{Sr}_{0.4}\text{Co}_{0.2}\text{Fe}_{0.8}\text{O}_{3-5}$
- Nickel Gadolinia-doped Ceria (Ni-GDC, Fuel Cell Materials Inc., OH, USA) of composition 60 wt% NiO, 40 wt% $\text{Gd}_{0.1}\text{Ce}_{0.9}\text{O}_{1.95}$

The following chemicals were also used in electrode preparation and fuel cell assembly:

- Terpinol-based ink vehicle (Fuel Cell Materials Inc., OH, USA)
- Pt ink (Metalor Technologies, Birmingham, UK)
- Ceramabond-552 (Aremco Inc., NY, USA)

The following gases were used during DCFC testing:

- N₂ (99.999 %, BOC)
- N₂/CO₂ mixture (Cellamix, 40 vol% CO₂ in N₂, BOC)

The following gases were used during TGA analyses:

- N₂ (99.999 %, high purity, Air Liquide)
- CO₂ (99.999%, ultra high purity, Air Liquide)

3.3.1 Electrolyte disc fabrication

The electrolyte powder (1.5 g) was uniaxially pressed in a die at 1 MPa for 60 seconds followed by isostatic pressing at 207 MPa (30 kpsi) for 30 seconds. The green electrolyte discs were then sintered at 1500 °C for 2 hrs in air with a heating rate of 300 °C hr⁻¹. The sintered discs had a diameter of 18 mm (GDC), and 17 mm (YSZ), and were ~1.0 mm thick. Archimedes density measurements confirmed the discs to be >98 % (GDC), and >99 % (YSZ), of the theoretical density. The thickness of the YSZ sintered discs was reduced to ~0.5 mm by grinding both sides on a grinding wheel, whereas for GDC the thickness was kept at ~1.0 mm.

3.3.2 Electrode application

LSCF was used as both the air and fuel electrode, unless otherwise stated. Its stability in direct carbon fuel cell environments and operating conditions has been demonstrated previously [4]. The electrode ink was made by ball milling LSCF powder and terpinol-based ink vehicle in a 1:1 weight fraction with 10 mm diameter zirconia balls as a grinding media for 4 hrs. An 8mm diameter air electrode (cathode) was screen printed on one side, in the middle of the electrolyte discs and the entire opposite face of the electrolyte disc was brush painted with the fuel electrode (anode) ink. Electrodes were sintered at 800 °C for 2 hrs in air with a heating and cooling rate of 180 °C hr⁻¹. Electrode thickness was 10 – 12 µm determined by SEM image of cell cross section. A thin coating of platinum ink was applied to the air electrode prior to assembly to assist with current collection. A few points of platinum ink was applied to the anode current collector in studies where the anode platinum mesh was attached to the anode face to assist with adhesion to the anode.

3.4 DCFC cell design and assembly

3.4.1 Test station

The DCFC test station used for all the work reported in the thesis is pictured in Figure 3.2.

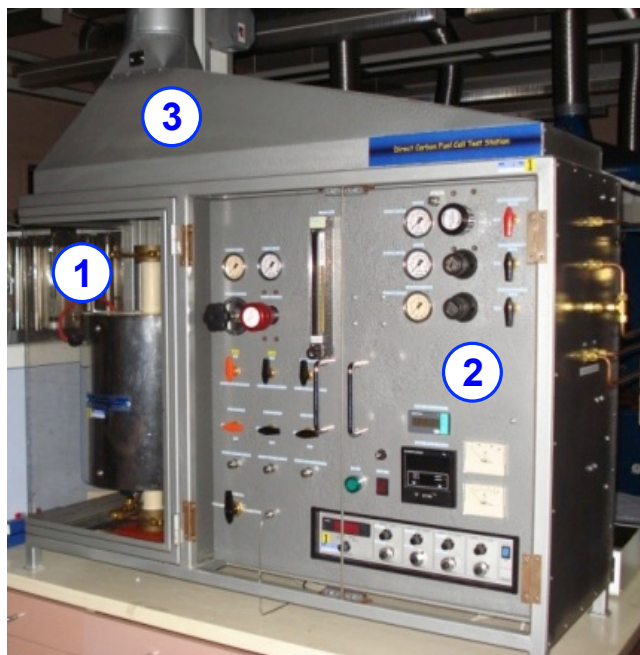


Figure 3.2: DCFC test station in CSIRO Laboratories, picture courtesy of CSIRO Energy, with: 1. DCFC and furnace; 2. Gas pressure regulators and flow valves; 3. Exhaust

The panel in Figure 3.2(2) allowed for control of cell temperature and gas flow to anode and cathode chambers of the DCFC housed in the furnace in Figure 3.2(1). All gas streams exiting DCFC system were vented to an exhaust system in Figure 3.2(3).

3.4.2 Test fixtures

The DCFC test fixture was housed within a vertical tubular furnace. The working part of the fuel cell underwent several iterations and updating of cell design and test fixture in order to produce the required outcomes from the experimental program. These arrangements are given schematically in Figure 3.3, with images of cell components provided in Figure 3.4. Carbon fuels were ground in ethanol in a mortar and pestle to make a paste. A nickel crucible of dimensions 18.7 mm ID x 19.0 mm OD x 2.7 mm in depth was used to contain carbon fuel powder to be tested. For each separate study and carbon fuel tested a separate button cell was used.

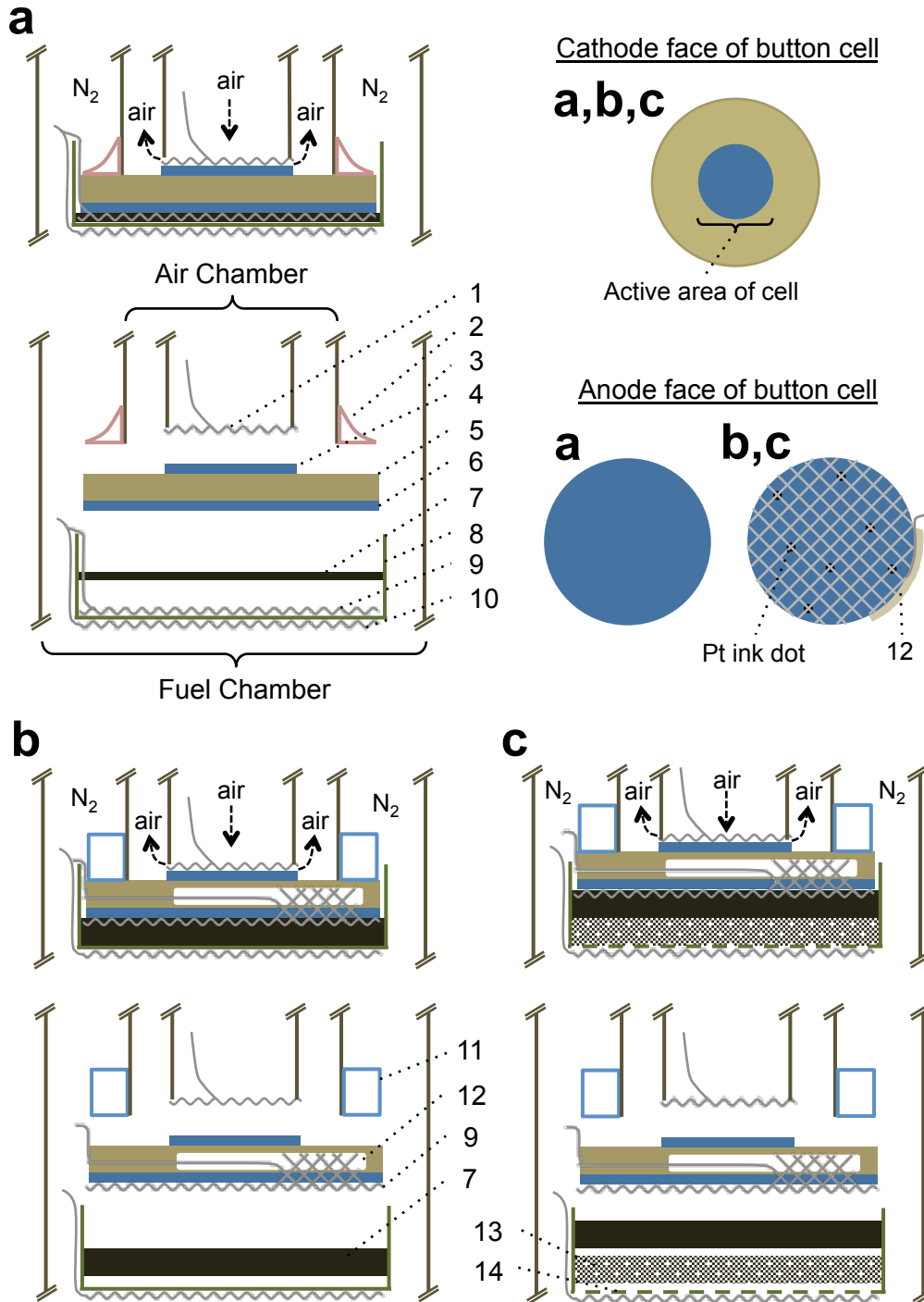


Figure 3.3: Schematic of cell arrangements with assembled cell (top) and exploded view (bottom) as well as electrode configurations for (a) Carbon embedded in Pt mesh on base of Ni crucible, (b) Anode current collector attached to anode face, (c) Perforated Ni crucible and porous stainless steel disc included: 1. Cathode current collector (Pt mesh); 2. Ceramabond; 3. Alumina tube; 4. Air electrode (cathode); 5. Electrolyte; 6. Fuel electrode (anode); 7. Carbon fuel; 8. Ni cup; 9. Anode current collector (Pt mesh); 10. Pt mesh; 11. Glass seal; 12. Ceramabond; 13. Porous stainless steel disc; 14. Perforated Ni crucible

For arrangement 'a' in Figure 3.3, a Platinum mesh of thickness 0.5 mm and diameter 17 mm was spot welded to the inside bottom of this crucible. A Pt wire was spot welded to the mesh for current collection. The carbon paste was then uniformly

applied to the Platinum mesh with the help of a brush, in a way that the carbon paste is in level with the Platinum mesh top as per Figure 3.4(b). Typical carbon loading was ~50 mg. Ceramabond-552 (Aremco Inc., NY, USA) was used as a sealant and was cured *in-situ* during the heating of the cell to isolate the air and fuel chambers.

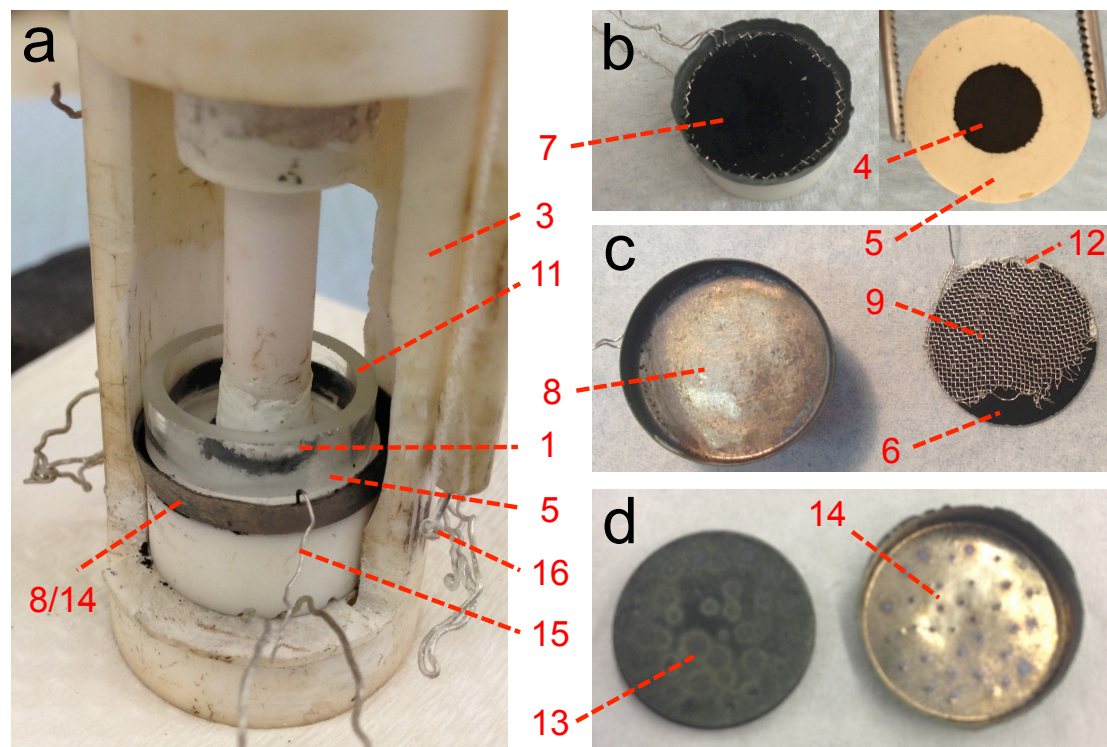


Figure 3.4: Fuel cell setup and components for (a) assembled cell with outer cathode tube raised, (b) Ni cup and anode current collector arrangement filled with carbon as in Figure 3.3(a) with adjacent image of air electrode side of button cell, (c) Ni cup and anode current collector attached to anode face as in arrangements in Figure 3.3(b) and 3.3(c), (d) porous stainless steel disc and perforated Ni cup as in arrangement in Figure 3.3(c): Numbering as in Figure 3.3 for 1. Cathode current collector (Pt mesh); 3. Alumina tube; 4. Air electrode (cathode); 5. Electrolyte; 6. Fuel electrode (anode); 7. Carbon fuel; 8. Ni cup; 9. Anode current collector (Pt mesh); 11. Glass seal; 12. Ceramabond; 13. Porous stainless steel disc; 14. Perforated Ni crucible, 15: anode current collector lead wires, 16: Pt-Rh thermocouple

In order to improve the contact between the carbon, anode, and anode current collector to allow for detailed studies into solid carbon consumption from the carbon/anode interface, changes in the anode Pt current collector were made from the original design in arrangement 'a'.

For arrangements 'b' and 'c' in Figure 3.3, the anode Pt mesh was secured to the anode face at a few points using Pt ink (Metalor Technologies, Birmingham, UK) and around the circumference of the cell using ceramabond-552 (Aremco Inc., NY, USA) as per Figure 3.4(c). A finer Pt mesh was used with a wire diameter of 0.12 mm and openings of 0.30 x 0.30 mm, except where otherwise stated. Carbon paste was applied *via* brush to the face of the anode within the Pt mesh openings, as well as

into the Ni crucible to create a carbon bed. For each carbon fuel a different button cell was used and carbon loading was typically ~150 mg. In arrangement 'b' of Figure 3.3, this carbon bed was layered on the Ni crucible base.

For arrangement 'c', the bed of carbon was applied onto a porous stainless steel disc within the nickel crucible, which was perforated to allow for effective gas diffusion. An image of the perforated Ni cup and stainless steel disc are provided in Figure 3.4(d). These design changes were made to allow for greater sensitivity of the cell to changes in the anode chamber gaseous environment for studies into the catalytic promotion of gas phase reactions within the DCFC.

In all arrangements, the button cell was then placed anode-side facing down on top of the carbon bed and held in place by a spring-loaded alumina tube in the in-house designed button cell fixture. Pt ink was also applied to the cathode to ensure good contact between the air electrode and current collector Pt mesh.

3.5 Fuel cell operation and electrochemical techniques

With exception to Ceramabond sealant used for GDC electrolyte-supported button cells, the anode and cathode chambers were isolated *via* a Borosilicate glass seal. The seal was formed by heating the cell at 300 °C hr⁻¹ to ~910 °C under 99.999 % N₂ and holding for 5-10 min before cooling slowly to the operating temperature (850 °C) over the course of ~90 min, after which air could be introduced into the cathode chamber. During heating, cooling, and normal operation, the anode purge gas flow rate of 40 ml min⁻¹ was used irrespective of the gas composition. The predominant anode purge gas in use was 99.999 % N₂, though on occasion this gas was switched to a N₂/CO₂ mixture (Cellamix, 40 Vol% CO₂ in N₂).

A two-electrode cell configuration was used and all electrochemical measurements were conducted at the given operating temperature. Measurements included constant current chronopotentiometric (CP) loading, electrochemical impedance spectroscopy (EIS) measurements under load and open circuit condition, as well as potentiodynamic and galvanodynamic voltage-current (V-j) scans. CP and V-j scans were taken using a Versastat 4 Potentiostat-Galvanostat (Princeton Applied Research, USA). V-j scans employed a sweeping scan rate of 5 - 25 mV s⁻¹. EIS measurements were taken over a frequency range of 1 MHz – 50 mHz at various constant current loads and under open circuit conditions using an IM6 Impedance

Analyser (Zahner, Germany). Prior to each EIS data acquisition under a constant current load, the cell was held at the appropriate loading for two minutes to allow for the voltage to stabilise before commencing the EIS scan. Both Versastat 4 Potentiostat-Galvanostat and IM6 Impedance Analyser were calibrated using standard RC circuits and were confirmed to reproduce data within $\pm 2\%$.

Corrections to measured cell voltages were made for ohmic losses due to lead and Pt connecting wires. This was determined by shorting the air and fuel side connections at the cell operating temperatures. Select EIS data was modelled using ZViewTM software (Scribner Associates, Inc., USA) using an adaptation of the Randles Circuit.

3.6 Laboratory XRD measurements and analysis

Laboratory X-ray diffraction (XRD) of powders and button cell samples was conducted using a Bruker D2 Phaser diffractometer with X'flash detector and Cu K α radiation. All phase analysis from XRD data was carried out using the software package Eva (Bruker Inc., USA) by using the ICDD crystal database (PDF4+).

Structural analysis of solid button cell anodes were obtained across an angular range of 10 – 90 ° in 2 Θ , with 0.02° step size and an acquisition time of 1 s. Lattice parameters were determined by Le Bail refinement of diffraction patterns using Topas v4.2 (Bruker Inc., USA).

XRD analysis of carbon powder samples was obtained using a silicon low-background sample holder. Diffractogram measurements were acquired over an angular range of 10-70° in 2 θ , with a step size of 0.02° and an acquisition time of 10 sec.

3.7 Scanning electron microscopy and SEM-EDX

Coal samples for SEM imaging were Au sputter coated prior to imaging with scanning electron microscope (Phenom S/N 0383 desktop SEM).

SEM images of the anode were obtained by using a Phillips XL30 Field Emission SEM, with Energy Dispersive X-ray (EDX) spectra recorded using Aztec (Oxford Instruments Pty. Ltd.).

3.8 Experimental design overview

An overview of the experimental design, cell configurations and operating conditions, and techniques used is given in Table 3.1, for chapters involving DCFC experiments.

Table 3.1: Experimental matrix for chapters involving DCFC experiments

	Ch. 4	Ch. 5	Ch. 6	Ch. 7
Temp. (°C)	700, 800	850	850	850
Fuel / (carbon loading)	RM, DM, CB (50 mg)	DM (150 mg)	DM & RM (150 mg)	CB doped with Ca, Fe, Mg (150 mg)
Seal type	Ceramabond	Glass	Glass	Glass
Anode / electrolyte / cathode	LSCF / GDC / LSCF	LSCF / YSZ / LSCF	Ni-GDC, YSZ / YSZ / LSCF	LSCF / YSZ / LSCF
Cell arrangement (Figure 3.3)	A	B	B	C
Scan rate (mV s ⁻¹)	25	5	5	5
Fuel chamber atmosphere	N ₂	N ₂ & N ₂ /CO ₂	N ₂ & N ₂ /CO ₂	N ₂ & N ₂ /CO ₂
Electrochemical techniques	V-j sweep, EIS	V-j sweep, CP, EIS	V-j sweep, CP, EIS	V-j sweep, EIS
Analytical techniques	TGA, ICP-OES, SEM, carbon conductivity	SEM, SEM- EDX, XRD, carbon conductivity		TGA, XRD
Objective / Investigation	Coal characterisation and testing in DCFC	Testing and extended operation of demineralised coal in DCFC	Testing of coal in DCFC with new cermet anode	Catalytic effect of impurities doped in synthetic carbon

References

1. Quyn DM, Wu H, Li C-Z. Volatilisation and catalytic effects of alkali and alkaline earth metallic species during the pyrolysis and gasification of Victorian brown coal. Part I. Volatilisation of Na and Cl from a set of NaCl-loaded samples. *Fuel*. **2002**;81:143-9.
2. Quyn DM, Wu H, Bhattacharya SP, Li C-Z. Volatilisation and catalytic effects of alkali and alkaline earth metallic species during the pyrolysis and gasification of Victorian brown coal. Part II. Effects of chemical form and valence. *Fuel*. **2002**;81:151-8.
3. Standards Australia. AS 2434.2. Methods for the analysis and testing of lower rank coal and its chars. Part 2: Lower rank coal - Determination of volatile matter, **2002**.
4. Kulkarni A, Ciacchi FT, Giddey S, Munnings C, Badwal SPS, Kimpton JA, et al. Mixed ionic electronic conducting perovskite anode for direct carbon fuel cells. *Int J Hydrogen Energy*. **2012**;37:19092-102.

Declaration for thesis chapter 4

Declaration by candidate

In the case of Chapter 4, the nature and extent of my contribution to the work was the following:

Nature of contribution	Extent of contribution (%)
Experimental work and analysis, writing	100

The following co-authors contributed to the work. If co-authors are students at Monash University, the extent of their contribution in percentage terms must be stated:

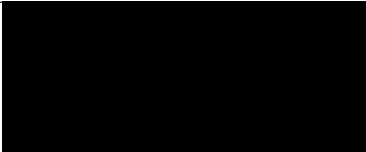
Name	Nature of contribution	Extent of contribution (%)
Dr Sukhvinder Badwal	Advisory role	-
Dr Sarbjit Giddey	Advisory role	-
Assoc Prof Bradley Ladewig	Advisory role	-
Prof Sankar Bhattacharya	Advisory role	-
Dr Aniruddha Kulkarni	Advisory role	-

The undersigned hereby certify that the above declaration correctly reflects the nature and extent of the candidate's and co-authors' contributions to this work.

Candidate's
Signature

	Date 27/02/2015
---	------------------------

Main
Supervisor's
Signature

	Date 27/02/2015
---	------------------------

4

Direct carbon fuel cell operation on brown coal

**Reproduced in part from: Rady AC, Giddey S, Kulkarni A, Badwal SPS, Bhattacharya S, Ladewig BP, Appl Energy, 2014;120:56-64.*

Chapter objective

In Chapter 2, a review of fuels used within direct carbon fuel cell (DCFC) systems highlighted the scope to trial a greater variety of fuel types within DCFCs. The use of low-grade fuels such as lignites or 'brown coals' within solid oxide DCFC systems has been very limited until rather recently, despite their natural abundance and established markets. Coals such as those from the Latrobe Valley, Victoria, are promising candidates for use in DCFCs owing to their low ash content, high thermochemical reactivity, and presence of inherent catalytic species for gasification.

In this chapter, the first results from the utilisation of Victorian brown coal in a DCFC is critically evaluated, and its performance compared with that of synthetic carbon fuel. The carbon fuels used in this chapter will be used throughout the bodies of work included in this thesis. As such, analysis of the carbon composition is also provided here.

Direct carbon fuel cell operation on brown coal

Abstract

The performance of a Victorian brown coal with minimal pre-treatment was assessed in a solid oxide electrolyte based direct carbon fuel cell (DCFC) at 700 and 800 °C. In order to evaluate the effect of inherent inorganic species in the coal on the electrochemical performance of DCFCs (voltage - power density - current density), characteristics of button cells fuelled with raw and acid washed (demineralised) coal were compared along with commercially available XC-72 carbon black. Peak power densities of 65 and 67 mW cm⁻² were observed for demineralised coal char and carbon black respectively at 800 °C, whereas the raw coal char achieved a superior power density of 89 mW cm⁻². The availability of reactive species at the anode, namely CO, is believed to be the primary differentiator of cell performance, and is related to variations in the physical and chemical makeup of carbon fuels. The reactivity of these fuels in the presence of CO₂ to generate CO (and power) *via* Boudouard gasification was assessed in the 700 – 800 °C temperature range *via* thermogravimetric analysis.

4.1 Introduction

The solid oxide DCFC is a high temperature fuel cell and operates between the temperatures of 600 and 900 °C. The high temperatures are necessary to ensure sufficiently high ionic conductivity of the ceramic electrolyte, but introduce other considerations, such as different reaction mechanisms and associated efficiency penalties. For example, at temperatures above 700 °C the reverse Boudouard reaction, hereinafter referred to as Boudouard gasification, becomes favourable when carbon dioxide is present (Eq. 1.7) [1,2].



Under these conditions, the fuel may be gasified and the fuel cell will operate off both the electrochemical oxidation of solid carbon (Eq. 1.4 and 1.5) and carbon monoxide available from Eq. (1.5) and (1.7) as per Eq. (1.6).





The mode of operation of the fuel cell is an important consideration for not only the performance, but also the efficiency of the system. Where Eq. (1.7) is allowed to compete with Eq. (1.5) for the consumption of carbon, some fuel may be lost as CO in the product gas, reducing the fuel utilisation and the overall efficiency of the system. For this reason Boudouard gasification is sometimes referred to as 'Boudouard corrosion' of the fuel, in the context of DCFC operation. Understanding what factors promote Eq. (1.7), and its effect on the system, and how the fuel properties contribute, are necessary studies in advancing this technology.

Due to the difficult nature of tracking intermediate reaction products in the gaseous reaction environment, limited work has been done to elucidate the reaction mechanisms for the carbon oxidation in the solid oxide electrolyte based DCFC. A more detailed description of carbon conversion mechanisms in the solid oxide DCFC for carbon deposited by CH₄ is given by Li and co-workers [3]. Their work outlined possible intermediate reaction steps such as the adsorption of oxygen onto the carbon surface, and the importance of carbon reactive sites. However, the interfacial conditions are expected to be quite different in a solid fuel fed DCFC compared to the methane fed solid oxide fuel cell.

Recent advances in DCFC technology as well as a greater understanding of the need for high efficiency and clean sources of power generation, has renewed interest in this area. However, the overwhelming fuel of choice for DCFC research to date is commercially produced carbon black [4,5-11] as it is considered a clean source of carbon with consistent properties. While carbon black has a lot to offer this field of research, there is a need to explore the possibility of using real world fuels that could be used as fuels for DCFC to produce power at a commercial scale, such as coals, and expand knowledge on fuel-based performance of these fuel cells [12].

Coal is widely used for electricity generation worldwide, at over 40% of the global share, and its global consumption is expected to increase well into the next century [13]. In Victoria, Australia, brown coal is also the dominant fuel source for electricity generation contributing almost 80% to the total power generation installed capacity [14]. With around 33 billion tonnes [15] of 'potentially economic' reserves

representing over 500 years of recoverable lignite at the current consumption rate, it is well positioned to retain this mantle for some time. However, it is widely accepted that the current methods of power generation have substantial negative environmental consequences. For example, the CO₂ emissions per MWh (more than 1.2 tCO₂ MWh⁻¹ [16]) of electricity produced in the Latrobe Valley, Victoria, are among the highest in the world. While the high moisture content of Victorian brown coal at 45-70% [17] is undesirable for thermal power generation, other properties such as its very low ash (<7 wt% db) and sulfur (<1 wt% db) contents make this coal an attractive fuel for use in fuel cells.

The present work examines the performance of two processed coals from the Morwell mine in the Latrobe Valley, Victoria, in a solid oxide electrolyte based DCFC using a mixed ionic electronic conductor (MIEC) anode, LSCF, which has been shown to be stable in DCFC operating environments [2,8]. Very few studies have involved the use of low rank coals within DCFCs to date and there is no reported data on the utilisation of Victorian (Australia) brown coal in this type of fuel cell. For comparison XC-72 carbon black fuel was also investigated.

4.2 Experimental

Three carbons were used in this study. These were Cabot XC72 carbon black, and chars produced from demineralised Morwell coal and the parent (air-dried raw) Morwell coal, herein referred to as 'CB', 'DM', and 'RM', respectively. The preparation of these fuels is discussed in Chapter 3. CB in its 'as-supplied' state was used for DCFC testing as well as in fuel characterisation and analysis.

4.2.1 Fuel characterisation and analysis

For investigations with thermogravimetric analysis (TGA), a temperature profile closely representing fuel cell operation was selected. The temperature was increased from room temperature to 200 °C at 600 °C hr⁻¹, with all subsequent heating at 300 °C hr⁻¹ to 600, 700 or 800 °C. A blank standard run with an empty crucible was subtracted from thermogravimetric profiles to account for buoyancy effects.

4.2.2 Fuel cell testing

A schematic of the cell arrangement in the test fixture has been given in Chapter 3 as Figure 3.3 (a). Typical carbon loading was 50 mg with a different cell used for each carbon fuel type. The fuel chamber was continuously purged under 99.999% N₂ for raw and demineralised Morwell chars, and 99.999% Helium for carbon black, at 40 mL min⁻¹ flow rate during heating and normal operation. The cell temperature was raised to 100 °C in ambient air environment to assist with seal formation. The inert gas purge was then started, and temperature raised to 600 °C, at a heating rate of 300 °C hr⁻¹. The cell was held at 600 °C for 1 hr before ramping to operating temperatures of 700 and then to 800 °C for both coal chars. For carbon black, the cell was only operated at 800 °C. The cell holding time at a temperature during testing was typically 1 hr with total cell operating time of about 2-3 hrs.

4.3 Results and discussion

4.3.1 Analysis of fuels

4.3.1.1 Proximate analysis and inorganic content of fuels

The moisture and volatile contents for all three fuels used in this study, as determined from heat treatment to 950 °C in the TGA furnace, are given in Table 4.1. The ash content in Table 4.1 was determined from adjusted chemical analysis data (ICP-OES), with fixed carbon as the balance. The volatile contents of RM, DM and CB were 38.4 wt%, 29.3 wt% and 2.8 wt% respectively. It is quite clear from Table 4.1 that previous charring at 600 °C had not removed all volatile matter. As the samples were all heated to 950 °C for this analysis, volatilisation of some inorganic species, in particular those of sodium [18,19] may have contributed to weight loss although this contribution is believed to be minor compared with the weight loss due to organic volatile matter.

Table 4.1: Proximate analysis of carbon fuels (wt%)

	Moisture	Volatile	Fixed Carbon	Ash
RM	2.4	38.4	56.6	2.6
DM	2.6	29.3	67.3	0.8
CB	0.6	2.8	96.6	-

A similar moisture content of 2.4 and 2.6 wt% for RM and DM respectively was observed. It appears that the hygroscopic coal chars reabsorbed some moisture from the atmosphere post-charring at 600 °C. Acid leaching of the coal appears to have been successful in reducing the inorganic content of the fuel substantially, resulting in an ash content of 0.8 wt% for DM, considerably lower than the 2.6 wt% for RM, despite DM having the higher fixed carbon content. The ash content of CB was deemed negligible. Not surprisingly, the commercially produced CB had the highest fixed carbon content at 96.6 wt% due to low moisture, volatile matter and inorganic content. RM had the lowest fixed carbon content of 56.6 wt%, due mostly to a high volatile content.

Table 4.2: Inorganic content of char samples as determined by ICP-OES (ppm as metals on dry basis)

	Si	Al	Fe	Ti	K	Mg	Na	Ca	S	Other
RM	324	135	2100	22.0	570	2900	1600	6100	2400	261
DM	200	6.10	273	19.0	585	173	1000	538	1700	201

The chemical analysis data of RM and DM (ICP-OES) are given in Table 4.2. Detailed analysis of both RM and DM chars indicated that the concentration of Ca, Mg and Fe was significantly high in RM but decreased considerably on acid leaching, by roughly an order of magnitude. Al content in DM was also substantially lower than in RM, suggesting its presence in RM is predominantly in the form of clays readily removed by acid leaching or rinsing. Though the specific mineral phases in the char samples were not determined, Si is well known to exist in forms resistant to mild acid treatment within coals and the majority of the residual Si in DM is likely in the form of stable quartz.

Na and K also showed a tolerance to acid treatment, despite their dominant presence in Victorian brown coal being in the form of salts and carboxylates which are easily removed *via* acid washing. The observed minor increase in K content in the DM sample may be a consequence of the sensitivity of the instrument. The residual Na in DM is in the form of sodium silicates, sulphate and nitrate. The nitrate results from the HNO₃ used during leaching and is difficult to remove completely despite intensive water washing following acid leaching. This also explains the relatively ineffective removal of S *via* acid leaching.

4.3.1.2 Assessment of volatile content of fuel

The TGA analysis, independent of that used in the proximate analysis described in section 4.3.1.1, and more representative of the DCFC operating temperature profile is presented in Figure 4.1. The weight loss was observed below the temperature of charring (600 °C) for both RM and DM samples. This weight loss is attributed primarily to incomplete charring of the coal. However, to a lesser extent, one can expect the release of additional volatiles upon reheating char as an unavoidable consequence of the nature of the coal. It is also important to note that these chars were produced by pyrolysis under N₂ atmosphere at 600 °C, and some weight loss for both coal samples above 600 °C can be attributed to the release of tars and other volatiles not removed below this temperature. This is observed in the temporary increase in rate of mass loss during heating from 600 to 700 °C for both DM and RM.

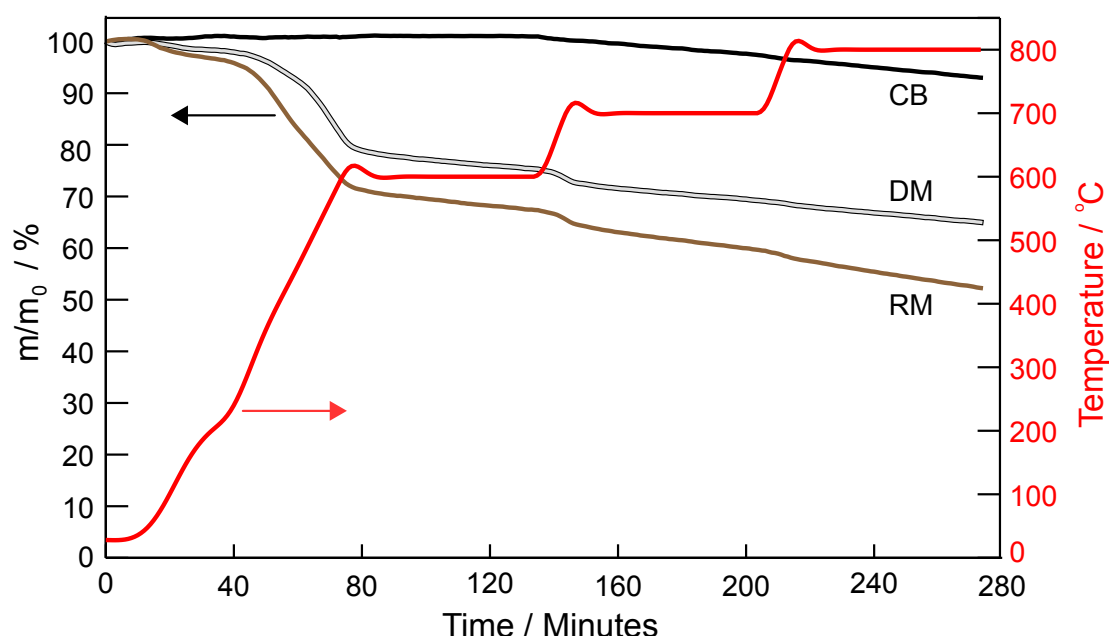


Figure 4.1: Temperature profile and thermogravimetric mass loss curves for carbon fuel samples during thermal treatment under N₂. *m*: sample mass at a given time ; *m*₀: initial sample mass

A linear weight loss during isothermal heat treatment at 700 and 800 °C in Figure 4.1 for all fuels was also observed. Four potential contributors to weight loss under these conditions cannot be ruled out. These include loss of volatile content and volatilisation of fixed carbon; CO and CO₂ desorption from decomposition of oxygen functional groups; oxidation of carbon due to trace level of oxygen in the inert gas; and from ingress of air into system *via* an unidentified leak. Of these possible scenarios, it is likely that the continued release of volatiles at these elevated temperatures is a major contributor to the observed linear weight loss profile. In addition, the decomposition of surface functional groups, predominantly into CO, was

observed for carbon black at temperatures above 700 °C in a temperature programmed desorption experiment by Li and co-workers [5]. This is consistent with the onset temperature for weight loss of CB in Figure 4.1 and presents as a possible source of CO for utilisation in a fuel cell reaction. Contributions to weight loss *via* oxidation from inherent impurities in inert N₂ (rated at < 2ppm O₂ and < 3ppm H₂O) and air ingress are considered minor.

4.3.1.3 Boudouard gasification reactivity of fuels via TGA

The relative reactivity of carbon fuels to Boudouard gasification were inferred by comparing mass loss versus time upon exposure to CO₂. This was achieved using thermogravimetric analysis (TGA) and a controlled atmosphere/temperature environment. The purge stream of 80 mL min⁻¹ was switched from N₂ to CO₂ after 1 hr at 700 °C or 800 °C as shown in Figures 4.2 and 4.3 respectively. These Figures compare rates of weight loss for RM and DM chars in the presence of N₂ and then CO₂ at 700 °C and 800 °C respectively. There was a significant loss of weight for both samples during heating in N₂. This is attributed to loss of weight due to organic volatile not removed completely during charring as mentioned above.

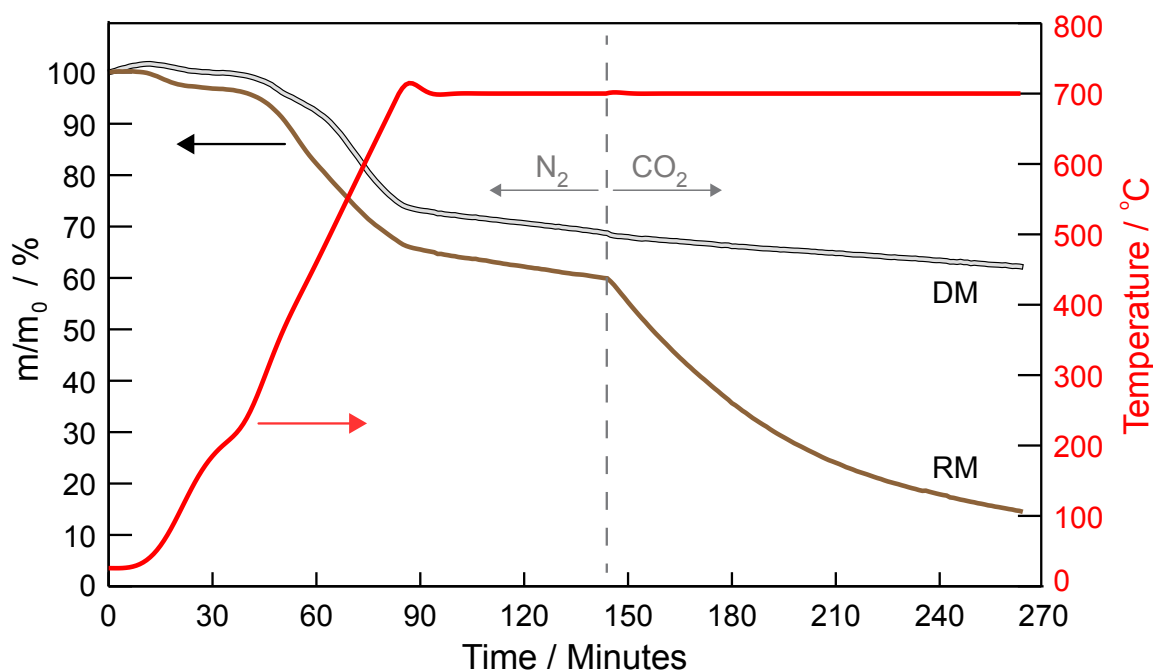


Figure 4.2: Temperature profile and thermogravimetric mass loss curves for DM and RM during CO₂ gasification at 700 °C. *m*: sample mass at a given time ; *m*₀: initial sample mass

For isothermal hold at 700 °C in N₂, although there was some loss of weight with time, the rate of weight loss was relatively small (Figure 4.2). However, on introduction of CO₂ into the furnace at ~145 minute mark, the rate of weight loss for

RM char became very notable (at 11.4 wt% over just first 15 min), leading to conversion of the reactive carbon with time as obvious in Figure 4.2. The residual mass is attributed to ash content and smaller amount of unreacted carbon. This is not the case for DM, where the rate of mass loss under CO₂ flow is indistinguishable (1.31 wt% over first 15 min) from the previous isothermal stage under N₂ (1.15 wt% over the 15 min immediately prior to the introduction of CO₂).

As mentioned earlier, in the presence of CO₂, the Boudouard gasification as per Eq. (1.7) becomes favourable only beyond 700 °C. Above this temperature, CO becomes increasingly dominant gaseous species in the Boudouard gasification equilibrium reaction [1]. Although the kinetics of this reaction is poor at 700 °C or below for pure carbon, RM contains several inherent inorganics that are well known as catalysts for Boudouard gasification [20]. These inorganic species in RM char are in the form of Alkali and Alkaline Earth Metallic species (AAEM) and transition metals (see Table 4.2). It is highly likely that at 700 °C, catalysis of this reaction, as observed in the RM case, is taking place for the reaction to proceed at an appreciable rate. Therefore, mass loss in RM in the presence of CO₂ is attributed to the consumption of solid carbon *via* Eq. (1.7). The TGA data also suggests minimal contribution to carbon consumption of the DM char *via* Boudouard gasification at this temperature [1]. This is attributed to the removal of catalytically active inorganic species and pore structure collapse during demineralisation of the coal [21].

In Figure 4.3, the rates of weight loss for all carbons (CB, RM and DM) in the presence of N₂ and CO₂ at 800 °C are presented. The samples were heated in the presence of high purity N₂ and held for 1 hr at 800 °C. The CO₂ was introduced after ~157 minutes from the start of the TGA run. The RM char was readily consumed within a few minutes *via* Boudouard gasification at this elevated temperature. DM showed a slightly enhanced rate of weight loss under CO₂ (1.8 wt% in first 15 min) over that observed under N₂ (0.8 wt% over 15 min immediately prior to the introduction of CO₂) suggesting that this fuel reacted with CO₂ at this temperature although slowly. The CB sample, however, did not show any noticeable enhanced weight loss that could be attributed to carbon consumption *via* Boudouard gasification. It may be concluded that the reactivity of fuels in the presence of CO₂ decreases in the order of RM >> DM > CB. As mentioned above, the presence of inorganic species, namely AAEM and transition metals, appear to play a central role in differentiating reactivity of these fuels *via* the catalysis of Eq. (1.7) at fuel cell operating temperatures of interest in this study. Furthermore, from the data in Table

4.2, it is apparent that of these species, Fe, Ca, and Mg are of most relevance due to their effective removal *via* acid leaching and their superior catalytic properties over other inorganic species present in the Victorian brown coal [21].

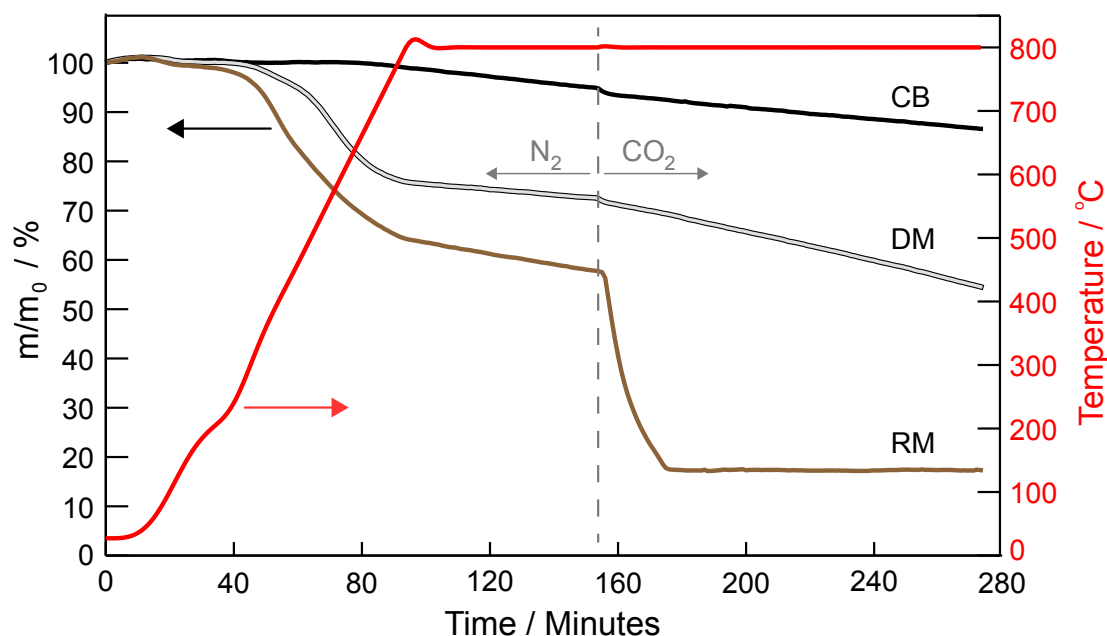


Figure 4.3: Temperature profile and thermogravimetric mass loss curves for carbon fuels during CO_2 gasification at $800\text{ }^\circ\text{C}$. m : sample mass at a given time ; m_0 : initial sample mass

Table 4.3: The weight loss as wt% of samples over a 15 min period just before (in N_2), and after CO_2 purge at a given temperature in TGA analysis.

	700 °C		800 °C	
	N_2	CO_2	N_2	CO_2
CB	-	-	1.02	1.04
DM	1.15	1.31	0.81	1.82
RM	1.45	11.42	1.61	31.48
Figure	4.2	4.2	4.3	4.3
Time (min)	126-141	144-159	135-150	157-172

Table 4.3 summarises the rates of weight loss observed from the TGA results, as a wt% of initial sample weight over 15 min periods, both immediately before (in N_2) and after (in CO_2) introduction of CO_2 into the sample chamber at both 700 and $800\text{ }^\circ\text{C}$.

4.3.2 Conductivity data for fuels

The conductivity measurements on compacted powders, with a four-probe direct current technique at high temperatures, showed that RM was the most resistive

followed by DM and CB. At 800 °C, the conductivity values for CB, DM and RM respectively were 1.0, 0.5 and 0.1 S cm⁻¹. Since the compacted powder density would be somewhat similar to that of carbon fuel used in direct carbon fuel cells, these results clearly show that mineral impurities in raw Morwell coal make substantial contribution to the resistivity of coal char and on acid leaching when most of these impurities are removed, the conductivity increases by a factor of about five.

4.3.3 Fuel Cell Results

Figure 4.4 shows the voltage – power density – current density (V-P-j) characteristics for DCFC button cells operating on DM and RM chars at 700 °C. The two fuels achieved similar peak power densities at 37 and 38 mW cm⁻² for DM and RM respectively. Despite a marginally higher open circuit voltage (OCV) for RM, V-j and P-j curves almost overlap at current densities up to the peak power for DM. At higher current densities, there is a clear indication for the onset of a mass transfer limited process for the DM sample, whereas the RM showed no such behaviour in the V-j and P-j curves.

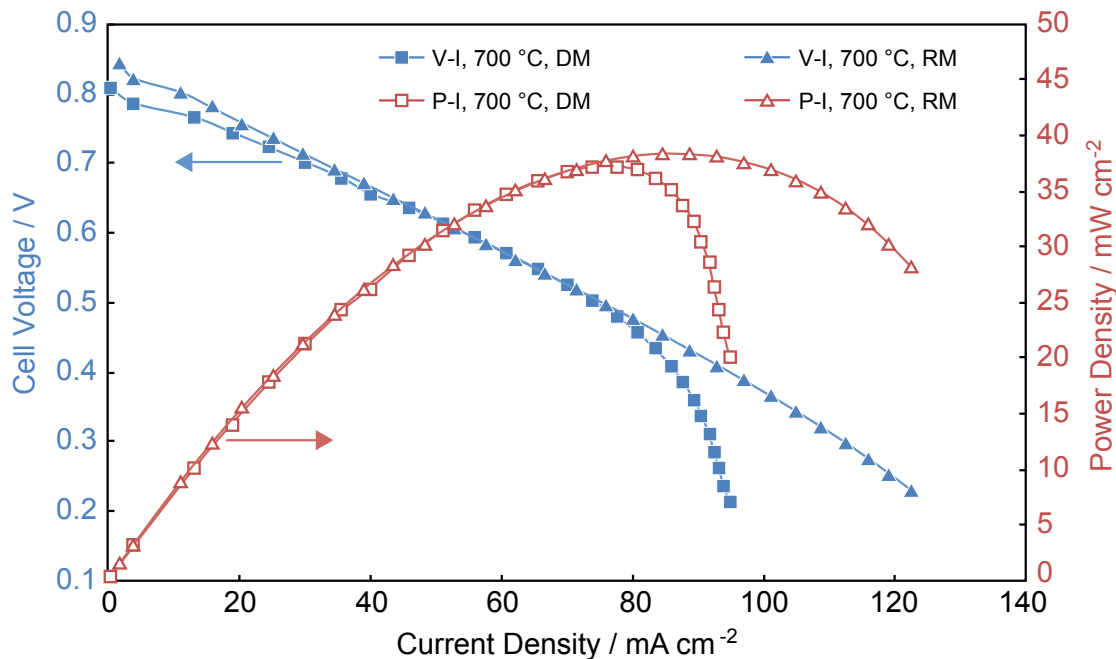


Figure 4.4: Voltage - Current density - Power density curves for DM and RM using two similar LSCF/GDC/LSCF button cells at 700 °C

The reason for varying nature of the curves beyond the peak power is believed to be primarily related to findings in the TGA study in Section 4.3.1.3. As shown in the TGA investigation, the Boudouard gasification kinetics for RM is far superior to that of DM at temperatures around 700 °C (Figure 4.2). With increasing current density, the

direct contacting carbon cannot sustain the fuel cell reaction ($C + 2O^{2-} = CO_2 + 4e^-$) and mass transfer limitation occurs, as is the case with DM. However, for RM, CO can be produced, *via* catalysis of Eq. (1.7) by the inherently present impurities in RM char. This CO generated *in-situ* then can react with migrating oxygen ions *via* Eq. (1.6) thus sustaining the fuel cell operation.

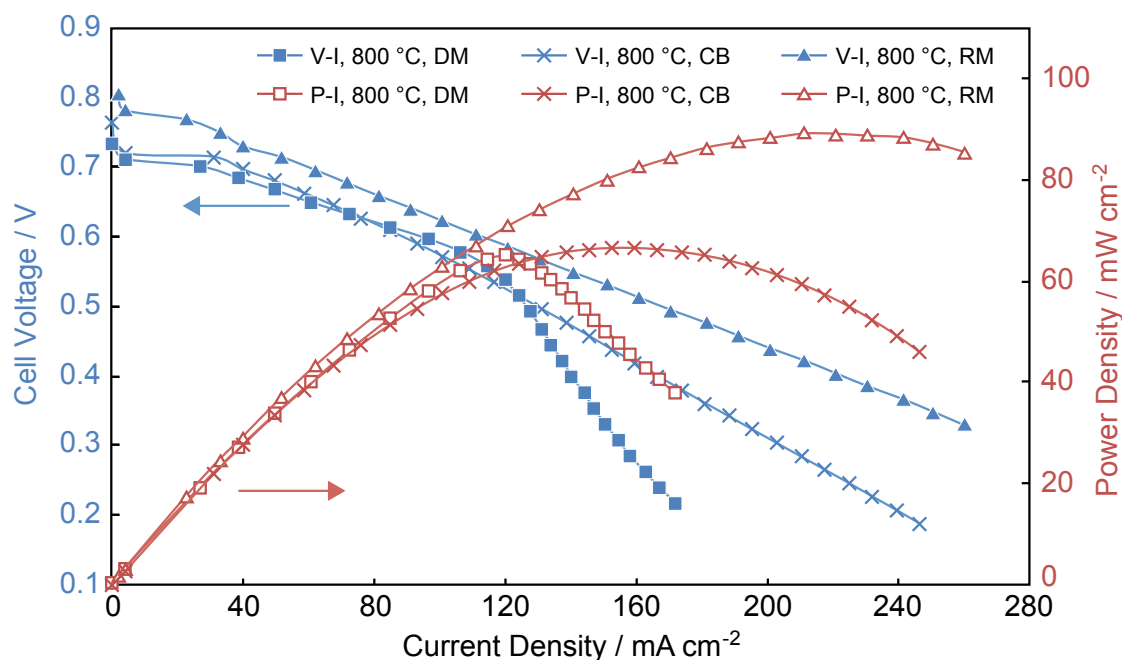


Figure 4.5: Voltage – Current density – Power density curves for DM, RM, and carbon black (XC-72) using three similar LSCF/GDC/LSCF button cells at 800 °C

Figure 4.5 shows the V-P-j characteristics for DCFC button cells operating on DM, RM, and CB at 800 °C. At this temperature, again a mass transfer limited behaviour was observed for DM at higher current densities and close to the peak power density obtained for this cell, although, it was not as severe as that observed at 700 °C (Figure 4.4). This may be attributed to enhanced reactivity of the fuel, including improved Boudouard gasification kinetics with increasing temperature. Any contributions from volatile species or reaction with oxygen in the N_2 purge gas stream are believed to be minor compared with Boudouard gasification as the values of weight loss from TGA analysis under N_2 are much more comparable than those under CO_2 (Table 4.3). The best fuel cell performance was achieved for RM char followed by CB and the DM char. The cell with CB could be operated at much higher current densities and has a broader peak power range than DM. RM also exhibited a broad peak power range and the highest peak power density of any fuel tested here. The peak power densities at 800 °C for DM, CB and RM were 65, 67 and 89 $mW\ cm^{-2}$ respectively.

As was observed at 700 °C, Boudouard gasification reactivity at 800 °C (Figure 4.3) is superior for RM over other fuels. This is a likely contributor to the higher current and power densities for RM, with a greater availability of CO at the anode. The extension of the V-j curve for DM beyond the peak power may also be due to DM showing improved gasification kinetics at 800 °C, with more evident weight loss under CO₂ atmosphere than at 700 °C, in the TGA studies.

It is not obvious why the cell with CB which had no mineral matter operated at much higher current densities and had a broader peak power range than DM. This may be attributed to a smaller particle size of CB and better flow characteristics as compared to DM. The Vulcan XC-72 (CB) is known to be a very high surface area material (250 m² g⁻¹) [22]. SEM images of three fuels in Figure 4.6 clearly show that CB consists of much finer particles as compared to large agglomerates in DM and RM. A smaller particle size would enable better fuel-to-anode contact and increase the effective reaction zone. A greater number of fuel-to-anode points of contact per unit area may ensure the availability of fuel at relatively higher currents as compared to DM leading to a broader peak power range. In addition, the higher electrical conductivity of carbon black compared with RM and DM would extend the active anode area beyond the anode / fuel interface [8].

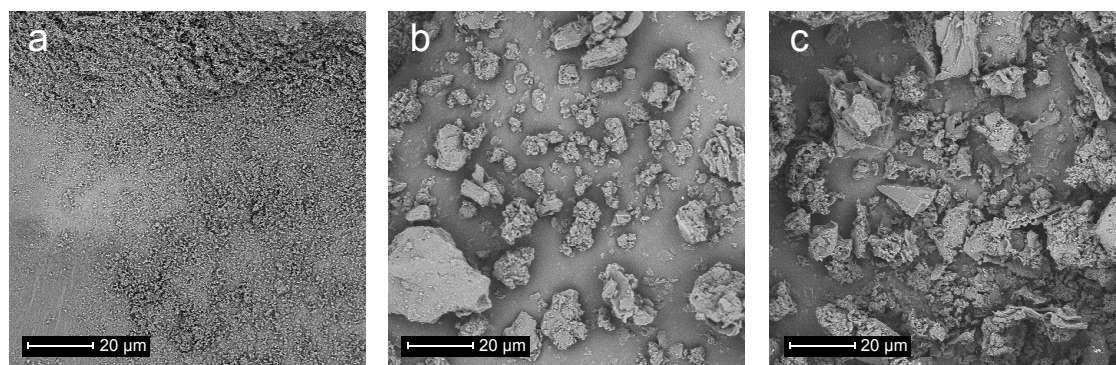


Figure 4.6: Scanning electron micrographs of (a) carbon black, (b) demineralised Morwell char, (c) raw Morwell char

The button cells in the present test setup were under spring loading with an anode continuously pressed on the carbon fuel particles. In such a system it is reasonable to assume that finer CB particles would be in better contact with the anode leading to broader V-P-j characteristics. In the absence of catalysts, as is the case with CB and to some degree with DM char, the availability of the fuel through better contact with the anode is essential to get performance from a DCFC. Furthermore a smaller particle size may possibly improve the flow characteristics of CB fuel as compared to

larger DM char particles which would provide continuous contacts of fresh fuel particles to the anode surface as the fuel is consumed with increasing current density.

It was observed that consistently cells with RM, both at 700 and 800°C, showed higher OCV than cells with DM and carbon black (CB). Some variations from cell to cell are not uncommon due to the lack of perfect sealing. However, more significantly it appears that some mineral impurities in Raw coal facilitate Boudouard gasification of carbon with residual oxygen in the inert gas thus producing a small amount of CO and shifting the equilibrium to somewhat lower oxygen partial pressure giving rise to higher OCV. There was also an observed drop in the OCV with increasing temperature for both RM and DM samples. This is consistent with literature and is due to an increasing electronic conductivity of GDC in reducing environments with increasing temperature [2,23,24] Nevertheless GDC has been shown to be a reasonably stable electrolyte material under a reducing environment of CO in a recent paper at temperatures similar to those used in this study [25].

Electrochemical impedance spectroscopy measurements performed on both coals at 700 and 800 °C showed the presence of more than one arc for the electrode behaviour. The mass transfer limitation experienced by DM at both temperatures is reflected in large low frequency arcs in the impedance spectra shown in Figures 4.7 and 4.8.

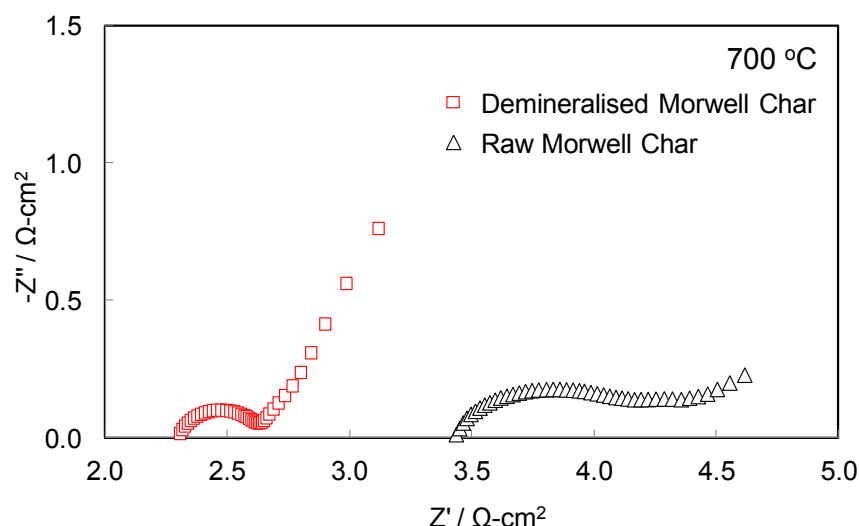


Figure 4.7: Impedance spectra for DM and RM at 700 °C under open circuit voltage

Such behaviour has been observed before and modelled in a previous publication [26]. It was related to Warburg-type diffusion limitation, the magnitude of which

depends on the availability of fuel near the anode/electrolyte interface. The same type of model was applied here and the values of Warburg resistive component was $4.0 \Omega \text{ cm}^2$ (total cell resistance calculated from the model is $6.7 \Omega \text{ cm}^2$) for DM char and $1.3 \Omega \text{ cm}^2$ (total cell resistance calculated from model is $5.5 \Omega \text{ cm}^2$) for RM char at 700°C . These results are consistent with V-j data.

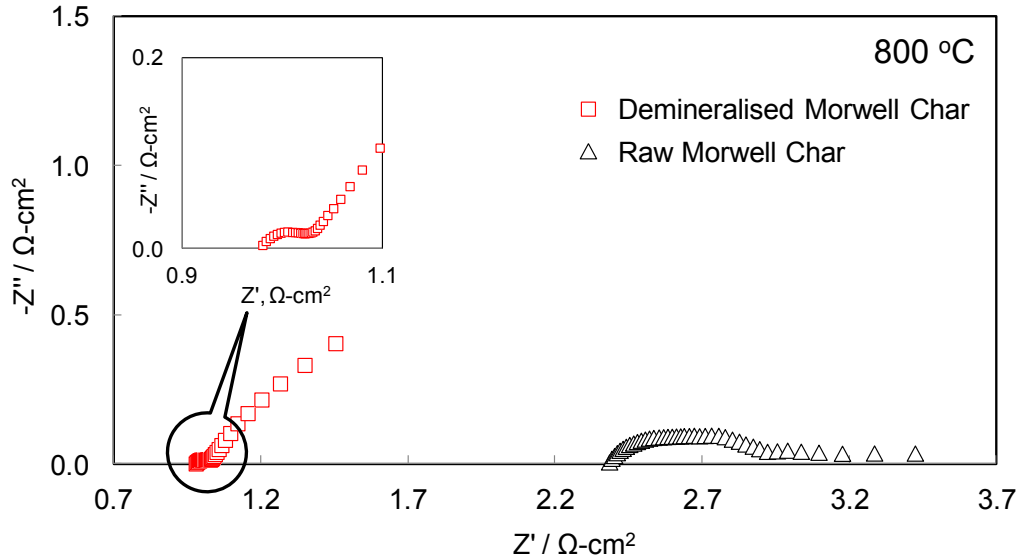


Figure 4.8: Impedance spectra for DM and RM at 800°C under open circuit voltage

With an increase in the DCFC operating temperature to 800°C , there was a marked decrease in the size of both high and low frequency arcs and the value of Warburg resistive component decreased to $1.5 \Omega \text{ cm}^2$ (total cell resistance calculated from the model is $3.0 \Omega \text{ cm}^2$) for the DM char. Due to the flat nature of the impedance curve for the diffusion arc, its magnitude could not be determined accurately for RM char at 800°C . Therefore, the relatively low diffusion-type limitation and the superior power density (89 mW cm^{-2} at 800°C) of the direct carbon fuel cell with RM char as the fuel source, suggests that the cell behaviour is strongly dependent on fuel reactivity and availability of reactive species at the anode. Of the reactive species, CO may be more abundant at the anode when RM was used as the fuel in comparison to DM and CB. This is due to greater Boudouard gasification reactivity of RM fuel as outlined in Section 4.3.1.3. Carbon dioxide produced by the cell *in-situ* via Eq. (1.4) is more likely to react with solid carbon via Eq. (1.7) for the RM fuel. Thus contributions to enhanced cell performance via additional reaction pathways, such as the CO-shuttle mechanism [27,28], may be the primary differentiator between cell performance for a given fuel. Such phenomena are well reported in the literature as a result of an increase in availability of CO at the anode [6,9,29]. Two of these studies [6,9] also investigated the effect of adding Boudouard gasification catalysts, in the

form of AAEM species, to the carbon black fuel and observed substantial increases in power densities of the cell. These findings are in line with the observations in this study, albeit for a different carbon-based fuel in partially charred coals.

It has been difficult to attribute the high frequency arc in the EIS spectra (Figures 4.7 and 4.8) to any specific anodic or cathodic process for a two-probe electrode study, and can be possibly due to a combination of cathodic reduction of oxygen (Eq. 1.3) and direct electrochemical oxidation of carbon (Eq. 1.4 and 1.5). These are temperature dependent processes and polarisation resistances decreased with increasing temperature for both fuels RM and DM chars.



As with the EIS spectra at 700 °C (Figure 4.7), the ohmic resistance component of the RM cell is significantly higher than that of the DM cell at 800 °C (Figure 4.8). It should be noted that the ohmic resistance (left intercept of the high frequency arc) consists of the electrolyte resistance and contact resistances between carbon particles and anode, and between carbon particles and current collectors. In a DCFC, the carbon fuel itself can act as a current carrier in addition to the platinum mesh, and the number of contacts between fuel and anode and the char conductivity can have an effect on the overall ohmic resistance. As discussed above, the conductivity of RM (0.1 S cm^{-1}) was considerably lower than that of DM (0.5 S cm^{-1}). It is highly likely that lower levels of impurities such as Si, Fe and Mg in DM in comparison to RM and a smaller particle size of DM char would have contributed to observed lower ohmic resistance for DM by allowing better contact between fuel particles with fewer insulating phases.

4.4 Conclusions

Partially charred Morwell coal, from the Latrobe Valley, Victoria, both acid washed (DM) and raw (RM), were tested in a solid oxide electrolyte based DCFC. Their performances were evaluated against a commercially produced carbon black (CB) as a benchmark fuel. At 700 °C, the peak power densities of raw and demineralised Morwell chars were similar, at 37 and 38 mW cm⁻², respectively. The V-P-j curves showed remarkable similarity at low current densities, however, at 800 °C, the raw Morwell char achieved much higher power densities. At 800 °C, the demineralised Morwell char produced a comparable peak power density (65 mW cm⁻²) to that of the carbon black (67 mW cm⁻²), with raw Morwell char achieving 89 mW cm⁻². A comparison of power and current densities obtained with carbon black and demineralised Morwell char indicates that a fuel with finer particle size could improve contact between the fuel and the anode, therefore sustaining higher current densities culminating in a broader V-P-j characteristic. It has also been proposed that the superior performance achieved by the raw Morwell char was primarily due to a greater availability of CO at the anode. Catalysis of Boudouard gasification by inherent inorganic species in the raw coal char namely Fe, Ca, and Mg, was observed. These species, largely removed in the demineralised Morwell char, and not present in carbon black, could create such contrasting anodic atmospheres. Thermogravimetric analysis of the carbons at operating temperatures confirmed superior Boudouard gasification kinetics of raw Morwell char over the other fuels. In the following chapter, the performance of a DCFC operated on DM over longer intervals of time and current passage will be assessed.

References

1. Gür TM, Huggins RA. Direct Electrochemical Conversion of Carbon to Electrical Energy in a High Temperature Fuel Cell. *J Electrochem Soc.* **1992**;139:L95-L7.
2. Kulkarni A, Giddey S, Badwal SPS. Electrochemical performance of ceria-gadolinia electrolyte based direct carbon fuel cells. *Solid State Ionics.* **2011**;194:46-52.
3. Li C, Shi Y, Cai N. Mechanism for carbon direct electrochemical reactions in a solid oxide electrolyte direct carbon fuel cell. *J Power Sources.* **2011**;196:754-63.
4. Desclaux P, Nürnberger S, Rzepka M, Stimming U. Investigation of direct carbon conversion at the surface of a YSZ electrolyte in a SOFC. *Int J Hydrogen Energy.* **2011**;36:10278-81.
5. Li X, Zhu Z, Chen J, De Marco R, Dicks A, Bradley J, et al. Surface modification of carbon fuels for direct carbon fuel cells. *J Power Sources.* **2009**;186:1-9.
6. Li C, Shi Y, Cai N. Performance improvement of direct carbon fuel cell by introducing catalytic gasification process. *J Power Sources.* **2010**;195:4660-6.
7. Chen M, Wang C, Niu X, Zhao S, Tang J, Zhu B. Carbon anode in direct carbon fuel cell. *Int J Hydrogen Energy.* **2010**;35:2732-6.
8. Kulkarni A, Ciacchi FT, Giddey S, Munnings C, Badwal SPS, Kimpton JA, et al. Mixed ionic electronic conducting perovskite anode for direct carbon fuel cells. *Int J Hydrogen Energy.* **2012**;37:19092-102.
9. Liu R, Zhao C, Li J, Zeng F, Wang S, Wen T, et al. A novel direct carbon fuel cell by approach of tubular solid oxide fuel cells. *J Power Sources.* **2010**;195:480-2.
10. Nabae Y, Pointon KD, Irvine JTS. Electrochemical oxidation of solid carbon in hybrid DCFC with solid oxide and molten carbonate binary electrolyte. *Energy & Environmental Science.* **2008**;1:148-55.
11. Cherepy NJ, Krueger R, Fiet KJ, Jankowski AF, Cooper JF. Direct Conversion of Carbon Fuels in a Molten Carbonate Fuel Cell. *J Electrochem Soc.* **2005**;152:A80-A7.
12. Rady AC, Giddey S, Badwal SPS, Ladewig BP, Bhattacharya S. Review of fuels for direct carbon fuel cells. *Energy Fuels.* **2012**;26:1471-88.
13. Burnard K, Bhattacharya S. Power Generation from Coal - Ongoing Developments and Outlook: *International Energy Agency*; **2011**.

14. Bureau of Resources and Energy Economics. Energy in Australia 2012. *Department of Resources, Energy and Tourism, Australian Government*.
15. Department of Environment and Primary Industries. Fact Sheet: Victoria, Australia, A principal brown coal province. *State Government, Victoria*; **2010**.
16. Johnson TR. Future Options for Brown Coal based Electricity Generation - the Role of IDGCC. ANZSES - Destination Renewables. Melbourne, Australia, **2003**. p. 371 - 80.
17. Allardice DJ, Chaffee AL, Jackson WR, Marshall M. Chapter 3 - Water in Brown Coal and Its Removal. In: Chun-Zhu L, editor. Advances in the Science of Victorian Brown Coal. Amsterdam: *Elsevier Science*; **2004**. p. 85-133.
18. Quyn DM, Wu H, Bhattacharya SP, Li C-Z. Volatilisation and catalytic effects of alkali and alkaline earth metallic species during the pyrolysis and gasification of Victorian brown coal. Part II. Effects of chemical form and valence. *Fuel*. **2002**;81:151-8.
19. Quyn DM, Wu H, Li C-Z. Volatilisation and catalytic effects of alkali and alkaline earth metallic species during the pyrolysis and gasification of Victorian brown coal. Part I. Volatilisation of Na and Cl from a set of NaCl-loaded samples. *Fuel*. **2002**;81:143-9.
20. Tomita A, Ohtsuka Y. Chapter 5 - Gasification and Combustion of Brown Coal. In: Chun-Zhu L, editor. Advances in the Science of Victorian Brown Coal. Amsterdam: *Elsevier Science*; **2004**. p. 223-85.
21. Bhattacharya S, Kabir KB, Hein K. Dimethyl ether synthesis from Victorian brown coal through gasification - Current status, and research and development needs. *Progr Energy Combust Sci*. **2013**;39:577-605.
22. Antolini E. Carbon supports for low-temperature fuel cell catalysts. *Applied Catalysis B: Environmental*. **2009**;88:1-24.
23. Wang S, Kato T, Nagata S, Kaneko T, Iwashita N, Honda T, et al. Electrodes and performance analysis of a ceria electrolyte SOFC. *Solid State Ionics*. **2002**;152-153:477-84.
24. Zha S, Xia C, Meng G. Effect of Gd (Sm) doping on properties of ceria electrolyte for solid oxide fuel cells. *J Power Sources*. **2003**;115:44-8.
25. Badwal SPS, Fini D, Ciacchi FT, Munnings C, Kimpton JA, Drennan J. Structural and microstructural stability of ceria - gadolinia electrolyte exposed to reducing environments of high temperature fuel cells. *Journal of Materials Chemistry A*. **2013**;1:10768-82.

26. Giddey S, Kulkarni A, Munnings C, Badwal SPS. Performance evaluation of a tubular direct carbon fuel cell operating in a packed bed of carbon. *Energy*. **2014**;68:538-47.
27. Nakagawa N, Ishida M. Performance of an internal direct-oxidation carbon fuel cell and its evaluation by graphic exergy analysis. *Ind Eng Chem Res*. **1988**;27:1181-5.
28. Gür TM. Mechanistic Modes for Solid Carbon Conversion in High Temperature Fuel Cells. *J Electrochem Soc*. **2010**;157:B751-9.
29. Tang Y, Liu J. Effect of anode and Boudouard reaction catalysts on the performance of direct carbon solid oxide fuel cells. *Int J Hydrogen Energy*. **2010**;35:11188-93.

Declaration for thesis chapter 5

Declaration by candidate

In the case of Chapter 5, the nature and extent of my contribution to the work was the following:

Nature of contribution	Extent of contribution (%)
Experimental work and analysis, writing	100

The following co-authors contributed to the work. If co-authors are students at Monash University, the extent of their contribution in percentage terms must be stated:

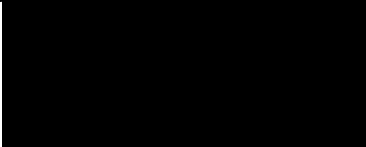
Name	Nature of contribution	Extent of contribution (%)
Dr Sukhvinder Badwal	Advisory role	-
Dr Sarbjit Giddey	Advisory role	-
Prof Sankar Bhattacharya	Advisory role	-
Dr Aniruddha Kulkarni	Advisory role	-

The undersigned hereby certify that the above declaration correctly reflects the nature and extent of the candidate's and co-authors' contributions to this work.

Candidate's
Signature

	Date 27/02/2015
---	------------------------

Main
Supervisor's
Signature

	Date 27/02/2015
---	------------------------

5

Degradation mechanism in a direct carbon fuel cell operated with demineralised brown coal

*Reproduced in part from Adam C Rady, Sarbjit Giddey, Aniruddha Kulkarni, Sukhvinder PS Badwal, and Sankar Bhattacharya, *Electrochimica Acta*, 2014, 143, 278-290.

Chapter objective

DCFC operation on Victorian brown coal and its derivatives has delivered promising performances, with the inherent inorganic catalytic species confirmed as an integral component of the fuel's high reactivity. However, the performance of the DCFC utilising Victorian brown coal over extended operating times remains unassessed. The current chapter investigates the nature of cell performance under various loading arrangements, including constant current load as well as idle standby for extended periods. The influence of CO₂ on cell performance is also scrutinised in terms of its contribution to carbon conversion within the DCFC.

In addition to *in-situ* electrochemical diagnosis of cell condition, post mortem analysis of the fuel cell anode is conducted to assess any physical and chemical changes as a result of DCFC operation.

Degradation mechanism in a direct carbon fuel cell operated with demineralised brown coal

Abstract

The performance of a demineralised and devolatilised coal from the Morwell mine in the Latrobe Valley, Victoria, has been investigated in a direct carbon fuel cell (DCFC) operated at 850 °C. The focus of the investigation has been on understanding degradation issues as a function of time involving a sequence of electrochemical impedance spectroscopy and voltage-current characteristic. Diffusion limited processes dominate the electrode polarisation losses in pure N₂ atmosphere, however, these decrease substantially in the presence of CO₂ as the anode chamber purge gas, due to *in-situ* generation of fuel species by the reaction of CO₂ with carbon. Post-mortem analysis of anode by SEM and XRD revealed only a minor degradation due to its reduction, particle agglomeration as well as the formation of small quantity of new phases. However, major fuel cell performance degradation (increase of ohmic resistive and electrode polarisation losses) occurred due to loss of carbon / anode contacts and a reduction in the electron-conducting pathways as the fuel was consumed. The investigations revealed that the demineralised coal char can be used as a viable fuel for DCFC, however, further developments on anode materials and fuel feed mechanism would be required to achieve long-term sustained performance.

5.1 Introduction

With DCFC research efforts entering the phase of laboratory scale-up [1], engineering issues such as fuel feed mechanism and anodic gaseous environment control will present a challenge in system and cell design [2]. It is therefore necessary to understand the fundamentals of how the solid fuel is consumed within the cell, both in the direct solid form and/or *via* gas phase reaction through its gasification. Further to this, knowledge of factors contributing to the degradation of critical cell components is essential for the development of a DCFC capable of reliable operation during long-term power generation applications.

There is very little data reported in the literature on the degradation behaviour in direct carbon fuel cells although there is considerable information available in the literature on anode (Ni/O^{2-} -conducting ceramic cermets) degradation [3,4]. In the case of DCFCs, the performance degradation has been broadly attributed to carbon consumption [5,6]. There have been no detailed reaction mechanism studies on real world fuels using a combination of electrochemical and material characterisation techniques to investigate the causes of cell performance degradation.

This study investigates the sources of performance degradation of the fuel cell operating on Morwell coal (Victoria, Australia) following demineralisation and devolatilisation to understand the effect of residual impurities in the demineralised coal. The fuel cell operation included loading the cell at various current densities for both short and extended times in different anode chamber gas atmospheres and performing electrochemical impedance spectroscopy diagnostics to deconvolute contributions of different factors to increasing cell resistance. In addition, the post-mortem of the cell anodes has been carried out to investigate the extent of degradation during fuel cell testing.

5.2 Experimental

The fuel used in this study was a Victorian brown coal from the Morwell mine, which has been demineralised and devolatilised, and will be referred to hereafter as 'DM char'. Details of the fuel preparation can be found in Chapter 3, and fuel analysis in Chapter 4.

Three cells (cell # 1, 2 and 3) were fabricated by employing the procedure as outlined in Chapter 3 for YSZ electrolyte button cells with LSCF electrodes. The cell test fixture including the fuel supply arrangement to the anode has been described in detail in Chapter 3 also and is represented by Figure 3.3(b). For cell #1, a Pt mesh with a wire diameter of 0.25 mm and sieve openings of 0.80 mm x 0.80 mm was used. In order to improve the current collection, in the case of cell # 2, the Pt mesh was attached to the anode by using Pt ink at few places on the electrode. The mesh was also finer, with a wire diameter of 0.12 mm and sieve openings of 0.30 mm x 0.30 mm.

Cells #1 and #2 were used to study the detailed cell anode side degradation behaviour with and without the cell under different current loads and also to study the effect of anode chamber gas atmosphere on the reaction mechanism. Cell #3 was not subjected to any fuel cell testing and was used to perform XRD (phase identification) and obtain SEM images of the electrode material fabricated in an identical fashion to the cells used in DCFC testing for comparison.

Cells #1 and #2 were subjected at 850 °C to a series of electrochemical measurements. A chronological summary of fuel cell experiments is given as Table 5.1. A N₂ flow rate of 40 mL min⁻¹ was used during heating, normal operation, and cooling. In the operation of cell #2, for the final few experiments the anode chamber purge gas was switched from N₂ to a N₂/CO₂ mixture (Cellamix, 40 vol% CO₂).

5.3 Results and interpretation

Table 5.1 details the sequence and timing of cell operation for cells #1 and #2, anode purge gas used and other experimental details. For cell #1, three V-j scans were conducted throughout the course of the experiment to gauge cell performance and the influence of prior cell loading on this, by taking EIS under load and running chronopotentiometric (CP) scans. Similarly, three EIS scans at open circuit were conducted following the V-j scans to monitor changes in the impedance of individual cell components. EIS scans under load were performed early and late in the experiment to determine the relative contributions of different rate processes to overall cell impedance for the fresh cell and following various cell loadings to determine the root cause of cell degradation. CP1 and CP2 were performed to establish the longer-term stability of cell performance and as carbon was consumed during cell loading. The experimental procedure of cell #2 was kept as close as possible to that of cell #1, up to the 4th EIS, in order to assess the effect of the new anode current collector arrangement on cell performance and cell resistances. The EIS loadings for cell #2 were adjusted accordingly. Changes to cell impedance and cell resistances following standby under N₂ anodic atmosphere were observed by comparing the 4th and 5th EIS and V-j Runs 2 and 3 respectively. Finally, changes to cell impedance and cell resistances following a change from N₂ to N₂/CO₂ anodic atmosphere were observed by comparing the 5th and 6th EIS and V-j Runs 3 and 4 respectively.

Table 5.1: Summary of cell #1 and #2 operation with time (hrs:min) after first loading.

Cell	Anode Gas	Time	V-j*	EIS*	CP*
Cell #1	N ₂	-	Run 1		
		0:13		1 st at OCV	
		0:26		2 nd at 10 mA cm ⁻²	
		0:41		3 rd at 20 mA cm ⁻²	
		1:08	Run 2		
		1:16		4 th at OCV	
		1:27			1 hr 47 min (CP1)
		3:17	Run 3		
		3:28		5 th at OCV	
		3:41		6 th at 20 mA cm ⁻²	
		3:53			2 hrs (CP2)
Cell #2	N ₂	-	Run 1		
		0:05		1 st at OCV	
		0:23		2 nd at 20 mA cm ⁻²	
		0:42		3 rd at 60 mA cm ⁻²	
		0:57	Run 2		
		1:10		4 th at OCV	
		2:11		5 th at OCV	
		2:20	Run 3		
	N ₂ /CO ₂	2:28	Run 4		
		2:36		6 th at OCV	

* V-j: voltage-current potentiodynamic sweep, EIS: impedance spectra, CP: chronopotentiometric scan (20 mA cm⁻²).

5.3.1 Cell #1

5.3.1.1 Cell loading and diagnostics

A visual representation of the test history of cell #1 and cell #2 operation is given as Figure 5.1(a) and (b), respectively. Each bar represents a particular measurement taken at a given time as per Table 5.1.

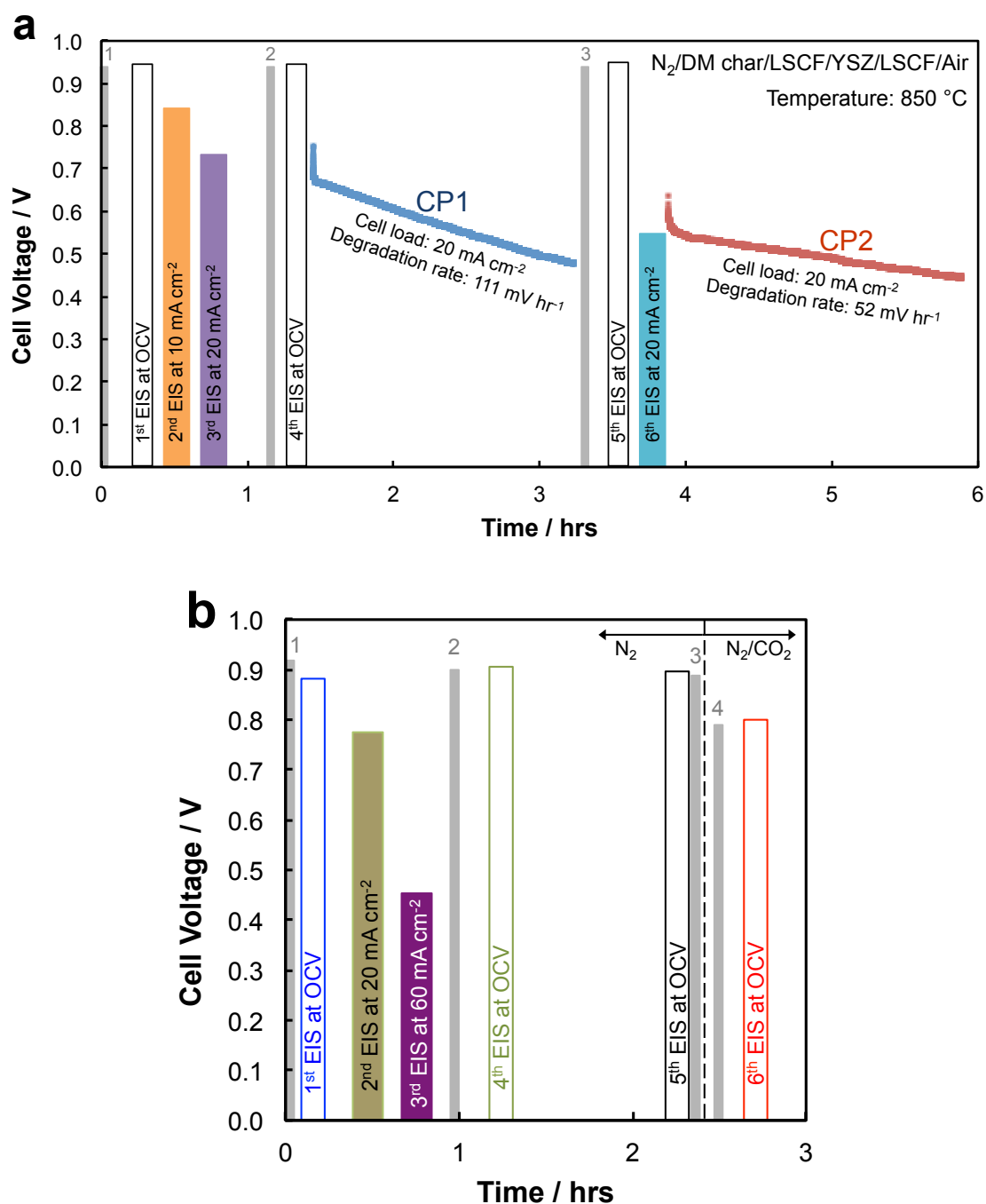


Figure 5.1 (a) Cell timeline of all electrochemical cell measurements and voltages with V-j runs in grey for Cell #1 including Chronopotentiometric cell loading (20 mA cm⁻²) at loading times of 1 hr 47 min (CP1): following 4th EIS, and 2 hrs (CP2) following 6th EIS. (b) Cell timeline of all electrochemical cell measurements and voltages with V-j runs in grey for Cell #2 including change of anode purge gas from N_2 to N_2/CO_2 between V-j Runs 3 and 4.

The height of each bar represents the voltage at which the measurement was taken, or started in the case of the V-j (grey) bars. Following the final cell #1 loading at 20 mA cm⁻² for about 2 hrs and after about 6 hours of total cell operation, the cell was left at 850 °C overnight at open circuit voltage (OCV).

No further testing was performed the next day on this cell as the glass seal appeared to have broken at a certain stage of the overnight operation as obvious from a significant decrease in the open cell voltage. This may have led to mixing of anode and cathode chamber gases. Since N_2 was at a higher positive pressure, its leak into the cathode chamber is more likely to have occurred. XRD analysis of the anode on cooling the cell as outlined in Section 5.3.1.2 below, confirmed that it remained in a reduced state and thus is unlikely to have been exposed to air.

Figure 5.2 shows the first four EIS spectra taken for cell #1. The first EIS curve was acquired shortly after the first V-j run and after the OCV had recovered and stabilised. The second and third EIS scans were obtained at 10 and 20 mA cm^{-2} loads respectively, to observe the effect of cell loading on its impedance behaviour. For all EIS under current load, the current was passed for a period of 2 minutes to stabilise the voltage before recording EIS spectra. The EIS scans take about 8 min during which the cell remained loaded. The fourth EIS was taken under OCV after second V-j scan.

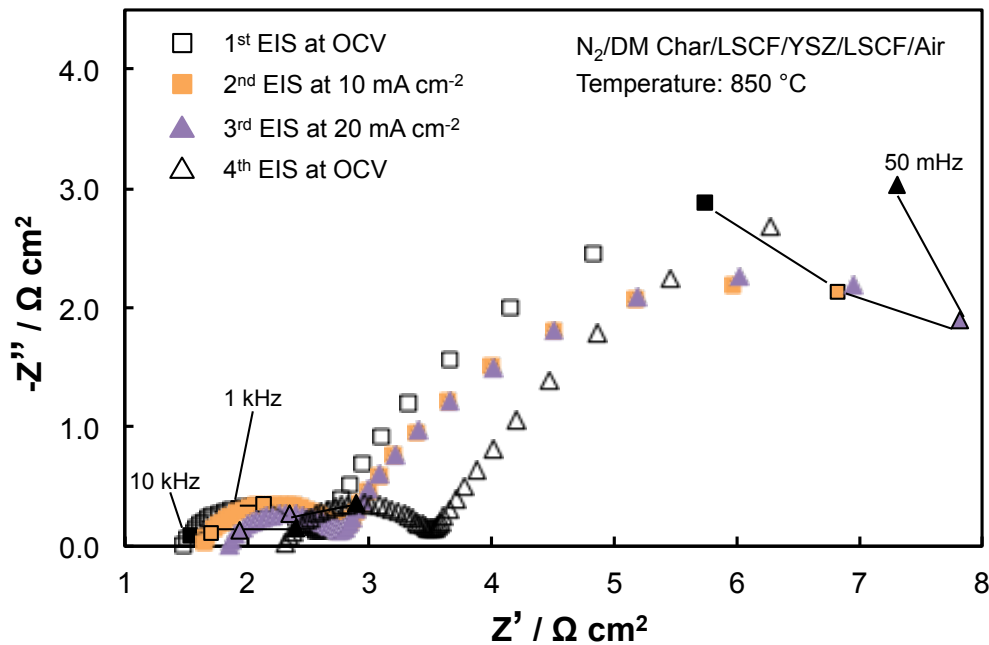


Figure 5.2: First four electrochemical impedance spectra for cell #1 at 850 °C.

Two impedance arcs were observed for the electrode behaviour, a small high frequency arc and a large low frequency arc. The high frequency intercept of the impedance arc on the Z' axis corresponds to the ohmic resistance (R_Ω) which included the electrolyte resistance, the resistance of the anode and cathode

materials, contact resistance between anode and solid fuel and resistance of electron conducting pathways in the fuel.

From the behaviour of the low frequency arc under different cell operating conditions, there is no doubt that the low frequency arc is associated with the anode. It is possible that the high frequency arc has some cathode contribution embedded in it. The polarisation resistances of these cathodes at fuel cell operating temperatures used in this work have been reported to be in the range of 0.1 to $0.2 \text{ } \Omega \text{ cm}^2$ [6-8] under open circuit as well as under loading conditions. Thus both the high and low frequency arcs in the impedance spectra can be attributed mainly to the anode. The magnitude of the high frequency arc, in general, decreased somewhat when the cell was loaded at low current densities compared with the open circuit condition. There was also a very noticeable reduction in the magnitude of the low frequency arc on loading of the cell (the second and third EIS spectra) when compared with the first and fourth EIS under open circuit conditions.

With each successive EIS spectra, there was a progressive increase in the ohmic resistance (R_Ω). There was a successive increase in the ohmic resistance with loading of the cell. The increase in the cell ohmic resistance between the first and second EIS ($0.17 \text{ } \Omega \text{ cm}^2$) and between the second and third EIS ($0.20 \text{ } \Omega \text{ cm}^2$) was small and comparable. The increase in R_Ω between the third and fourth EIS was the largest at $0.46 \text{ } \Omega \text{ cm}^2$.

Following the fourth EIS measurement, the cell was held under a load of 20 mA cm^{-2} for 107 minutes, given as the first chronopotentiometric (CP1) plot in Figure 5.1(a). On loading, there was an initial drop in voltage of around 75 mV over the first 30 seconds from 0.75 V, followed by almost constant voltage decay at a rate of 111 mV hr^{-1} .

The fifth EIS measurement was taken under OCV and is given in Figure 5.3, which includes the previous EIS measurement (fourth EIS, for reference) also at open circuit as well as a final EIS (sixth EIS) under a load of 20 mA cm^{-2} . The cell had experienced significant loading over a two hr time period between the fourth and fifth open circuit EIS measurements *via* the first CP scan given in Figure 5.1(a). This coincided with a large increase in R_Ω between the fourth and fifth EIS of $3.3 \text{ } \Omega \text{ cm}^2$. This was by far the single largest increase in the ohmic resistance observed in EIS

spectra for cell #1. The fifth EIS also exhibited a large increase in the size of the high frequency arc, when compared with the previous EIS. This suggests that the polarisation resistance associated with electrode processes responsible for the high frequency arc has also increased following the CP scan.

The sixth EIS was taken under a load of 20 mA cm^{-2} and exhibits a closure of the low frequency arc, as observed for the second and third EIS taken under load in Figure 5.2. The high frequency arc is also somewhat smaller than the previous EIS under open circuit as was observed for the second and third EIS in Figure 5.2 under load.

Shortly after the completion of the sixth and final EIS for cell #1, the cell was reloaded again at 20 mA cm^{-2} and left for 2 hrs. The results are given as the second CP curve (CP2) in Figure 5.1(a). As observed in the first CP scan (CP1), there was an initial fast drop in the voltage by 65 mV over the first 30 seconds in this case. The starting voltage was also lower at 0.64 V, but once stabilised there was a linear voltage decay (CP2), as observed in the previous CP1 curve also at a loading of 20 mA cm^{-2} . However, the subsequent linear voltage decay of 52 mV hr^{-1} over the 2 hr period was comparatively smaller than that during the first CP measurements. Reloading of the cell had also allowed for a partial recovery of voltage under load, from 0.48 V at the end of the first CP scan (CP1) to $\sim 0.55 \text{ V}$ for the sixth EIS and initial stabilised voltage of the second CP scan (CP2).

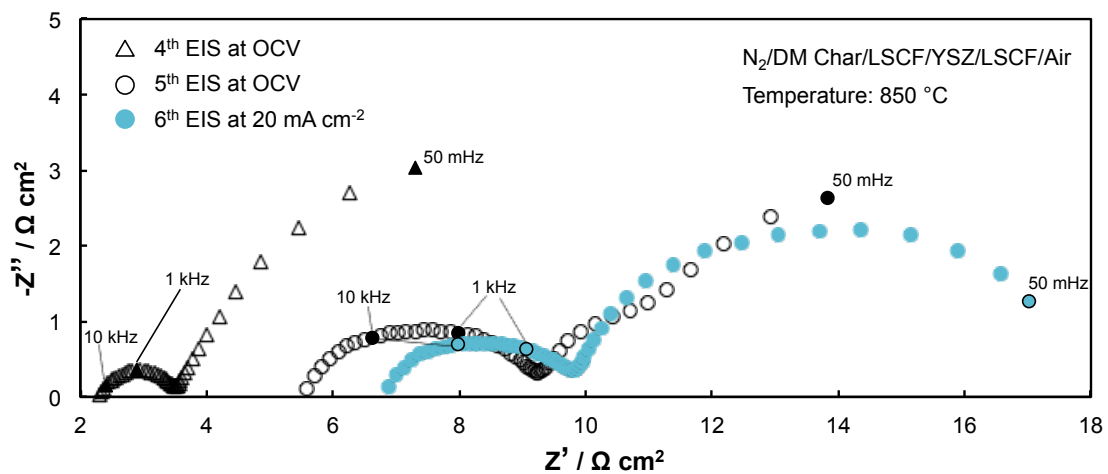


Figure 5.3: Electrochemical impedance spectra for cell #1 at 850 °C before and after first CP loading (CP1).

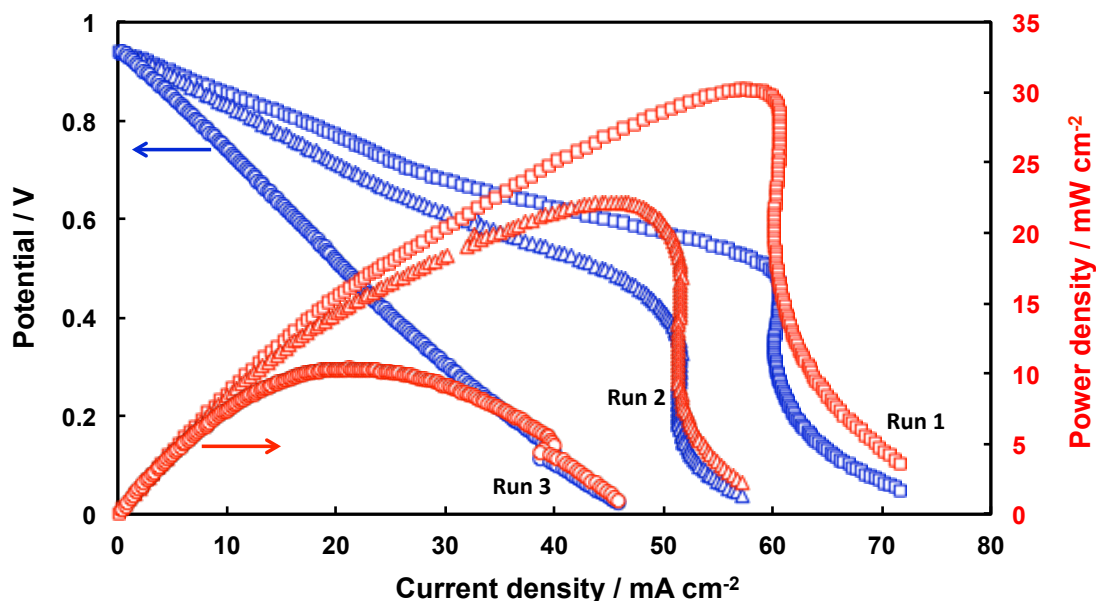


Figure 5.4: Voltage-current density and power density-current density curves of cell #1 under high purity N_2 at 850 °C for Runs 1, 2 and 3. Run 2 taken 68 min after Run 1 & Run 3 taken 3 hrs, 17 min after Run 1.

The three V-j and P-j polarisation curves for cell #1 are given in Figure 5.4. Run 1 is the first V-j measurement of cell #1 where a peak power density of 30 mW cm^{-2} was achieved. Run 2 was taken 68 minutes after Run 1, following second and third EIS scans taken under load, and has produced a lower peak power density of 22 mW cm^{-2} , due in part to a steeper voltage decay with increasing current density for the linear portion of the V-j curve. Run 3 was recorded 129 minutes after Run 2 and followed the first (CP1) loading. The curve showed the largest decay of voltage with increasing current density, resulting in the lowest peak power density of only 10 mW cm^{-2} , less than half that of the previous V-j run.

Another significant observation worth noting here is that during the potentiodynamic voltage-current scans, the current through the cell (or cell loading) first increases and then at some point, it started decreasing. Run 1 achieved a current density of 61 mA cm^{-2} before a twist in the V-j curve occurred and the current started decreasing (current reversal) with decreasing cell voltage. This behaviour also manifested in power density – current density curves, with the power density starting to decrease rapidly around the point of current reversal. For Run 2, the current reversal occurred at a current density of 52 mA cm^{-2} , however, for Run 3, the current reversal occurred at 40 mA cm^{-2} , but well beyond the current density where the peak power was obtained.

5.3.1.2 Investigation of anode structure and microstructure

In order to assess the extent of any physical degradation to the anode of cell #1, the disc was salvaged from the fuel cell post-DCFC operation and compared with another disc (cell #3) of identical fabrication but was otherwise unused. SEM images of the anode surfaces of the two cells showed a more uniform surface of the unused electrode (Figure 5.5(a)) with only minor cracks and a finer pore structure compared with the used anode (Figure 5.5(b)) which had a higher concentration of cracks, larger pore structure and a greater surface roughness. At a higher magnification (Figure 5.5(c) and (d)), a bimodal structure is apparent with grains of two distinct particle sizes and shapes in the microstructure of both used and unused anode surfaces. The larger particles appear flat and angular whereas the smaller particles are rounder in nature. The two particle types are evenly dispersed for both the used and unused discs, however, the particles appear to have coarsened somewhat for the used disc in Figure 5.5(d). There is also a reduction in the number of smaller particles for the used cell anode, resulting in an increase in the void fraction. Overall, the anode microstructure of the tested cell appears to be less dense than that of the unused anode.

On the anode surface of cell #1 there was a non-uniform distribution of some foreign particles. The particles were glassy in nature and likely the result of deposition of any residual minerals following demineralisation of the coal. SEM with energy dispersive X-ray spectroscopy (SEM/EDX) was employed to confirm the source of these particles. Figure 5.6(a) shows a backscatter electron image (BSE) of the anode face for cell #1, post-DCFC operation, with foreign particles on the surface. Four SEM/EDX spectra were taken, three of the foreign particles and one of the general anode area for reference. The scan windows are given in Figure 5.6(a). Figure 5.6(b) is a SEM image of the particle in Figure 5.6(a), for which Spectrum 1 in Figure 5.7 was taken, and showed charging of the micrograph as well as the glassy nature of the particle. A fifth spectrum was taken of the electrode surface of the unused cell #3 (with the scan window given on a BSE image in Figure 5.6(c)) for comparison with the fourth spectrum (shown in Figure 5.6(a) of used anode).

The SEM/EDX spectra recordings for spectra 1-5 are supplied as Figure 5.7(a) - (e), respectively. All scans contain trace readings of Ir, from the sputter coating of SEM samples, as well as C, not uncommon in vacuum systems. The scan (Figure 5.7(a)) of the particle in Figure 5.6(b), reveals a composition of mostly Si and O with lesser concentrations of Na, Al, and Fe, and trace amounts of S and Cl, at least for the area

indicated by the scan window in Figure 5.6(a). The particle is most likely dominant in SiO_2 and other silicates, common for Morwell and other brown coals [9], which are known to be heterogeneous in respect of minerals.

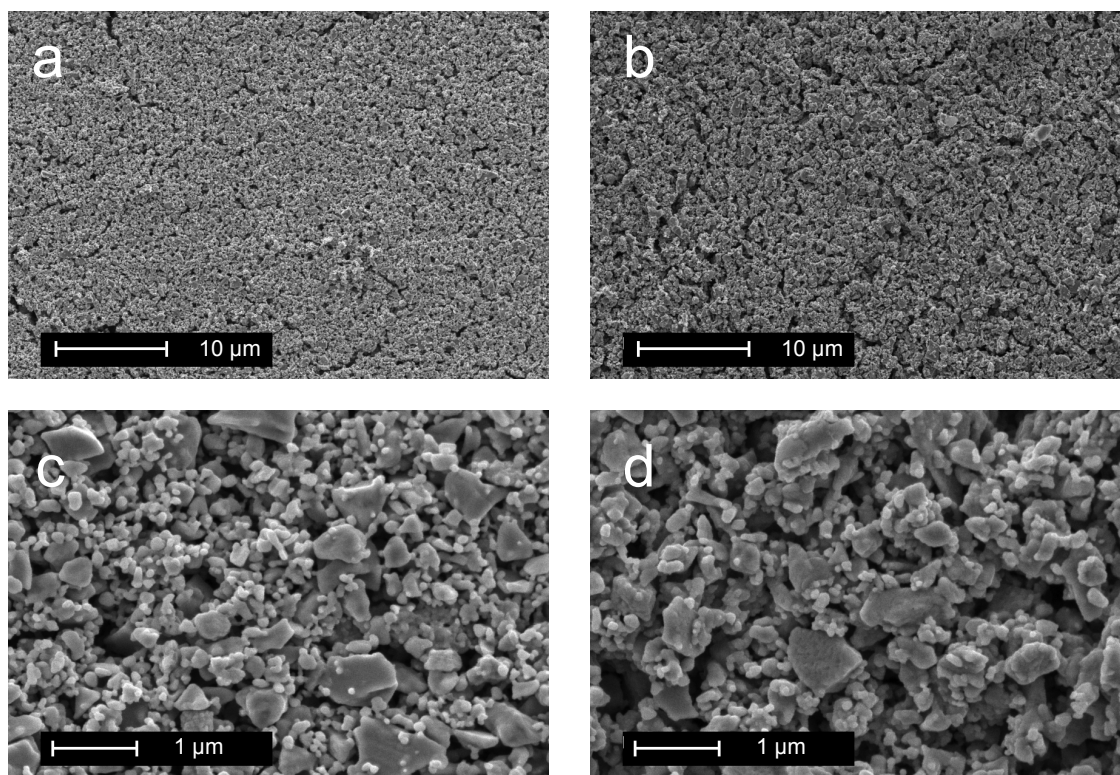


Figure 5.5: SEM images of anode surfaces. (a) & (c): Cell #3 – unused cell. (b) & (d): Cell #1 – post-DCFC testing.

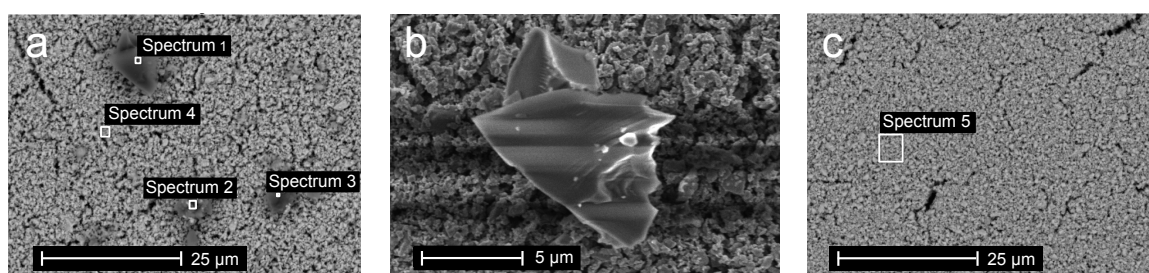


Figure 5.6: SEM images of anode surfaces. (a) Cell #1 anode - post-DCFC testing showing surface particles and EDX scan windows for Spectrums 1-4. (b) showing surface particle scanned in Spectrum 1. (c) Cell #3 anode surface showing EDX scan window for Spectrum 5.

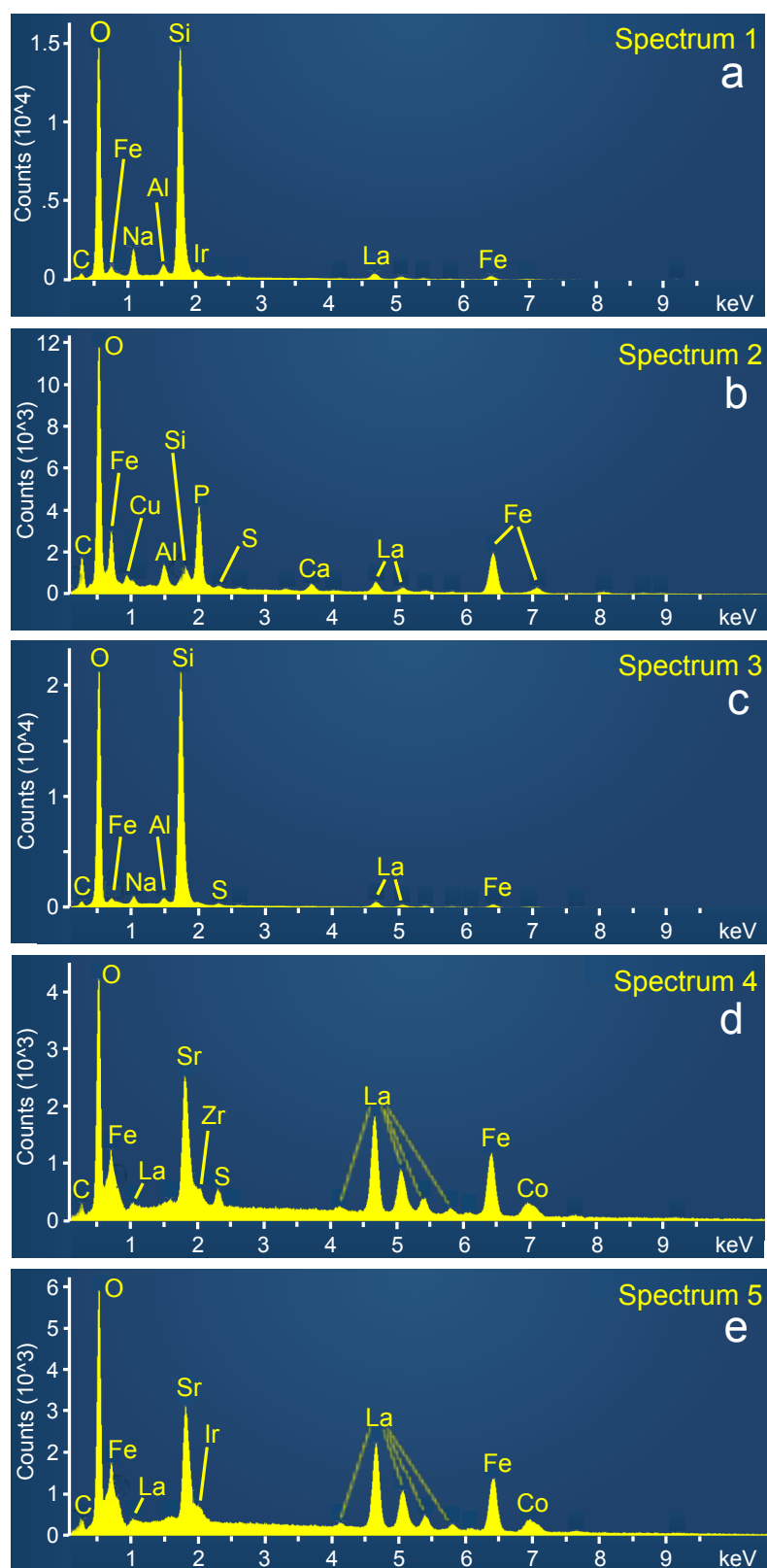


Figure 5.7: EDX Spectra of cell #1 anode, post-DCFC testing, for windows as displayed in Fig. 5.6(a) as (a) Spectrum 1, (b) Spectrum 2, (c) Spectrum 3, (d) Spectrum 4; and for cell #3 as displayed in Fig. 5.6(c) as (e) Spectrum 5.

Spectrum 2 (Figure 5.7(b)) reveals a region with high concentrations in P, Fe and O, and to a lesser extent Al, Cu, Zn, Cl, Si and S. The high P reading is perhaps surprising given the low phosphorous content of the coal (<75 ppm, dry basis), however, it is important to note that the scan is not necessarily representative of the entire particle.

Spectrum 3 (Figure 5.7(c)) is closer to that of spectrum 1, with a high Si and O content, and trace readings for Al, Na, Fe, S and Cl. Spectrum 1-3 reveal the foreign particles on the anode surface of cell #1 to contain many inorganic elements inherent in Victorian brown coals, and those found to be present in the demineralised Morwell char, determined by ICP-OES analysis, as residual species post acid-treatment of the coal (Chapter 4). Trace amounts of the anode material elements La, Sr, Co, and Fe, also appear in most scans mentioned above.

Spectrum 4 (Figure 5.7(d)) and spectrum 5 (Figure 5.7(e)) show the SEM/EDX spectra of the anode/electrode surfaces of cell #1 and #3, as per Figure 5.6(a) and (c), respectively. The two spectra correlate well and show a very similar anode surface composition, with the exception of S appearing in spectrum 4 for the used anode of cell #1. Sulphur is present in the DM char at 1700 ppm, dry basis, and is the likely source in spectrum 4.

In addition to SEM/EDX spectra, EDX-mapping was also performed on a section of the anode of cell #1 post-DCFC testing, with a SEM image of the window given as Figure 5.8(a). The EDX-mapping micrographs are given as Figures 5.8(b) – (h) and cover the elements O, Co, Fe, La, Sr, C, and S, respectively. Oxygen (Figure 5.8(b)) is well distributed across the surface, as is expected from a perovskite structure such as LSCF. Carbon (Figure 5.8(g)), which may have been deposited during cell operation or from the vacuum system of the SEM, is also distributed evenly. Cobalt (Figure 5.8(d)), in addition to background coverage of the surface, shows several concentrated regions that appear to correspond to certain discrete grains in Figure 5.8(a). Iron and Lanthanum (Figure 5.8(e) and (f), respectively), both have an even surface coverage, with minor deficiencies only where Strontium (Figure 5.8(g)) exhibits a concentrated region. Sulphur (Figure 5.8(h)) shows a concentrated deposit matching that of Strontium.

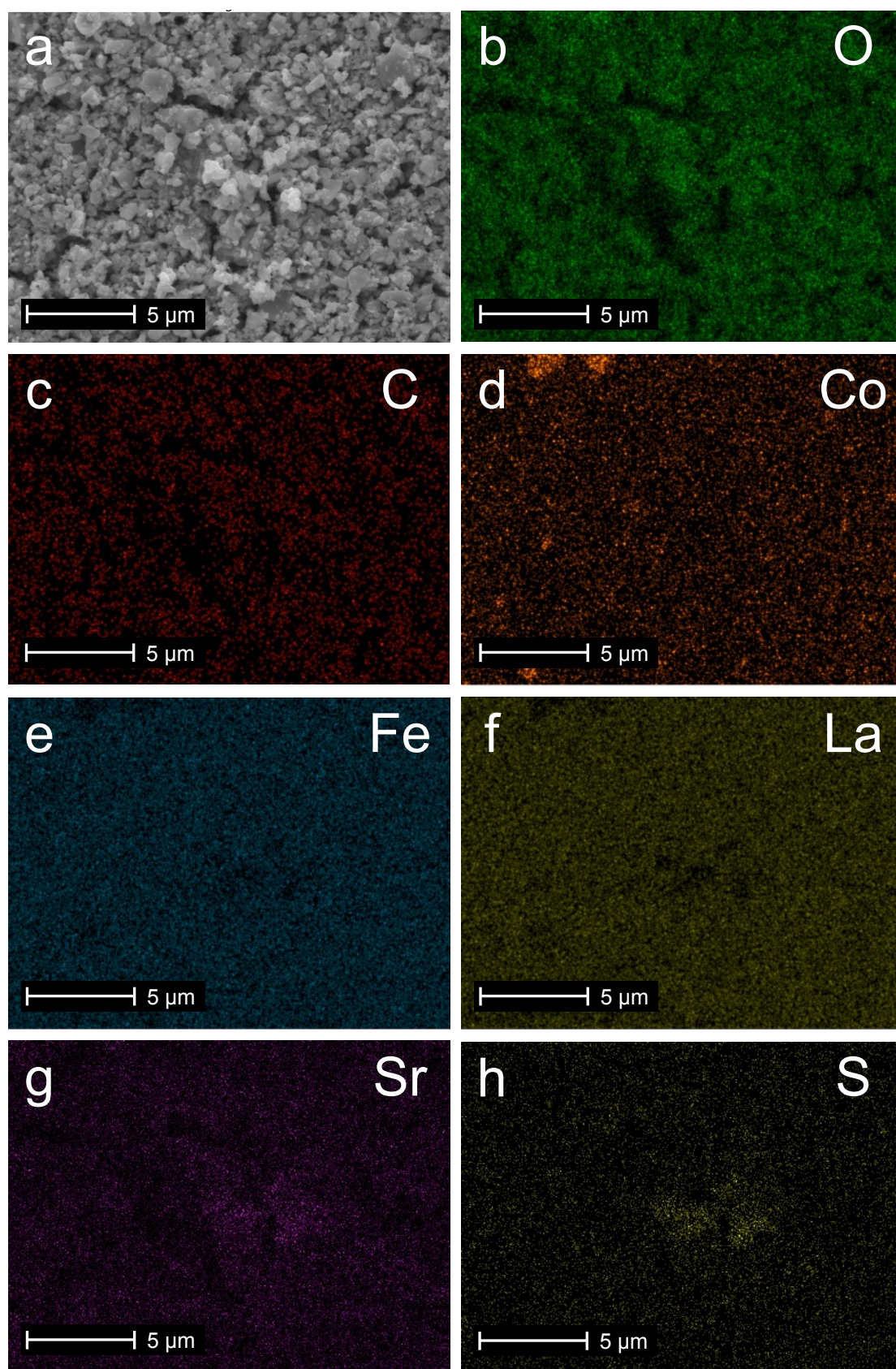


Figure 5.8: SE Image of scan area for cell #1 anode post-DCFC testing, (a) with EDX-mapping micrographs for: (b) Oxygen, (c) Carbon, (d) Cobalt, (e) Iron, (f) Lanthanum, (g) Strontium, (h) Sulphur.

In order to determine the extent of reduction, if any, of the cell #1 anode, as well as to detect the formation of any new phases, XRD was undertaken on the anode of cell #1 and #3 (shown in Figure 5.9). The blue diffraction line shows a pattern of standard LSCF peak positions for $\text{La}_{0.6}\text{Sr}_{0.4}\text{Co}_{0.2}\text{Fe}_{0.8}\text{O}_{3-\delta}$, and minimal contribution from the underlying YSZ electrolyte. Although the main LSCF phase structure was largely retained, the red diffraction pattern for the used cell #1 varied from the unused pattern in some ways. The LSCF peaks have shifted to lower angles with greater shift occurring for peaks at higher angles. In addition, YSZ peaks have appeared at standard peak positions for composition of $(\text{ZrO}_2)_{0.92}(\text{Y}_2\text{O}_3)_{0.08}$. Numerous additional peaks of relatively minor intensity have also emerged between $26 - 46^\circ 2\theta$ values.

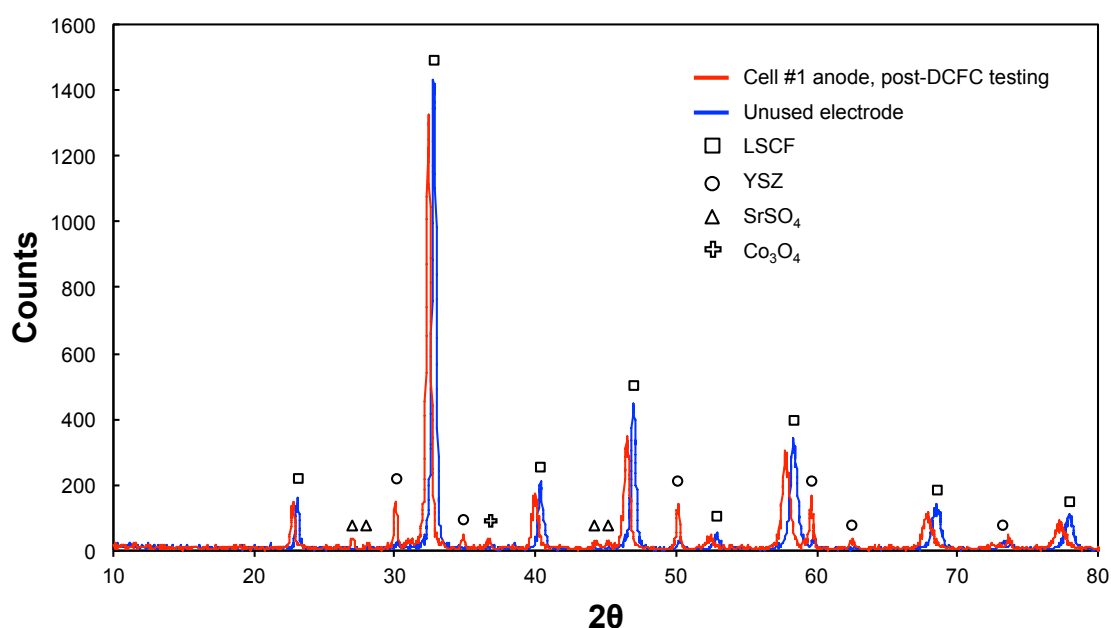


Figure 5.9: XRD spectrum of an unused LSCF electrode (blue line) overlaid with used cell #1 anode diffractogram (red line), with phases as identified by Diffrac.EVA software.

The LSCF peak shift, to lower 2θ values, is characteristic of an expansion in the lattice, and is related to a reduction in the LSCF phase. The unit cell volume of LSCF has been shown to expand in the presence of CO at a cell operating temperature of 800°C [10]. Although at the end of cell test, there was potential broken glass seal causing mixing of anode and cathode chamber gases as evident by the decreased OCV, XRD pattern in Figure 5.9 clearly showed that the anode was in a reduced state.

The Le Bail fitting of XRD patterns obtained for sample before and after test indicated that cell volume changed from $351.7 (\pm 0.05)$ to $357.1 (\pm 0.09) \text{ \AA}^3$. Both volumes, before and after the test, are reasonably consistent with previously reported volumes

for LSCF anodes in DCFC environments [10,11]. The increased lattice volume obtained for the sample after the DCFC test confirmed that the anode was not exposed to air (oxidant) after seal cracking.

5.3.2 Cell #2

5.3.2.1 Cell loading and diagnostics

In a separate study, cell #2 was tested with the same fuel, DM char, to validate observations from cell #1 and further investigate the effects of cell operating variables on its performance. In an attempt to enhance anode current collection a finer Pt mesh was used and was attached to the anode surface as mentioned in the Experimental section. In addition, the effect of introducing CO₂ into the anode chamber, to promote Boudouard gasification, on cell performance was also investigated.

The experimental history of cell #2 is given in Figure 5.1(b) and is somewhat similar to that of cell #1 in order and timing of cell operation up to the fourth EIS measurement which was recorded at 1 hr 10 min (1 hr 16 min for cell #1) although the current loading was significantly higher for cell #2 during recording of EIS. The second EIS for this cell was recorded at 20 mA cm⁻² load and third EIS at 60 mA cm⁻² load. The fourth EIS and the fifth EIS for cell #2 (around one hr apart) were recorded at OCV with no cell loading in between to observe changes to cell impedance behaviour during idle operation at 850 °C.

Three voltage-current (V-j) polarisation curves were obtained under N₂ atmosphere in the anode chamber and are shown in Figure 5.10. Run 1 is the first V-j curve obtained from the cell. Run 2 was taken 57 minutes later. EIS measurements were made at 20 and 60 mA cm⁻² load between the Runs 1 and 2. Run 3 was recorded 83 minutes after Run 2, with cell left under OCV in between the two runs (2 and 3). Run 1 achieved the highest power density of 62 mW cm⁻², almost twice that of Run 2 and Run 3 at 36 and 34 mW cm⁻² respectively, and more than twice that of Run 1 for cell #1 at 30 mW cm⁻².

For this cell #2, where higher current densities were achieved, the current reversal and its manifestation in power density curves was also more pronounced than that observed for cell #1. For Run 1 a current density of 133 mA cm⁻² was reached before

current reversal. The current reversal is considerably more severe for Run 1 compared with Run 2 and Run 3 as was the case with cell #1.

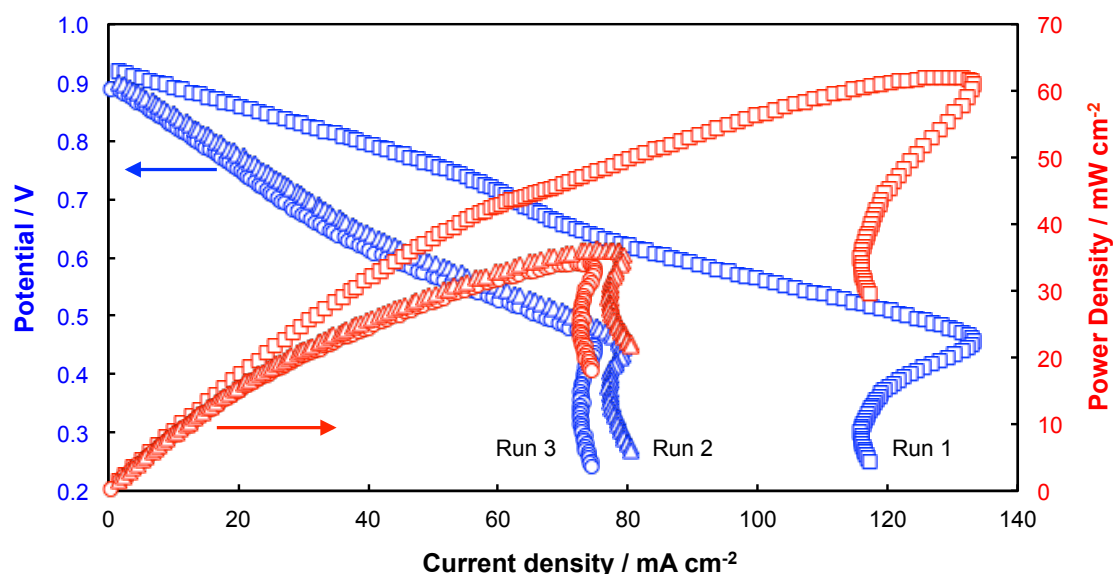


Figure 5.10: Voltage-current density and power density-current density curves of cell #2 under N_2 at 850 °C for Runs 1, 2 and 3. Run 2 taken 57 min after Run 1, and Run 3 taken 2 hrs, 20 min after Run 1.

The slope of linear portion of the V-j curves in Figure 5.10 showed that the cell overall ohmic resistance has significantly increased in Run 2 and 3 compared to Run 1, and this is also observed in impedance results presented in Figure 5.11 which includes the first, fourth and fifth EIS measurements, all acquired under open circuit voltage conditions.

As with the first EIS for cell #1, the first EIS for cell #2 has the lowest ohmic resistance, with a value of $1.02 \Omega \text{ cm}^2$. The fourth EIS, recorded 65 min after the first EIS, experienced an increase in R_Ω of $0.40 \Omega \text{ cm}^2$ to $1.42 \Omega \text{ cm}^2$, following two EIS spectra taken at 20 and 60 mA cm^{-2} loads, as well as a V-j scan ('Run 2'). For the fifth EIS, recorded after a similar interval following the fourth EIS (61 min, no cell loading), there was no further increase in R_Ω , which reinforces the relationship between increasing cell ohmic resistance and loading of the cell. The polarisation resistance, however, had increased during cell operation in the standby mode with a visibly larger high frequency arc for the fifth EIS, suggesting that the cell operating conditions are contributing to an increase in resistances associated with electrode processes.

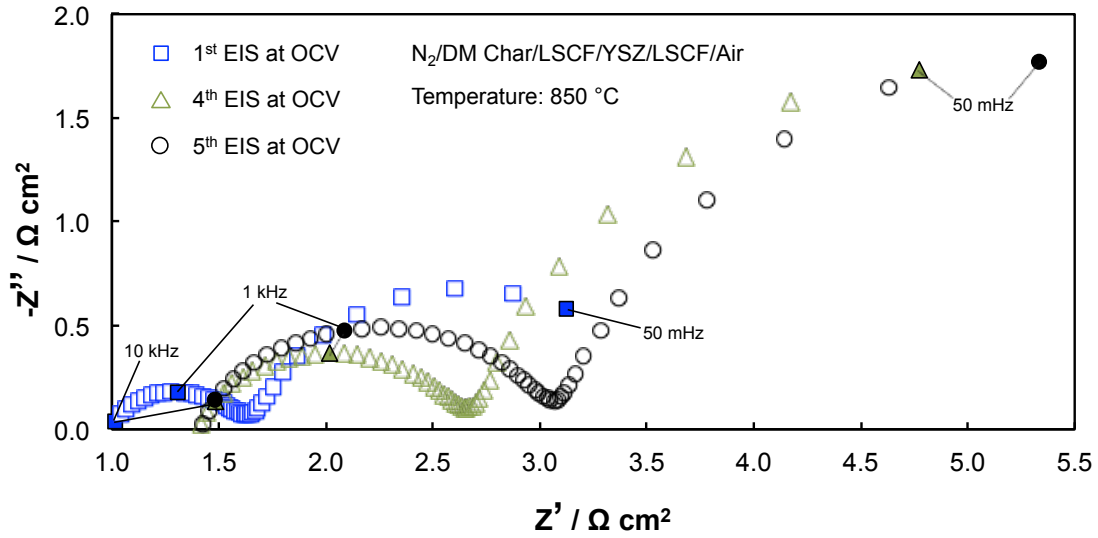


Figure 5.11: First three (taken under open circuit voltage) electrochemical impedance spectra for cell #2 at 850 °C, illustrating the effect of cell loading inbetween and holding time on cell resistances.

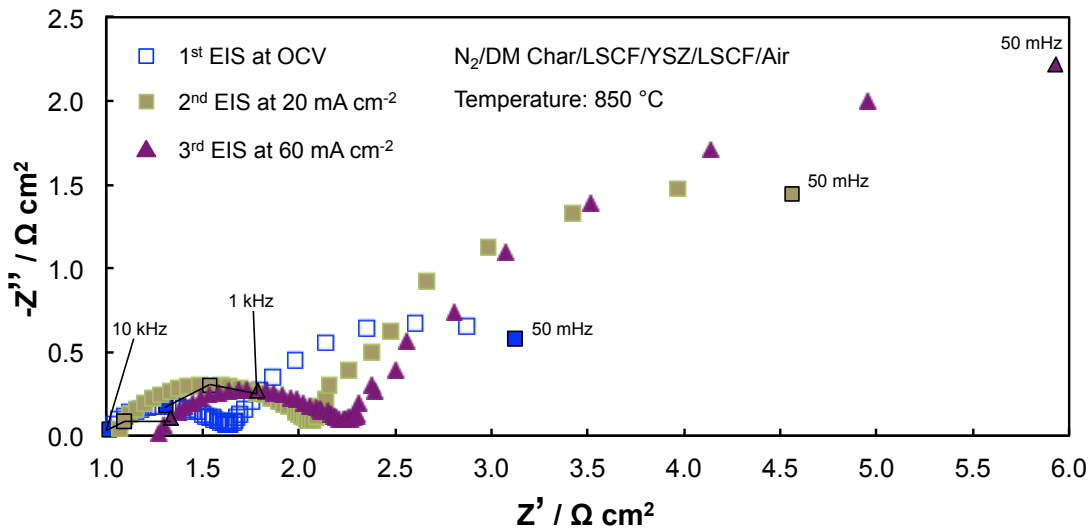


Figure 5.12: Electrochemical impedance spectra (EIS) taken for cell #2 at 850 °C at OCV and under different loads.

As mentioned, the second and third EIS for cell #2 were taken at 20 and 60 mA cm⁻² of current load respectively, and are given along with the first EIS at OCV in Figure 5.12. As observed in Figure 5.2 for cell #1, the increase in R_{Ω} is relative to the magnitude of prior cell loading. However, in this instance it is apparent that the low frequency arc behaviour is somewhat different to that of cell #1. The low frequency arc showed a dependence on load and is larger for the higher loading of 60 mA cm⁻².

This is a significantly high loading and is approaching the current density at which peak power was achieved for Run 2 in Figure 5.10.

5.3.2.2 Effect of anode chamber atmosphere

In order to study the effect of gas atmosphere in the anode chamber on cell performance and the mechanism of carbon oxidation, the anode purge gas was switched from high purity N_2 to a N_2/CO_2 mixture (40 vol% CO_2) following the third V-j measurement under N_2 (Run 3). The voltage rapidly stabilised at 0.79 V under open circuit conditions although it decreased somewhat from 0.89 V in N_2 . A similar OCV response to the switching of anode chamber gases has been observed in chapter 5, and reported elsewhere [12]. For a solid electrolyte DCFC system, this is most probably associated with the higher partial pressure of oxygen generated in the presence of CO_2 near the anode/electrolyte interface. The V-j measurements under the N_2/CO_2 purge gas were taken shortly after voltage stability was achieved (Run 4) and V-j scans for Runs 3 and 4 are compared in Figure 5.13.

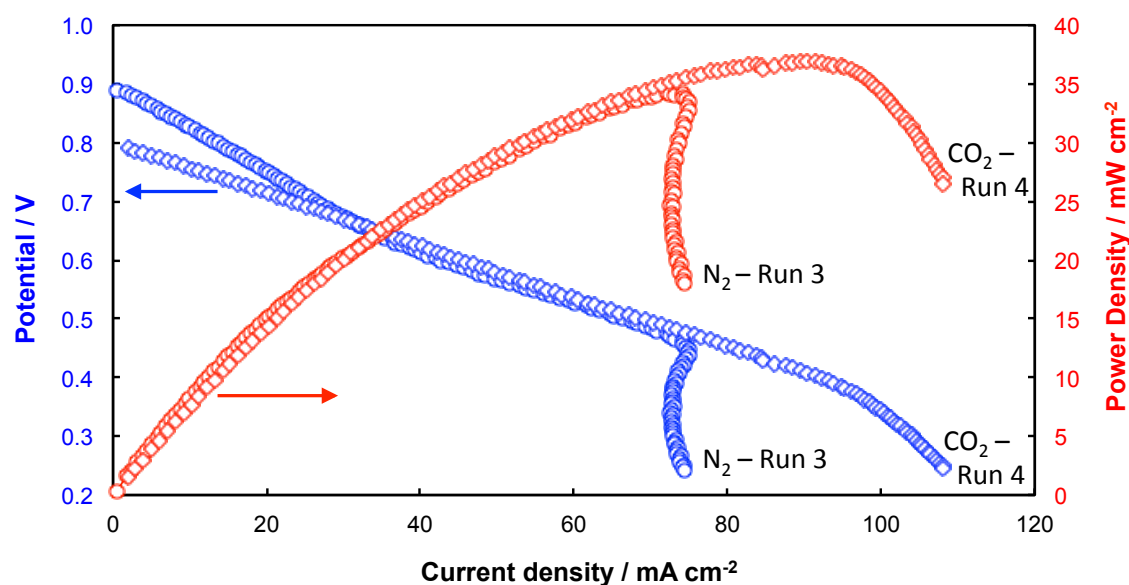


Figure 5.13: Voltage-current density and power density-current density curves of cell #2 at 850 °C for Runs 3 (N_2 anode purge gas), and Run 4 (N_2/CO_2 anode purge gas) at 850 °C.

The V-j curve of Run 4 is almost linear across all current densities up to the point of peak power density at around 90 $mA\ cm^{-2}$ which is substantially higher than that for the previous run (Run 3) in nitrogen atmosphere. Moreover there was no current reversal in N_2/CO_2 mixture as was the case for pure N_2 , which occurred at 75 $mA\ cm^{-2}$.

Following the fourth V-j measurement (Run 4), an EIS scan was taken under the N_2/CO_2 anodic chamber atmosphere at open circuit voltage (6th EIS) and compared with the previous EIS (5th) recorded during N_2 purge also taken at OCV (Figure 5.14). The two spectra showed very similar values of ohmic resistance (R_Ω) of 1.42 and 1.44 $\Omega\text{ cm}^2$ for the fifth and sixth EIS, respectively and the high frequency arcs also had similar magnitude. However, there was a marked decrease in the size of the low frequency arc in the presence of N_2/CO_2 anode chamber atmosphere compared with that of N_2 .

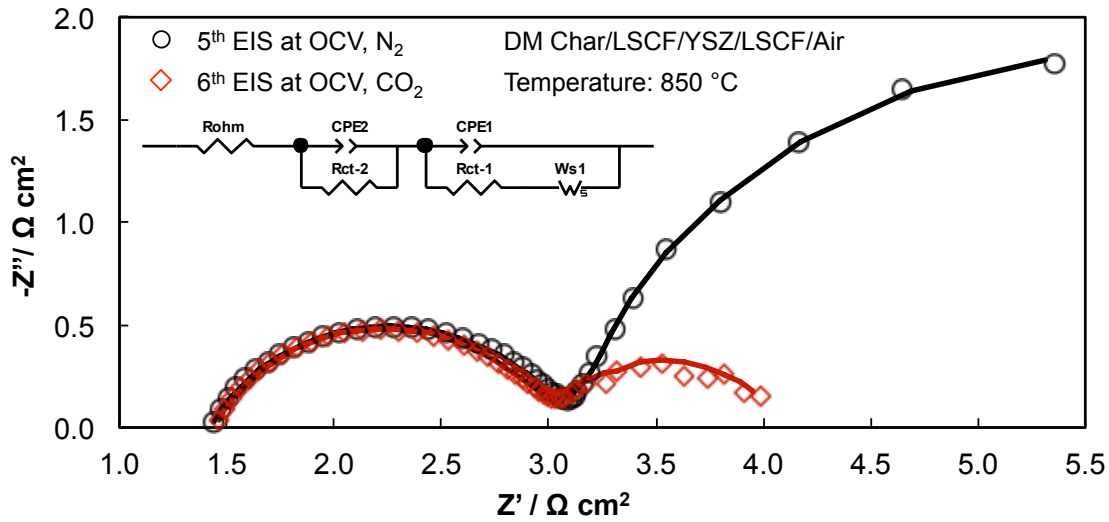


Figure 5.14: Effect of anode purge gas on electrochemical impedance spectra for cell #2 at 850 °C at OCV: 5th EIS (N_2), and 6th EIS (N_2/CO_2). Inset: equivalent circuit diagram used for modelling to calculate impedance data in Table 5.2.

5.4 Discussion

The major observations from the previous section can be summarised as follow:

- Apart from reduction of the anode lattice and some sintering and grain growth of particles leading to less denser microstructure, there was no other structural and micro-structural damage to the anode material. Some contamination of the anode was observed with impurities present in brown coal char.
- The ohmic resistance of the cell (consisting of the electrolyte resistance, the resistance of the anode and cathode materials, contact resistance between anode and solid fuel and resistance of electron conducting pathways in the fuel and to current collection Pt mesh) generally increased with the cell

operating time. However, it was much more conspicuous when the cell was loaded with current for a period of time.

- In high purity N_2 , during V-j scans, power overshoots were observed, which led to current reversal around or after the peak power density was achieved. Thus for controlled voltage scans, the current first increased and then started decreasing rapidly at some point. These were more obvious where V-j scan were possible at higher current densities.
- The power overshoot and current reversal were not observed when the gas atmosphere was changed from high purity N_2 to N_2/CO_2 gas mixture. This is despite the higher current density which was achieved during the V-j scans.
- In high purity N_2 anode chamber atmosphere, in general in the impedance spectra, two arcs were observed for the electrode behaviour at all points of testing, a large low frequency arc and a small high frequency arc. The magnitude of the low frequency arc was affected by the current loading and was dependent on the state of the fuel cell in operation, most probably related to how the fuel contacted the MIEC electrode, and current loading [6].
- The impedance curves in N_2/CO_2 anode chamber atmosphere also consisted of two arcs, however, the magnitude of the low frequency arc was considerably smaller compared with that in high purity N_2 . The high frequency arc was not affected by change in the anode chamber gas atmosphere.

These observations are discussed in detail below.

5.4.1 Anode structure and microstructure

Both the anode microstructure of used and unused anode surfaces looked very similar apart from minor changes discussed below. There was some grain growth and appearance of more cracks in the microstructure of the used anode, leading to less dense and more open microstructure. This may also explain the appearance of YSZ peaks in the X-ray diffraction pattern of the used anode surface as such a microstructure would allow penetration of X-rays to a greater depth. A number of new minor phases were identified in the used anode, $SrSO_4$ was the most prominent resulting from reaction of sulphur in the coal with the LSCF anode. The affinity between Strontium and Sulphur is also highlighted from EDX-mapping given in Figure 5.8(f) and (h), respectively, which shows an overlap of concentrated portions of both elements. Traces of Co_3O_4 phase was also identified, and may be responsible for concentrated regions of Co in EDX-mapping (Figure 5.8(c)). Co,

which is known to precipitate as a metal out of the A-site deficient LSCF structure when subjected to reducing environments in the anode chamber [10,11], may have been present but was below the detection limit of the equipment used. However, these phase were present in very small quantities and apart from reduction of the LSCF lattice as expected, the overall crystal structure was maintained.

5.4.2 Cell ohmic resistance

The ohmic resistance for both cell #1 and cell #2 in general, increased with cell operating time, however, the increase was mostly related to loading of the cell including during collection of EIS data under load. Although there is some change in the microstructure of the anode due to its reduction in fuel cell operating environments, and appearance of minor other phases, its main phase structure is maintained and therefore, cannot be the major cause of this large increase in the cell resistance. A more plausible explanation, for which there is sufficient evidence in the sequence of experiments, is that as the carbon is consumed in the electrochemical Eq. (1.4) and (1.5), there is a loss of conducting pathways.



The current collection from the anode is by both the Pt mesh and the carbon embedded in the perforations of Pt mesh. The consumption of carbon, even on the nano-scale, from anode/current collector interface regions would reduce the number of electron conducting pathways between the anode and current collector. Calculations show that at a current density of 20 mA cm^{-2} , in an area of 8 mm diameter anode, and assuming a fully packed bed of carbon (atomic radii 0.76 Å), around 7 layers of carbon atoms per second would be consumed *via* Eq. (1.4), thus contributing to lost contact if all of the consumed carbon is not replaced by the rest of the carbon bed. Although the electrical conductivity of DM char measured at 850 °C in a packed bed was 2.2 S cm^{-1} , the lateral resistance of a thin carbon embedded in Pt mesh would still be quite high. This indeed was obvious from the results of cell #2 where the improved contact between the anode and the current collector, as well as the use of finer mesh, lead to the observed lower values of R_{Ω} . A finer mesh size would reduce the reliance on carbon for providing conductive pathways and thus reduce the ohmic resistance of the cell. In addition, attaching the mesh to the anode surface with Pt paste further reduced the reliance on carbon conductive pathways by providing more points of contact between the current collector and the anode.

Separate studies on measuring the resistance of electrode and electrolyte materials used here under the fuel cell testing conditions showed minimal change in the material resistivity following initial reduction [4,10]. Furthermore, no such increase in the ohmic resistance is observed when fuel cells constructed with similar mixed ionic/electronic conducting (MIEC) materials are tested with gaseous fuels such as CO or hydrogen [13]. The fact that this behavior has been observed with a solid fuel, adds substantial credence to the hypothesis proposed here.

The direct electrochemical oxidation of solid carbon in solid electrolyte DCFC systems is supported by research involving non-porous anodes [14] as well as bare electrolyte arrangements [15]. Detailed mechanisms for carbon oxidation have also been proposed from studies involving carbon deposition [16]. If carbon consumption is indeed responsible for the observed increase in cell ohmic resistance, then the magnitude of this increase should relate somewhat to the quantity of carbon consumed, or current drawn from the cell. In Figure 5.2, observing the progressive increase in R_{Ω} for successive EIS spectra as a function of current drawn, the smallest increase in R_{Ω} ($0.17 \Omega \text{ cm}^2$ between the first and second EIS) occurred during the 2 min voltage stabilisation period at 10 mA cm^{-2} prior to the commencement of the second EIS recording. The next $0.20 \Omega \text{ cm}^2$ increase in R_{Ω} was between the second and third EIS following cell loading at 10 mA cm^{-2} during second EIS (8 min) and 2 min voltage stabilisation period before the third EIS at 20 mA cm^{-2} . The increase in R_{Ω} of $0.46 \Omega \text{ cm}^2$ between the third and fourth EIS followed the highest cell loading at 20 mA cm^{-2} during third EIS and V-j scan 'Run 3'. A similar trend was observed for cell #2 in Figure 5.11, which covered an interval of comparable cell operation. The largest increase in the ohmic resistance of $3.3 \Omega \text{ cm}^2$ for cell #1 occurred between the fourth and fifth EIS (Figure 5.3) following the constant current (10 mA cm^{-2}) passage over a period of 1 hr 47 min (CP1 measurement), in addition to a V-j scan (Run 3). Thus increase in the ohmic resistance is clearly associated with loss of contacts between carbon, current collector and the anode as carbon is consumed near the anode / carbon interface.

The increase in R_{Ω} of $1.11 \Omega \text{ cm}^2$ between the fifth and sixth EIS can be attributed to carbon consumption during the 2 min voltage stabilisation period under a load of 20 mA cm^{-2} . In this instance, the increase in R_{Ω} is relatively large considering only two minutes of loading had taken place prior to the sixth EIS measurement. However, with the continued removal of carbon from reactive sites leaving fewer and fewer

conductive pathways for electron transfer, one could expect an acceleration in observed increase in ohmic resistance as the remaining carbon is consumed.

The increase in the ohmic resistance of cell #1 between the start of the first and second CP measurements is partially (in addition to increase in the polarisation resistance of the cell) responsible for the reduction in the observed initial cell voltage.

5.4.3 V-j measurements, current reversal and power overshoots

The high power densities achieved in Run 1 of cell #1 (Figure 5.4) is a reflection of the availability of more reaction sites (carbon particles in direct contact with the anode) at start of the cell loading experiments. As the carbon is consumed, there is a decrease in the reaction sites resulting in lower power densities in the subsequent runs as observed in Run 2 and Run 3, and reflected in the increasing value of R_Ω as discussed in Section 5.4.2. The same trend is observed for cell #2 (Figure 5.10), with earlier V-j measurements achieving higher power and current densities than subsequent runs. Interestingly, the peak power density for Run 1 of cell #1 is similar to that of Run 3 of cell #2, at 30 and 34 mW cm⁻², respectively. This is due to the use of finer mesh and better contact between the mesh and anode surface resulting in lower overall cell resistance.

As detailed in Sections 5.3.1.1 and 5.3.2.1, the V-j and P-j curves of both cells experienced current reversal at some stage around or after achieving peak power. The observed behaviour is not new for fuel cell systems [17-20] and often is described as ‘power overshoot’. In the context of solid electrolyte DCFC systems this behaviour has been related to the accumulation of CO at the anode [21] followed by fuel starvation at sufficiently high current densities. During the initial stages of the V-j scan, the cell is likely running predominantly off solid carbon *via* Eq. (1.4) and (1.5), producing CO and CO₂ in the gas phase. Additional CO may be formed *via* Eq. (1.7) given the close proximity of the anode and solid carbon, with the kinetics of this reaction dependant on the reactivity of the carbon fuel at the operating temperature of the cell. It is highly likely that over the course of the V-j scan, the oxidation of CO, formed *in-situ*, is contributing to the current generation in the cell, *via* Eq. (1.6), in parallel with the direct consumption of solid carbon.



These two reactions can proceed in parallel up to certain cell loading. However, at higher forced cell loading, CO is consumed faster than it can be generated and

supplied to the anode. Thus higher currents cannot be sustained by gaseous CO formed *in-situ* and direct reaction of solid carbon in contact with the anode surface. Once the CO is depleted, a limiting current type situation develops for this Eq. (1.6) leading to a drop in current for subsequent voltages under a potentiodynamic scan.

The current reversal for Run 1 of cell #1 is more prominent than any other V-j measurement. This is most likely due to Run 1 achieving high current densities than the following V-j scans, thus demanding more CO to sustain these high current densities. Therefore a more significant drop in current density (~13% from the peak value), and a larger power overshoot was observed for Run 1. Run 2 and Run 3 showed a comparatively minor current reversal (~3% drop from peak value). It therefore appears that reactive gas phase species CO generated during cell loading contributes to power overshoots. The current reversal for cell #1 is less conspicuous than that of cell #2 and this is again most likely due to the lower current densities that could be achieved by cell #1 compared with cell #2.

The initial drop in voltage, that was observed during constant current passage as a function of time (Figure 5.1(a), CP1 and CP2), can be attributed to the rapid consumption of carbon near the anode / fuel interface and/or residual gaseous reactive species (CO) formed by the reaction of residual oxygen in N₂ with carbon in the anode chamber. Within about 30 seconds the system had reached equilibrium and settled to a constant voltage decay which then remained steady over the remainder period of the data recording. This almost linear portion of the decay in voltage is resulting from an increase in the observed ohmic and polarisation resistance of the cell with time and as discussed previously related to consumption of carbon during cell loading. It is not obvious why the decay rate for the second CP measurement (CP2) is lower, although the first CP measurement (CP1) showed some indication of a slight tail of reduced decay rate toward the end of the loading, which is somewhat similar to that for CP2.

5.4.4 Analysis of electrode behaviour with electrochemical impedance spectroscopy

Two arcs observed in the impedance spectra at various stages of cell testing can be attributed to the anodic cell reactions as the contribution of cathode is relatively small even at very high current densities well above those used in this study [6]. In high purity N₂ atmosphere in the anode chamber, the large low frequency arc is attributed

to diffusion related processes and the high frequency arc to charge transfer processes [6,22,23]. The observed decrease in the magnitude of the low frequency arc under load from that under OCV, has been discussed previously in literature and it has been attributed to the generation of the gaseous reactive species (CO) at the anode *via* Eq. (1.7), that becomes available for the anodic reaction during cell loading [6,24].



However, at higher current densities, the fuel starvation can occur, leading to an increase in the size of the low frequency arc. This is reflected in the large low frequency arc (cell #2) for the third EIS than that of the second EIS (Figure 5.12). Here the third EIS was obtained under a load approaching the limiting current of 60 mA cm^{-2} as obvious in Run 2 (Figure 5.10). This clearly reflects the fuel starvation experienced by the cell at such high loadings with Warburg type diffusion controlled process discussed in previous publications [6,11], as well as in Chapter 4.

The decrease in the high frequency electrode arc on loading is also caused by the availability of higher number of reaction sites to gaseous CO formed *via* Eq. (1.5) as it can diffuse through the electrode pore structure compared with solid carbon which can react only at the anode / fuel interface.

Growth of both high and low frequency arcs with cell operating time was observed and related to loss of contacts between anode and fuel with time as the fuel is consumed during loading of the cell as discussed in Section 5.4.2 for ohmic resistance.

5.4.5 Effect of gas atmosphere in the anode chamber

The higher concentration of CO_2 in the anode chamber resulted in increase in the partial pressure of oxygen at the anode/electrolyte interface, with no change to oxygen partial pressure at the cathode, thus producing a slight drop in the open circuit voltage (Figure 5.13). No current reversal was observed with N_2/CO_2 as the purge gas in the anode chamber as was the case with high purity N_2 (Figure 5.13). It is obvious that the externally supplied CO_2 and subsequent higher concentration of CO available to the anode *via* Eq. (1.7), is the most likely reason for the expansion of the V-j and P-j curves to higher current densities (Run 4), and consequently, higher power densities. An increase in concentration of gas-phase reactive species at the anode is synonymous with a reduction in Warburg impedance, as observed in

Chapter 4, previous publications [6,11], and here in the sixth EIS spectra over that of the fifth spectra (Table 5.2), manifesting in the small low frequency arc in Figure 5.14.

Table 5.2: EIS model parameters calculated from the impedance data in Figure 5.14. The values are in $\Omega \text{ cm}^2$. The total cell impedance from model has been compared with that from the V-j data in Figure 5.13. The cell resistance was calculated from the linear portion of V-j curves. In the case of C/N₂, the first linear segment closer to OCV has been considered. The values in bracket are the per cent errors given by the model circuit fitted to the experimental impedance data.

Fuel	R_{Ω}	$R_{\text{ct-2}}$	$R_{\text{ct-1}}$	W_{s1}	Total	From V-j
C-N ₂ /CO ₂	1.42	1.56 (± 1.0)	1.10 (± 6)	0.01	4.09	4.00
C-N ₂	1.40	1.66 (± 1.0)	0.20 (± 10)	5.17 (± 9)	8.43	7.80

* R_{Ω} in the table is the value at the intersection of high frequency arc on the real axis.

Normally for a mixed ionic electronic conducting electrode, oxygen-ions would move from the electrolyte into electrode and react with carbon at the anode/fuel interface. However, in this study, despite LSCF being a good mixed ionic electronic conductor, there is obviously less resistance associated with the diffusion of CO to the anode/electrolyte interface than for the oxygen ions to migrate to the anode/carbon interface. Thus for N₂/CO₂ as the anode chamber purge gas where formation of CO occurs *via* Eq. (1.7), shifting of the anode reaction from anode/carbon interface to anode/electrolyte interface should have resulted in a decrease in R_{Ω} to the extent of the anode's contribution to ohmic resistance [6,11]. However, this phenomenon may have offset any expected increase in the ohmic resistance associated with carbon consumption during Run 3, under N₂, resulting in similar values of R_{Ω} observed in Figure 5.14 for 5th and 6th EIS spectra. With similar values of R_{Ω} and $R_{\text{ct-2}}$ for the fifth and sixth EIS, Figure 5.14 illustrates that the overwhelming differentiator between Runs 3 and 4 for cell #2 is in the form of additional gaseous species present during Run 4, nominally CO generated by the Boudouard gasification (Eq. 1.7) otherwise as per cell #1, an increase in R_{Ω} would have been expected.

In order to further analyse the impedance data obtained in nitrogen and CO₂ atmospheres in the anodic chamber, the data were modelled by employing a model equivalent circuit as shown in the inset of Figure 5.14. This representative equivalent circuit is appropriate to describe all the impedance data presented in this manuscript (Figures 5.2, 5.3, 5.11, 5.12, 5.14) with contribution of individual elements varying depending on the cell operating conditions. The solid lines through the data points represented by the symbols are the fitted curves as per the model. The high

frequency arcs for both the fifth and sixth EIS spectra are of similar size with R_{ct-2} components of 1.66 and 1.56 $\Omega \text{ cm}^2$, respectively, determined from modelling and also presented in Table 5.2. The low frequency arc in the sixth EIS, however, is much smaller compared with the fifth EIS, with a Warburg impedance component of only 0.01 $\Omega \text{ cm}^2$ under N_2/CO_2 , down from 5.17 $\Omega \text{ cm}^2$ under N_2 clearly indicating that the low frequency arc is related to diffusion controlled processes which are considerably more pronounced for the direct reaction of the solid fuel.

5.5 Conclusions

A demineralised and devolatilised coal, from Morwell mine of the Latrobe Valley, Victoria, was tested in solid oxide electrolyte supported direct carbon fuel cells. The cells consisted of 8 mol% yttria-stabilised zirconia (YSZ) electrolyte and Lanthanum Strontium Cobalt Ferrite (LSCF) electrodes. Potentiodynamic V-j scans and electrochemical impedance spectroscopy (EIS) measurements were employed to investigate the effect of cell loading and holding time at 850 °C. An increase in the ohmic resistance of the fuel cell was associated with the consumption of carbon at the fuel/anode interface on loading the cell. The largest increase in cell ohmic resistance occurred following significant carbon consumption by an extended chronopotentiometric operation. It is believed that the consumption of solid carbon from anode/Pt current collector interface causes a loss in additional electron conducting pathways provided by the carbon between the anode and the current collector. The post-mortem analysis of anode by SEM and XRD revealed reduction in the density with noticeable growth of smaller LSCF grains and the deposition of ash particles onto the anode surface. XRD analysis of the used anode indicated reduction of the LSCF lattice as expected in the reducing environments of the anode chamber. The crystal structure of the anode was maintained while formation of some minor impurity phases such as SrSO_4 detected. In voltage-current (V-j) scans, taken at a 5 mV s^{-1} sweep rate, in high purity N_2 power overshoots were observed, which led to current reversal around or after the peak power density was achieved. The current reversal was more obvious where V-j scan were possible at higher current densities. The power overshoot and current reversal were not observed when the gas atmosphere was changed from high purity N_2 to N_2/CO_2 gas mixture. In the impedance spectra, two arcs were observed for the electrode behaviour at all points of testing. The contribution from the low frequency arc dominated the total electrode resistance in an inert atmosphere, which was affected by the current loading and the state of the fuel cell in operation and related to how carbon fuel was available near the anode. The introduction of CO_2 into the anode chamber resulted in a significant reduction in the magnitude of the low frequency arc recorded in EIS spectra. Modelling of the EIS spectra revealed substantial contribution from diffusion limited processes to the electrode resistance in high purity anode chamber atmosphere. However, this decreased substantially in N_2/CO_2 mixture due to the availability of higher concentrations of CO at the fuel/anode/electrolyte interface *via* Boudouard gasification of the carbon fuel leading to improved cell performance.

References

1. Badwal SPS, Giddey SS, Munnings C, Bhatt AI, Hollenkamp T. Emerging electrochemical energy conversion and storage technologies. *Frontiers in Chemistry*. **2014**;2.
2. Munnings C, Giddey S, Badwal S. Direct carbon fuel cells: an ultra-low emission technology for power generation. *CORNERSTONE MAG*. **2014**;2.
3. Trembly JP, Marquez AI, Ohn TR, Bayless DJ. Effects of coal syngas and H₂S on the performance of solid oxide fuel cells: Single-cell tests. *J Power Sources*. **2006**;158:263-73.
4. Badwal SPS. Stability of solid oxide fuel cell components. *Solid State Ionics*. **2001**;143:39-46.
5. Jewulski J, Skrzypkiewicz M, Struzik M, Lubarska-Radziejewska I. Lignite as a fuel for direct carbon fuel cell system. *Int J Hydrogen Energy*.
6. Giddey S, Kulkarni A, Munnings C, Badwal SPS. Performance evaluation of a tubular direct carbon fuel cell operating in a packed bed of carbon. *Energy*. **2014**;68:538-47.
7. Esquirol A, Brandon NP, Kilner JA, Mogensen M. Electrochemical Characterization of La_{0.6}Sr_{0.4}Co_{0.2}Fe_{0.8}O₃ Cathodes for Intermediate-Temperature SOFCs. *J Electrochem Soc*. **2004**;151:A1847-A55.
8. Kulkarni A, Giddey S, Badwal SPS. Electrochemical performance of ceria-gadolinia electrolyte based direct carbon fuel cells. *Solid State Ionics*. **2011**;194:46-52.
9. Li C-Z. Chapter 1 - Introduction. In: Chun-Zhu L, editor. *Advances in the Science of Victorian Brown Coal*. Amsterdam: Elsevier Science; **2004**. p. 1-10.
10. Kulkarni A, Ciacchi FT, Giddey S, Munnings C, Badwal SPS, Kimpton JA, et al. Mixed ionic electronic conducting perovskite anode for direct carbon fuel cells. *Int J Hydrogen Energy*. **2012**;37:19092-102.
11. Munnings C, Kulkarni A, Giddey S, Badwal SPS. Biomass to power conversion in a direct carbon fuel cell. *Int J Hydrogen Energy*. **2014**;39:12377-85.
12. Jiang C, Irvine JTS. Catalysis and oxidation of carbon in a hybrid direct carbon fuel cell. *J Power Sources*. **2011**;196:7318-22.
13. Kulkarni A, Giddey S, Badwal SPS, Paul G. Electrochemical performance of direct carbon fuel cells with titanate anodes. *Electrochim Acta*. **2014**;121:34-43.

14. Nürnberger S, Bußar R, Desclaux P, Franke B, Rzepka M, Stimming U. Direct carbon conversion in a SOFC-system with a non-porous anode. *Energy & Environmental Science*. **2010**;3:150-3.
15. Werhahn MG, Schneider O, Stimming U. Thin Film Gadolinia Doped Ceria (GDC) Anode for Direct Conversion of Carbon Black Particles in a Single Planar SOFC. *ECS Trans*. **2013**;50:73-87.
16. Li C, Shi Y, Cai N. Mechanism for carbon direct electrochemical reactions in a solid oxide electrolyte direct carbon fuel cell. *J Power Sources*. **2011**;196:754-63.
17. Nien P-C, Lee C-Y, Ho K-C, Adav SS, Liu L, Wang A, et al. Power overshoot in two-chambered microbial fuel cell (MFC). *Bioresour Technol*. **2011**;102:4742-6.
18. Cheng S, Logan BE. Increasing power generation for scaling up single-chamber air cathode microbial fuel cells. *Bioresour Technol*. **2011**;102:4468-73.
19. Ieropoulos I, Winfield J, Greenman J. Effects of flow-rate, inoculum and time on the internal resistance of microbial fuel cells. *Bioresour Technol*. **2010**;101:3520-5.
20. Jia L, Tian Y, Liu Q, Xia C, Yu J, Wang Z, et al. A direct carbon fuel cell with (molten carbonate)/(doped ceria) composite electrolyte. *J Power Sources*. **2010**;195:5581-6.
21. Li C, Shi Y, Cai N. Effect of contact type between anode and carbonaceous fuels on direct carbon fuel cell reaction characteristics. *J Power Sources*. **2011**;196:4588-93.
22. Jain SL, Barry Lakeman J, Pointon KD, Marshall R, Irvine JTS. Electrochemical performance of a hybrid direct carbon fuel cell powered by pyrolysed MDF. *Energy & Environmental Science*. **2009**;2:687-93.
23. Liu R, Zhao C, Li J, Zeng F, Wang S, Wen T, et al. A novel direct carbon fuel cell by approach of tubular solid oxide fuel cells. *J Power Sources*. **2010**;195:480-2.
24. Li C, Shi Y, Cai N. Performance improvement of direct carbon fuel cell by introducing catalytic gasification process. *J Power Sources*. **2010**;195:4660-6.

Declaration for thesis chapter 6

Declaration by candidate

In the case of Chapter 6, the nature and extent of my contribution to the work was the following:

Nature of contribution	Extent of contribution (%)
Experimental work and analysis, writing	100

The following people contributed to the work. If persons are students at Monash University, the extent of their contribution in percentage terms must be stated:

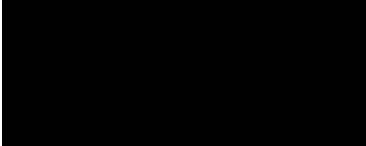
Name	Nature of contribution	Extent of contribution (%)
Dr Sukhvinder Badwal	Advisory role	-
Dr Sarbjit Giddey	Advisory role	-
Assoc Prof Bradley Ladewig	Advisory role	-
Prof Sankar Bhattacharya	Advisory role	-
Dr Aniruddha Kulkarni	Advisory role	-

The undersigned hereby certify that the above declaration correctly reflects the nature and extent of the candidate's and co-authors' contributions to this work.

Candidate's
Signature

	Date 27/02/2015
---	------------------------

Main
Supervisor's
Signature

	Date 27/02/2015
---	------------------------

6

Direct carbon fuel cell operation on brown coal with a Ni-GDC/YSZ anode

Chapter objective

In the previous study, demineralised brown coal char was used as a fuel for extended operability studies in a DCFC. While the anode appeared to show reasonable stability under the operating conditions, there was a notable deterioration in cell voltage during periods of sustained loading. *Ex-situ* analysis of the anode revealed evidence of mild anode sintering and ash deposition as a result of DCFC operation. In addition, cell loading during electrochemical impedance spectroscopy (EIS) was found to influence the high and low frequency arcs of the spectra.

In studies included in this thesis, the contribution of Boudouard gasification to cell performance has been clearly demonstrated, and enhanced by the presence of catalytic species in the carbon fuel as well as by the introduction of CO₂ into the anode chamber. However, the influence inorganic constituents in coal, and anodic atmosphere, on the extended operability of a DCFC has not been evaluated.

In the present study, an alternative anode arrangement is trialled for its stability in the presence of Victorian brown coal during extended operation under different cell loadings, atmospheres, and fuel types. The influence of the inorganic content in coal as well as the introduction of CO₂ into the anode chamber on long-term cell operability is assessed. Further to this, a detailed examination of loading on EIS spectra is performed.

Direct carbon fuel cell operation on brown coal with a Ni-GDC/YSZ anode

Abstract

Char products derived from Morwell coal from the Latrobe Valley, Australia, were tested in a solid oxide electrolyte DCFC at 850 °C. An electrolyte supported button cell was used with a Ni-GDC (gadolinia doped ceria) anode with 15 wt% YSZ (yttria stabilised zirconia) loading for thermal stability and good adhesion with the YSZ electrolyte. The cell performed well under N₂ when using demineralised Morwell char as the fuel, generating reproducible V-j curves and sustaining chronopotentiometric loading of 20 mA cm⁻² for 2 hours with no appreciable signs of voltage decay. Operation with raw Morwell char initially achieved comparable peak power densities to that of the demineralised char, at 33.3 and 33.1 mW cm⁻², respectively. However, subsequent runs involving raw Morwell char exhibited decreasing power densities and signs of diffusion-limitations at higher current densities. Ash deposition at the anode is proposed as a possible differentiator of extended cell operability between the two fuels. In addition to fuel-based performance of the DCFC, the response of the anode and system as a whole was closely monitored using electrochemical impedance spectroscopy. Introduction of CO₂ into the anode chamber instead of N₂ enhanced cell performance and longevity of cell operation under sustained loading.

6.1 Introduction

Due to the step change in electricity generation efficiency promised by direct carbon fuel cell (DCFC) technology, DCFCs are gaining increasing interest with research efforts in this field increasing in recent years [1-4]. Current efforts are broadly focussed on material selection for critical fuel cell components, DCFC system design, and understanding reaction mechanisms for surrounding carbon conversion [1,4]. For solid electrolyte DCFCs, solid carbon conversion necessarily occurs at the anode surface. Mixed ionic electronic conductor (MIEC) anodes allow for extension of the reaction zone away from the anode/electrolyte interface [5]. One group of materials that display such properties under DCFC operating conditions, of reducing atmospheres and high temperatures, are ceria-based oxides [6-8]. Ceria-based materials, such as gadolinium-doped ceria (GDC) are attractive anode materials for DCFCs as they also catalyse the electro-oxidation of various fuels [9-12]. Ceria

possesses a reasonable ionic conductivity in reducing environments, however, the electronic conductivity is lower with a total conductivity of about 1 S cm^{-1} in reducing atmospheres (H_2 or CO) at 800°C [13]. The electronic conductivity of ceria can be improved by addition of oxides such as NiO , which after reduction forms a Ni particle network enabling current collection and conduction.

Despite the favourable properties of ceria-based oxides for direct electrochemical carbon conversion, these materials have not been used extensively or as anodes in SOFCs and even to lesser extent in direct contact DCFC systems [14-16]. One of the issues with ceria-based materials is the reactivity of ceria with YSZ at traditional anode sintering temperatures (1400°C). Another reason is the mismatch in thermal expansion coefficient between YSZ electrolyte and GDC. This can result in poor adhesion and cracking of the electrode during high temperature treatment. [17,18].

The present study investigates the performance of DCFCs with YSZ electrolyte-supported button cells with a Ni-GDC/YSZ anode material. To improve the adhesion between anode and YSZ electrolyte, 15 wt % YSZ powder was added to the anode as an 'anchoring' phase. Also the sintering temperature was kept low at 1050°C to avoid possible solid state reaction between YSZ and GDC which is known to occur above about 1200°C [19]. The DCFC was operated on two chars produced from brown coal to assess the performance of DCFCs with Ni-GDC/YSZ anode material using a 'real world' fuel.

6.2 Experimental

The two carbon fuels used in this study were chars derived from coal from the Morwell mine, Latrobe Valley, Victoria in Australia. A detailed description of fuel preparation is provided in Chapter 3. The chars of raw, and demineralised Morwell coal, will be herein referred to as 'RM', and 'DM', respectively. Characterisation and analysis of RM and DM is provided in Chapter 4.

Electrolyte-supported button cells were fabricated by employing the procedure as outlined in Chapter 3 for YSZ electrolyte button cells with LSCF electrodes. The cell test fixture including the fuel supply arrangement to the anode has been described in detail in Chapter 3 also and is represented by Figure 3.3(b). For each carbon fuel a different button cell was used and carbon loading was typically 150 mg.

6.2.1 Anode preparation and fuel cell conditioning

For anode preparation, 0.75 g of YSZ powder (8 mol% Y_2O_3 , Tosoh Corporation, Japan) was added to 4.25 g of nickel gadolinia doped ceria (Ni-GDC, Fuel Cell Materials Inc., OH, USA) of composition 60 wt% NiO, 40 wt% $\text{Gd}_{0.1}\text{Ce}_{0.9}\text{O}_{1.95}$. The powder mixture was milled in 50 ml deionised water with 10 mm diameter zirconia balls as a grinding media for 2 hrs and dried overnight to produce a Ni-GDC/YSZ anode powder of 15 wt% YSZ + 85 wt% Ni-GDC composition. A terpinol-based ink vehicle (Fuel Cell Materials Inc., OH, USA) was added to the powder in a 40:60 wt% (ink vehicle : powder) and ball milled for a further 2 hrs to produce the fuel electrode (anode) ink. The electrode ink was applied to one entire face of the electrolyte disc *via* brush coating and dried in a vacuum oven overnight at 60 °C. The anode-coated button cell was heat treated in air at 1050 °C for 2 hrs with a heating and a cooling rate of 150 °C hr^{-1} . Following this preliminary heat treatment and a return to room temperature, the electrolyte discs coated with anode were then treated at 850 °C for two hours in 5 vol% H_2 (balance N_2) atmosphere with a heating and cooling rate of 150 °C hr^{-1} . LSCF was applied to the air electrode side of the disc *via* screen-printing as per Chapter 3, Section 3.3.2. The cell was left to sit in a vacuum oven overnight at 60 °C to allow the air electrode to dry before cell assembly.

Once the borosilicate glass seal was formed and a temperature of 850 °C achieved (Chapter 3, Section 3.5), air was introduced into the cathode chamber. Anode chamber purge gas was then switched from N_2 to high purity H_2 (BOC, 99.98%) for 20 min to ensure NiO in the anode has reduced to Ni [20] during which time the ohmic resistance of the cell was monitored using Electrochemical Impedance Spectroscopy (EIS) measurements. After anode reduction, the anode chamber purge gas was switched back to high purity N_2 and the cell was left in this state for 17 hrs before commencing cell testing the following day.

6.2.2 Fuel cell operation and diagnostics

Three identically fabricated cells were tested in this study. One cell was tested using the DM char and the other two were tested using the RM char. All electrochemical measurements were conducted at an operating temperature of 850 °C and involved a series of measurements under constant current chronopotentiometric (CP) loading, EIS measurements in open circuit condition and under load, and potentiodynamic voltage-current (V-j) scans, as per Chapter 3, Section 3.5.

Throughout operation, care was taken to ensure that the cell was kept above 0.4 V during intervals of loading to avoid electrochemical re-oxidation of Ni at sufficiently high overpotentials [21]. All experiments were conducted under flowing air through the cathode chamber and flowing N₂ (BOC, 99.999% purity, 40 ml min⁻¹) on the anode chamber side. For one set of experiments involving RM char, the anode chamber purge gas was switched from N₂ to a N₂/CO₂ mixture (BOC, Cellamix, 40 vol% CO₂ in N₂, flow rate: 40 ml min⁻¹).

Select EIS data was modelled using ZViewTM software (Scribner Associates, Inc., USA) using equivalent circuits similar to those described in previous publications [5,14,22].

6.3 Results and interpretation

The performance of the fuel cell was assessed using various electrochemical techniques. Potentiodynamic voltage-current (V-j) scans were employed at various intervals throughout cell operation to gauge the cell condition in terms of peak power densities as well as any diffusion limitations at higher current densities. Chronopotentiometric (CP) scans were conducted to assess cell stability under sustained loading, as well as providing a means of exacting considerable carbon consumption. To gain insight into system behaviour and determine the contribution of various cell components to the total impedance, Electrochemical Impedance Spectroscopy (EIS) measurements were made while the cell was under load, and also during continuous cell operation under load. In addition numerous EIS scans under open circuit conditions were taken throughout the experiments as an effective means of monitoring the progress of cell ohmic and polarisation resistance as a function of time and experiment progression.

6.3.1 Demineralised Morwell char

Figure 6.1(a) shows six EIS spectra, consisting of one initial EIS taken under open circuit, followed by four consecutive EIS measurements taken under a load of 10, 20, 30, and 40 mA cm⁻², respectively, and finally another EIS taken under open circuit. The spectra have been normalised by horizontal translation in the real axis such that all spectra intercept at the origin to clearly show the effect of current loading on electrode arcs. All six spectra show three distinct regions, or arcs.

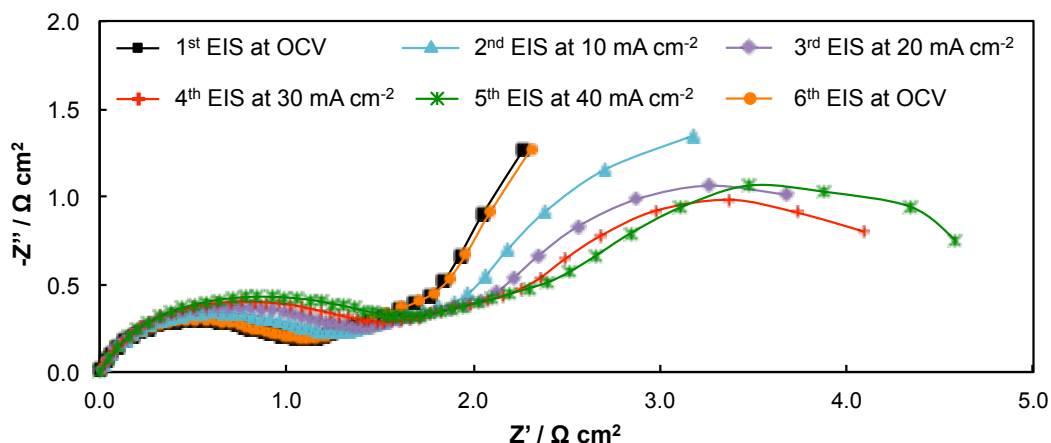


Figure 6.1(a): Impedance spectra for DM under open circuit and under loadings of 10, 20, 30, and 40 mA cm⁻² at 850 °C. Impedance spectra translated in the real axis so that all spectra intercept the graph origin.

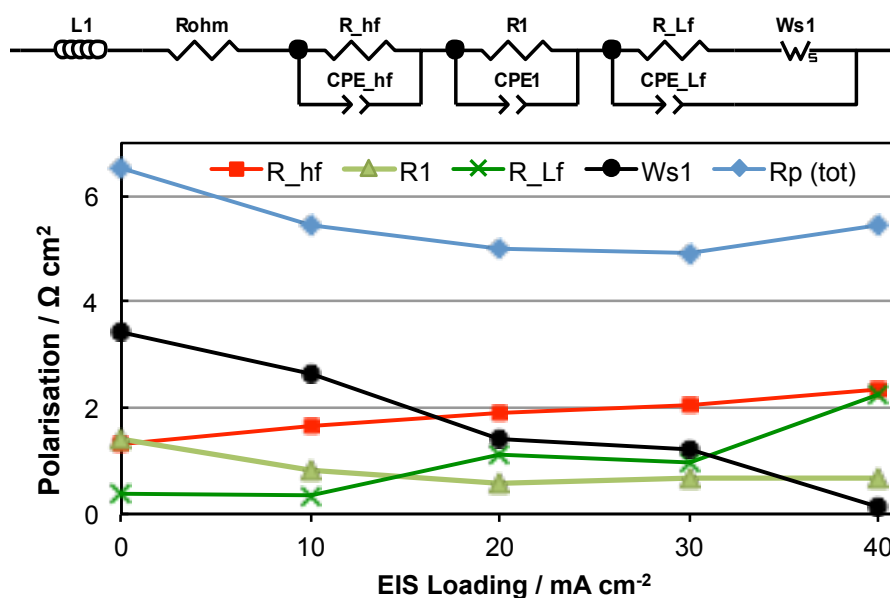


Figure 6.1(b): EIS model fit impedance values as a function of loading for the high frequency arc (R_{hf}), intermediate frequency arc ($R1$), low frequency arc (R_{Lf} and $Ws1$), and sum of these values (R_p (tot)), with the ZViewTM model's equivalent circuit diagram included above plot.

The high frequency arc spans the frequency range of ~ 20 kHz - 50 Hz. The intermediate frequency arc produces a flatter section of the spectra and generally exists in the frequency range of 50 Hz – ~ 500 mHz. The low frequency arc is the largest of the three arcs present and occupies the ~ 500 – 50 mHz range. The size of the high, intermediate, and low frequency arcs each show a dependence on the magnitude of the current loading, most notably for the high frequency arcs.

The high frequency arc is the smallest in magnitude for the EIS spectra taken under open circuit, and increases in size with increasing loading. The trend is reversed for the low frequency component of the spectra, with the arc size decreasing and the spectra exhibiting a closure of the low frequency arc as the current loading is increased. Shortly after completion of the loaded EIS measurements, an EIS was taken under open circuit, which overlapped closely the initial EIS spectrum across the entire frequency range, recorded under open circuit. Figure 6.1(b) shows the trends of model fit as well as the equivalent circuit used for fitting the data, which is based on previous proposed models [5,14,22,23]. In the model, the low frequency arc is modelled using two resistive components in series, charge transfer resistance (R_{Lf}) and a Warburg component ($Ws1$). The high and intermediate frequency arcs are modelled using a constant phase element and charge transfer resistance component in parallel. The total polarisation resistance ($R_p(tot)$) is also included in Figure 6.1(b) as the sum of electrode arc impedances (i.e. $R_{hf} + R_1 + R_{Lf} + Ws1$).

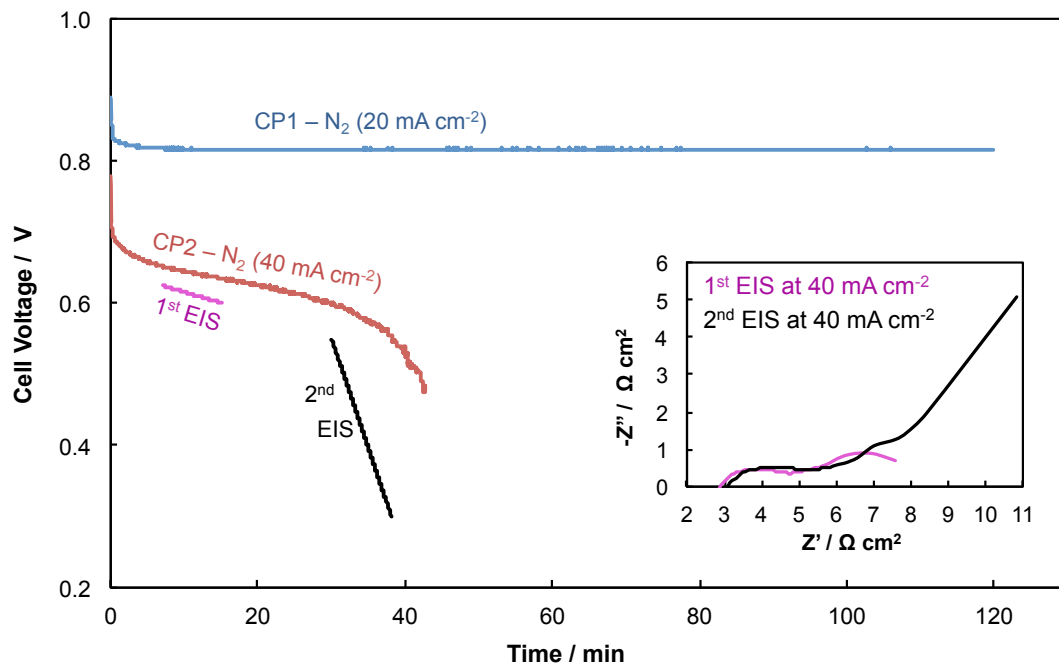


Figure 6.2: Chronopotentiometric loadings of 20 mA cm⁻² (CP1) and 40 mA cm⁻² (CP2) for DM. Inset: EIS spectra taken after 7 min and 30 min of sustained loading at 40 mA cm⁻² for first and second EIS, respectively, with voltage ranges of scans indicated on main axis.

Following the EIS measurements, the cell was held under a load of 20 mA cm⁻² for a period of 2 hrs, and voltage recorded as a function of time (CP1). CP1 along with a subsequent CP loading at 40 mA cm⁻² (CP2) are given in Figure 6.2. Apart from an initial drop in voltage for CP1 of 63 mV in the first minute of loading, the voltage remained steady at 0.82 V for the duration of the loading with no appreciable voltage

decay. The cell was then allowed to recover before loading at 40 mA cm^{-2} for CP2, which experienced a drop in voltage of 94 mV in the first minute of loading. Following this initial voltage drop, the cell experienced a more stable voltage decay of 131 mV hr^{-1} over a period of roughly 20 min, before experiencing acceleration in voltage decay and eventual termination of the run at 0.48 V after 43 minutes of loading. In order to gain insight into the cause of cell voltage degradation under the higher loading of CP2, during different modes of voltage decay, two additional EIS spectra, separate to those presented in Figure 6.1(a), were recorded during this loading and are shown as inset in Figure 6.2.

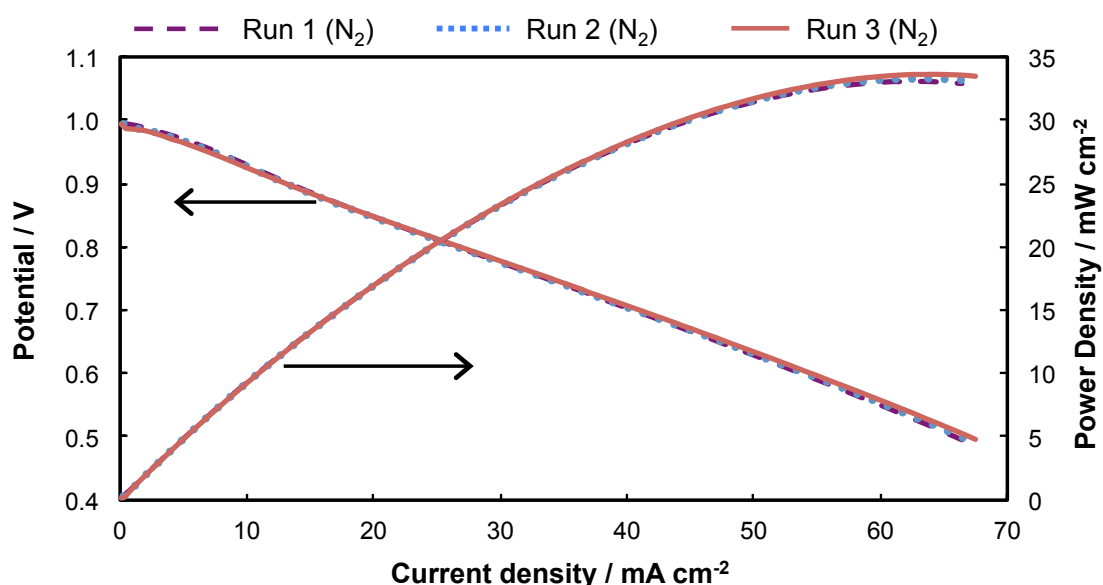


Figure 6.3: Voltage-current density-power density curves for DM under N_2 at 850°C .

The EIS measurements take about 8 minutes to complete over the frequency range of 500 kHz – 50 mHz. The first EIS measurements commenced after 7 min of loading during the region of linear voltage decay, starting at 0.625 V and finishing at 0.600 V. The cell remained under the sustained load with a second EIS measurement commenced after 30 min of loading, starting at 0.550 V and included the accelerated voltage decay region to finish at 0.300 V. The time periods of impedance spectra recording are shown as straight lines connecting initial and final voltages of EIS measurements. The first EIS resembles the EIS at the same loading taken previously, included in Figure 6.1(a), with three arcs including a low frequency arc that is closing to approach a total polarisation resistance of $\sim 5.5 \Omega \text{ cm}^2$. The second EIS includes marginally larger high and intermediate frequency arcs, as well as the beginning of a low frequency arc before the onset of a possibly severe diffusion-limited process dominating at the low frequency region of the spectra.

As mentioned, V-j scans were also conducted at various stages throughout testing to monitor the condition of the cell, with three such scans included in Figure 6.3. Considerable loading of the cell had occurred between each of the three V-j runs with Run 1 taken prior to the EIS spectra given in Figure 6.1(a). Run 2 was taken following the EIS measurements of Figure 6.1(a) but prior to the CP loadings of Figure 6.2, and Run 3 taken after the second CP measurement. The consistent peak power densities of 33.1, 33.3, and 33.6 mW cm^{-2} , for Run 1, 2 and 3, respectively, demonstrates a good reproducibility of results, as well as the absence of notable deterioration in cell performance across all experiments. All V-j measurements also exhibit considerable overlap in voltage over the entire range of current density with no notable current limiting diffusion limitation characteristics in the current range measured, for a scan rate of 5 mV s^{-1} .

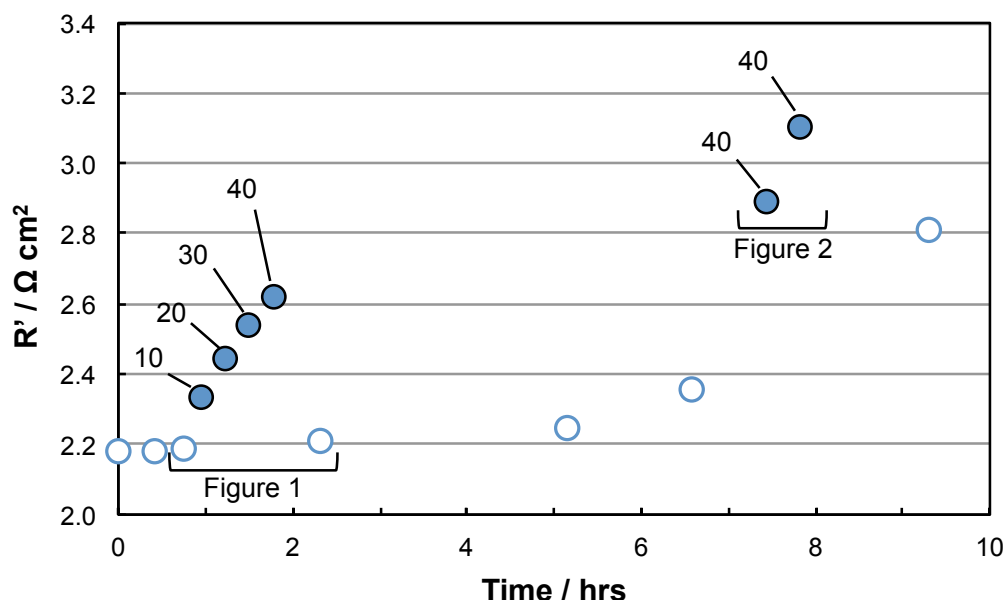


Figure 6.4: System ohmic resistance, taken as real axis intercept of impedance curves, as a function of time for all EIS taken in DM cell operation under N_2 . Results from loaded EIS marked as outlined data points with EIS loading indicated (mA cm^{-2}), open circuit EIS scans included as solid data points. Results from EIS spectra included in Figures 6.1(a) and 6.2 as indicated.

In addition to tracking cell performance with experimental progression using V-j measurements, the cell ohmic resistance was monitored *via* EIS measurements. A plot of cell ohmic resistance in N_2 (taken as the high frequency intercept of the real impedance axis) from EIS spectra as a function of time, is given in Figure 6.4. The open circuit EIS data points (open symbols) show a relatively stable ohmic resistance with time for the first ~5 hrs of cell operation, increasing marginally from 2.18 to 2.25

$\Omega \text{ cm}^2$. Open circuit EIS measurements taken later, after the cell was subjected to limiting current and the cell voltage had dropped to 0.3 V, showed higher cell ohmic resistances of $2.81 \Omega \text{ cm}^2$ after 9.3 hrs of cell operation.

A notable trend from Figure 6.4 is the elevated ohmic resistance obtained from EIS measurements when the cell was under load (solid symbols). This increase appears linear in nature with respect to the magnitude of the current loading. The cell ohmic resistance increased from $2.19 \Omega \text{ cm}^2$ under open circuit to 2.34, 2.44, 2.54, and $2.62 \Omega \text{ cm}^2$ under loads of 10, 20, 30, and 40 mA cm^{-2} , respectively. After removing the load, the ohmic resistance recovered to $2.21 \Omega \text{ cm}^2$ under open circuit. Results included from Figure 6.2 also illustrate a moderate increase in the ohmic resistance with time during sustained loading from 2.89 to $3.10 \Omega \text{ cm}^2$ during a period of 23 min under a load of 40 mA cm^{-2} .

6.3.2 Raw Morwell char

As mentioned previously in section 6.2.2, two additional cells, fabricated identically to that used for the DM char results, were used in separate studies with RM char as the fuel. The experimental matrix was also kept similar for all cells, with the exception of the switching of anode chamber atmosphere to a N_2/CO_2 mixture at certain stages in the RM char experiments.

6.3.2.1 Cell #1

Figure 6.5 shows three V-j scans taken at different intervals during cell testing under N_2 anode purge gas, as per the scans in Figure 6.3 for DM char. The first scan (run 1) achieved a peak power density of 33.3 mW cm^{-2} , comparable to that attained from DM char (33.6 mW cm^{-2}). Run 1 for the RM char also exhibits a linear behaviour in voltage-current dependency with no obvious sign of diffusion limitations at higher current densities. Also worth noting is the higher OCV value for the RM char of 1.06 V for Run 1, compared with 0.99 – 1.00 V for DM char. However, in the case of RM char there is substantially less consistency between runs than for those of the DM char, despite being subjected to comparable intervening loadings. The subsequent V-j measurements in Figure 6.5 produced decreasing power densities (28.4 and 24.5 mW cm^{-2}), and lower OCV values (1.02 and 1.01 V) for runs 2 and 3, respectively. In addition, the emergence of diffusion-related limitations at high current densities was increasingly pronounced for the latter runs.

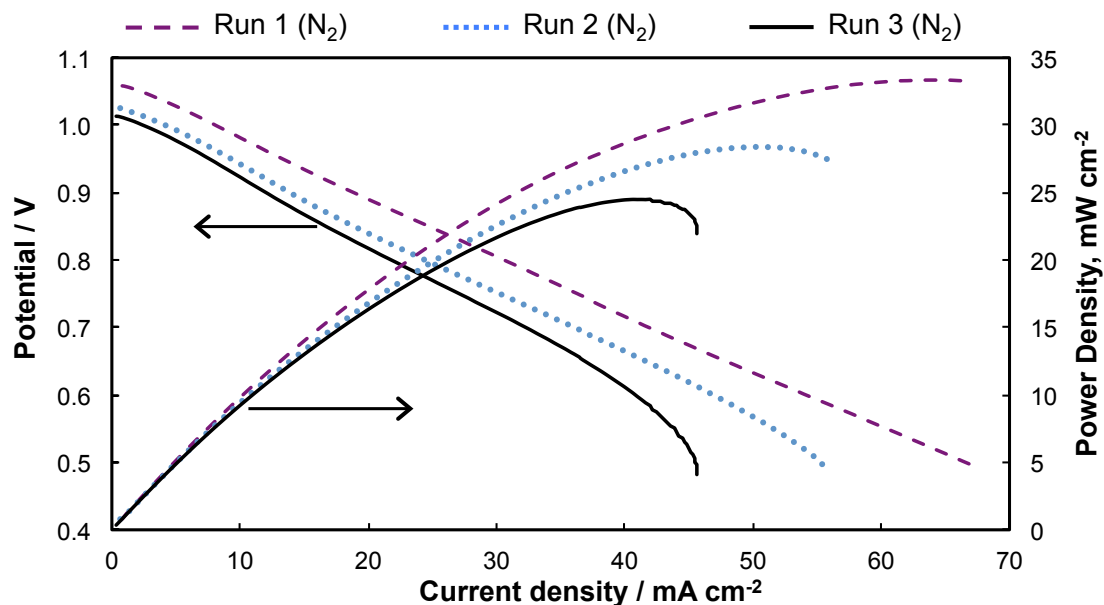


Figure 6.5: Voltage-current density-power density curves for RM cell #1 under N_2 at 850 °C.

Following the V-j run 3 of Figure 6.5, the anode purge gas was switched from N_2 to a N_2/CO_2 mixture (40 vol% CO_2 in N_2). A V-j measurement under the new gaseous environment was recorded and is included in Figure 6.6, along with run 3 under N_2 for comparison. The introduction of CO_2 into the anode chamber resulted in a significant decrease in OCV from 1.01 V to 0.89 V. However, the change in atmosphere also eliminated the current-limiting diffusion polarisation in the V-j curve observed in N_2 . This enabled the cell to produce a slight improvement in peak power of 26.1 mW cm^{-2} , compared with 24.5 mW cm^{-2} under N_2 alone, despite the lower OCV.

In order to further assess the influence of the anode purge gas atmosphere on diffusion polarisation within the cell, EIS measurements were performed both immediately prior to the switching of anode chamber gas (in N_2) and after in N_2/CO_2 mixture once the OCV had reached equilibrium.

The two spectra are given in Figure 6.7 and have been normalised by horizontal translation such that they both intercept the origin of the graph. This was done to make direct comparison of the electrode contribution. The two spectra share similar magnitudes of their high frequency arcs, with significant variations at lower frequencies. The EIS collected under N_2 anode purge gas resembles those of the DM char (Figure 6.1(a)), having three distinct arcs, however the magnitude of the high frequency arc for the RM case in particular is much larger (Figures 6.1(a) and

6.7). For the case of the RM char under the N_2/CO_2 gas mixture, the low frequency arc is significantly depressed and is much smaller in magnitude.

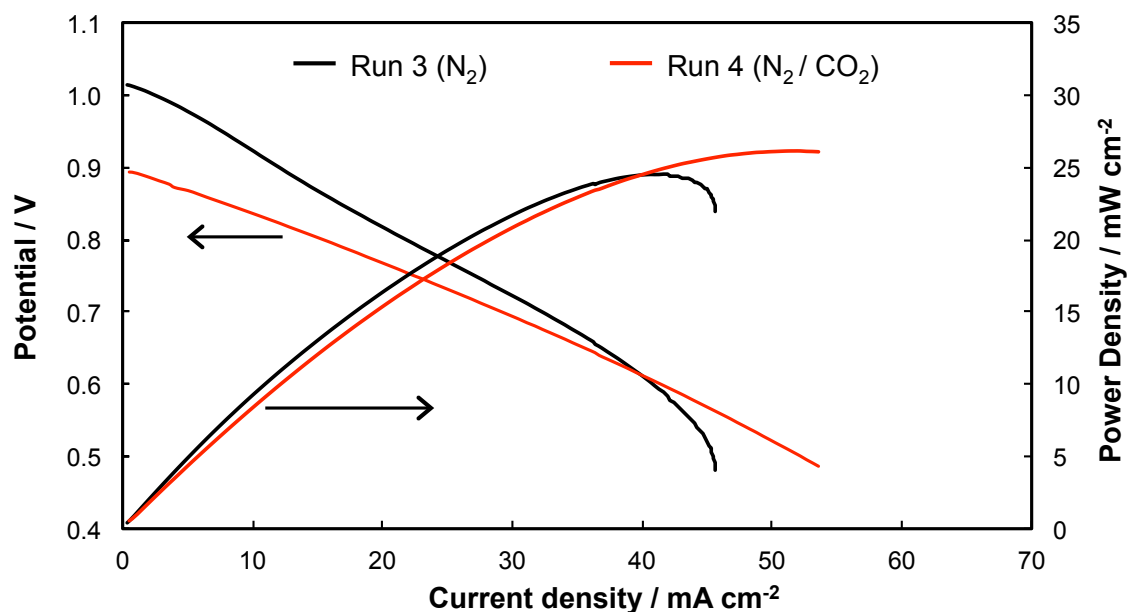


Figure 6.6: Voltage-current density-power density curves for RM cell #1, final run under N_2 (run 3) and subsequent run under N_2/CO_2 mixture (run 4) at 850 °C.

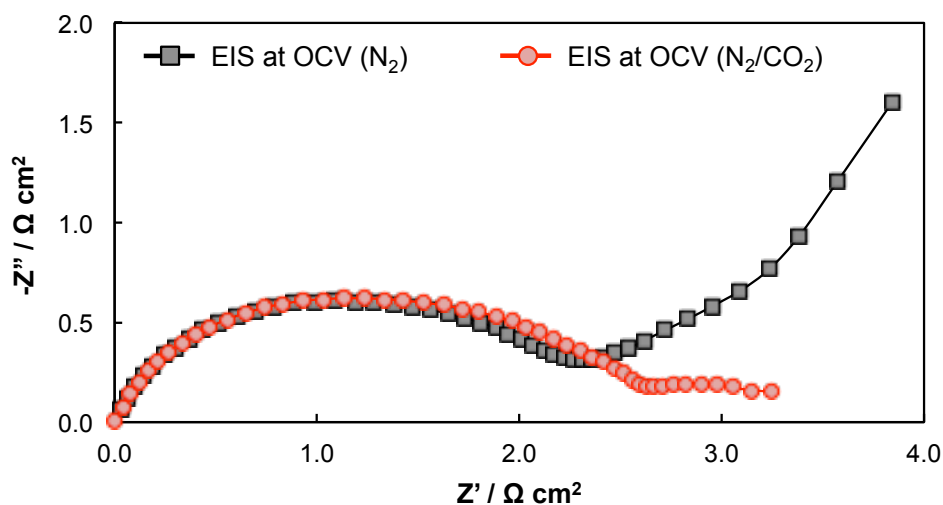


Figure 6.7: Impedance spectra for RM cell #1 under open circuit for anode atmospheres of N_2 and N_2/CO_2 gas mixtures at 850 °C. Impedance spectra translated in the real axis so that all spectra intercept the graph origin.

6.3.2.2 Cell #2

In a separate study, the stability of cell performance under constant load was assessed under both N_2 and N_2/CO_2 mixture anode chamber purge gases for the RM char. Cell loading was 20 mA cm^{-2} and the results are shown as CP measurements in Figure 6.8. In the case of N_2 purge (CP1), after an initial drop of 66 mV in the first 20 sec, the cell experienced a steady voltage decay of 254 mV hr^{-1} for approximately 13 min before eventually experiencing rapid voltage decay and cell termination after ~19 min. This was a substantially poorer performance than the sustained cell operation attained under the same loading for DM char (Figure 6.2). CP2, conducted under the N_2/CO_2 atmosphere, commenced at the lower voltage of 0.75 V and an initial rapid drop in operating voltage is visibly absent. In addition, the cell operated for longer period under a lower voltage decay of 163 mV hr^{-1} , eventually terminating after 33 min of operation.

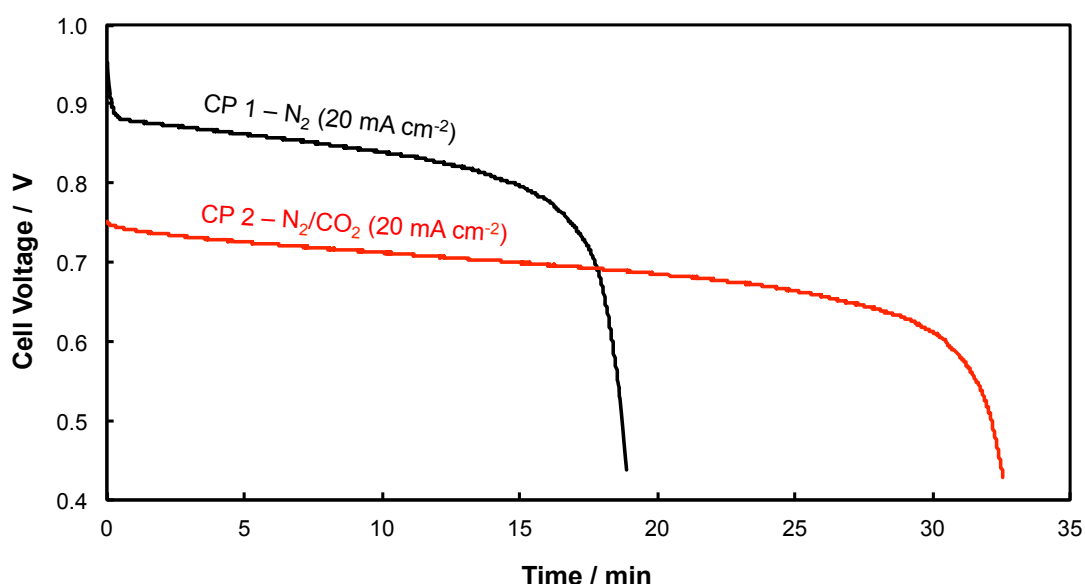


Figure 6.8: Chronopotentiometric loadings of 20 mA cm^{-2} for RM cell #2 taken under anode atmospheres of N_2 (CP1) and N_2/CO_2 gas mixture (CP2).

Similar to DM char experiments, the cell ohmic resistance for RM char cell #2 was monitored by means of EIS under open circuit as well as under load conditions and are given as Figure 6.9. The ohmic resistance under N_2 at open circuit was reasonably constant with time and ranged between $3.01 - 3.07\ \Omega\text{ cm}^2$, which was somewhat higher than initial values for the DM char ($2.18\ \Omega\text{ cm}^2$). The increase in ohmic resistance with increasing load during EIS measurements showed a similar trend to the DM results, however, reaching $3.55\ \Omega\text{ cm}^2$ at the highest loading of 40 mA cm^{-2} . Two additional loaded EIS measurements were taken under N_2 at 10 and

20 mA cm⁻², after about 3 hrs of operation, which also showed an elevated ohmic resistance value of 0.13 Ω cm² above the open circuit (3.14 Ω cm²) for the higher loading. However, the loading of 10 mA cm⁻² had a similar ohmic resistance to the previous EIS recording under open circuit, at 3.04 and 3.01 Ω cm², respectively. The introduction of CO₂ into the anode chamber, after about 5 hrs of operation under N₂, resulted in an increase in the cell ohmic resistance to 3.33 Ω cm² (open circuit). Loading the cell at 20 mA cm⁻² under the N₂/CO₂ anode chamber atmosphere resulted in an increase in the ohmic resistance by 0.13 Ω cm² above the open circuit, comparable to that of the previous loading at 20 mA cm⁻² under N₂.

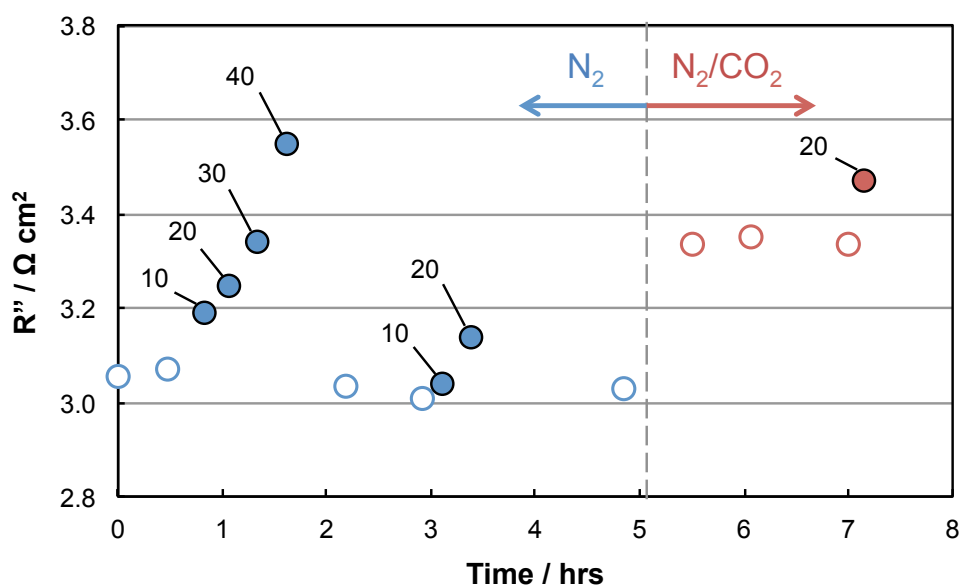


Figure 6.9: System ohmic resistance, taken as real axis intercept of impedance curves, as a function of time for all EIS taken in RM cell #2 operation under anode atmosphere of N₂ and N₂/CO₂ gas mixture as indicated. Results from loaded EIS marked as outlined data points with EIS loading indicated (mA cm⁻²), open circuit EIS scans included as solid data points.

6.4 Discussion

The major observations from the previous section can be summarised as follow:

- The polarisation resistance of high and low frequency arcs in EIS spectra are responsive to cell loading during EIS measurements. With increasing cell loading, the high frequency arc magnitude increased, whereas the low frequency arc decreased in magnitude
- When EIS is recorded under near limiting current conditions, as per inset in Figure 6.2, there is significant change to the low frequency region of the spectra, which includes the appearance of another arc

- In all cases in N_2 and N_2/CO_2 atmospheres the cell ohmic resistance increased with cell loading during EIS measurements. For RM, the ohmic resistance was higher in N_2/CO_2 atmosphere than in N_2
- The OCV was lower for DM than for RM in N_2 atmosphere. The OCV is also lower for RM in N_2/CO_2 than in N_2
- For CP measurements of both DM and RM in N_2 , the voltage decays rapidly when load is applied, while for RM in N_2/CO_2 there is no such behaviour. Following this initial voltage decay in N_2 , the voltage is steady for significantly longer time periods for DM at 20 mA cm^{-2} , but not for RM. In addition, for RM, the voltage decay rate is much higher in N_2 compared with that in N_2/CO_2
- There is no observable change to the behaviour in V-j and P-j curves for DM with time, whereas RM experiences consistent decay in performance
- For RM (Figure 6.6) the performance is better in N_2/CO_2 with no limiting current, compared with that in N_2 , despite an increase in the ohmic resistance. Also, as per Figure 6.7, the low frequency arc magnitude is substantially smaller in N_2/CO_2 compared with that in N_2

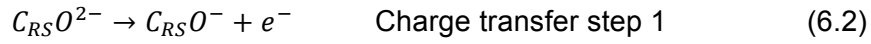
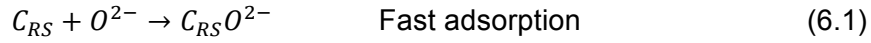
6.4.1 Impedance behaviour of DM fuelled cell

6.4.1.1 Cell polarisation resistance

Figure 6.1(a) presents data for EIS taken during cell operation on DM char and reveals polarisation components in EIS spectra with at least three distinct arcs. Based upon equivalent circuit analysis the trends in magnitude of resistive components associated with each arc are shown in Figure 6.1(b) along with the equivalent circuit used. There is a near-linear increase in the size of the high frequency arc (R_{hf}) with increasing loading. There is also a staggered increase in the charge transfer component of the low frequency arc (R_{Lf}) with increasing loading. Both the low and high frequency arcs are primarily associated with anodic processes (Chapter 5) as polarisation resistances of the LSCF cathode under similar operating conditions reported is only $(0.1 - 0.2 \Omega \text{ cm}^2)$ [24-26].

The high frequency arc (R_{hf}) can be attributed to solid carbon oxidation into gaseous CO which can either remain adsorbed on the carbon itself or may be released as gaseous CO and react at the anode/electrolyte interface as reported previously [26]. Although the mechanism behind the observed increase in the (R_{hf}) under current loading is not clear, it could be attributed to sluggish kinetic of O^{2-}

adsorption and CO desorption on the carbon surface [26]. According to model proposed by Hapin et al. for Hall process [27] and later extended for Solid electrolyte DCFCs [28,29], the electrochemical oxidation of solid carbon proceeds in steps involving adsorption/desorption of gaseous species (O_2 and CO) and charge transfer processes as:



Where C_{RS} is a reactive site on solid carbon surface where O^{2-} ion from the electrode may be adsorbed. Under loading conditions it may be possible that one of these processes or combination therein can limit the kinetics leading to apparent increase in charge transfer resistance. The above sequence of reaction steps may be summarised as Eq. (1.5):



The low frequency arc can be related with diffusion and charge transfer associated with gaseous CO as reported by Giddey et al. [22]. The significant decrease in Warburg component under loading could be the effect of Boudouard gasification of solid carbon into CO by CO_2 generated *in-situ* as Eq. (1.7):



The CO_2 may be present in the system as a direct result of cell operation *via* the further oxidation of CO generated in Eq. (1.5) above, as per Eq. (1.6), with the overall cell reaction given as Eq. (1.4):



It is expected that higher currents will lead to greater rates of CO_2 generation, which in turn produces more CO *via* Eq. (1.5) leading to a decrease in diffusion losses. Giddey et al [22] have previously reported an analogous observation for solid electrolyte DCFCs operated with solid carbon in the presence of CO_2 .

It is important to note that these polarisation components return to their initial values upon returning to OCV as evidenced by the 6th EIS at OCV in Figure 6.1(a), which reinforces that the trends discussed here are related to cell loading.

6.4.1.2 Cell ohmic resistance

A key observation in this work is the increasing ohmic resistance of the cell under loading. Usually the ohmic resistance of a cell is expected to remain unchanged or decrease due to 'self-heating' effect under cell loading conditions. Various resistive components contribute to system ohmic resistance such as resistances in electronic conductive pathways in the anode, cathode, carbon fuel with its inherent impurities, and current collection wires, as well as in ionic conductive pathways in the electrolyte and anode. The resistance due to LSCF cathode can be assumed to be negligible as LSCF has high electronic conductivity in air and is compatible with YSZ in the operating temperature range and duration. Although there is no conclusive evidence, possible sources of increase in ohmic resistance under loading could be the combination of loss of carbon particles in contact with the anode and possibly the decrease in electronic conductivity of ceria in the anode. It is known that ceria has electronic conductivity of about 1 S cm^{-1} in reducing atmosphere however the influx of oxygen ions from the electrolyte under loading conditions may result in decreased electronic conductivity. More investigation would be required to explain the phenomenon completely.

6.4.2 Cell performance under different atmospheres

6.4.2.1 Effect on cell OCV

The open circuit voltage (OCV) of a fuel cell is a good measure of the relative states of both electrodes and in turn gives insight into the nature of the gas-phase environments of anode and cathode chambers. In this experiment minimal variation in the state of the cathode with time is expected and hence the OCV relates more to the reducing nature of the anode chamber environment. The N_2 anode chamber purge gas used in this study contains an O_2 impurity level of $< 10 \text{ ppm}$. At low oxygen partial pressures the amount of O_2 present has a substantial effect on OCV [30].

Under a N_2 anode atmosphere, the observed OCV of V-j scans for RM (Figure 6.5) at $1.01 - 1.06 \text{ V}$ was significantly higher than for DM (Figure 6.3) at 0.99 V . Victorian brown coal and its derivatives are known to be highly reactive in O_2 [31]. The RM fuel used in this study has also been shown to be significantly more thermochemically reactive than DM towards Boudouard gasification (Chapter 4). It is likely that RM fuel scavenges free O_2 in the anode chamber near the anode much more readily than the DM fuel does, hence maintaining a higher OCV. The ability of

the RM fuel to maintain low oxygen partial pressure at the anode appears to wain with time as the reactive carbon is consumed and the OCV of later V-j runs for RM approaches that of DM.

The introduction of CO₂ into the anode chamber also has a profound effect on the OCV as observed in Figure 6.6 for RM fuel. This can also be related to the partial pressure of O₂ present in the anode chamber. Although not specified by the supplier, it is likely that the O₂ impurity level in the food grade N₂/CO₂ gas mixture used in this study is higher than that for the high purity N₂. Additional O₂ may be formed *via* the establishment of a CO/O₂/CO₂ equilibrium with the introduction of excess CO₂ into the system forcing the equilibrium towards the CO/O₂ side as per Le Chatelier's principle.

Another contributor to a lower OCV under the N₂/CO₂ gas mixture is the preferential electrochemical reactions and their associated reversible voltages. When CO₂ is introduced into the anode chamber, CO is generated *via* Boudouard gasification (Eq. 1.7). The presence of abundant CO at the anode enables the cell to generate current increasingly *via* Eq. (1.6), which has a reversible voltage of 0.9 V. Under N₂, the dominant anodic reactions are likely those of Eqs. (1.5) and (1.4) which have reversible voltages of 1.03 and 1.16 V respectively (at 980 °C), which contributes to a higher OCV for runs performed under a N₂ anode purge. The influence of the dominant reaction mechanism on V-j and CP scans will be discussed later.

6.4.2.2 Effect on cell ohmic resistance

As discussed in the previous section, there are various reasons why the partial pressure of O₂ in the anode chamber may be higher under the purge gas of the N₂/CO₂ mixture than under N₂ alone. In addition, it is understood that the electronic conductivity of ceria decreases in the presence of oxygen, as outlined in Section 6.4.1.2. It is possible that a decrease in ceria electrical conductivity in the anode under such environments may have contributed to the observed increase in ohmic resistance for the cell under N₂/CO₂ atmosphere in Figure 6.9.

6.4.2.3 Effect on cell performance

Initial rapid decay in voltage during the first minute of constant (CP) loading for DM (Figure 6.2) and RM (Figure 6.8) under N₂ anode purge gas was observed. This phenomenon has been previously reported for a MIEC anode (LSCF) (Chapter 5)

and was attributed to the rapid consumption of carbon and/or residual gaseous CO that may be present in the anode chamber during cell standby [32]. Following this initial voltage decay, the cell likely operates on a combination of solid carbon conversion *via* Eq. (6.1) and (6.3), and gaseous CO conversion as per Eq. (6.4), with gaseous CO made available *via* Eq. (6.2) and (6.3). Such a cyclic mechanism for carbon conversion in the gas phase was popularised by Gür and co-authors [33].

When N₂/CO₂ anode purge gas was used (CP2, Figure 6.8), there was no observed initial rapid voltage decay. This may be due to the presence of gaseous CO at the anode prior to cell loading *via* Boudouard gasification of the carbon fuel.

Under the N₂/CO₂ purge gas atmosphere, the cell voltage was sustained for longer than under N₂. This may also be attributed to CO generation *via* Boudouard gasification of the fuel. Although *in-situ* generation of CO is believed to occur as discussed above, the external supply of CO₂ allows for additional CO generation *via* Boudouard gasification that has contributed to the extended cell operation under constant current load. The extension of the V-j curve in Figure 6.6 under N₂/CO₂ is also linked to additional supply of CO, with the negation of diffusion-limitations at high current densities further suggesting an increase in gas-phase reactive species.

Of course, only CO present at the anode itself is available to the fuel cell, and this appears to have been exhausted within 30 minutes of cell operation at 20 mA cm⁻² in the case of the CP measurements (Figure 6.8). Alternative cell designs with more effective delivery of gaseous reactive species to the anode would further extend cell operation under sustained loadings.

6.4.3 Cell long-term chronopotentiometric tests

For CP loaded runs, following the initial rapid voltage decay under N₂, more stable voltage decay was established. However, this stability varied with CP loading and fuel type. Under a loading of 20 mA cm⁻², DM fuel showed impressive stability over the course of 2 hrs (CP1, Figure 6.2), whereas for the same loading the RM fuel did not last for even 20 min before the run termination due to severe voltage decay. One possible contributor to the inability for RM to sustain constant current loading for a significant period of time under the current arrangement is the inorganic content of the char. Proximate analysis of the fuels used in this study gives a volatile- and moisture-free ash content of 4.4% wt% for RM and 1.2 wt% for DM (Chapter 4). Ash

deposition on the anode surface following carbon consumption at the anode/carbon interface would progressively reduce the active area available for solid carbon conversion that is critical for sustaining current.

However, under the higher loading of 40 mA cm^{-2} (Figure 6.2) the DM-fuelled cell shows behaviour similar to that of the RM fuel under 20 mA cm^{-2} in terms of its inability to sustain voltage under the constant load. The subsequent EIS spectra taken during constant cell loading of 40 mA cm^{-2} provides insight into the nature of voltage decay for the DM cell. The 2nd EIS recorded under 40 mA cm^{-2} during accelerated voltage decay shows a large Warburg component at low frequencies, which may have evolved during the late stages of data acquisition, and hence the beginning of a closing low frequency arc is also present. The Warburg component here suggests that at such high loadings, gaseous CO produced *via* Eq. (6.2) and (6.3) is consumed at a much faster rate than can be formed, which presents as a diffusion limitation in cell operation.

6.4.4 V-j curve trends and additional support for ash deposition

V-j curve data for RM char (Figure 6.5) also suggests that the observed increase in diffusion polarisation with experimental progression is responsible for a deterioration in cell performance, with voltage decay becoming more pronounced at high current densities for later runs. The proposed mechanism of ash deposition on the anode with carbon consumption would contribute to such a response over time. The initial run (run 1) under N_2 for RM is quite comparable to that for DM (Figure 6.3) with no observable current limitations, however DM fuel experiences no such deterioration in cell performance with time. The significantly reduced ash content of the DM fuel may be key to the cell's sustained performance over the course of the experiments as well as during moderate CP loadings of 20 mA cm^{-2} .

The behaviour of EIS spectra under the two anode gaseous environments provides further insight into possible controlling reaction mechanisms (Figure 6.7). Only low and intermediate frequency arcs show a response to the change in gaseous environment, both experiencing a significant reduction in magnitude. In contrast, the high frequency arc is not visibly influenced by the changes in the gas-phase. It seems reasonable to assume that charge transfer processes of solid carbon conversion dominate the high frequency arc.

A comparison of the size of the high frequency arcs of EIS spectra for both RM and DM under N_2 supports theory that RM cell operation is limited in its solid carbon conversion. Modelling of the EIS at OCV under N_2 in Figure 6.7 (RM fuel) gives a high frequency arc of $2.6 \Omega \text{ cm}^{-2}$, compared with $1.3 \Omega \text{ cm}^{-2}$ for DM fuel (Figure 6.1(b)). As the high frequency arc is thought to be related to solid carbon conversion, then the larger magnitude of the high frequency arc for RM over DM suggests a hindrance to solid carbon conversion at the anode for RM fuel, which could be due in part to ash deposition on the anode.

6.5 Conclusions

Extended operation of a DCFC by passage of constant current has highlighted the importance of the continuous delivery of gaseous reactive species to the anode. This is evidenced by improved cell performance upon introduction of CO₂ into the N₂-purged anode chamber. Boudouard gasification of the fuel under the N₂/CO₂ purge gas is believed to be responsible for the extended cell operation under CP loading and to higher current densities in V-j testing, supported by a reduction in the magnitude of the low frequency arc in EIS spectra. In addition to the important gas phase reactants, a mechanism for reduction of anode active area via ash deposition was proposed which would account for the observed deterioration in cell performance when operated on RM fuel and not observed for the low-ash DM fuel.

EIS was also employed to assess the effect of cell loading on cell impedances. A growth in the high frequency arc with increased loading was attributed to solid carbon conversion to gaseous or adsorbed CO, and shrinkage in the low frequency arc related to increasing rates of CO generation. In addition, cell ohmic resistance was also monitored with EIS spectra and was found to increase when under load. Although there is no conclusive evidence at this stage, it is believed that during cell loading, the influx of oxygen ions to the anode results in a decrease in the electrical conductivity of ceria. With gas phase reactions thought to occur at the interface of the anode and electrolyte, the passage of electrons through the ceria phase is necessary in regions of non-continuous Ni metal phase. An increase in ohmic resistance under N₂/CO₂ anode atmosphere was also observed and was similarly related to the state of the ceria phase under a higher oxygen partial pressure in this case. The partial pressure of O₂ in the anode chamber is also believed to have primarily influenced the OCV throughout testing, and resulting in a reduced OCV under N₂/CO₂ atmosphere. A higher OCV for RM over DM is attributed to the ability for RM fuel to more effectively scavenge available oxygen at the ppm level due to its higher reactivity.

The anode used in this study shows stable performance under the favourable conditions of CP loading at 20 mA cm⁻² and using DM char as the fuel. As such, the Ni-GDC/YSZ anode is a promising electrode material and the importance of using a low-ash fuel in direct contact DCFC arrangements has been highlighted.

References

1. Giddey S, Badwal SPS, Kulkarni A, Munnings C. A comprehensive review of direct carbon fuel cell technology. *Progr Energy Combust Sci.* **2012**;38:360-99.
2. Alexander BR, Mitchell RE, Gür TM. Model of Carbon Utilization in a Solid Carbon Fuel Cell. *ECS Trans.* **2012**;41:45-55.
3. Hemmes K, Cooper JF, Selman JR. Recent insights concerning DCFC development: 1998-2012. *Int J Hydrogen Energy.* **2013**;38:8503-13.
4. Gür TM. Critical review of carbon conversion in "carbon fuel cells". *Chem Rev.* **2013**;113:6179-206.
5. Kulkarni A, Ciacchi FT, Giddey S, Munnings C, Badwal SPS, Kimpton JA, et al. Mixed ionic electronic conducting perovskite anode for direct carbon fuel cells. *Int J Hydrogen Energy.* **2012**;37:19092-102.
6. Tuller HL. Mixed Conduction in Nonstoichiometric Oxides. In: Soerensen OT, editor. *Nonstoichiometric Oxides: Academic Press*; **1981**. p. 271-335.
7. Zhu WZ, Deevi SC. A review on the status of anode materials for solid oxide fuel cells. *Materials Science and Engineering: A.* **2003**;362:228-39.
8. Putna ES, Stubenrauch J, Vohs JM, Gorte RJ. Ceria-Based Anodes for the Direct Oxidation of Methane in Solid Oxide Fuel Cells. *Langmuir.* **1995**;11:4832-7.
9. Liu J, Ye K, Cheng K, Wang G, Yin J, Cao D. The catalytic effect of CeO₂ for electrochemical oxidation of graphite in molten carbonate. *Electrochim Acta.* **2014**;135:270-5.
10. Cowin PI, Petit CTG, Lan R, Irvine JTS, Tao S. Recent Progress in the Development of Anode Materials for Solid Oxide Fuel Cells. *Advanced Energy Materials.* **2011**;1:314-32.
11. Kim S-G, Yoon SP, Nam SW, Hyun S-H, Hong S-A. Fabrication and characterization of a YSZ/YDC composite electrolyte by a sol-gel coating method. *J Power Sources.* **2002**;110:222-8.
12. Ge X-M, Chan S-H, Liu Q-L, Sun Q. Solid Oxide Fuel Cell Anode Materials for Direct Hydrocarbon Utilization. *Advanced Energy Materials.* **2012**;2:1156-81.
13. Badwal SPS, Fini D, Ciacchi FT, Munnings C, Kimpton JA, Drennan J. Structural and microstructural stability of ceria - gadolinia electrolyte exposed to reducing environments of high temperature fuel cells. *Journal of Materials Chemistry A.* **2013**;1:10768-82.
14. Kulkarni A, Giddey S, Badwal SPS. Yttria-doped ceria anode for carbon-fueled solid oxide fuel cell. *J Solid State Electrochem.* **2015**;19:325-35.

15. Werhahn MG, Schneider O, Stimming U. Thin Film Gadolinia Doped Ceria (GDC) Anode for Direct Conversion of Carbon Black Particles in a Single Planar SOFC. *ECS Trans.* **2013**;50:73-87.
16. Magdalena Dudek, Robert Socha. Direct Electrochemical Conversion of the Chemical Energy of Raw Waste Wood to Electrical Energy in Tubular Direct Carbon Solid Oxide Fuel Cells. *Int J Electrochem Sci.* **2014**;9:7414-30.
17. Prashant Soral, Uday Pal, Wayne L. Worrell. Comparison of power densities and chemical-potential variation in SOFC's with multi-layer and single-layer oxide electrolytes. In: U. Stimming, S. C. Singhal, H. Tagawa, W. Lehnert, editors. Solid Oxide Fuel Cells V: *The Electrochemical Society, Inc.*; **1997**. p. 264-9.
18. E. Perry Murray, S. A. Barnett. Improved performance in (La,Sr)MnO₃ and (La,Sr)(Co,Fe)O₃ cathodes by the addition of a Gd-doped ceria second phase. In: S. C. Singhal, M. Dokiya, editors. Solid oxide Fuel Cells (SOFC VI): *The Electrochemical Society*; **1999**. p. 369-74.
19. Badwal SPS. Stability of solid oxide fuel cell components. *Solid State Ionics.* **2001**;143:39-46.
20. Pihlatie M, Kaiser A, Mogensen M. Redox stability of SOFC: Thermal analysis of Ni-YSZ composites. *Solid State Ionics.* **2009**;180:1100-12.
21. Faes A, Hessler-Wyser A, Zryd A, Van herle J. A Review of RedOx Cycling of Solid Oxide Fuel Cells Anode. *Membranes.* **2012**;2:585-664.
22. Giddey S, Kulkarni A, Munnings C, Badwal SPS. Performance evaluation of a tubular direct carbon fuel cell operating in a packed bed of carbon. *Energy.* **2014**;68:538-47.
23. Rady AC, Giddey S, Kulkarni A, Badwal SPS, Bhattacharya S. Degradation Mechanism in a Direct Carbon Fuel Cell Operated with Demineralised Brown Coal. *Electrochim Acta.* **2014**;143:278-90.
24. Esquirol A, Brandon NP, Kilner JA, Mogensen M. Electrochemical Characterization of La_{0.6}Sr_{0.4}Co_{0.2}Fe_{0.8}O₃ Cathodes for Intermediate-Temperature SOFCs. *J Electrochem Soc.* **2004**;151:A1847-A55.
25. Kulkarni A, Giddey S, Badwal SPS. Electrochemical performance of ceria-gadolinia electrolyte based direct carbon fuel cells. *Solid State Ionics.* **2011**;194:46-52.
26. Kulkarni A, Giddey S, Badwal SPS, Paul G. Electrochemical performance of direct carbon fuel cells with titanate anodes. *Electrochim Acta.* **2014**;121:34-43.
27. Haupin W, Frank W. Electrometallurgy of Aluminum. In: Bockris JOM, Conway BE, Yeager E, White RE, editors. Comprehensive Treatise of Electrochemistry:

Springer US; **1981**. p. 301-25.

28. Cherepy NJ, Krueger R, Fiet KJ, Jankowski AF, Cooper JF. Direct Conversion of Carbon Fuels in a Molten Carbonate Fuel Cell. *J Electrochem Soc.* **2005**;152:A80-A7.
29. Li C, Shi Y, Cai N. Mechanism for carbon direct electrochemical reactions in a solid oxide electrolyte direct carbon fuel cell. *J Power Sources.* **2011**;196:754-63.
30. Hirata Y, Matsumoto K, Sameshima S, Matsunaga N, Nagamori M, Shimonosono T. Cell performance of strontium ruthenium oxide cathode/Gd-doped ceria (GDC) electrolyte/nickel-GDC anode system. *J Ceram Soc Jpn.* **2009**;117:1141-6.
31. Bhattacharya SP. Gasification Performance of Australian Lignites in a Pressurized Fluidized Bed Gasifier Process Development Unit Under Air and Oxygen-enriched Air Blown Conditions. *Process Saf Environ Prot.* **2006**;84:453-60.
32. Gür TM. Critical review of carbon conversion in "carbon fuel cells". *Chem Rev.* **2013**;113:6179-206.
33. Gür TM. Mechanistic Modes for Solid Carbon Conversion in High Temperature Fuel Cells. *J Electrochem Soc.* **2010**;157:B751-9.

Declaration for thesis chapter 7

Declaration by candidate

In the case of Chapter 7, the nature and extent of my contribution to the work was the following:

Nature of contribution	Extent of contribution (%)
Experimental work and analysis, writing	100

The following people contributed to the work. If persons are students at Monash University, the extent of their contribution in percentage terms must be stated:

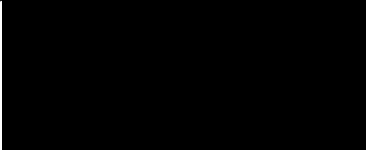
Name	Nature of contribution	Extent of contribution (%)
Dr Sukhvinder Badwal	Advisory role	-
Dr Sarbjit Giddey	Advisory role	-
Assoc Prof Bradley Ladewig	Advisory role	-
Prof Sankar Bhattacharya	Advisory role	-
Dr Aniruddha Kulkarni	Advisory role	-

The undersigned hereby certify that the above declaration correctly reflects the nature and extent of the candidate's and co-authors' contributions to this work.

Candidate's
Signature

	Date 27/02/2015
---	------------------------

Main
Supervisor's
Signature

	Date 27/02/2015
---	------------------------

7

Catalytic gasification of carbon in direct carbon fuel cells

Chapter objective

The influence of inorganic species inherent in Victorian brown coal has been established as a key factor in DCFC performance in the works contained in this thesis. Chapter 4 identified the ash constituents in Morwell coal as contributing significantly to the power output of the DCFC *via in-situ* catalysis of Boudouard gasification. Though the assignment of individual species to enhanced cell performance could only be speculated, the successful removal of Ca, Fe, and Mg, from the raw coal *via* acid washing (demineralised coal) and the literature available on the role of these species in Boudouard gasification catalysis were highly suggestive of the enhanced cell performance of raw Morwell char over demineralised Morwell char and carbon black.

The present work aims to deconvolute the contribution of each of Ca, Fe, and Mg, to Boudouard gasification and ultimately to the performance of a physical contact type solid oxide DCFC.

Catalytic gasification of carbon in direct carbon fuel cells

Abstract

The present study investigates the catalytic properties of the metallic species commonly present in brown coal (Ca, Fe, and Mg), towards Boudouard (CO_2) gasification, by individually impregnating these species in pure carbon black, and examining their electrochemical performance in a direct carbon fuel cell (DCFC). Reactivity studies on catalysed carbon fuels were carried out at 850 °C with thermogravimetric analysis and were compared to those of chars produced from a Victorian brown coal. The relative catalytic activities of the added species were found to increase from $\text{Mg} < \text{Fe} < \text{Ca}$, in the presence of CO_2 . The catalysed carbon black fuels, tested in a direct carbon fuel cell with the catalytic species, were also found to influence the fuel cell performance under both N_2 and N_2/CO_2 anode purge gases in line with relative catalytic activities of the added species. Electrochemical impedance spectroscopy measurements were employed under open circuit conditions to assess the nature of the performance variations in fuel cell environments. Availability of gaseous CO *via in-situ* Boudouard gasification of the fuel is believed to be the primary differentiating factor for various carbon fuels in cell operation. Finally, a relation between the cell open circuit voltage and reactivity of carbon fuel is proposed.

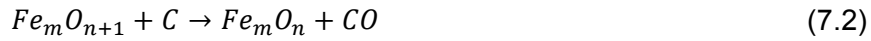
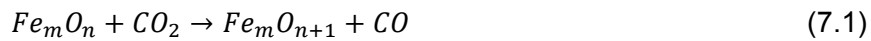
7.1 Introduction

The high temperature (600 - 900 °C) environment of a DCFC anode chamber is conducive to Boudouard gasification, since CO_2 is a product of cell operation and is generated in close proximity to the carbon fuel. However, a fuel with low reactivity towards Boudouard gasification will not contribute significantly to cell performance *via* gasification reactions.

The inorganic content inherent in coals and biomass is known to influence Boudouard gasification kinetics through catalysis and in some cases inhibition [1]. Of these inorganic species, Fe is particularly well known for its catalytic properties in

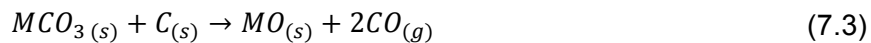
coal gasification [2]. In addition, alkaline earth metal carbonates exhibit catalytic activity at temperatures around 900 °C [3,4].

Iron in all of its oxide states as well as its metallic state is catalytically active through redox reactions with carbon and CO₂ [5,6]. However, as with most transition metal catalysts, its activity increases as it is reduced [7]. Furimsky et al. [6] proposed an Fe-catalysed Boudouard gasification mechanism which involves a redox cycle of Fe *via* various intermediate oxide states, summarised by Tang and Liu [7] as shown in Eqs. (7.1) and (7.2), which are analogous to Eqs. (2.11) and (2.12), given in Chapter 2, respectively:



The mechanism also extends to metallic Fe, i.e. $n = 0$, [6]. The reduction of CO₂ *via* chemisorption onto Fe_mO_n (Eq. (7.1)) is a fast process, whereas the reduction of the formed Fe_mO_{n+1} by carbon (Eq. 7.2) is a solid-solid interaction and is identified as the rate-determining step in this redox catalysis process [6]. Tang and Liu [7] observed an OCV increase for their Fe-catalysed activated carbon over that of pure carbon fuel and attributed this to the greater CO concentration in product gas of the Fe-catalysed system. The authors used an Fe(NO₃)₃ precursor to achieve a C:Fe mixture (4:1 weight ratio), and heat treated the mixture at 800 °C in Ar for 30 min.

For alkaline earth metal carbonates such as CaCO₃ and MgCO₃, McKee et al. [8] proposed the following mechanism, where “M” is the metal cation:



Eq. (7.3) may also be written as a combination of Eq. (7.5) and (1.7):



The authors observed the decomposition of CaCO₃ *via* either Eq. (7.3) or (7.5) occurs between temperatures of 700 – 900 °C under an inert atmosphere, and commence between 850 – 900 °C under CO₂, completing at 1000 °C. MgCO₃ is not stable under either inert or CO₂ atmospheres at fuel cell operating temperatures [8] and decomposes to MgO through the evolution of gaseous CO₂. The inability of the stable MgO to readily form MgCO₃ may be the reason for its poor catalytic properties in terms of Boudouard gasification. The catalytic activity of carbonates of group IIA

metals, in terms of gasification, has been reported to increase with increasing atomic radii for the temperature range of 700-1100 °C [8].

While there is substantial information in the literature on gasification reaction mechanisms, investigations into specific and targeted fuel-based catalysis in DCFC systems and the effect on fuel cell performance is very limited [7,9,10]. In the present work, the performance of carbon black impregnated with a selection of gasification catalysts has been studied in direct contact solid electrolyte based DCFCs. The selected catalysts are common to lignite fuels and are known to demonstrate a range of catalytic activity towards Boudouard gasification. The relative activities of these catalysts under CO₂ atmosphere were also investigated *via* thermogravimetric analysis (TGA) and have been related to their performance in DCFCs.

7.2 Experimental

Electrolyte-supported button cells were fabricated by employing the procedure as outlined in Chapter 3 for YSZ electrolyte button cells with LSCF electrodes. The cell test fixture including the fuel supply arrangement to the anode has been described in detail in Chapter 3 also and is represented by Figure 3.3(c). For each carbon fuel a different button cell was used and carbon loading was typically 150 mg.

Four types of carbon fuels were used in this study: pure carbon and carbon with the addition of Mg, Fe and Ca salts. Nitrates of Magnesium (as Mg(NO₃)₂•6H₂O, Univar, WA, USA), Iron (as Fe(NO₃)₃•9H₂O, Merck Millipore, Germany), and Calcium (as Ca(NO₃)₂•4H₂O, Sigma-Aldrich, MO, USA) were mixed separately with carbon black (CB - Vulcan XC-72, Cabot Corporation, USA) in a 97.5:2.5 wt% carbon to respective metal component ratio. Mixing was achieved in an agar mortar with Millipore water, and samples were left to dry overnight. The three impregnated carbon black samples were then heat-treated at 700 °C under N₂ (99.999%) atmosphere for 30 min in order to thermally decompose the nitrates, prior to use in the DCFC. For clarity, a list of the weights of carbon and metal additives is given in Table 7.1, along with the corresponding wt% of phases that metallic species exist in.

Table 7.1: Catalysed CB makeup as C (carbon as XC-72) plus either Mg (for CB-Mg), Fe (for CB-Fe), or Ca (for CB-Ca) catalysed carbon fuels

	Form	Weight (mg)	Wt % in sample
C	XC-72	2,500	-
Mg	Metal	64	2.50
	MgO	106	4.07
Fe	Metal	64	2.50
	Fe ₂ O ₃	92	3.53
	Fe ₃ O ₄	88	3.42
Ca	Metal	64	2.50
	CaO	90	3.46
	CaCO ₃	160	6.01

XRD analysis of carbon fuels was undertaken to ascertain the oxidation states of the metal species present during fuel cell operation, a key variable in their catalytic activity. Prior to this XRD analysis, all CB samples were subjected to further heat treatment in a tubular furnace. The samples were heated under N₂ to 910 °C at a heating rate of 300 °C hr⁻¹ and held for 10 min, then reduced by 40 °C hr⁻¹ to 850 °C and holding for 4 hrs before cooling to room temperature at 300 °C hr⁻¹. This temperature profile was chosen to simulate as closely as possible a typical DCFC experiment with heating and cooling rates to match those used during seal formation. A separate batch of CB samples were heat treated using the same temperature profile under N₂, with the purge gas switched to N₂/CO₂ (Cellamix, 40 Vol % CO₂ in N₂) for the final 2 hrs at 850 °C and during cooling for XRD analysis. XRD measurements of carbon samples were performed as per Chapter 3, Section 3.6, using an acquisition time of 10 sec.

As with heat treatment of carbons for the XRD study, the temperature profile used for TGA analysis was based on DCFC start-up and operation. The temperature was first raised to 200 °C from room temperature at 600 °C hr⁻¹ under N₂ (high purity 99.999%, Air Liquide), followed by a 300 °C hr⁻¹ increase to 910 °C and hold time of 10 min, cooling to 850 °C at 60 °C hr⁻¹ and holding for 1 hr. CO₂ (Ultra high purity, Air Liquide) was then introduced as the purge gas and the sample held at 850 °C for a further 2 hrs before cooling to room temperature. A protective (“cell gas”) flow rate of 20 mL min⁻¹ N₂ was used at all times to protect the balance. A purge gas (“reactive gas”) flow rate of 80 mL min⁻¹ N₂ was used during heating, cooling, and initial 1 hr

dwelt at 850 °C. The purge gas was switched to 40 mL min⁻¹ each of N₂ and CO₂ following change in atmosphere at 850 °C.

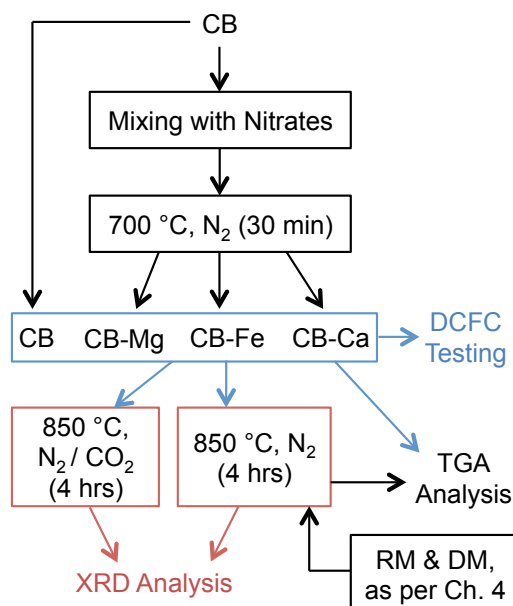


Figure 7.1: Fuel preparation, treatment, and utilisation flow diagram

In addition to the four CB-derived fuels, two additional carbon materials were used in TGA analysis for the purpose of comparison with CB reactivity. These carbons were derived from coal from the Morwell mine, Latrobe Valley, Victoria, Australia. Details of their preparation and characterisation are given in Chapters 3 and 4, respectively. The chars of raw, and demineralised Morwell coal, will be herein referred to as 'RM', and 'DM', respectively. For the purposes of the current investigation, both DM and RM were further heat-treated under N₂ to remove the vast majority of volatile components prior to TGA analysis. This second round of charring was carried out under the same conditions and temperature profile as for the preparation of CB fuels for XRD analysis. A summary of the fuel preparation and analysis for carbons used in this study is given in Figure 7.1.

EIS spectra in this chapter have been translated on the real axis (by subtracting ohmic losses), such that all intercept the graph origin. This was done for ease of visual comparison of the magnitude of low and high frequency electrode arcs.

7.3 Results and discussion

7.3.1 Fuel analysis

XRD analysis of thermally treated coals was used to identify phases of added species in the CB fuels after thermogravimetric analysis (TGA) and direct carbon fuel cell (DCFC) operating conditions. Figure 7.2 shows the room temperature diffraction patterns for all CB fuels following heat treatment under N_2 and under N_2/CO_2 mixture (denoted as CO_2). For CB-Plain, the (002) and (100/101) diffraction peaks assigned to graphitic carbon are obvious at $2\theta \cong 24.8^\circ$ and 43.7° , respectively.

The diffraction patterns of impregnated CB samples show a decomposition of the original nitrate salts to other compounds. The Mg salt in CB-Mg is observed to decompose to MgO under both N_2 and N_2/CO_2 environments, and is expected to assume this stable state at fuel cell operating temperature ($850^\circ C$) [8]. Likewise, the Fe salt in CB-Fe was converted to Fe_2O_3 or Fe_3O_4 . These two cubic phases contain very similar diffraction patterns and cannot be differentiated here. However, at temperatures above $570^\circ C$ Iron may exist in a range of oxide states including FeO, Fe_2O_3 , Fe_3O_4 , [11], and even metallic Fe [5], depending on how reducing the anode chamber atmosphere is. At the temperatures of interest in this study, it is possible for iron oxides to be reduced by carbon alone or CO generated *in-situ* to a metallic Fe [12].

Diffraction patterns for CB-Ca show a dependence on the gaseous atmosphere with the stable Ca-compounds being $Ca(OH)_2$ under N_2 and $CaCO_3$ under N_2/CO_2 atmospheres. $Ca(OH)_2$ is likely to have formed under ambient conditions following the initial heat treatment of the CB-Ca sample, due to the hygroscopic nature of CaO. However, $Ca(OH)_2$ is not thermally stable under either N_2 or N_2/CO_2 atmospheres in the absence of steam and at the temperatures of interest in this study and will decompose to CaO under N_2 atmosphere [13]. $CaCO_3$ is stable up to very high temperatures (in the vicinity of $850 - 900^\circ C$ in air [8,14]) and CaO itself will readily form $CaCO_3$ in the presence of any CO_2 . Therefore $CaCO_3$ is likely to be the dominant phase under the N_2/CO_2 atmosphere at $850^\circ C$ in anode chamber environments.

It should be noted that the strongest diffracting phases are not necessarily the most abundant, nor representative of catalytic activity. Finely dispersed phases may exist

as crystallites too small in size for detection *via* XRD. However, the XRD studies do reveal that all impregnated samples contain metallic compounds that are capable of reverting to catalytically active forms under fuel cell operating conditions.

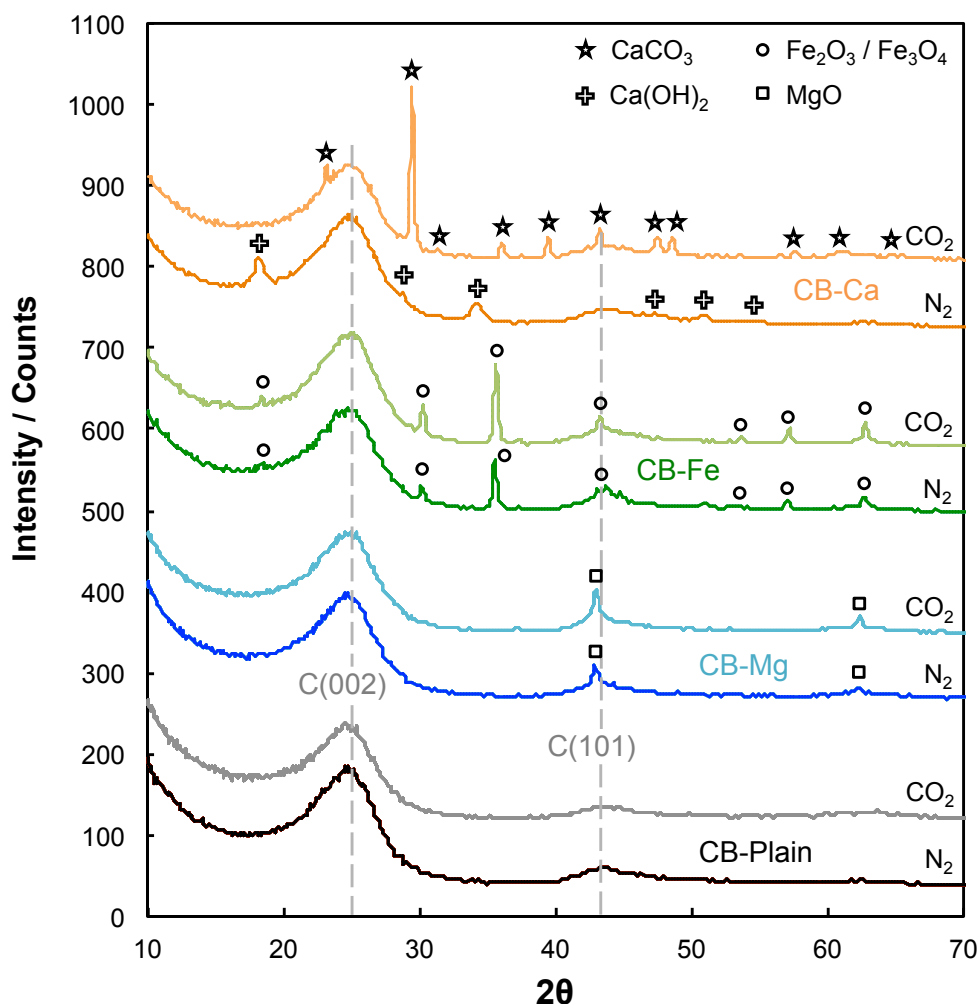


Figure 7.2: XRD spectra and identified phases of Vulcan XC-72 as-received (CB-Plain), Mg-added (CB-Mg), Fe-added (CB-Fe), and Ca-added (CB-Ca), following heat treatment under N_2 and CO_2

7.3.2 Carbon reactivity studies

The influence of catalytic species added to carbon black on enhanced reactivity under N_2 and CO_2 will be discussed in this section. The term ‘reactivity’ is used to describe the reactivity of carbon towards Boudouard gasification. Figure 7.3 gives the weight loss curves (from TGA measurements) of all carbon fuels as a percentage of weight loss against time, with temperature as indicated.

There is a constant weight loss with time for all samples under N_2 atmosphere at temperatures above ~ 400 °C and at 850 °C as a function of time. This type of

behaviour has been observed previously for CB, RM and DM chars (Chapter 4), and may be due in part to reaction of the carbon with trace amounts of O_2 present in the N_2 stream.

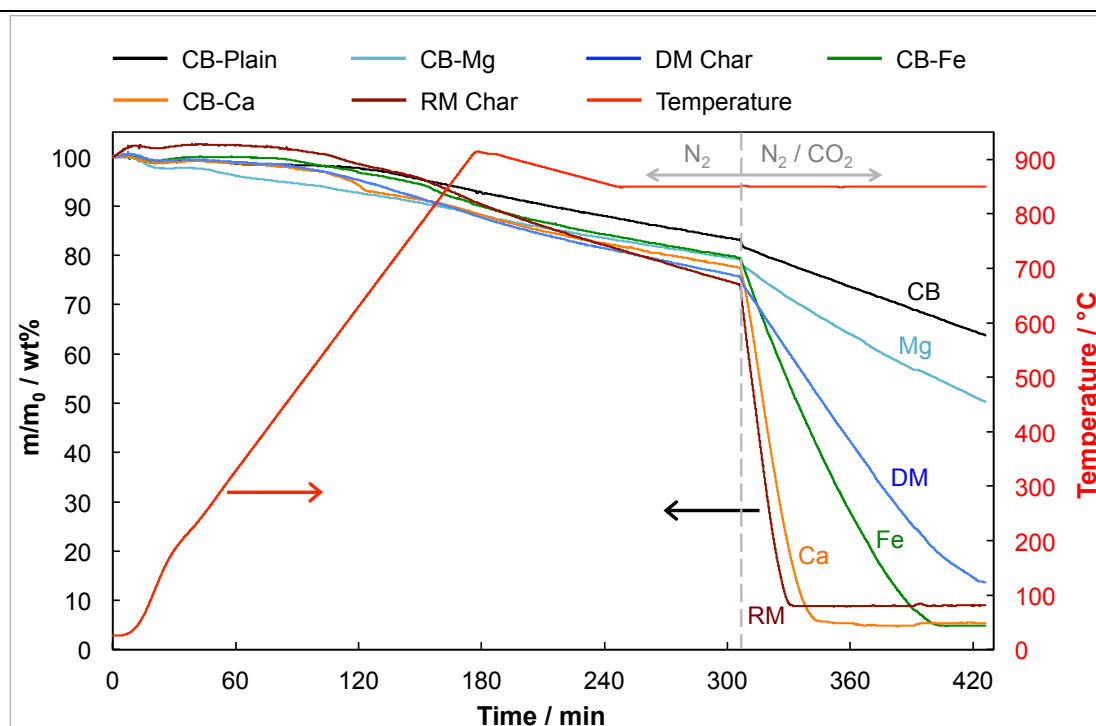


Figure 7.3: Thermogravimetric weight loss curves for carbon fuels under N_2 (during heating and cooling) and N_2/CO_2 (at 850 °C), as indicated, with temperature profile included. m : instantaneous sample mass, m_0 : initial sample mass

Due to small weight fraction of added species, the likelihood of any contribution from metal nitrate additives in weight loss is expected to be minimal. On the introduction of CO_2 into the system at 850 °C, all carbon samples experienced an increase in the rate of weight loss with time, to varying degrees. This enhanced weight loss is attributed to reaction of the carbon with CO_2 via Boudouard gasification, as per Eq. (1.7). Therefore, the relative gradients of the weight loss curves is a good indication of the fuels' reactivity towards Boudouard gasification and can be summarised as $CB\text{-}Plain < CB\text{-}Mg \ll DM < CB\text{-}Fe \ll CB\text{-}Ca < RM$. Not surprisingly, the uncatalysed $CB\text{-}Plain$ exhibited the most sluggish reaction kinetics ($9.3 \text{ wt}\% \text{ loss hr}^{-1}$) of any fuel under N_2/CO_2 , relying solely on reactive carbon sites within the fuel itself and its typically high surface area [15] for reactivity. $CB\text{-}Mg$ showed a marginal improvement in reactivity ($13.8 \text{ wt}\% \text{ loss hr}^{-1}$) over that of $CB\text{-}Plain$. In terms of the other catalysed carbon black samples however, $CB\text{-}Fe$ ($44.4 \text{ wt}\% \text{ loss hr}^{-1}$) and $CB\text{-}Ca$ ($121.2 \text{ wt}\% \text{ loss hr}^{-1}$) far outperformed those of $CB\text{-}Mg$ and $CB\text{-}Plain$ in terms of weight loss, exhibiting significant catalytic activity, as expected [2].

Calcium's tendency to chemisorb CO_2 [16,17], and operating temperatures of 850 °C falling within the temperature window for CaCO_3 decomposition [8], may have resulted in the exceptional catalytic behaviour observed from CB-Ca in this study.

Notably, the catalysed carbon black samples demonstrated visibly comparable reactivities under N_2/CO_2 to those of the chars produced from coal (Figure 7.3). The reactivity of DM (31 wt% loss hr^{-1}) fell between that of CB-Mg and CB-Fe, whereas the reactivities of RM (155.5 wt% loss hr^{-1}) and CB-Ca (121.2 wt% loss hr^{-1}) were quite similar, with RM showing marginally higher conversion rates than CB-Ca. This demonstrates that reactivity of a pure carbon such as XC-72 carbon black can be enhanced and even rival that of a well-known reactive lignite fuel by the simple addition of an inorganic catalytic species.

The residual weights of 4.9, 5.4 and 8.9 wt% for CB-Fe, CB-Ca, and RM, respectively, are the result of this inorganic content and perhaps, to a much lesser extent due to some unreacted carbon. This may occur when most carbon is consumed and some discrete particles of carbon are not making contact with catalytic species. The residual weight for CB-Ca of 5.4 wt% is slightly less than that may be expected (6.01 wt% as CaCO_3 – Table 7.1). With small sample sizes of ~5 mg for TGA measurements, the variance in inorganic content within samples may account for this slight discrepancy. It is obvious from the results that addition of higher amounts of Ca to carbon black above 2.5 wt% would not deliver an exceptional enhancement to Boudouard gasification kinetics [18].

7.3.3 Fuel cell testing

The DCFCs were operated under both N_2 and N_2/CO_2 anode purge gas regimes in order to compare the contribution to Boudouard gasification from CO_2 generated *in-situ* by the electrochemical oxidation of carbon or from CO_2 supplied externally, on fuel cell performance. In the following sections, results will be compared directly with TGA analysis in order to validate the relation between carbon conversion *via* Boudouard gasification and fuel cell performance. In addition, electrochemical impedance spectroscopy (EIS) measurements under open circuit conditions were taken to provide further insight into prevailing reaction mechanisms.

7.3.3.1 Cell ohmic resistance

The initial value of the ohmic resistance component was similar for all cells with a small variation of 1.20 to 1.55 $\Omega \text{ cm}^2$ for various cells with CB-Mg showing the highest value. Considering that same materials were used for cell construction (anode, electrolyte, cathode) and the electrolyte thickness was the same in all cases, the only variation being the fuel composition, these minor inconsistencies can be attributed to the cell fabrication and assembly procedure.

All cells showed an increase in the ohmic resistance with time and over the first ~2 hours of operation in N_2 with 2-4 V-j and P-j curves obtained in between and some current loading. The ohmic resistance increased by 0.2 $\Omega \text{ cm}^2$ for all cells except for CB-Mg which showed an increase of 0.9 $\Omega \text{ cm}^2$. There was further increase in the ohmic resistance in N_2/CO_2 mixture, however, over the ~3 hour period, the ohmic resistance increased by only 0.10 and 0.13 $\Omega \text{ cm}^2$ for CB-Plain and CB-Ca respectively but by 0.58 for CB-Mg and 1.18 $\Omega \text{ cm}^2$ for CB-Fe.

There are some inconsistencies as to the rate of ohmic resistance increase for different fuels and the reason for large increases for CB-Mg and CB-Fe is not clear and may be associated with different cell loading conditions. However, such an increase in the ohmic resistance has been observed previously and has been attributed to loss of carbon / anode contacts and a reduction in the electron conducting pathways as the fuel was consumed (Chapter 5).

7.3.3.2 DCFC operation under N_2/CO_2

Figure 7.4 gives the voltage-current density (V-j) and power density-current density (P-j) curves from DCFC operation under the N_2/CO_2 anode purge gas. It should be noted that the N_2/CO_2 purge was started approximately 2 hours after each cell was in N_2 gas atmosphere where a number of V-j and P-j scans were performed and EIS spectra were obtained. The performance in N_2/CO_2 can be broadly classified in terms of peak power density as CB-Ca >> CB-Fe >> CB-Plain > CB-Mg, with respective power densities of 49, 36, 26, and 19 mW cm^{-2} . This ordering is generally in good agreement with the TGA reactivity study under N_2/CO_2 discussed in the previous section. The more reactive the fuel is towards Boudouard gasification, the greater is the potential supply of gaseous CO to the anode, which in turn contributes to current generation *via* Eq. (1.6) and higher power density.



It is not exactly clear why the performance of CB-Mg was somewhat lower than that of CB despite TGA results suggesting some contribution to gasification kinetics from the added Mg. However, this contribution was minor and has clearly not contributed to improved cell performance in terms of P-j measurements.

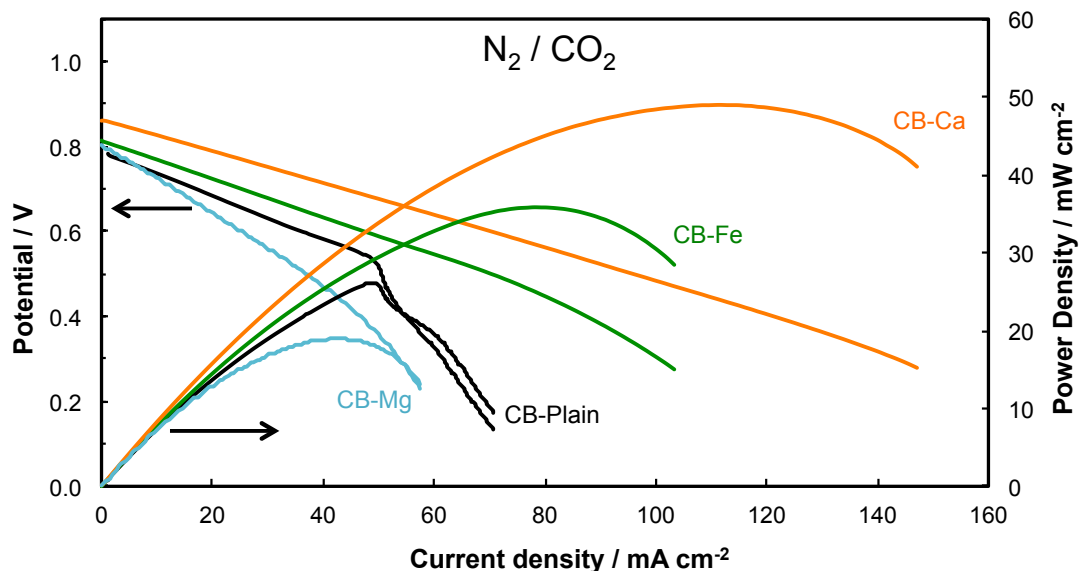


Figure 7.4: Voltage – current density – power density curves for CB fuels at 850 °C under N_2/CO_2 anode purge

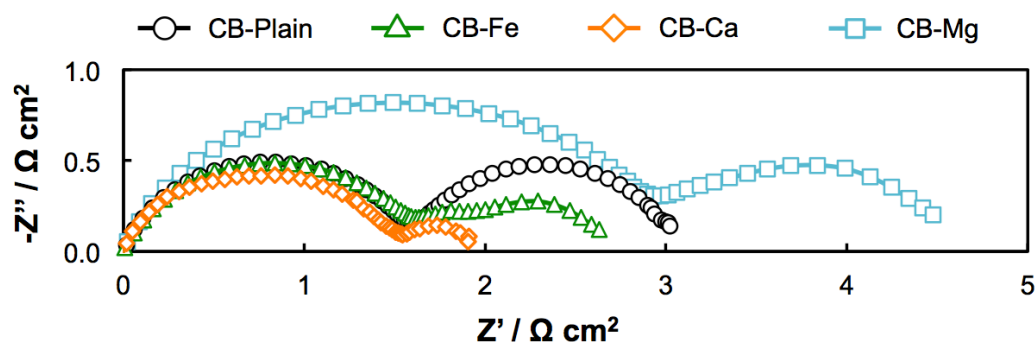


Figure 7.5: Impedance spectra for CB fuels at 850 °C under open circuit conditions and N_2/CO_2 anode purge

EIS measurements for each fuel taken under open circuit conditions and N_2/CO_2 purge are given in Figure 7.5. The impedance response of direct contact solid oxide DCFCs with MIEC anodes has been shown to have, at least, two distinct arcs related to anodic processes [19,20]. Each arc may envelope intermediate sub-steps involved in overall electrochemical oxidation processes [19]. The high frequency arc has been shown to be associated with conversion of solid carbon to CO *via* oxygen anion adsorption on carbon reactive sites and may include small contribution from the cathode. The low frequency arc has been attributed to mass transport / diffusion and

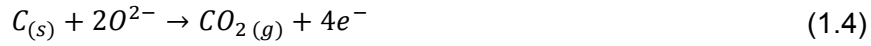
charge transfer processes in electrochemical oxidation of fuel to CO_2 [9,21]. In this work, as with previous studies included in this thesis, the magnitude of the low frequency arc was observed to be inversely proportional to the availability of CO at the anode (Figure 7.5), and this is consistent with TGA analysis and in V-j and P-j data except for CB-Mg. The size of the low frequency arcs here varied substantially between fuels in the order of $\text{CB-Ca} < \text{CB-Fe} < \text{CB-Plain} \leq \text{CB-Mg}$.

CB-Mg displayed an enlarged high frequency arc over that of other fuels (with no cell loading - OCV conditions), which are all quite comparable. It is not clear what has caused this, but it has contributed to the poorer performance observed by CB-Mg in fuel cell testing. The larger total polarisation resistance observed for CB-Mg (Figure 7.5) has resulted in steeper voltage decay with increasing current density in Figure 7.4 compared with the other fuels, and a poorer power density despite a similar OCV to CB-Plain and CB-Fe.

In general the size of the high frequency arc increased with time of testing and trend was clearly obvious in N_2/CO_2 purge gas mixture for all catalysed fuels. Since this arc has been attributed to direct carbon oxidation, these observations are consistent in that as carbon is consumed *via* electrochemical reaction and more so *via* CO_2 gasification, there is a loss of contact between carbon and the anode leading to higher polarisation resistance associated with this arc. In the case of low frequency arc, apart from the large difference in the size of this arc between N_2 and N_2/CO_2 purge gases (see below – Section 7.3.3.3), the effect of time on the size of this arc became quite obvious when tests were performed over longer period of time in N_2/CO_2 . There was a large increase in the size of the low frequency arc and was clearly observed in the case with both CB-Plain and CB-Mg for which long term tests (~20 hrs) data were obtained. This is attributed to consumption of substantial amount of fuel with time *via* Boudouard gasification in N_2/CO_2 during cell standby. In the case of CB-Fe and CB-Ca, the cell ran out of carbon fuel when left overnight, therefore no data could be recorded. However, it confirmed the faster gasification of carbon catalysed with Fe and Ca.

The V-j and P-j curves for CB-Plain contained a kink at current densities above 48 mA cm^{-2} . Such V-j and P-j responses have been observed previously in Chapters 4 and 5 in DCFC systems and are characteristic of mass transport limitations during fuel cell operation at higher loadings. It is likely that during the galvanodynamic mode scan, once the cell had consumed all available CO, produced *via* Eq (1.7), the

reliance of power generation on solid carbon conversion only *via* Eq. (1.4) and (1.5) would result in an increased voltage decay rate.



The OCV's for the DCFC V-j measurements under N_2/CO_2 increased for CB-Plain < CB-Mg < CB-Fe < CB-Ca, with values of 0.78, 0.80, 0.81, and 0.86 V, respectively. The cell OCV is potentially another indicator of the anode gaseous environment, given that it is responsive to the reducing nature of the anode chamber, as well as electrode reactions taking place. An increased concentration of CO at the anode would lead to increase in OCV since it is a reducing gas, and has been observed previously in gasification-catalysed DCFC systems [7,22]. The trend in OCV matches that of the carbon reactivity in TGA analysis and the assertion that CO concentration at the anode might be higher for more reactive carbons.

7.3.3.3 DCFC operation under N_2

V-j and P-j curve under N_2 anode purge gas (Figure 7.6) display signs of diffusion limitations at high current densities, with acceleration in voltage decay for all fuels.

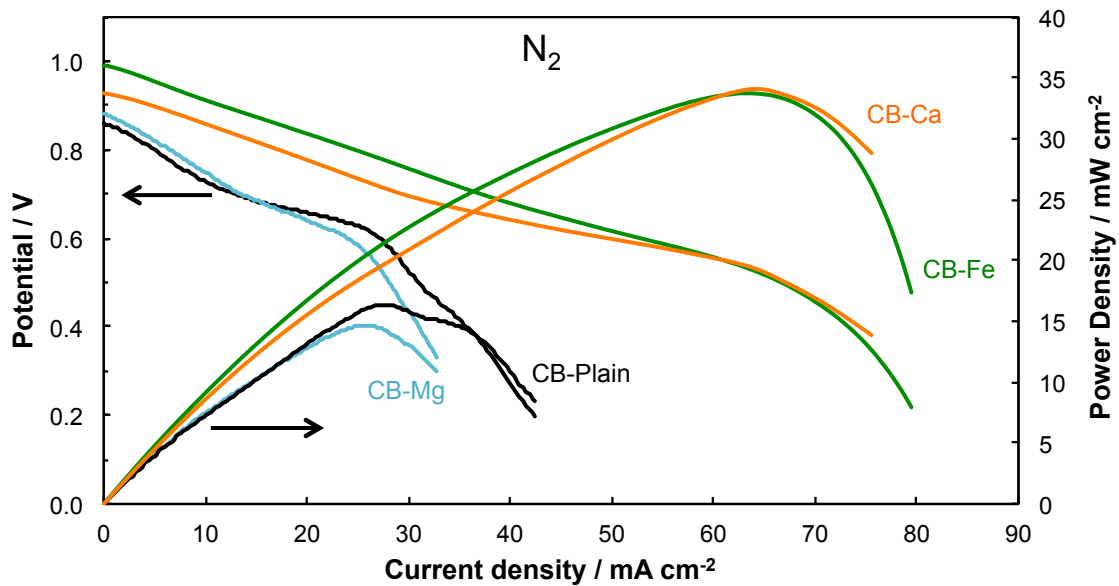


Figure 7.6: Voltage – current density – power density curves for CB fuels at 850 °C under N_2 anode purge

This was largely absent for runs under N_2/CO_2 and is likely a result of a limited supply of CO to the anode in N_2 atmosphere. In an inert atmosphere such as N_2 , the only significant source of gaseous CO is *via in-situ* gasification of CO_2 produced initially *via* the electrochemical conversion of solid carbon (Eq. 1.4). The dependence on the direct electrochemical conversion of solid carbon for current generation has resulted

in the decreased power densities observed under N_2 compared with those under N_2/CO_2 (Figure 7.4).

This behaviour has been observed in previous studies and throughout this thesis when comparing the performance of carbon fuels in inert and CO_2 atmospheres [19-21]. The dependence on electrochemical conversion of solid carbon has also resulted in limiting current densities for less reactive CB-Plain fuel under N_2/CO_2 (Figure 7.4).

There was again an apparent dip in the V-j and P-j curves in Figure 7.6 for the less reactive CB-Plain and CB-Mg fuels similar to that observed in Figure 7.4 for CB-Plain in N_2/CO_2 atmosphere during scans in the galvanodynamic mode. This was followed by a temporary correction in voltage and power decay as additional CO becomes available to the anode *via* Boudouard gasification of the fuel with CO_2 generated *in-situ* from cell operation as observed in previous work (Chapter 5). This behaviour was also somewhat evident for CB-Ca and CB-Fe in N_2 although it was considerably less conspicuous. Depending on the gas atmosphere and scan conditions, the generation of additional CO *via* reactions in Eq. (1.5) and (1.7) may lead to temporary mass transport limitation and occurs at lower current densities for the less reactive fuels (Chapter 4) with the behaviour amplified in the case of N_2 as reaction in Eq. (1.7) is less prevalent in an inert atmosphere (Chapter 5) and [21].

Summarising each fuels' performance under N_2 in terms of peak power density gives $CB-Ca \approx CB-Fe \gg CB-Plain \geq CB-Mg$, achieving power densities of 34, 34, 16, and 15 $mW\ cm^{-2}$, respectively. This is in general agreement with the observations under N_2/CO_2 with the main exception being the comparable performances of the CB-Ca and CB-Fe fuels. It is likely that Fe is present in a more reduced state under N_2 than when under the oxidising presence of CO_2 , and therefore more catalytically active [7]. The high OCV of the cell under N_2 for the CB-Fe fuel (0.99 V) as per the Nernst equation indicates a low partial pressure of oxygen (pO_2) at the anode of $< 10^{-16}$ atm pO_2 , conditions under which Fe will be in its metallic state at 850 °C. Likewise, CaO is probably the dominant phase under N_2 , though it readily undergoes transformations between CaO and $CaCO_3$ at this temperature *via* Eq. (7.3) – (7.5), depending on the availability of CO_2 [8]. This property possibly makes CaO/ $CaCO_3$ a particularly good catalyst for carbon conversion *via* Boudouard gasification.

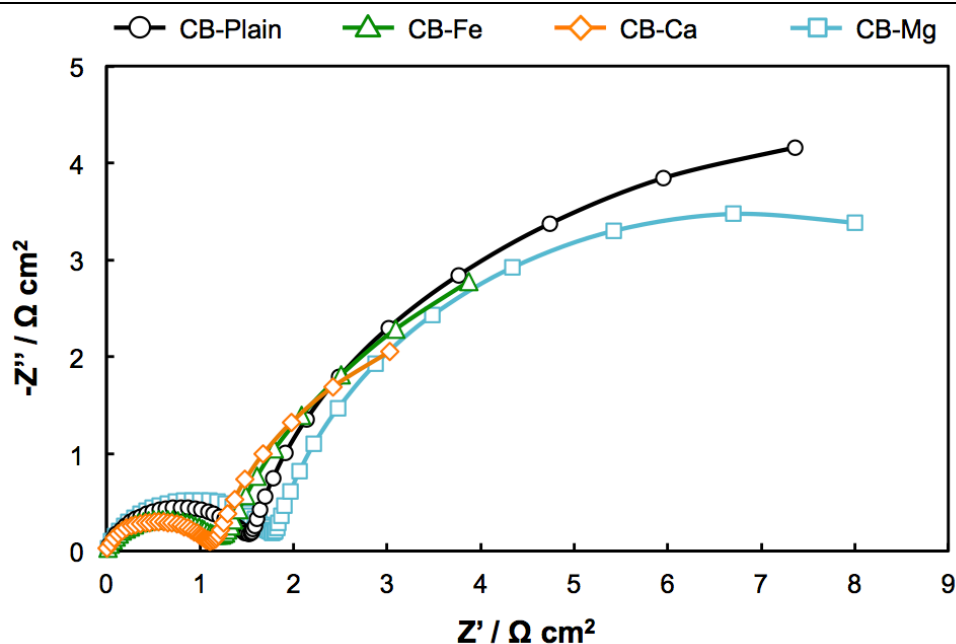


Figure 7.7: Impedance spectra for CB fuels at 850 °C under open circuit conditions and N_2 anode purge

EIS measurements taken under N_2 atmosphere in open circuit voltage conditions (Figure 7.7) show marginally reduced polarisation values for CB-Fe and CB-Ca arcs compared with those of CB-Plain and CB-Mg. The size of the low frequency arc was smaller for the more reactive fuels (CB-Ca, CB-Fe) compared with CB-Plain and CB-Mg, but significantly higher for all fuels in N_2 compared to that observed for N_2/CO_2 . This is likely due to lower concentration of CO at the anode under the inert purge gas. Since Boudouard gasification of the fuel is not occurring under N_2 purge and at open circuit voltage, the reduced concentration of gaseous reactive species such as CO at the anode results in mass transport limitations leading to significantly larger low frequency arcs under N_2 . [9,19,21].

The size of the high frequency arc is similar under both N_2 and N_2/CO_2 atmospheres for all carbon fuels (Figures 7.5 and 7.7) reaffirming the hypothesis proposed in a previous study where this arc was attributed to the electrochemical oxidation of solid carbon with a small contribution from the cathode [20].

The OCV under N_2 for all fuels was significantly higher than under N_2/CO_2 . This has been observed previously (Chapter 5) and has been related to $CO/CO_2/O_2$ equilibrium as well as the higher impurity levels of O_2 in the food grade N_2/CO_2 gas than in the high purity N_2 . The same purge gases are used in the present study, and the concentration of molecular oxygen in the anode chamber is likely just as relevant

to OCV here. In addition, Eq. (1.4) has a higher associated reversible voltage than Eq. (1.6) at operating temperature [23]. An increased reliance on the electrochemical conversion of solid carbon under N_2 via Eq. (1.4) may also have contributed to a higher OCV.

As was observed for V-j results under N_2/CO_2 atmosphere, the more reactive fuels (CB-Fe and CB-Ca) again show higher OCV values under N_2 (Figure 7.6) than CB-Mg and CB-Plain, at 0.99, 0.93, 0.88, and 0.86 V, respectively. As mentioned above, the OCV of a fuel cell is a complicated product of many factors, however, the trends observed in both anode purge gas environments for various fuels do indicate the possibility that OCV and carbon reactivity are somewhat linked.

7.4 Conclusions

Carbon black (Vulcan XC-72) as received, and with addition of 2.5 wt% Ca, Fe, and Mg (metal basis), was tested for reactivity towards Boudouard (CO_2) gasification by conducting TGA at 850 °C. It was found that under CO_2 , the reactivity increased from CB-Plain < CB-Mg << CB-Fe << CB-Ca, indicating the relative catalytic properties of the additives. In addition, CB-Ca displayed a similar level of reactivity in the presence of CO_2 to that of a highly reactive char produced from Victorian brown coal which had Ca and a number of other inorganic metallic species. The performance study of the carbon black fuels was extended to DCFC testing under both N_2 and N_2/CO_2 anode atmospheres. A good correlation was found between TGA analysis and DCFC performance, particularly under N_2/CO_2 . It is possible that the state of the metallic species may vary between N_2 and N_2/CO_2 atmospheres at the temperature used in this study, which influenced the performance of CB-Ca and in particular CB-Fe. EIS measurements confirmed the variation in fuel-based performance was largely due to availability of gaseous reactants, presumably CO, at the anode. In relation to this, OCV was also observed to increase for more reactive fuels.

References

1. Tomita A, Ohtsuka Y. Chapter 5 - Gasification and Combustion of Brown Coal. In: Chun-Zhu L, editor. *Advances in the Science of Victorian Brown Coal*. Amsterdam: *Elsevier Science*; **2004**. p. 223-85.
2. Hüttinger KJ, Nattermann C. Correlations between coal reactivity and inorganic matter content for pressure gasification with steam and carbon dioxide. *Fuel*. **1994**;73:1682-4.
3. McKee DM. *Chemistry & Physics of Carbon*: *CRC Press*; **1981**.
4. Hippo E, Walker Jr PL. Reactivity of heat-treated coals in carbon dioxide at 900 °C. *Fuel*. **1975**;54:245-8.
5. Ohtsuka Y, Kuroda Y, Tamai Y, Tomita A. Chemical form of iron catalysts during the CO₂-gasification of carbon. *Fuel*. **1986**;65:1476-8.
6. Furimsky E, Sears P, Suzuki T. Iron-catalyzed gasification of char in carbon dioxide. *Energy Fuels*. **1988**;2:634-9.
7. Tang Y, Liu J. Effect of anode and Boudouard reaction catalysts on the performance of direct carbon solid oxide fuel cells. *Int J Hydrogen Energy*. **2010**;35:11188-93.
8. McKee DW. Catalytic effects of alkaline earth carbonates in the carbon-carbon dioxide reaction. *Fuel*. **1980**;59:308-14.
9. Li C, Shi Y, Cai N. Performance improvement of direct carbon fuel cell by introducing catalytic gasification process. *J Power Sources*. **2010**;195:4660-6.
10. Li X, Zhu Z, De Marco R, Bradley J, Dicks A. Evaluation of raw coals as fuels for direct carbon fuel cells. *J Power Sources*. **2010**;195:4051-8.
11. Olszewski T. Oxidation Mechanisms of Materials for Heat Exchanging Components in CO₂/H₂O-Containing Gases Relevant to Oxy-fuel Environments. Jülich: *Forschungszentrum Jülich*; **2012**.
12. Furimsky E, Palmer A. Catalytic effect of lignite ash on steam gasification of oil sand coke. *Applied Catalysis*. **1986**;23:355-65.
13. Molinder R, Comyn TP, Hondow N, Parker JE, Dupont V. In situ X-ray diffraction of CaO based CO₂ sorbents. *Energy & Environmental Science*. **2012**;5:8958-69.
14. Hippo EJ, Jenkins RG, Walker Jr PL. Enhancement of lignite char reactivity to steam by cation addition. *Fuel*. **1979**;58:338-44.
15. Ma Y, Wang H, Ji S, Goh J, Feng H, Wang R. Highly active Vulcan carbon composite for oxygen reduction reaction in alkaline medium. *Electrochim Acta*. **2014**;133:391-8.

16. Emmett PH, Brunauer S. Accumulation of Alkali Promoters on Surfaces of Iron Synthetic Ammonia Catalysts. *J Am Chem Soc.* **1937**;59:310-5.
17. Radović LaR, Walker PL, Jenkins RG. Importance of catalyst dispersion in the gasification of lignite chars. *J Catal.* **1983**;82:382-94.
18. Spiro CL, McKee DW, Kosky PG, Lamby EJ, Maylotte DH. Significant parameters in the catalysed CO₂ gasification of coal chars. *Fuel.* **1983**;62:323-30.
19. Kulkarni A, Giddey S, Badwal SPS. Yttria-doped ceria anode for carbon-fueled solid oxide fuel cell. *J Solid State Electrochem.* **2015**;19:325-35.
20. Kulkarni A, Giddey S, Badwal SPS, Paul G. Electrochemical performance of direct carbon fuel cells with titanate anodes. *Electrochim Acta.* **2014**;121:34-43.
21. Giddey S, Kulkarni A, Munnings C, Badwal SPS. Performance evaluation of a tubular direct carbon fuel cell operating in a packed bed of carbon. *Energy.* **2014**;68:538-47.
22. Munnings C, Kulkarni A, Giddey S, Badwal SPS. Biomass to power conversion in a direct carbon fuel cell. *Int J Hydrogen Energy.* **2014**;39:12377-85.
23. Giddey S, Badwal SPS, Kulkarni A, Munnings C. A comprehensive review of direct carbon fuel cell technology. *Progr Energy Combust Sci.* **2012**;38:360-99.

8

Conclusions and recommendations

8.1 Conclusions

This research has advanced the knowledge in the field of direct carbon fuel cells (DCFCs), in particular regarding the influence of fuel-based properties on DCFC performance.

The first major contribution is in the identification that the inorganic content inherent in Victorian brown coal (VBC) has a profound influence on the DCFC performance. Boudouard gasification kinetics of raw and demineralised brown coal chars, as well as a pure synthetic carbon (carbon black), were compared *via* thermogravimetric analysis (TGA). The raw coal char was found to have exceptional reactivity in CO₂ and was related to the role of catalytic species within the coal. The superior performance of the raw coal char in DCFC testing, in terms of voltage – current density – power density measurements, was attributed to its ability to generate significant additional CO *in-situ* via Boudouard gasification during cell operation. This finding highlights the importance of Boudouard gasification kinetics in DCFC operation and its contribution to cell power output. The role of individual catalytic species (Ca, Fe, Mg) in this process was also investigated. In terms of peak power density of the cell, the contribution of catalytic species to cell performance under anode chamber atmospheres of N₂ was found to be Ca \approx Fe \gg Mg, and in the presence of CO₂ was Ca \gg Fe \gg Mg. The performance of Mg-catalysed carbon black in both cases was similar or lower than that of plain carbon black, suggesting little to no catalytic contribution to cell performance. The introduction of CO₂ directly into the anode chamber also resulted in improved DCFC performance and prolonged operation under constant load due to gasification of the carbon.

The second major contribution of this work came from extended operating time, over the course of a day, of the DCFC involving VBC. A mechanism for deterioration in cell performance with the passage of current was related to carbon consumption from the anode/current collector interface. The ohmic resistance of the cell was observed to increase following the passage of current under various loading conditions. This

was attributed to the loss of electronic conducting pathways at this interface as the carbon was consumed, and resulted in a steady drop in cell performance. Electrochemical impedance spectroscopy measurements taken during cell operation provided further insight into carbon conversion, by the association of low and high frequency arcs to charge transfer processes and diffusion limitations, in line with other work in this field. The inorganic content in the raw char was also found to have a detrimental effect on cell performance during prolonged DCFC operation *via* deposition of ash on the anode surface resulting in a reduction in anode active area. Due to the greatly reduced ash content, the demineralised char sample offered superior stability in DCFC performance over time and under constant current load.

The third contribution involving anode studies revealed that Lanthanum Strontium Cobalt Ferrite (LSCF), a mixed ionic electronic conducting electrode, was overall stable under DCFC operation with Victorian brown coal over the course of a day's experiment. However, the LSCF anode experienced some coarsening and minor phase instabilities which is suggestive of long-term instability under the highly reducing atmosphere of a DCFC. The evaluation of an alternative Nickel-Gadolinia Doped Ceria/Yttria Stabilised Zirconia (Ni-GDC/YSZ) anode delivered stable performance when operated on demineralised brown coal and as such is a promising anode candidate for future DCFC studies.

The high performance and stability of cell operation on Victorian brown coal with minimal pre-treatment is encouraging, and warrants further investigation into its use as a fuel for DCFCs.

8.2 Contribution to knowledge in the field

The major specific contributions of findings reported in this thesis are listed as:

- (1) A critical review of solid fuels used within DCFCs,
- (2) Identification of Victorian brown coal as a promising fuel for use in direct carbon fuel cells,
- (3) Enhanced power output of the cell by inherent and introduced Boudouard gasification catalysts,
- (4) Proposed DCFC performance degradation mechanisms including the deposition of ash at the anode surface as well as the consumption of solid,

carbon from the anode/current collector interface with associated loss of electronic conductive pathways,

- (5) Further insight into carbon conversion in a DCFC under different anode atmospheres *via* the use of electrochemical impedance spectroscopy measurements during cell loading and cell standby, and
- (6) Identification of Ni-GDC/YSZ anode as a promising electrode material for use in DCFCs.

8.3 Recommendations for future works

The work contained in this thesis has identified Victorian brown coal as a promising candidate for future DCFC operation and research. The following specific recommendations are made:

- A study investigating the effect of carbon particle size distribution on physical contact type solid oxide DCFCs.
- Though it is highly likely that near-complete devolatilisation of the coal chars occurred during heating and seal formation in studies included in this thesis, the influence of volatile products on DCFC performance in a closed system or system under continual carbon feed is warranted.
- For applications where the highly efficient direct electrochemical conversion of solid carbon is a priority, the benefits of pre-treatment in the removal of inorganic species from coal has been demonstrated. However, the high reactivity of Victorian brown coal and promising DCFC performances suggest that a solution to the accumulation of ash residues at the anode surface would greatly contribute to prolonged cell operation in addition to maintaining high DCFC performance. In addition, an engineering solution to the delivery of fresh solid carbon to the anode/current collector interface is also essential to the continual operation of a DCFC.
- A detailed investigation of the effect of impurities in coal on the chemical, structural, and phase stability of materials used in DCFCs would provide further insight into the nature of degradation of critical DCFC components during operation. A high-temperature *in-situ* study would provide the greatest benefit to the identification of candidates for future use in commercial DCFC systems.